UNIVERSITY OF
CAMBRIDGE

High Frequency Induction Welding & Post-Welding Heat Treatment of Steel Pipes

A dissertation submitted for the
degree of Doctor of Philosophy

by Yan Pei
Girton College

Department of Materials Science and Metallurgy
University of Cambridge
June 2011

Pipelines: the world's energy lifeline

Preface

This dissertation is submitted for the degree of Doctor of Philosophy at the University of Cambridge. The work reported was carried out under the supervision of Professor H. K. D. H. Bhadeshia in the Department of Materials Science and Metallurgy between October 2007 and September 2010. To the best of my knowledge, this work is original, except where suitable references are made to previous work or work done in collaboration. Neither this, nor any substantially similar dissertation has been submitted for any degree, diploma or qualification at any other university or institution. This dissertation does not exceed 60,000 words in length.

Some of the work described herein has been presented in the following publications:

P. Yan, Ö. E. Güngör, P. Thibaux, and H. K. D. H. Bhadeshia, Crystallographic texture of induction-welded and heat-treated pipeline steel, Advanced Materials Research, Vol. 89–91 (2010) 651–656.

P. Yan, Ö. E. Güngör, P. Thibaux, and H. K. D. H. Bhadeshia, Induction welding and heat treatment of steel pipes: evolution of crystallographic texture detrimental to toughness, Science and Technology of Welding and Joining, Vol. 15 (2010) 137–141.

Ö. E. Güngör, P. Yan, P. Thibaux, M. Liebeherr, H. K. D. H. Bhadeshia, and D. Quidort, Investigations into the microstructure–toughness relation in HFI welded pipes, IPC2010-31372, Proceedings of 8th. International Pipeline Conference, 27 September–1 October 2010, Calgary, Alberta, Canada.

Yan Pei

June 2011

Acknowledgments

First of all I would like to acknowledge my supervisor, Professor Harry Bhadeshia, for his enthusiasm and guidance on my research work.

I am indebted to ArcelorMittal Research and Development, Gent, Belgium, who provides financial support, the materials and data for this project. I would like to express my sincere thanks to Ms. Özlem Esma Güngör, Dr. Philippe Thibaux, Dr. Martin Liebeherr, Mr. Eric Hivert, and Dr. David Quidort for their trust in me and inspired discussions about this project.

I would also like to thank Professor Lindsay Greer for the provision of laboratory facilities in the Department of Materials Science and Metallurgy at the University of Cambridge, a lot of technical staff in the department for help on experiments, and all the current and previous members of the Phase Transformations and Complex Properties research group during these three years, for making my time in Cambridge more enjoyable with their help and friendship, especially Mathew for all the constructive suggestions and help whenever I was not having a clear mind.

At last, I take this opportunity to express my gratitude to my family and friends for their love and support.

Abstract

Steel pipelines for the transmission of gas and oil may extend thousands of kilometres and they represent one of the most sophisticated engineering achievements of the modern era.

Some of the steel tubes are manufactured from plates which are formed into an appropriate shape and then seam welded. An efficient and high productivity process for achieving this involves high-frequency induction welding in which the abutting surfaces are forged together following localised heating. This disrupts the structure of the steel, so the joining operation is followed immediately by one or more induction heat-treatments, with the aim of regenerating the properties degraded by the welding operation. It is found, unfortunately, that the toughness at the location of the weld junction does not improve as a result of the heat treatment. An investigation of this phenomenon is the essential aim of this thesis.

The method involved the use of a variety of characterisation techniques to investigate, for example, the possibility of a high density of non-metallic particles decorating the junction, the passive role of decarburisation, microstructural gradients, micromechanical gradients, *etc.* The breakthrough came when it was established for the first time that the poor toughness is due to the existence of a coarse crystallographic grain size (as opposed to a metallographic grain size), because clusters of grains adopt a similar orientation in space. This reduces the resistance to cleavage crack propagation. The effect is not eliminated by heat-treatment because of an “austenite memory effect” which regenerates the coarse structure on cooling the pipe to ambient temperature.

The crystallographic grain size is the major effect which embrittles the weld of the pipelines in sour service environment. When it comes to less sophisticated pipelines steels joined by the same process, both crystallographic texture and inclusions in the weld junction play important roles in causing low toughness.

In order to propose a method of remedial measures to strengthen the welds, a modified post-welding heat treatment has been investigated experimentally, which may in the future be implemented on an industrial scale.

Contents

Chapter 1

Introduction

Pipelines used for the transportation of natural gas and oil, can be fabricated using high frequency induction welding [1]. There is a variety of steels used in such manufacturing operations, but this study is focused on a grade of commercial steel, designated X65, which belongs to the category of strong steels and is used widely by the pipeline industry [1–3]. The process of pipe-making involves the mechanical forming of a plate into a cylinder, and then the joining of the abutting faces by a rapid, localised induction heating and joining process.

The final joint is quite narrow, but has a central region about 2 mm in width which may to some extent be decarburised. Yu [4] mentioned that the carbon concentration at the joint was reduced by as much as 30% relative to the base metal. The decarburised zone naturally represents a source of weakness. However, the welding process is then followed immediately by an induction heat treatment, with the aim of replacing the coarse microstructure associated with the welding operation with smaller prior austenite grains and fine ferritic phases. Another aim of this austenisation is to homogenise the carbon at the weld junction and hence remove the decarburised layer. A second cycle of post-welding heat treatment is then applied to produce the final microstructure which is destined for service [5]. Quality control tests including cross-weld tensile tests and cross-weld Charpy tests are carried out to establish the suitability for application [3, 5, 6]

High frequency induction welding has been a common industrial processing method since 1960s [7]. However, not much information related to this technique and the welds it produces is available in the academic literature. In particular, the properties of induction welds, although well-characterised, are simply not understood. It follows that the methods available to control the properties are not clear. The work presented in this thesis has been conducted with the aim of identifying the problem of low toughness at the weld junctions when compared against the metal which is not influenced by the welding process.

To achieve the goal it has been necessary to employ high resolution microstructural and micromechanical characterisations. The process involves the systematic validation or dismissal of all the speculative theories that have been proposed to explain the local mechanical behaviour of the induction welds. As will be seen later, there were some surprising outcomes and novel ideas which seem to rationalise observations and reveal the way forward towards quality welds.

Chapter 2

Literature Review

2.1 Pipe manufacturing process

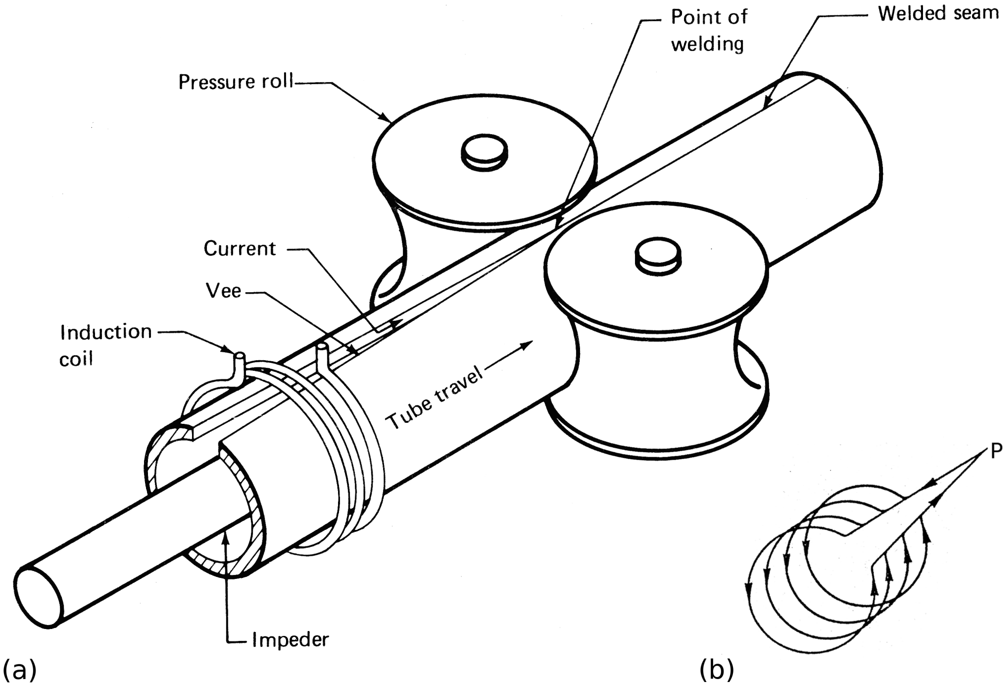

Figure 2.1: Illustration of (a) the high frequency induction welding process [8] and (b) path of the high frequency current [7]. 'P' is the point where welding occurs.

There are two main types of pipes for industrial use. One is the seamless pipe and the other is produced in the form of a pipe by welding. The most widely used categories of welding methods for pipe-making are gas-metal/submerged arc welding and electric resistance/induction welding. The work presented in this thesis is particularly focused on the steel pipes produced by high frequency induction welding. It needs to be mentioned here that this technology is also suitable for tubing made of other metals for different purposes [8].

2.1.1 High frequency induction welding

High frequency induction welding is a modern manufacturing method, by which hot-rolled plates of high strength steels can be made into pipes for long distance gas and oil transportation. Both longitudinal and spiral seams can be welded by this technology. Figure 2.1a shows an example of the mill set-up in the welding station for longitudinal seam-welding, where the hot-rolled steel plates are curled into a tube shape by pressure rolls, the two abutting edges of the plate are heated up during their passage through the induction coils, and pressed together by the welding station pressure rolls. The convergence point, and the separated abutting edges in front of it forms a V shape. This point is called the 'Vee' apex, which defines the onset of the joint formation that leads to a weld. The high frequency current flows along the outside surface of the tube and along the edges of the Vee, so that the electrical circuit is completed, as shown in Fig. 2.1b. This circuit is formed in the context of three principal features of high frequency induction heating [7]:

- an induction effect allows the contactless transmission of power to the workpiece with the aid of an alternating magnetic field. The induction coil generates this alternating field according to:

  $$P_i = k \cdot \sqrt{f} \cdot A_W^2 \tag{2.1}$$

  where P_i is the induced power (kW cm^{-2}), k is a constant, A_W represents the Ampére-turns per cm of the inductor and f is the frequency (Hz).

- A skin effect occurs because at high frequencies, electrical currents and magnetic fields can exist only in a thin layer at the conductor's surface [9]. The thin layer is defined as a skin depth, ε, in cm:

  $$\varepsilon = 5030\sqrt{\frac{\varrho}{\mu f}} \tag{2.2}$$

  where ϱ is the specific resistance (Ω cm), and μ is the relative permeability of the material of which the conductor is made [7].

- The proximity effect means that the high-frequency currents always flow along the path of least resistance. Two currents flowing in opposite directions on the same material are mutually attracted, as in the Vee [7]. Warren [10] suggested that the position of welding should be within 6 to 14 mm upstream from the centreline of the induction coils, so that Vee angle is kept within an acceptable range.

Only the heating along the edges of the Vee is useful for welding. The temperature rise is localized there because of the combination of the skin and proximity effects. The current flowing at the tube periphery gives rise to a heat loss which must be kept small. This is achieved by reducing the resistance at the tube circumference through substantially broadening the current path. A suitably designed induction coil is essential [7]. The distribution and penetration of heat from the high frequency current are controlled by the skin and proximity effects together with the frequency of the power supply and the mill speed, so the welding frequency and mill speed must be chosen carefully [11].

Although the proximity effect makes the two abutting edges mutually attract, it can be impeded by [10]:

- roughness on the contacting surfaces;
- an oxide layer or foreign matter;
- a thin layer of absorbed gas on the oxide surface;
- the relative positions of the abutting edges during the introduction of the high frequency current to achieve heating.

By applying pressure from the rolls, the melted material with relatively high content of impurities is expelled from the joint. The metal at the junction flows towards the inner and outer surfaces of the pipes. The quantity expelled is defined as the difference between the circumference measured at the Vee angle in front of the rolls and at pipes at the rear of the rolls, which is usually $1 \sim 5$ mm. The extent of squeezing can affect the weld strength and toughness [4]. After welding, the rejected materials are mechanically trimmed off from both the inner and outer surfaces of the pipe.

Certain mill adjustments and roll designs also determine the quality of the welding. Figure 2.2 shows five different configurations of the pressure rolls used in the welding station. Some criteria were followed in the design, such as, the fact that the top flange must be large enough in diameter to fully contain the top edges, and the head rolls located on top should be as thin as possible since they should not do any edge forming in bending. The top head rolls can be used to correct only minor edge mismatches [10]. The ideal disposition of the abutting edges, their melting and two kinds of mismatch are illustrated in Fig. 2.3. Both vertical (Fig. 2.3c) and angular mismatch (Fig. 2.3d) result in uneven heating and heat distribution.

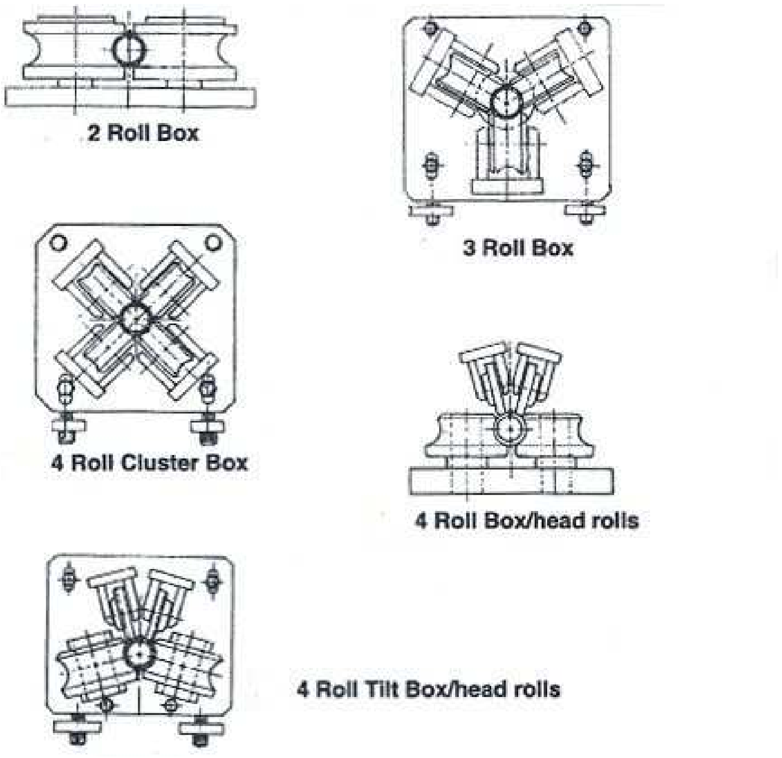

Figure 2.2: Illustration of a variety of roll configurations used in the welding of pipes [10].

2.1.2 Advantages

High frequency welding includes induction and electric resistance welding. The latter requires electrical contact to heat the weld area, while deterioration of the final microstructure of the welds and pipes by the electrical contact normally is not a concern for high frequency induction welding.

High frequency welding is more energy-efficient than conventional electrical resistance or induction welding. As the data from the 1980s show, 60% of the energy from the power line turns into useful heat during the process [8].

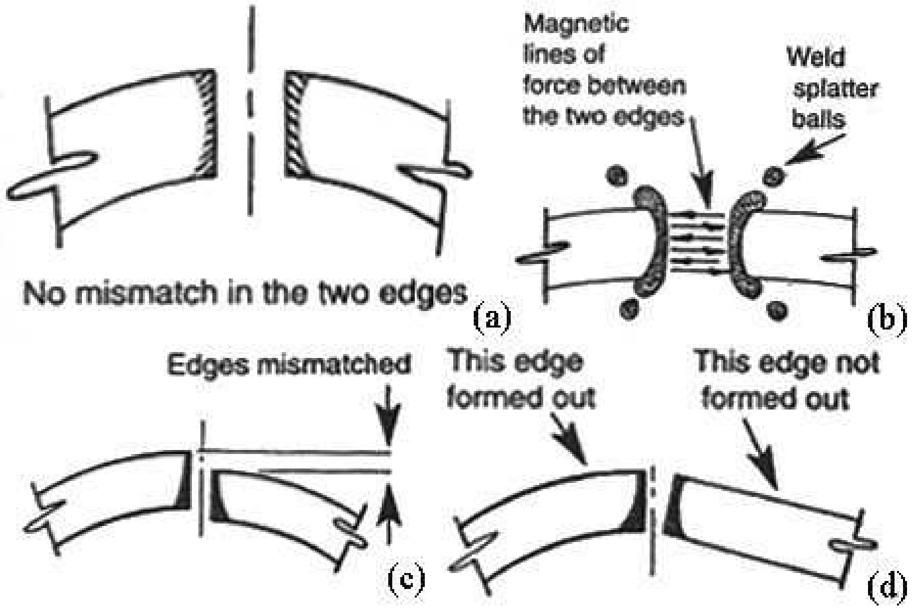

Figure 2.3: (a) Ideal relationship is to have the two abutting edges parallel and matched in the vertical direction. (b) The electro-magnetic force ejects hot metal during the high frequency pipe welding. (c) Two edges are mismatched in the vertical direction. (d) Two edges are mismatched angularly [10].

Compared to submerged arc welding, the induction process does not require filler metal and hence it has greater productivity [8, 12].

The narrow weld joint and heat affected zone resulting from high frequency induction welding is stronger than the wider weld from many other welding processes because of the absence of cast structure and the minimization of the distortion of the joining parts [8]. In order to guarantee the quality of the welded joint, a lot of details need to be controlled. These are discussed in the following section.

2.1.3 Quality control

There are several parameters which must be controlled at the welding station in order to make the products of steel tubes/pipes satisfy the requirements of service under the gas or fluid pressure. Some of these parameters are: trimmed width of the material entering the mill, circumferential reduction in the forming stands and welding station, and size and shape of the unwelded steel entering the welding station. The circumference of the welded and outer-diameter trimmed pipe must be less than the girth of the unwelded tube, so as to make sure that a certain amount of material is squeezed out of the weld junction. All these efforts aim to avoid defects due to improper power adjustment, which can cause a cold, pasty weld, or no weld at all, or a hot weld with blow hole type voids [10].

The magnitude of heat input is directly reflected in the microstructure, which can reveal the quality of the weld so as to determine whether the variables are adjusted properly or not. The main control parameters are [4]:

- f_n, f_i, f_o: width of the weld junction measured at the geometric neutral line, inside and outside wall of the pipe.
- h_n, h_i, h_o: width of heat-affected zone measured at the corresponding position as above.
- Standard range: $f_o \approx f_i \approx (1.3 \sim 3)\ f_n$, $f_n = 0.02 \sim 0.14$ mm
- Warning range: $f_o \approx f_i \approx (3 \sim 5)\ f_n$, $f_n = 0.01 \sim 0.02$ mm or $f_n = 0.14 \sim 0.17$ mm

The optimum welding condition for the input power could be determined experimentally using an electric resistance welding simulator, nondestructive defect inspection and impact energy measurements. The optimum heat input range should be re-established whenever the material conditions are changed.

As the contemporary demand for oil and natural gas continues to increase, the principal specifications driving these demands have been [3]:

1. achievement of higher strength grades which are capable of preheat free welding with cellulosic electrodes;
2. high steel cleanness for resistance to ductile fracture propagation in the transportation of natural gas, and high integrity of the longitudinal weld seam;
3. control of centreline segregation levels to ensure weld quality in strong small-diameter pipes made from centre slit coils.

The requirement for pipes of higher strength and ductility has led to an increase in manganese contents in the hot rolled sheet steels. However, a higher manganese content ($\geq$1.2 wt%) and a greater wall-thickness are likely to induce "penetrator" defects in the welded zone. These defects are generally classified as:

1. residual FeO-MnO-SiO_2-(Al_2O_3) oxides left without being squeezed out from the joint;

2. exposed cracks on the external surface of the pipe due to cavity formation and hot cracking;
3. blow-holes including oxides.

Penetrator defects become more frequent as the heat input is increased and the mill speed reduced, and the Mn/Si ratio. The manganese and silicon content at the welded joint noticeably decreases with the heat coefficient Q, which is defined as:

$$Q = \frac{E_P I_P}{vt} \tag{2.3}$$

where E_P is the voltage on the plate (kV), I_P is the current on the plate (A), v is pipe welding speed (m/min) and t is the wall-thickness of pipe. This heat coefficient is generally employed as an index for pipe welding conditions. This value is higher with a decrease in the mill speed and with an increase of the welding heat input [13].

Generally speaking, a weld joint in an induction welded pipe may contain defects caused by environmental factors or inappropriate power during seam welding [14]. A lot of previous work was done to detect and analyse these defects from the aspect of fatigue properties [15, 16], since they can initiate fatigue failure. The fatigue crack propagation rate of a welded joint is generally lower than that of base metal. This may be caused by the hardened microstructure and distorted fatigue crack propagation path within irregularly arrayed coarse grains in the weld joint [17, 18]. Fine oxides formed at the weld joint at optimum input power did not lead to a deterioration of the fatigue propagation rate [19]. Beller and Holden [20] introduced a nondestructive test method for the detection and classification of defects.

Steel cleanliness requires low sulphur contents to optimise the pipebody fracture toughness and avoidance of clustered alumina inclusions to minimise the occurrence of ultrasonic testing indications in the vicinity of the longitudinal weld seam. Thus the maximum sulphur content is restricted to 0.005 wt% and the actual level of calcium is typically lowered from 0.0035 wt% post injection to 0.0008 wt% post vacuum degassing during steel-making [3, 21]. For more severe requirements of ‘rich’ gas[1] transportation where higher Charpy energy values may be needed, restrictions on sulphur content of 0.003 wt% may be necessary.

---

[1] Natural gas containing large amount of liquefiable hydrocarbons.

2.1.4 Post-welding heat treatment

The main difficulty in welding is the prevention of an abrupt deterioration of properties as a result of the appearance of structures, which reduce the resistance to brittle fracture in the heat-affected zone [22]. For this reason, a two-cycle post-welding heat treatment is used in this study. The weld was cooled down to room temperature twice during this process. Treiss [5] revealed that on a commercial grade of steel, StE 415.7 TM[2], a single normalising treatment produces a slight increase in the toughness and a small increase in the scatter of the measured data. The toughness properties of the parent metal were realised in the weld area only when this area is water-quenched after the first normalising and subsequently reheated into the austenite phase field. This condition requiring a localised heat treatment of the weld without impairing the whole pipe can only be achieved by induction heating.

2.2 Pipeline steel

2.2.1 Metallurgy and microstructure

High strength pipeline steel falls into the category of high-strength low-alloy steels and is produced by controlled rolling, in order to achieve the weldability and toughness demanded by the oil and gas industry [6, 23]. The steel weldability is defined by the Ito-Besseyo formula for the low carbon contents ($\mathrm{C}<0.18$ wt%) [24]:

$$C_{equiv} = \mathrm{C} + \frac{\mathrm{Si}}{30} + \frac{\mathrm{Mn}+\mathrm{Cr}+\mathrm{Cu}}{20} + \frac{\mathrm{Ni}}{60} + \frac{\mathrm{Mo}}{15} + \frac{\mathrm{V}}{10} + 5\mathrm{B}\ wt\% \tag{2.4}$$

$C_{equiv} < 0.4$ is an essential requirement of any structural material to be welded [25], which helps to avoid cold cracking or hydrogen-induced cracking induced by high hardness and the presence of martensite [24].

Such steels are hot-rolled at elevated temperatures when they have an austenite crystal structure followed by cooling using air, forced air, water or mist depending on the preferred cooling rate [26–28]. This production route is called thermomechanically controlled processing. During cooling the austenite transforms partially into allotriomorphic ferrite, and the remaining carbon-enriched austenite transforms into pearlite, as illustrated in Fig. 2.4. The microstructure of this X65 pipeline steel shows banding of pearlite-rich and ferritic-rich areas. The volume fraction of the allotriomorphic ferrite was

---

[2] Chemical composition: Fe–(0.04∼0.14)C–0.45Max.Si–(1.00∼1.60)Mn–0.035Max.P–0.025Max.S wt%

stated as 0.93 and the ferrite grains were about 10 μm in size with curved grain boundaries. The isolated pearlite colonies mostly occurred at boundary triple junctions or at α/α grain boundaries. The pearlitic cementite was found to be Mn-rich. There was no Mn segregation at the boundaries between pearlitic ferrite and pearlitic cementite [29].

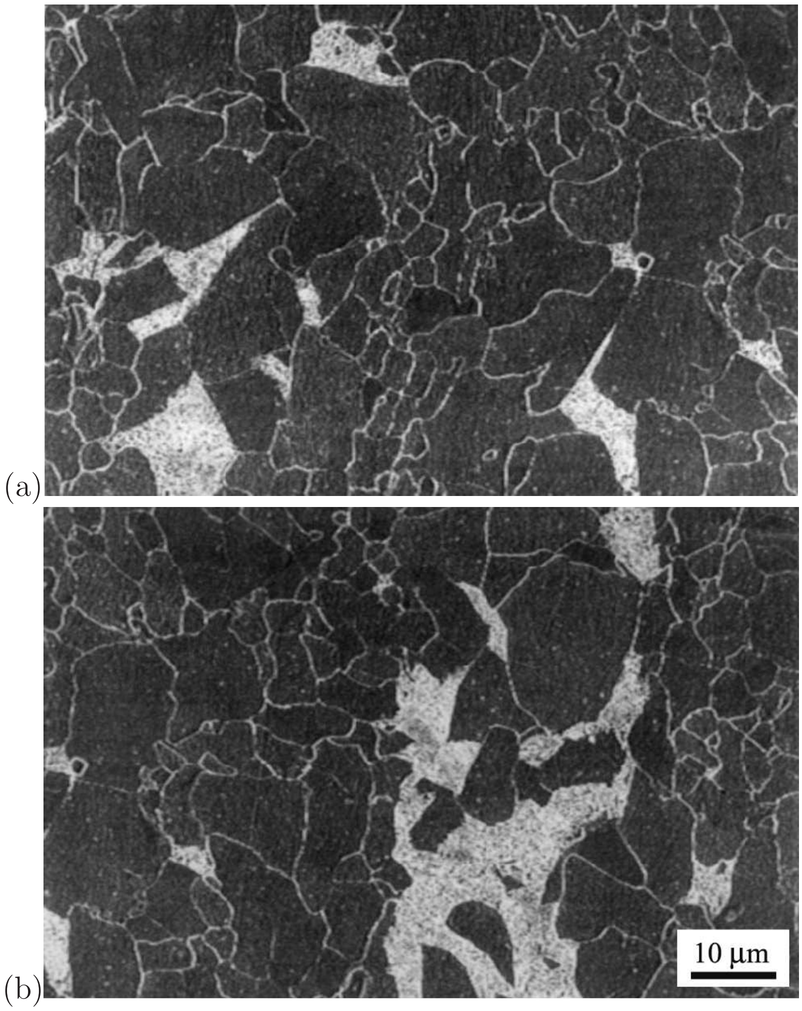

Figure 2.4: Microstructure of a X65 steel (Fe–0.07C–1.36Mn–0.19Si–0.002S–0.013P–0.01Ni–0.2Cr–0.04Nb–0.011Al wt%) consisting of ferrite and (a) isolated pearlite colonies; (b) interconnected pearlite colonies [29].

The strength and toughness of the pipeline steel can be related directly to the ferrite grain size developed as a result of the thermomechanical treatment. The principal grain refinement mechanism in controlled rolling is recrystallization of austenite during hot deformation, known as dynamic recrystallization [23]. This process is affected by the temperature and the degree of deformation which takes place in each pass during rolling. The austenite microstructure obtained after rolling, and the cooling conditions, determine the kinetics of the austenite to ferrite transformation. In the absence of retained strain in the austenite, ferrite predominantly nucleates at the austenite grain boundaries [30]. Subsequent ferrite growth is usually discussed as a process governed by carbon diffusion in austenite ahead of the transformation interface [31, 32]. Experimental results, however, indicate a solute drag-like effect from alloying elements such as Mn [33, 34]. Frequently, semi-empirical relationships, based on the Avrami equation [35], are proposed to quantify the effect of chemical composition and austenite grain size on the transformation kinetics [36, 37].

The ferrite grain size, d_α, has been described by Tamura [38], based on theoretical consideration:

$$d_\alpha \propto \varphi^{-0.17} \tag{2.5}$$

where φ is the cooling rate (°C s^{-1}). The undercooling, which is required to start the transformation, increases with increasing cooling rate and austenite grain size. The increased undercooling encourages ferrite nucleation. The Mn solute drag effect at the moving α–γ interface decreases with undercooling [30].

For small austenite grain size and low cooling rate, ferrite nucleation occurs only at a few preferred sites at the boundary, *i.e.*, at grain corners or in areas with favourable crystallographic orientation. In the 1980s, Aaronson and co–workers performed pioneering studies to shed some light on the mechanisms of this type of ferrite nucleation [39–42]. The nucleation temperature was estimated from Enomoto and Aaronson's model [39–41]. However, an insufficient quench from the isothermal testing temperature encouraged ferrite nucleation also on the other grain boundary areas, which is consistent with the present findings for continuous cooling conditions. Further, Enomoto and Aaronson favour a nucleus composition which is associated with the maximum driving force and a pillbox shape of the nuclei in accordance with minimal interfacial energy. The nucleation sites are at preferred grain corners first and then grain edges and finally grain surfaces. Growth of earlier formed nuclei actually determines how much austenite boundary area remains available for additional nucleation to take place. This fact is used under mill conditions by employing accelerated cooling to obtain significant grain refinement in the final ferrite microstructure [30].

The austenite grain size can be suppressed by micro-alloying the steel with Al, V, Nb and/or Ti. The carbides and carbonitrides of these elements precipitate progressively during the controlled rolling as the temperature falls. The fine dispersion of particles can not only control the ferrite grain size but also strengthen the steel. The concentration of the microalloying elements, the carbon content of the steel and the austenizing temperature of the process must be optimised to obtain full benefit from the precipitation and to avoid the formation of undesirable coarse carbides [23, 43].

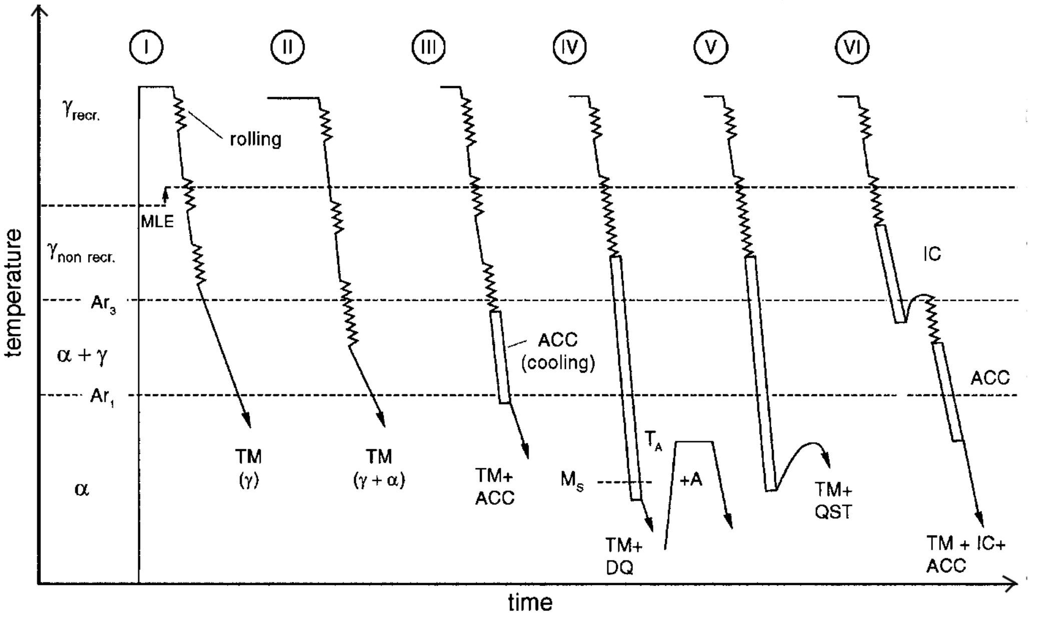

Figure 2.5: Illustration of different methods of thermomechanically controlled processing [44]. recr.: recrystallised, MLE: maximum likelihood estimation of the critical temperture, TM: thermomechanical treatment, ACC: accelerated cooling, DQ: direct quenching, QST: quenching and self-tempering, IC: intermediate cooling, A: annealing.

Because of the microsegregation of the alloying elements [45], ferrite/ pearlite banding can happen in the pipeline steels. The effect of banding on the anisotropy of tensile properties is negligible, but it is significant on the anisotropy of reduction in the area and impact properties [46–48]. It also makes the steel susceptible to hydrogen-induced cracking [49]. There are advanced thermomechanically controlled processes designed carefully to eliminate the banding of pearlite. Examples of various routes of thermomechanically controlled processing are shown in Fig. 2.5. Process I is the conventional thermomechanical treatment aiming at reduction of the austenite grain size and consequently the final ferrite grain size. Further strengthening can be achieved through finishing in the intercritical temperature range, as shown in process II. With accelerated cooling, designated process III, a microstructure of very fine polygonal ferrite and acicular ferrite/bainite can be obtained [44]. By using different combinations and sequences of the steps in the thermomechanically controlled processing, different microstructures and properties can be produced from the same chemical composition. Fig. 2.6 compares the microstructures from a thick-walled (31.4 mm) X65 steel plate manufactured using thermomechanical rolling schedules (a) with intermediate cooling only and (b) with accelerated cooling. The former schedule produced ferrite with bands of pearlite. A maximum grain size of ASTM 10 (standard E112) was reported [44]. The latter resulted in even finer ferrite.

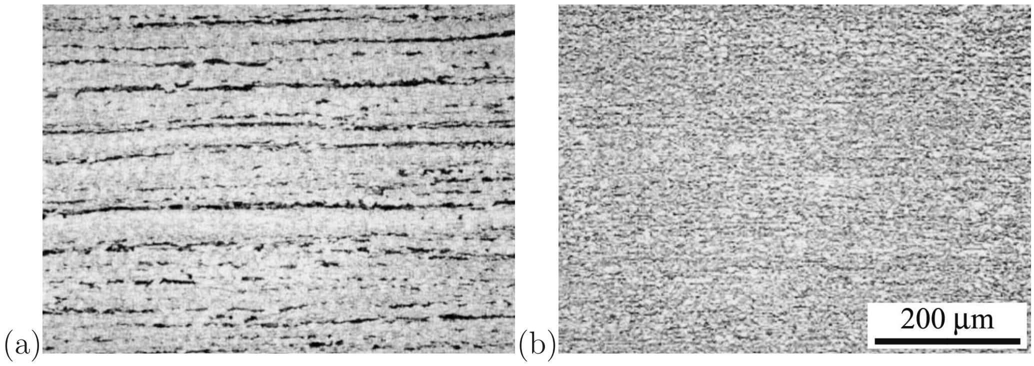

Figure 2.6: Microstructures of a X65 steel [Fe–(0.04∼0.16)C–0.55Max.Si–(1.00∼1.60)Mn–0.035Max.P–0.025Max.S wt% according to standard API (American Petroleum Institue) 5L] applied (a) thermomechanical treatment and intermediate cooling; and (b) thermomechanical treatment and accelerated cooling [44].

A uniform microstructure in a clean steel has the best resistance to hydrogen-induced cracking, which is the most common damage mechanism in pipelines conducting corrosive materials. The hydrogen is produced during any corrosion reactions taking place within the pipe. The high concentration of hydrogen sulphide in the transmitted natural gas reacts with iron as follows:

$$\mathrm{Fe} + \mathrm{H_2S} \rightarrow \mathrm{FeS} + 2\mathrm{H},\ 2\mathrm{H} \rightarrow \mathrm{H_2}$$

The atomic hydrogen moves easily within the steel. Cracks begin when the hydrogen is trapped in the sites of hard phase or inclusions, so the quantity of non-metallic inclusions in the steel must be minimized in order to avoid accumulation of the hydrogen. Hydrogen-induced cracking-resistant steels contain low carbon (optimum range from 0.01 to 0.05 wt% [50]) and low sulphur (as discussed in section 2.1.3). Such steels are designed with inclusion shape control and limited manganese segregation, since elongated MnS is found to be detrimental to the hydrogen-induced cracking resistance of the steel [45, 49, 51, 52].

2.2.2 Mechanical properties

The work presented in this thesis is particularly focused on an API 5L grade X65 steel and the high frequency welded pipes made from it. Pipeline steels are designated as Grade A, B and X [53]. X indicates that the steel contains niobium, vanadium, nitrogen, or other alloying elements. The two digits after X indicate minimum yield strength requirement of the steel in ksi [50, 54]. The requirements in ISO3183:2007 for the mechanical properties of the steel are listed in Table 2.1. It is also required that in the bend test the test pieces shall not reveal any cracks or ruptures in the base metal, heat-affected zone or weld junction longer than 3.2 mm or deeper than 12.5% of the wall thickness. The pipe should withstand a hydrostatic pressure test without leakage through the weld seam or the pipe body. In the drop weight tear test, the average shear fracture area should be greater than or equal to 85% at a test temperature of 0 °C. All of the three tests are specified in ISO3183:2007, but the latter two methods are not used in this work, since the focus is on the toughness of the weld.

Table 2.1: Strength and toughness of X65 welded pipe (According to product specification level 2 (PSL2) in ISO3183:2007) with outside diameter less than 1422 mm. The yield strength is the value obtained when the sample gets to 0.5% total extension. The absorbed energy required is the result of Charpy V-notch impact test conducted at 0 °C. The sample size is specified in the next chapter.

Pipe body	Yield strength $R_{t0.5}$ / MPa	450–600
	Tensile strength R_m / MPa	535–760
	$R_{t0.5}/R_m$ max.	0.93
	Absorbed energy K_V min. / J	40
Weld	Tensile strength R_m min. / MPa	535
	Absorbed energy K_V min. / J	27

2.3 Impact toughness of the weld

Impact toughness represents the ability of a material to absorb energy under impact loading in the presence of a notch [55]. The impact toughness of most structural steels can be described in terms of the transition from ductile to brittle behaviour as the test temperature decreases. The most widely used characterisation method for the ductile-to-brittle transition behaviour is the Charpy V-notch impact test.

The impact toughness of the weld is a complex phenomenon, which is affected by many microstructural parameters. Generally speaking, a uniform and fine microstructure across the weld with the least quantity of inclusions on the junction leads to satisfactory toughness. Particular features in steels, including grain size, various constituents of steel, inclusions, and crystallographic texture all have influence on the ductile-to-brittle transition temperature (DBTT). These features exist in the weld junction and affect its toughness. This section describes the current knowledge about these features based on available literature.

2.3.1 Grain size

Grain refinement is well-known to lower the DBTT in steels. The relation between grain size and DBTT originates from the Cottrell model [56], which describes the occurrence of ductile-to-brittle transition according to the following condition:

$$\sigma_f = \sigma_y + \Delta\sigma \geq \frac{C\mu\gamma}{k_y} d^{-\frac{1}{2}} \tag{2.6}$$

where σ_f is the fracture stress, σ_y is the yield strength, d is the grain size, $\Delta\sigma$ is the increase in yield strength from work-hardening beyond the yield point, k_y is the Hall-Petch slope, μ is the shear modulus, γ is the effective surface energy of the implied crack, and C is a constant related to stress state and average ratio of normal to shear stress on the slip plane. The direct effect of grain size on the DBTT was then described by [57, 58]:

$$DBTT = D \ln d^{\frac{1}{2}} \tag{2.7}$$

where D is a constant.

A large amount of work followed to investigate the dependency of the transition temperature, on grain size for various kinds of materials. It is common to plot the transition temperature against the inverse square root of the grain size as shown in Fig. 2.7. This kind of plot leads to a relationship of the form [59]:

$$T = B^* + Ad^{-\frac{1}{2}} \tag{2.8}$$

where the transition temperature, T was termed to be DBTT in some references [59] or fracture appearance transition temperature (FATT) in some others [60]. A and B^* are constants which can be obtained from the graphs similar to Fig. 2.7 for different steels. d in this relation was defined more accurately as the effective grain size, which is not always the metallographic grain size, the packet size of laths in bainite or martensite was one of the earliest discovered exceptions. The toughness of these steels was affected greatly by the packet size which corresponds to the cleavage unit crack path [61–63]. This is the distance between two nearest high-angle boundaries, since the crack will tend to ignore the low-angle boundaries [64]. An effective grain is a packet or cluster of neighbouring grains or units sharing the same or similar crystallographic orientation, which is also called the crystallographic grain. The effective grain size should match the facet size observed on the fracture surface. By applying this criterion, the measurement of effective grain size on the orientation images was suggested to be taken using the misorientation threshold between 15 and 18 ° for the bainitic steels [65] and 12 ° for the thermomechanical controlled rolled steels [66].

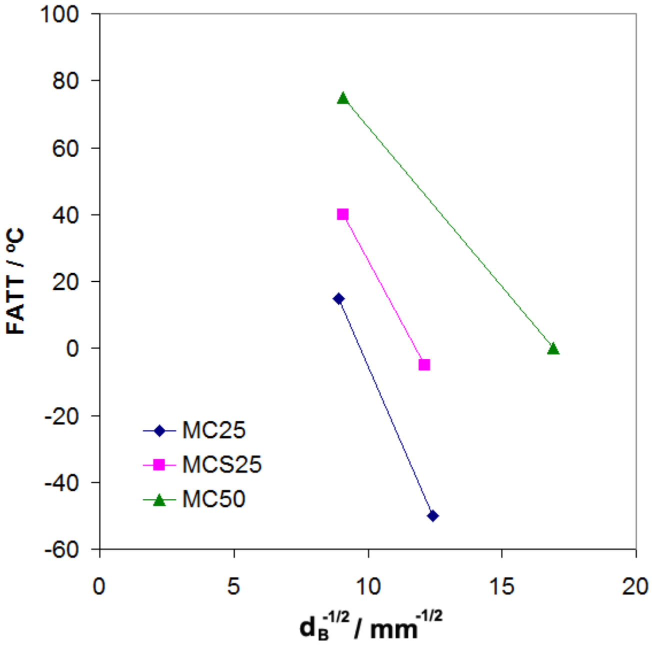

Figure 2.7: Effect of bainite packet size ($d_B^{-\frac{1}{2}}$) on the FATT. Compositions of the steels are listed in Table 2.2 [60].

2.3.2 Inclusions

The size, distribution and shape of the inclusions are all parameters affecting the toughness of the steels and their welds. Large non-metallic inclusions

Table 2.2: Chemical compositions of steels from which the data were plotted in Fig. 2.7 [60].

Steels	C	Si	Mn	P	S	Cr	N	O	Al
MC25	0.025	0.04	2.04	0.015	0.006	3.0	0.005	0.007	0.005
MCS25	0.028	0.04	2.05	0.015	0.012	3.10	0.005	0.01	0.005
MC50	0.050	0.04	2.07	0.015	0.003	3.06	0.005	0.007	0.005

(>1 µm) within the matrix are internal sites of stress concentration, which can either act as cleavage crack initiation sites or facilitate the crack propagation [67]. The stress concentration in the case of an axisymmetric loading can be evaluated by [68]:

$$\sigma = \Sigma_m + \frac{2}{3}\Sigma_{eq} + kE_P E_{eq}^P \tag{2.9}$$

where Σ_m is the remote hydrostatic applied stress, Σ_{eq} is the remote equivalent applied stress, k is a stress concentration factor which depends on the shape of the inclusion and is given in Table 2.3, E_P is the slope of the hardening curve, and E_{eq}^P is the remote equivalent plastic strain. Thus the stress concentration is higher on the axial direction of a prolate (needlelike) inclusion and on the radial direction of a oblate inclusion, both of which result in easier cleavage. The existence of elongated non-metallic inclusions is therefore one of the causes for the anisotropy of the impact properties of the steel after rolling, a subject which is discussed in section 2.3.5. These inclusions are effective obstacles to crack propagation transverse to the rolling direction (RD) [69].

Table 2.3: Stress concentration factor associated with various shapes of inclusions. s is the ratio of axial to radial dimension [68].

Shape	Direction	k
Prolate inclusion (s >>1)	Axial	$\frac{2}{3}[\frac{1}{3}\frac{1+2s^2}{2\log(2s-1)-1} - 1]$
	Radial	$\frac{1}{2}[\frac{1}{9}\frac{1+2s^2}{2\log(2s-1)-1} + 1]$
Spherical inclusion	Any	1
Oblate inclusion (s <<1)	Axial	$\frac{2}{3}(\frac{4}{3\pi s} - 1)$
	Radial	$\frac{2}{3}(\frac{10}{3\pi s} - 1)$

The size of inclusions or the size of clusters of inclusions is another essential parameter to influence the cleavage fracture resistance. Derived from the Griffith's equation [70], the critical stress required to propagate the crack from a penny-shaped inclusion of radius c into a ferrite matrix is given by [67, 71]:

$$\sigma_f = \frac{\pi}{2}\left(\frac{2E_m\gamma}{\pi(1-\nu^2)c}\right)^{\frac{1}{2}} \tag{2.10}$$

where E_m is the Young's modulus of the matrix, c is the half crack-length, and ν is the Poisson's ratio. Because c is proportional to the particle size, this equation suggests that a material containing larger inclusions is more prone to cleavage cracking. Similarly a cluster of inclusions acting together as a big inclusion is detrimental to the toughness of the material. Consequently, a high content of inclusions weakens the weld by increasing the DBTT and decreasing the upper shelf energy level, as shown in Fig. 2.8.

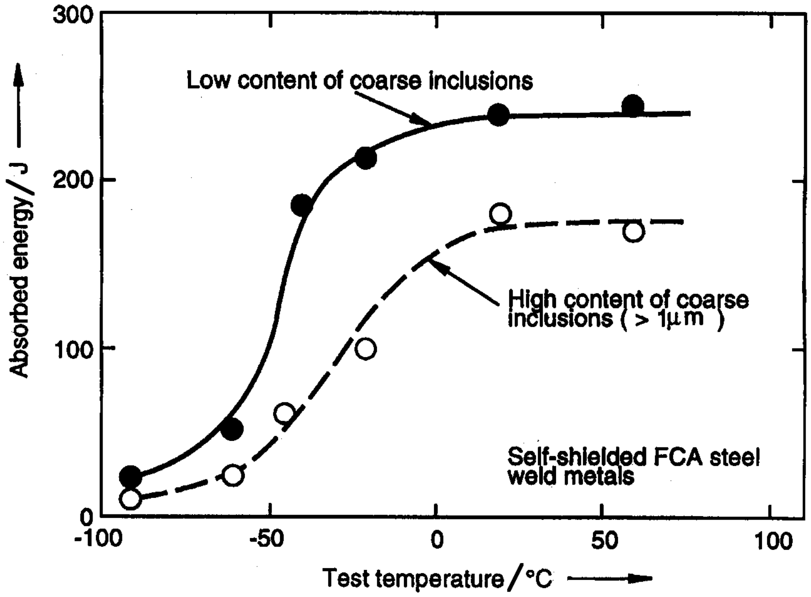

Figure 2.8: The effect of inclusions on the weld metal Charpy V-notch toughness [72].

Small inclusions (<1 µm) are of importance in controling the microstructure in welds and its heat affected zones. During the austenite-to-ferrite transformation, small oxide and sulphide inclusions concentrated at the austenite grain boundaries restrict the grain growth and result in large surface area to volume ratio. This increases the possibility of occurrence of the grain boundary ferrite and reduces the grain size. Furthermore, the inclusions inside the austenite grains provide nucleation sites for acicular ferrite, which is a steel constituent beneficial to the toughness of the weld and will be discussed in the following section. In summary, a controlled population of small non-metallic inclusions is necessary in welded steels for optimum properties [73, 74]. Proper dispersion of other second phase particles, *i.e.*, carbides and nitrides of titanium, vanadium and niobium is beneficial to toughness in a similar way through promotion of fine grained structure.

2.3.3 Constituents of the steels

Acicular ferrite An increased volume fraction of acicular ferrite results in a decrease in Charpy V-notch transition temperature, as shown in Fig. 2.9. It replies on the fine lath size (typically less than 5 µm) of the acicular ferrite microstructure obtained by rapid cooling.

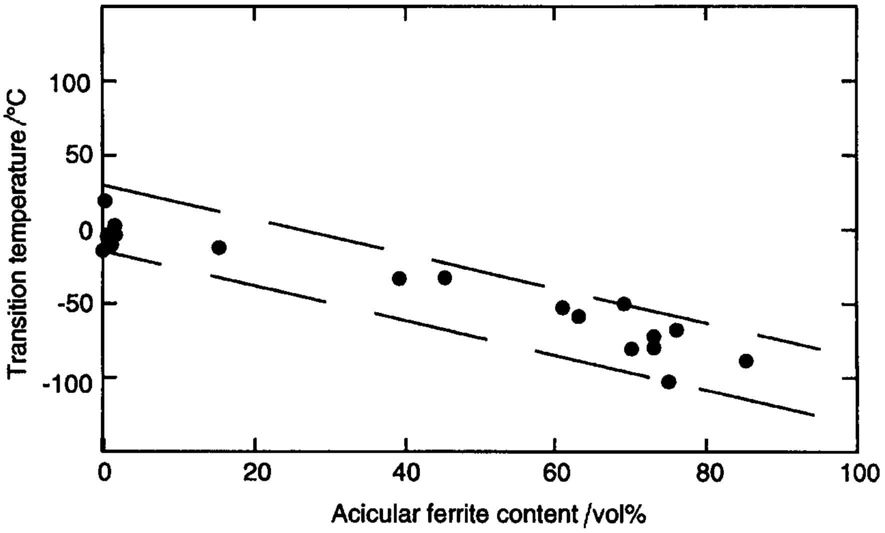

Figure 2.9: The effect of acicular ferrite content on the 35 J Charpy V-notch transition temperature of a submerged arc weld metal [75].

Martensite with limited slip possibilities and high yield strength is generally known as a brittle phase which should be minimised in the weld joint. The twinned structure of martensite often acts as a crack nucleation site, but lath martensite with small packet size produced by rapid cooling is not necessarily detrimental to toughness [68].

Retained austenite in the form of martensite–austenite (M–A) constituents[3] can have a strong embrittling effect, which is widely present in the weld metal and heat-affected zone due to the rapid cooling and possible segregation of carbon involved during the process [76]. The FATT can be assumed as a linear function of the area fraction of M–A constituents ($\%MA$)

---

[3] An unresolvable mixture of martensite and austenite.

in the weld [77]:

$$FATT = A + B(\%MA) \tag{2.11}$$

where B is in a range of 3.4–25.9. Considering the M–A constituent as a second phase in the matrix, its morphological effect should be discussed. It is found that volume fraction of elongated M–A constituent (aspect ratio greater than four) influences the toughness of the weld more seriously than the total content of M–A constituent [77].

Carbides The size of cementite which is the most common form of carbide in steels plays an important role in affecting the toughness. The fine cementite precipitates within lower bainite laths can arrest or deviate cracks and decrease the DBTT [78]. This effect might be even stronger in tempered martensite because of the multi-directional nature of the cementite. The cementite formed during tempering is small in size because the fast cooling rate minimises the diffusion of carbon and hence carbide segregation [68].

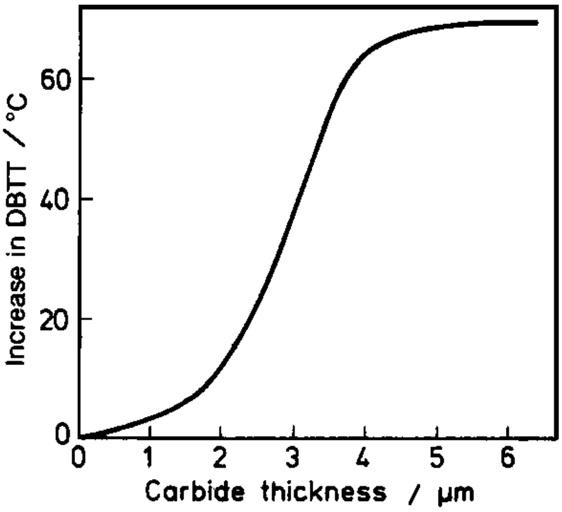

Figure 2.10: The effect of carbide thickness on the DBTT [79].

The transition temperature increases dramatically with the thickness of carbide, t_c (μm), as shown in Fig. 2.10. The following equation was proposed to predict the FATT (°C) taking into account the carbide thickness [80]:

$$FATT = 46 + 0.45\sigma_p + 131t_c^{\frac{1}{2}} - 12.7d^{-\frac{1}{2}} \tag{2.12}$$

where the precipitation strengthening coefficient $\sigma_p = 1$, d is in mm. Carbide filament along ferrite grain boundaries, large inter-lath cementite in upper bainite and cementite lamella as those consisting of pearlite are brittle and fracture-prone so as to initiate or facilitate the prorogation of cleavage cracks [68, 69]. The DBTT increases with the pearlite content, the pearlite colony size, p (mm) and the thickness of the cementite lamella, t_p (mm). The increase of interlamellar spacing, S (mm) however, has an opposite effect on DBTT. Thus the DBTT (°C) can be predicted by an empirical equation for a fully pearlitic structure [69]:

$$DBTT = -335 + 5.6S^{-\frac{1}{2}} - 13.3p^{-\frac{1}{2}} + (3.48 \times 10^6)t_p \qquad (2.13)$$

Considering the role of large cementite particles in cleavage cracking, decreasing the carbon content leads to improvement on toughness, as shown in Fig. 2.11.

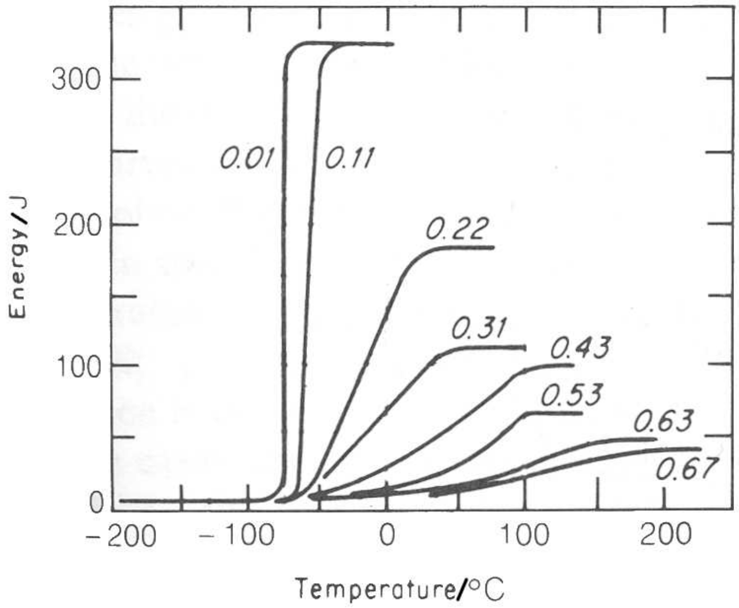

Figure 2.11: The effect of carbon content on the energy-transition-temperature curves for steel [81].

The influence of other kinds of carbides on the toughness of steel is determined by their nature. For instance, M_7C_3 precipitates during slow cooling and grows easily during tempering, which increases the DBTT. On the other hand, $M_{23}C_6$ carbides which do not grow to large sizes are beneficial to toughness [68]. Chromium, tungsten and molybdenum are often found in this kind of carbides [69]. A dispersion of NbC or VC precipitates in steel retards grain growth and can therefore lead to improved impact toughness [81].

2.3.4 Composition

In addition to the carbon content as discussed in previous section, increasing quantities of oxygen are progressively embrittling, as shown in Fig. 2.12.

Oxygen, and in some cases nitrogen, reduces the effective surface energy for fracture [58]. The role of nitrogen is not straightforward because of its interaction with other elements as discussed on page 20, but it is generally considered to be detrimental to toughness [81]. The formation of non-harmful nitrides (AlN, VN, TiN and *etc.*) effectively removes the nitrogen from solution, which benefits toughness.

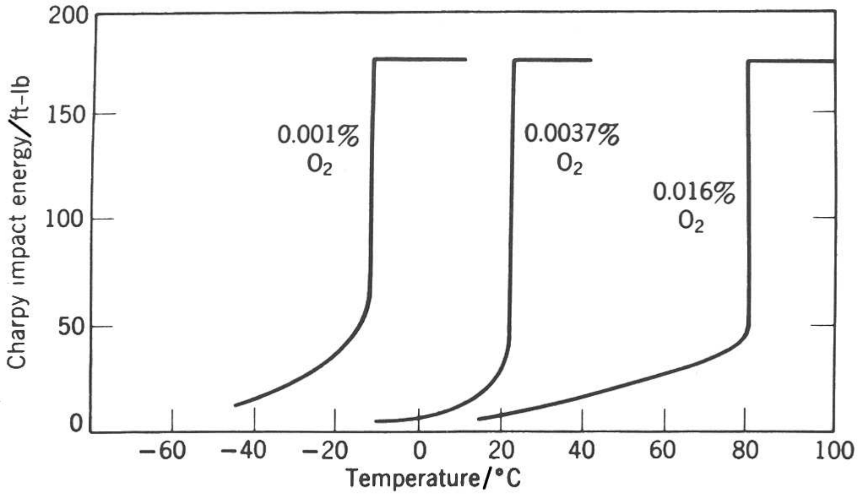

Figure 2.12: The effect of oxygen on the Charpy impact energy of ferrite [58].

The alloying elements in steel detrimental to low-temperature toughness are ferrite stabilizers, while the elements which improve toughness are austenite stabilizers, as shown in Table 2.4 [58, 69]. Manganese is particularly beneficial to toughness, the increase of which not only lowers the transition temperature but raises the upper shelf energy, Fig. 2.13. The most plausible explanation for this is that manganese reduces the thickness of grain boundary carbides and redistributes them to intragranular sites. Higher solute content of manganese beyond the range shown in Fig. 2.13 increases the transition temperature again due to the formation of martensitic structure.

Many empirical equations have been developed to describe the transition temperature based on combinations of effects on impact toughness by various factors mentioned previously. Among them, the Gladman–Pickering equation is proposed for ferrite–pearlite microstructured high strength low alloy steels [69]:

$$ITT = -19 + 44(\text{wt\%Si}) + 700(\text{wt\%N}_{\text{free}})^{\frac{1}{2}} + 2.2(\text{\%pearlite}) - 11.5d^{-\frac{1}{2}} \quad (2.14)$$

where ITT is the impact transition temperature (°C), wt%N_{free} is free nitrogen content, %pearlite is the volume percentage of pearlite, and d is in

Table 2.4: The effect of alloy elements on the shift of impact transition temperature (ΔITT) in ferrite–pearlite structure [58].

Solute	ΔITT / °C at%$^{-1}$
Sn	500
P	400
Cu	40
Mn	-50
Si	40
Ni	-6
Mo	25
Co	-10
Cr	40

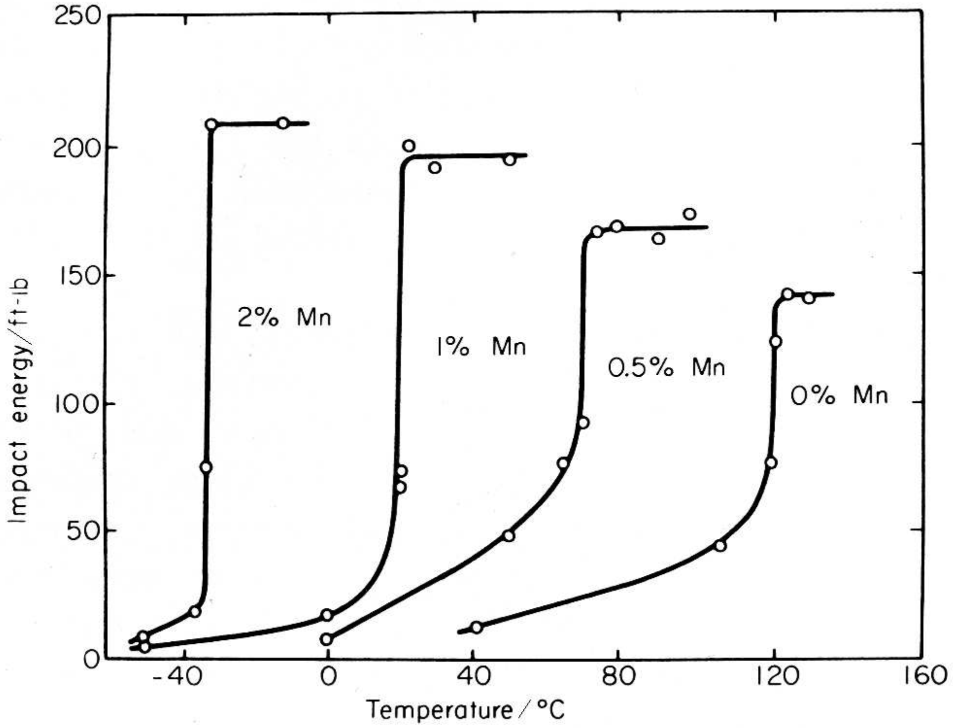

Figure 2.13: The effect of manganese on the transition curves of iron [58].

mm.

2.3.5 Crystallographic texture

The impact toughness of the rolled products, most commonly steel plates, varies with the orientation in the plates. Figure 2.14 shows that the Charpy specimen has lowest upper shelf energy when the V-notch is oriented towards the rolling direction of the plate. Attempts were then made to relate the transition temperature to the crystallographic texture of the ferrite. Bramfitt and Marder [82] defined a texture parameter:

$$TP = I_{111} \times I_{110} - 1 \tag{2.15}$$

where I_{111} is the relative intensity of $\{111\}$ in the rolling plane and I_{110} is the relative intensity of $\{110\}$ in the transverse plane. Several researchers [82–84] reported that the transition temperature of the steels decreased as TP was increased, which is demonstrated in Fig. 2.15. Morrison [85] however, developed the relation of transition temperature in the longitudinal testing (the Charpy sample's long axis parallel to the rolling direction) to TP showing the opposite trend, which can be described by [69]:

$$T = 75 - 13d^{-\frac{1}{2}} + 0.63\,TP \tag{2.16}$$

where T is in °C and d is in mm.

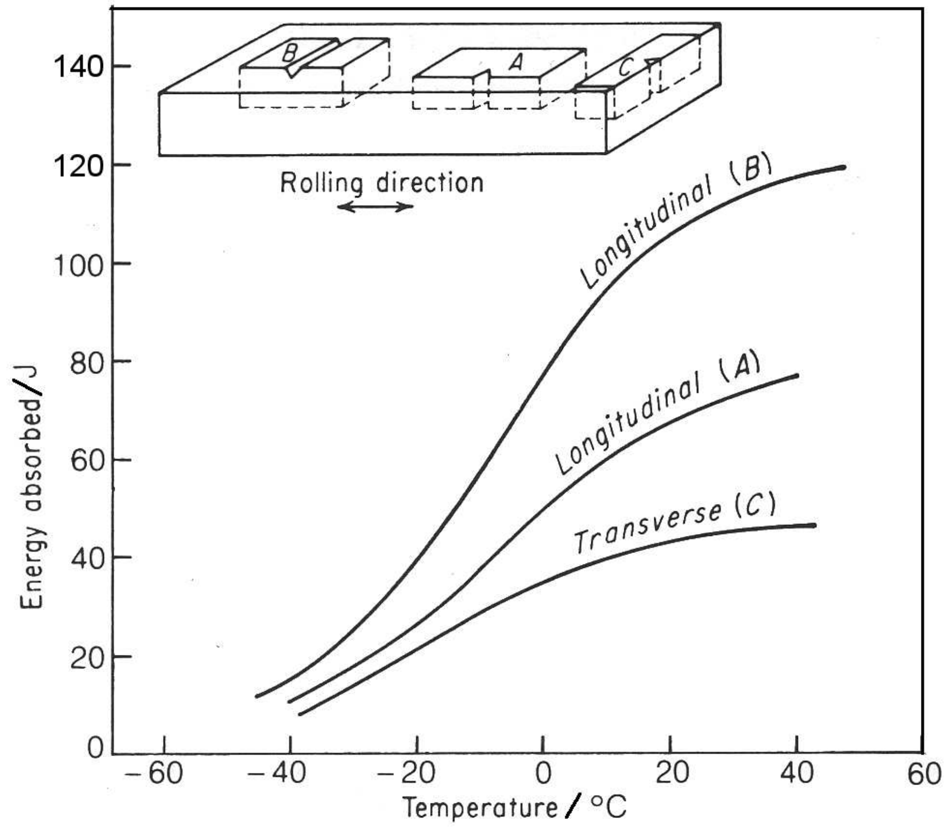

Figure 2.14: The effect of specimen orientation on the Charpy transition curves [81].

Later studies have been undertaken to clarify the influence of preferred orientations on the impact toughness. In the low temperature regime, where

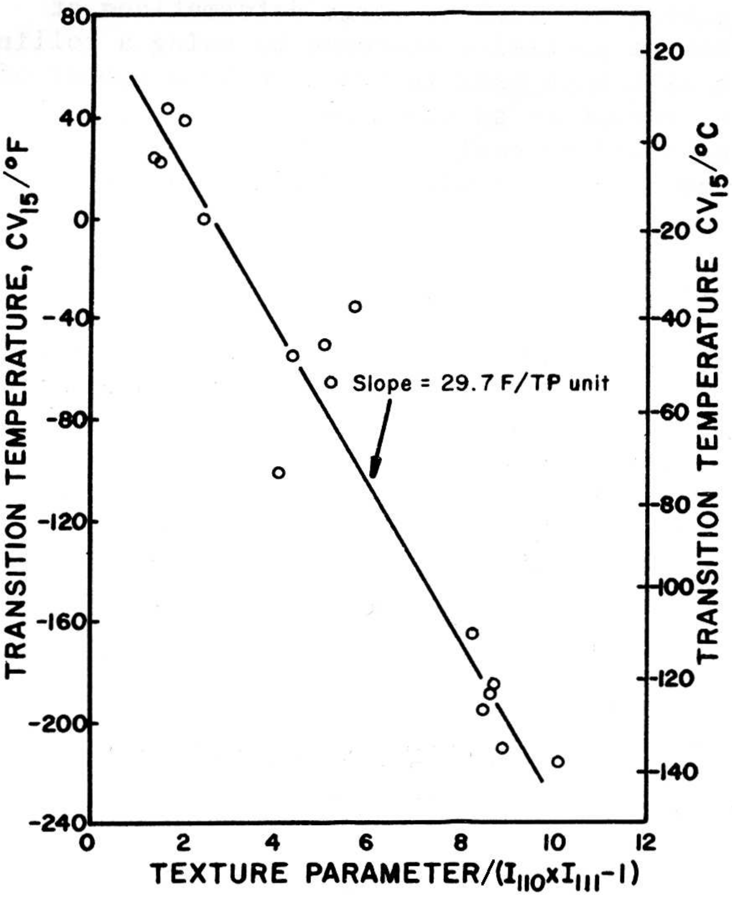

Figure 2.15: The relation of transition temperature at Charpy V-notch energy of 15 ft-lb (CV_{15}) to the texture parameter [83].

the fracture happens exclusively in a brittle mode, the orientation and distribution of the {100} plane, which is the cleavage plane of body-centred cubic crystal [86, 87], is the most important factor affecting the toughness. The smaller angles between the long axis of the Charpy specimen (normal to the notch plane) and normal to the {100} planes correspond to more brittle crystals. Increasing the number of {100} planes subject to the maximum principal stress leads to easy cleavage [88].

As the temperature rises, the fracture mechanism gradually changes to a mixed plastic-brittle mode and then to a fully plastic mode at room temperature, when the fracture occurs by the nucleation and coalescence of microvoids [55]. The more extensive plastic deformation involved in this process, the higher absorbed energy is needed for fracture. Since the void nucleation and growth is mainly through glide and generation of pile-ups on slip planes, the {110}<111> slip system is the main source of plastic deformation in BCC crystals [89]. Several studies have shown that the upper shelf energy increased with the volume fraction of grains with {110} planes parallel to the notch plane [88, 90]. Attention may also be paid to the distributions of other possible slip planes in BCC crystals, *i.e.* {112} and {123}, affecting the impact toughness of the steels at room temperature, because relatively more carbon atoms in solution can fit on the {110} plane and they act as obstacles to the movement of the dislocations [91].

A mixture of deformation and transformation texture is associated with induction welding. It is a complicated phenomenon and there is little information available in the literature. The base metal for the seam-welded line-pipe has endured the thermomechanically controlled processing as discussed in section 2.2.1 and the continuous forming process in order to form the circular shape before welding [92]. Supposing that the final microstructure of the base metal consists of ferrite and pearlite only, the deformation texture develops in when the finish-rolling temperature falls into the intercritical region where austenite and ferrite coexist. The ferrite grains which have already formed by that time do not possess random orientations after the rolling. The ideal texture components for rolling deformation are listed in Table 2.5. The continuous forming process, Fig. 2.16, is then carried out by cold rolling, which obviously adds to the deformation texture.

Table 2.5: Main ideal orientations after rolling deformation. The designation {hkl}<uvw> refers to rolling plane and rolling direction [93].

BCC crystal		FCC crystal	
Label	Orientation	Label	Orientation
Cube (D)	{100}<001>	Cube (D)	{100}<001>
Rotated cube (RC)	$\{001\}<1\bar{1}0>$	Rotated cube (RC)	$\{001\}<1\bar{1}0>$
Goss (G)	{011}<100>	S (S_1, S_2, S_3, S_4)	$\{123\}<63\bar{4}>$
Taylor (T_1)	$\{\bar{1}11\}<211>$	Copper (C_1, C_2)	$\{112\}<11\bar{1}>$
Taylor (T_2)	$\{111\}<2\bar{1}\bar{1}>$	Brass (B_1, B_2)	$\{110\}<1\bar{1}2>$
Cross Taylor (CT_1)	$\{\bar{1}\bar{1}1\}<011>$	Goss (G)	{011}<100>
Cross Taylor (CT_2)	$\{\bar{1}11\}<011>$	α fibre	{011}<uvw>

The texture of the base metal is altered locally by welding. During the high frequency induction welding process, the weld joint is subjected to compression from both sides by the pressure rolls in order to squeeze out a certain amount of molten material and form a steady weld. The deformation at the joint is bound to induce the change of texture, as indicated by the metal flow that will be evidenced later in Fig. 4.6a and 5.5. Among the possible texture components, shear texture as listed in Table 2.6, is possibly predominant due to the characteristics of the deformation.

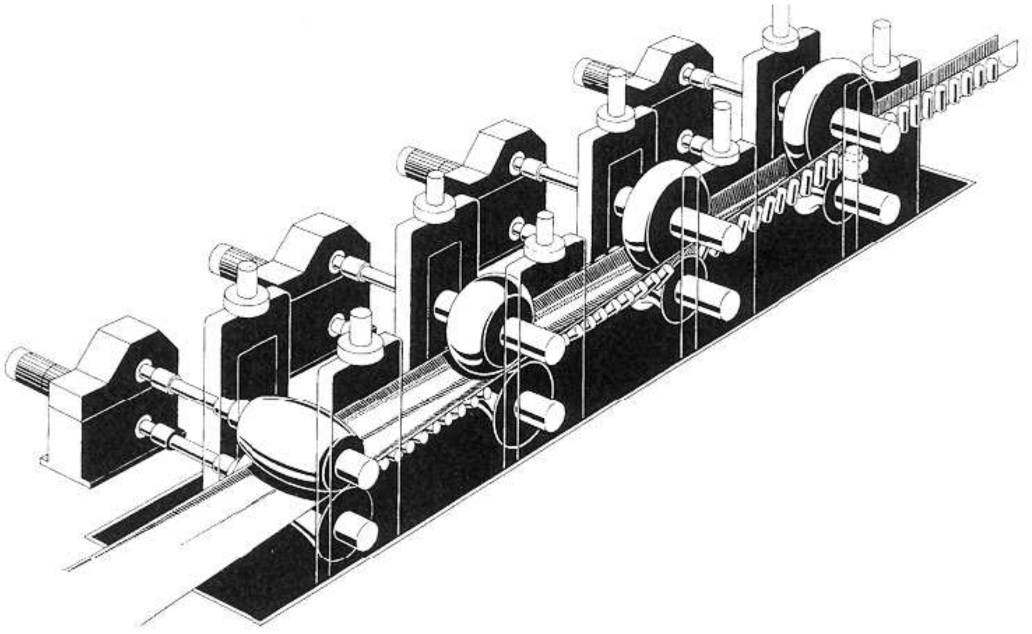

Figure 2.16: Illustration of the continuous forming process [92].

Table 2.6: Main ideal orientations in simple shear deformation. The designation {hkl}<uvw> refers to shear plane and shear direction [94, 95].

BCC crystal		FCC crystal	
Label	Crystal orientation	Label	Crystal orientation
D_1	$\{\bar{1}\bar{1}2\}<111>$	A_1^*	$\{111\}<\bar{1}\bar{1}2>$
D_2	$\{11\bar{2}\}<111>$	A_2^*	$\{111\}<11\bar{2}>$
E	$\{110\}<1\bar{1}1>$	A	$\{1\bar{1}1\}<110>$
$\bar{E}$	$\{\bar{1}\bar{1}0\}<\bar{1}11>$	$\bar{A}$	$\{\bar{1}1\bar{1}\}<\bar{1}\bar{1}0>$
J	$\{110\}<1\bar{1}2>$	B	$\{1\bar{1}2\}<110>$
$\bar{J}$	$\{\bar{1}\bar{1}0\}<\bar{1}1\bar{2}>$	$\bar{B}$	$\{\bar{1}12\}<\bar{1}\bar{1}0>$
F	$\{110\}<001>$	C	$\{001\}<110>$

The transformation texture in steel develops as a consequence of the displacive transformation of plastically deformed austenite. When displacive transformation occurs, the orientation of martensite or bainite can have 24 possible crystallographic variants. However, when the transformation occurs under the influence of stress, some variants have a greater probability to form so as to generate texture, because the shape deformation from austenite to martensite or bainite complies with the external stress [96]. The transformation texture adds to the complication of the texture of the weld, since the displacive transformation products are likely to form in conditions of the thermal history and stress involved in the high frequency induction welding.

If bainitic or martensitic structure forms in the base metal by accelerated cooling at the end of thermomechanical controlled rolling, it will introduce transformation texture, because the prior autenite grains have been deformed during the rolling process.

There is another mechanism which is believed to affect the microstructure of displacive transformation products. It has been suggested in published works [97–99] that two forms of austenite were observed during the heating of steels, termed 'globular' and 'acicular'. The globular grains are considered to be the result of normal diffusion controlled growth accompanying the dissolution of cementite, which leads to grain refinement [98]. Acicular austenite nucleation occurs on stabilised retained austenite at bainitic or martensitic lath boundaries. The acicular austenite was stated to form by a reverse martensitic reaction, which is governed by a diffusion-less shear mechanism [98]. Acicular grains within a given prior austenite grain have a common orientation owing to growth from retained austenite, and they coalesce on impingement, leading to a reconstitution of the original prior austenite grain structure, which is termed the austenite memory effect. The stronger the memory effect, the higher the ratio of acicular/globular austenite [97]. This mechanism may apply to the post-welding heat treatment process in the current topic of interest. If the prior austenite grain structure resulting from welding is reconstructed upon austenisation, the heat-treated weld will inherit the microstructural characteristics including grain size and crystallographic texture of the as-welded structure.

The presence of both the retained austenite and the stabiliser of the lath boundaries is necessary to enable the austenite memory effect to operate [97]. The minimum content of retained austenite needed for the austenite memory effect to operate is not clear. Kimmins and Gooch [97] found the evidence of the memory effect in a steel[4] with less than 0.8 wt% retained austenite, heated up to 980 °C at the rate of $4\,^{\circ}\mathrm{C\,min^{-1}}$. However, this steel did not maintain the austenite memory at the heating rate of $17\,^{\circ}\mathrm{C\,min^{-1}}$. The higher heating rate results in a larger proportion of the globular nuclei at a given temperature above A_{c1}, because the nucleation rate increases with the heating rate according to classic theory, whereas the density of the acicular nuclei resulted from a diffusion-less mechanism may be considered relatively constant [97, 98]. When the content of retained austenite was 13.9 wt%, the

---

[4] Chemical composition: Fe–0.22C–0.05Al–0.055As–0.005B–1.02Cr–0.02Co–0.19Cu–0.94Mo–0.21Ni–<0.01Nb–0.36Si–0.51Mn–0.015P–0.013S–0.02Sn–0.1Ti–<0.05W–0.67V wt%

above steel showed a strong memory effect at the heating rate from ∼1000 down to 2 °C min^{-1}. At very slow heating rates, most retained austenite transforms into ferrite and carbide, and recovery and recrystallisation occurs below the A_{c1}, which disrupts the oriented growth of acicular austenite. The presence of residual elements Al, P, Sn and As, and most of the alloying elements stabilises the martensitic or bainitic lath boundaries and strengthens the austenite memory, because it encourages the acicular austenite nucleation and favours a closer Kurdjumov-Sachs orientation relationship between the acicular austenite and the ferrite from which it forms [97, 98, 100]. Matsuda and Okamura discovered that the acicular austenite started to form above A_{c1}, started to coalesce when the temperature was approaching A_{c3}, and eventually reconstituted the prior austenite grain just above A_{c3}. For austenisation above A_{c3}, increasing the austenisation temperature or time at a given temperature eliminates the memory effect and leads to grain refinement because of the austenite recrystallisation [97].

Chapter 3

Experimental Work

3.1 Sample preparation

The high frequency induction welding and annealing process used in the fabrication of pipes is illustrated in Fig. 3.1, which shows also the length and separation of the annealing units. The hot-rolled steel strip after edge trimming using high-speed cutting is welded during its passage through the induction coil. There is no external cooling applied to the pipe after welding; cooling to room temperature before heat–treatment is due mainly to the conduction between the narrow heated region and the rest of the pipe. This is followed by the induction heat treatment. The processing parameters of the heat treatment applied on the as-welded pipes are listed in Table 3.1. Three pipes were studied in this work. One of them is made from hydrogen-induced cracking-resistant steel, X65HIC and the other two are normal API 5L PSL2

This figure removed for copyright reasons

(a)

(b)

Figure 3.1: (a) A sketch map of the production line of high frequency induction (HFI) welding and annealing, Pyr. is the pyrometer for temperature observation. (b) Specification of the annealing line.

pipes made from grade X65 strips with different thicknesses. The compositions of the steels are shown in Table 3.2.

Table 3.1: Processing parameters of the post-welding heat treatment.

Table removed for copyright reasons

Table 3.2: Compositions of the unwelded steels in wt%

Table removed for copyright reasons

Sampling was carried out on the pipe just after welding and after having gone through the whole process. All the samples were cut normal to the welding direction, which happens to be parallel to the rolling direction, along the length of the pipes. A pipe segment with the weld is illustrated in Fig. 3.2a.

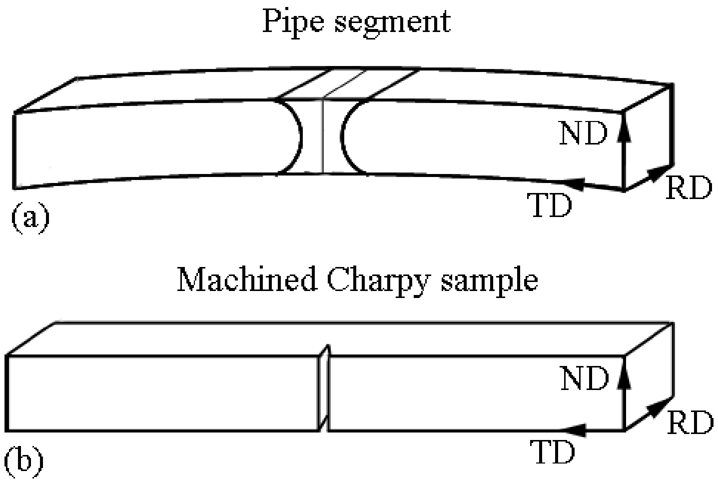

Figure 3.2: (a) The orientation of the pipe segment relative to steel processing directions. (b) Orientation of Charpy specimen.

3.2 Mechanical tests

3.2.1 Tensile

Some of the pipe segments, which obviously have curvature, were flattened to make tensile specimens. The tensile tests were carried out at room temperature on strip test pieces made according to API 5L standard. The geometry is illustrated in Fig. 3.3. The experiments were performed on an INSTRON hydraulic tensile machine with a capacity of 1200 kN. Cross-weld tensile tests were conducted following standard ASTM A370:2005 which requires the weld junction to be placed in the middle of the gauge length. The cross-head speed at the beginning of the tensile test was 3 $\text{mm}\,\text{min}^{-1}$, but after 4 % elongation and to the point of fracture, it was increased to 20 $\text{mm}\,\text{min}^{-1}$.

Samples from as-welded X65 pipe with 8.6 mm wall-thickness, which were heat-treated in the Gleeble system, have also been used to carry out tensile tests. They are in a size of 8.6 × 10 × 30 mm with the weld junction placed in the middle of the reference length (25 mm), specified by standard EN10002-1 annex B. The experiments were performed on an electromechanical testing machine Zwick Z250. The cross-head speed at the start of the tensile test was 1.5 mm min^{-1}, but after 0.6 % elongation and to the point of fracture, it was increased to 10 mm min^{-1}.

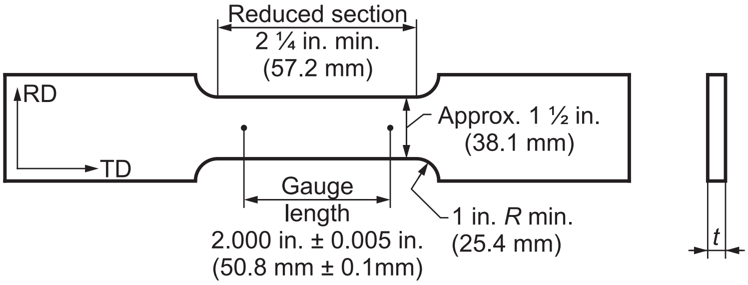

Figure 3.3: Specification for strip tensile specimen, where t is the wall thickness of the pipe.

3.2.2 Charpy

The Charpy tests were conducted according to standard ISO 148-1 at a variety of temperatures. The orientation of the test specimen relative to the pipe is shown in Fig. 3.2b. For the thick-walled X65 pipe, full size specimens 55 × 10 × 10 mm were used. For the X65HIC and thin-walled X65 pipe, $\frac{2}{3}$ size specimens were used, with just 6.7 mm in the normal direction (ND). In the cross-weld Charpy tests, the V-notch was placed on the weld junction, and at 1, 2 and 3 mm away from the junction.

3.2.3 Bend

Cross-weld bend tests were performed at room temperature on the pipe segments, illustrated in Fig. 3.2a, according to standard EN910. For thick-walled X65 pipe segments, the tests were carried out for the as-welded state and after post-welding heat treatment. For the other two kinds of pipes, only samples after post-welding heat treatment were tested. Two testing conditions were used, designated 'face bend' and 'side bend'. In the face-bend tests, the force was applied in the normal direction. The width of the sample from thick-walled X65 in the rolling direction was 20 or 40 mm. The samples from the other two kinds of pipes were all 20 mm wide in the rolling direction. In the side-bend tests, the force was applied in the rolling direction along which the samples were 10 mm wide.

All of the above three kinds of tests were carried out in ArcelorMittal Research and Development Laboratories. Tested samples were then sent to

Cambridge for investigation.

3.2.4 Microhardness

Microhardness measurements were carried out across the welds on the as-etched ND–TD surfaces of the as-welded samples and after post-welding heat treatment, using a Mitutoyo microhardness tester with a load of 200 gf and dwell time of 10 s. The metallographic procedures are discussed in section 3.3.1.

3.2.5 Nano-indentation

During nano-indentation, the depth of penetration is recorded as the load is applied, which enables the measurement of hardness as a function of the depth. Although the hardness is obtained by dividing the load by the area of contact as in conventional testing, the area of contact is calculated from the depth of the penetration and the known values of the angle or the radius of the indenter, as shown in Fig. 3.4, where A is the contact area, h is the depth of penetration, θ is the angle between the axis and one surface of the Berkovich indenter, R and a is the radius and the radius of the contact area respectively of the spherical indenter.

Nano-hardness was measured using a MTS XP system. A Berkovich indenter made of diamond was used. Indentations were made on colloidal silica polished ND–TD surfaces of all three kinds of pipe segments down to 200 nm. Surface finishing with colloidal silica (0.06 μm) is necessary, because the roughness of the surface must be of a smaller amplitude than the impression depth so that it does not affect the calculation of the contact area.

3.3 Microstructural observations

3.3.1 Metallography

Most of the microstructural observations were carried out on the ND–TD surfaces of the pipe segments unless otherwise stated. The surfaces were ground starting with 240-grit silicon carbide grinding paper and finishing with 2500-grit, and then polished with diamond paste of 6 μm and 1 μm grade. Some as-polished samples for optical microscopy, scanning electron microscopy, investigation in the focused ion beam workstation and X-ray

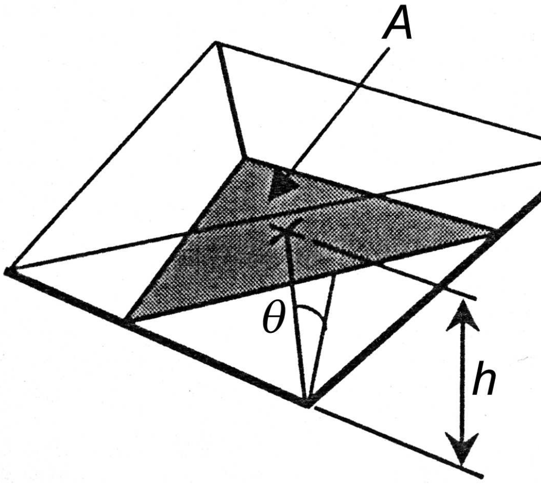

(a) A Berkovich indenter.

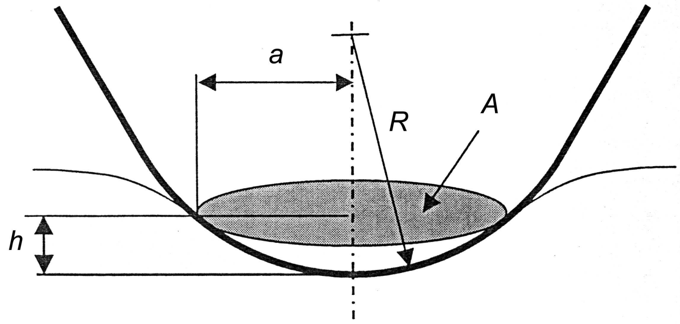

(b) A spherical indenter.

Figure 3.4: Geometry of the nano-indenter.

diffractometry were then etched with 2 % nital (2 ml nitric acid with 98 ml methanol). For orientation imaging using the electron back-scattered diffraction (EBSD) technique, the samples were finish-polished using colloidal silica (0.06 μm).

The optical microscopes used included a Zeiss Axiotech hi-specification optical microscope and an Olympus BH microscope, each fitted with a digital camera. Grain size measurements were made on as-welded samples using the Hilliard single-circle intercept procedure [101] according to ASTM standard E112.

3.3.2 Scanning electron microscopy

Besides ordinary imaging by scanning electron microscopy, energy dispersive X-ray (EDX) analysis and the EBSD technique were also used. These last two methods respectively take advantage of the X-rays and back-scattered electrons emitted from the sample during the bombardment of the sample surface with incident electrons.

EDX analysis

The energy dispersive detector tries to collect as many as possible X-rays emitted from the specimen, so it is usually positioned inside the chamber of the scanning electron miroscope at a similar distance or angle to the sample stage as the secondary electron detector. The key component inside the detector is a small piece of semiconductor. For each incoming X-ray, the number of electron–hole pairs generated is proportional to the energy of that X-ray photon detected. When a voltage is applied across the semiconductor, the magnitude of the current will also be proportional to the energy of the X-ray. The time during which a current flows between electrodes is referred to as a pulse, normally less than 1 μs [102]. Each pulse is amplified and registered on the multichannel analyser, which can distinguish X-ray energies and is normally attached to a computer. Finally a histogram of energies from all the X-rays arriving at the detector can be shown on the display.

There is pulse processing speed limit which is decided by the system hardware, because a pulse can only be dealt with after the previous pulse is detected, amplified and sorted by the multichannel analyser. During the time of this process, the detector ignores the coming X-rays and diverts them to the pulse pile-up rejection circuit. The total time needed for an analysis includes the *live time* when the detector is actually counting the pulse and the *dead time* when it is rejecting the pulse [102]. Only when an input count rate is lower than a threshold are most of the incoming pulses satisfactorily processed. Exceeding the threshold results in a larger fraction of pulses being rejected. The input count rate depends on the accelerating voltage of the electron source and the current of the electron beam. The dead time is displayed as the percentage of pulses rejected in some commercial software for EDX analysis.

The minimum detectable concentration, MDC can be approximated as:

$$MDC = \frac{200\sqrt{b}}{(p-b)\sqrt{t}}\% \tag{3.1}$$

where b is the background count rate, p is the peak count rate and t is the counting time. By increasing the time of analysis, the MDC can be lowered. The MDC by using an EDX system is typically around 0.1 wt% [102], but this figure may need corrections for some or all of the three factors which are atomic number effect (Z), absorption (A) and fluorescence (F). Use of these corrections is commonly known as ZAF technique. The absorption correction often has the most significant effect. The magnitude of this correction can be quite large for detection of light elements with an atomic number less than that of sodium. This is because a significant portion of the low energy X-rays get absorbed by the heavier elements in the specimen and the protective window of the detector. Another limitation applied when measuring the distribution of an element by the intensity of the X-rays is that the spatial resolution is around 1 μm [102].

The EDX analysis in this work was carried out on a JEOL 5800LV and a Camscan MX2600 scanning electron microscope. The latter was equipped with a field emission gun. Both of them have an Inca-act EDX system.

EBSD technique

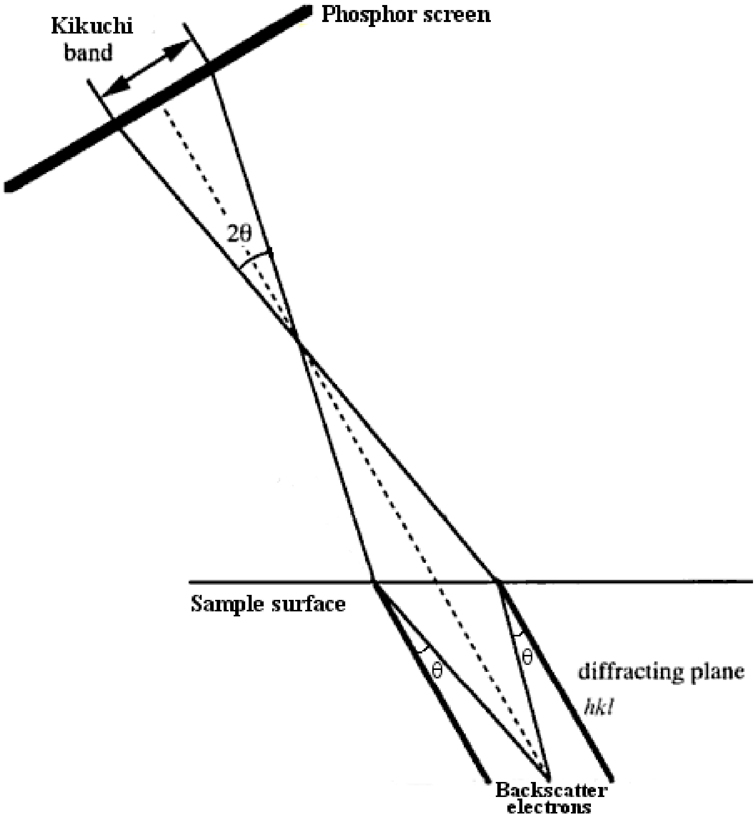

Figure 3.5: Formation of the Kikuchi band from electron back-scattered diffraction.

When an electron beam bombards the specimen, back-scattered electrons are generated by inelastic scattering. These electrons can travel in all possible directions from a thin layer less than 200 nm beneath the sample surface [103–105]. Those which satisfy the Bragg diffraction condition for a particular plane show a change in intensity. They are then projected onto an imaging plane (a phosphor screen) as Kikuchi lines [106]. A pair of Kikuchi lines called a Kikuchi band, represents a particular family of crystal planes, as illustrated in Fig. 3.5, the width of the Kikuchi band is related directly to the lattice parameter of the crystal. All the Kikuchi bands collected on the screen consist of the electron back-scattered diffraction pattern (EBSP) from the place of interest where the electron beam strikes the sample. The intersection of the Kikuchi bands correspond to a zone axis in the crystal. The EBSP can be indexed after identifying at least two zone axes. It is then possible to work out the orientation of the crystal relative to the pre-defined sample axis. Nowadays the indexing process can be fully automated and operated by a computer. The pattern recognition is done by using a mathematical method, called Hough transformation [107, 108]. Spatially resolved EBSPs can be recorded to form an orientation map of the surface of the specimen, which is called orientation imaging (OIM) [109, 110].

The crystal structrual information, mainly the inter-planar spacings and the angles between the planes, obtained from the EBSP are also used to search the diffraction database to get the best match. In this way, automated phase identification can also be achieved. In practice, several possible phases are selected before starting the OIM, so that the computer will only try to match the experimental data to these candidate phases, which saves on calculation time and actually makes the automation feasible. Qualitative chemistry determination by EDX or wavelength dispersive spectrometry is also implemented to assist phase identification [111].

Compared to X-ray diffraction, the EBSD technique allows results relating to crystal orientations, e.g. pole figures, to be obtained on a finer scale. It provides information about the grain distribution in space and the microtexture of the material, *i.e.* the texture on a microstructural scale. In addition, it provides information about much larger areas than those investigated by transmission electron microscopy. Compared to optical microscopy and scanning electron microscopy, the OIM can reveal the microstructure with greater clarity, because the grain structure can be defined exclusively by the degree of misorientation.

The EBSD technique has been used to study pipeline steels [112–114], with the focus on the microstructure of the steel itself, but not on the weld seams. Interestingly, Venegas et al. [113, 114] studied the role of crystallographic texture in hydrogen induced cracking of API 5L grade X46 steel (Fe–0.212C–0.037Si–1.334Mn–0.028P–0.032S–0.009Cr wt%). They pointed out that the crack propagates intergranularly through the high angle boundaries and transgranularly on the cleavage plane oriented to favour propagation. The latter mechanism is also studied in the present work on the fracture resistance of the welds.

In this study, a EBSD system with HKL Channel 5 software, attached to the Camscan MX2600 scanning electron microscope was used to carry out the analysis on both the unaffected materials and the welds. The orientation images were taken at an operating voltage of 25 kV, a working distance of 30 mm and a tilt angle of 70 °.

3.3.3 Electron probe microanalysis

Further microstructural characterisation includes electron probe microanalysis, which was carried out using a CAMECA SX100 system at an operating voltage of 15 kV. A beam current of 300 nA was used on X65HIC as-welded sample while 100 nA on thin X65 as-welded sample. A step size of 0.1 μm and a dwell time at each point for 60 ms was used to obtain the distribution maps of manganese and silicon respectively.

The electron microprobe is designated for quantitative chemical analysis at the microscopic level. It can in principle detect an element with the atomic number as small as that of boron. The absolute detection limit is about 10^{-14} g in an analysing volume of 10 μm^3 [115].

3.3.4 Transmission electron microscopy

Transmission electron microscopy (TEM) was carried out by using a JOEL 200CX microscope. A Helios Focused Ion Beam Workstation was used to prepare thin lamellae from strings in the weld junction of thin X65 as-welded sample. A beam current of 34 pA was used to finish-thin on both sides of the specimen.

3.3.5 X-ray diffrcation

A Philips PW1820 X-ray diffraction goniometer with Cu Kα =1.5406 Å radiation was used for continuous scanning with scan step time of 12.5 s at a step size of $2\theta = 0.05\,^{\circ}$ on the weld junction. The base metal adjacent to the weld junction was removed.

3.4 Metallurgical experiments

3.4.1 Heat treatments

Two kinds of heat treatments have been done. One is tempering at 400 °C for 2 h on all three kinds of as-welded samples. This was carried out in a CARBOLITE tube furnace. The other one is normalisation at 900 °C for half an hour on the thick-walled X65 as-welded samples. All the samples were sealed in quartz tubes beforehand, heat-treated in a CARBOLITE chamber furnace and followed by air cool.

3.4.2 Simulations

For the X65HIC grade, three kinds of experiments were carried out as below.

- Simulation of the induction welding process was done on the base material using a THERMECMASTER thermomechanical simulator. As specified by the system, the sample is machined into a cylinder with diameter 8 mm and height 12 mm along the rolling direction.

- Simulations of the induction austenisation were done by placing the as-welded sample into a CARBOLITE chamber furnace at 960 °C, followed by air cooling or by quenching in brine.

- Experiments of modified post-welding heat treatments consist of annealing at different temperatures followed by tempering at 480 °C. Three annealing temperatures were chosen, which were 830, 890 and 1000 °C. All the cycles were executed by placing X65HIC as-welded sample into a furnace with a preset temperature. The samples used are small weld segments approximately 30 mm long in the transverse direction (TD) and 1–3 mm thick in the rolling direction. K-type thermocouple was attached to each sample to reveal the thermal history of the heat treatment.

Modified post-welding heat treatments were also carried out on the thin X65 as-welded sample using the Gleeble system at ArcelorMittal Research and Development, Ghent. The temperatures 1054 and 1150 °C were selected as the peak values of the first cycle, with a holding time of 12, 23 or 27 s, followed by quenching. Peak temperatures of the second cycle was 890, 922 or 950 °C with the choices of holding time among 12, 23 or 38.4 s and followed by air cooling. Some experiments were stopped half way to investigate the microstructure of the weld after the first cycle of the heat treatment.

Chapter 4

Welds from X65HIC Grade of Steels

4.1 Mechanical properties

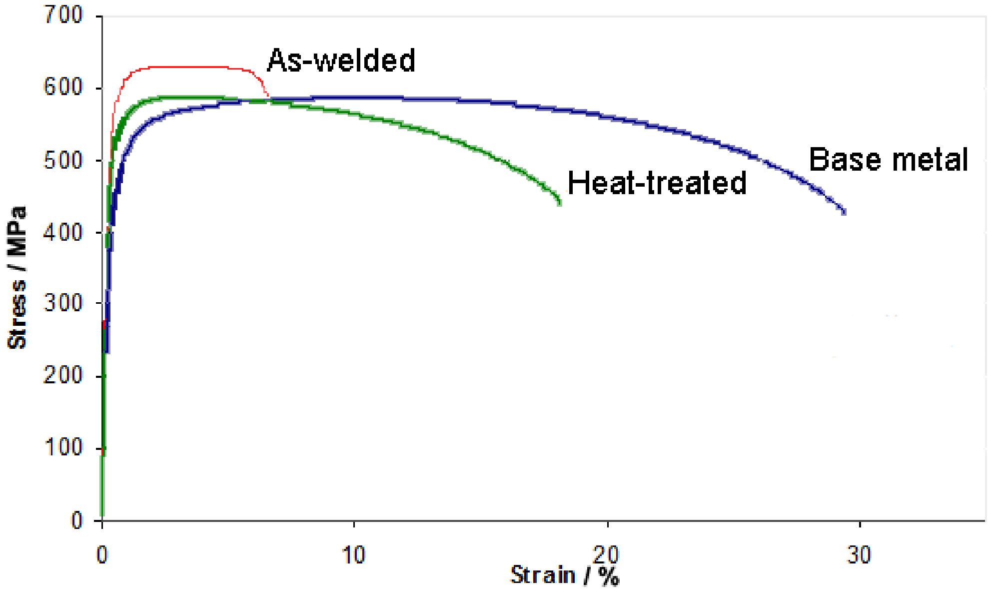

Figure 4.1: Stress-strain curves of high frequency induction welded X65HIC pipe.

The mechanical properties of the welded pipe were evaluated using tensile and Charpy impact tests, which are the fundamental requirements to ensure structural integrity. The tensile test results are shown in Fig. 4.1 and listed in Table 4.1. The ultimate strength and elongation of the sample after post-welding heat treatment was approaching that of the base metal, while the as-welded sample is relatively brittle. The post-welding heat treatment

Table 4.1: Critical values of the results from three tensile tests on high frequency induction welded X65HIC grade pipe.

	Ultimate tensile strength/ MPa	Total elongation/ %
Base metal	588	33
As-welded	627	8
Heat-treated	589	27

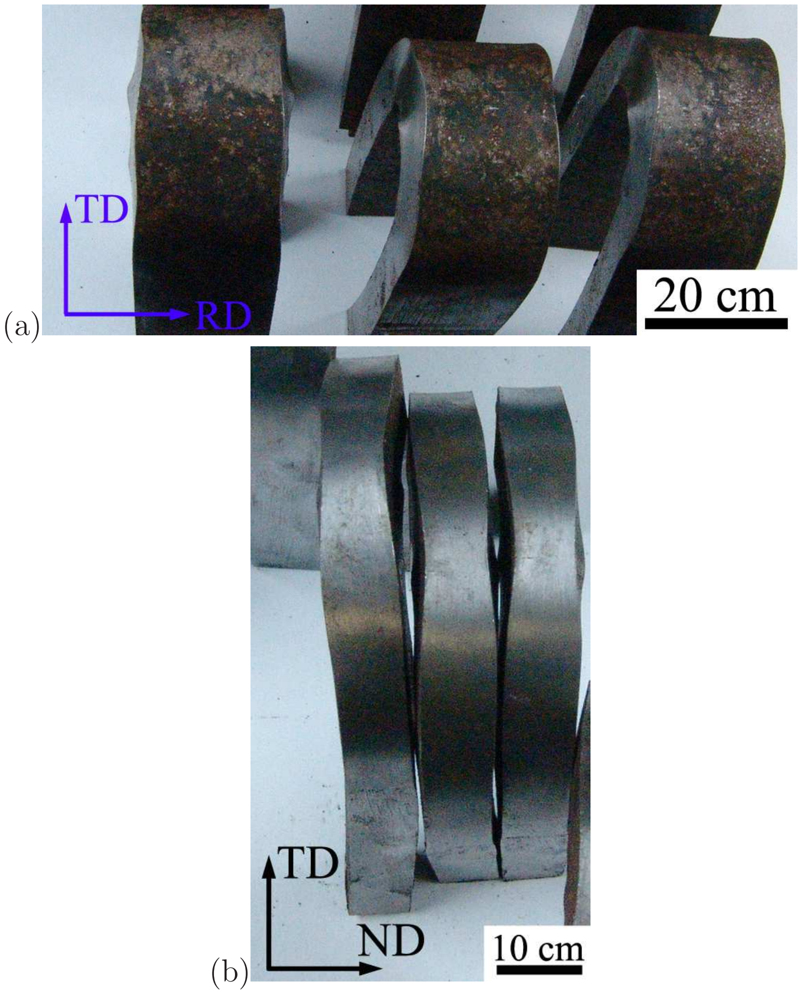

Figure 4.2: Macrographs of the heat-treated X65HIC weld segment after bend tests (a) 3 samples after face bend. (b) After side bend.

is clearly effective in restoring the ductility of the weld. This was further confirmed by a U-bend test, in which the heat-treated weld segment remained integral without any openings on either ND-TD or RD-TD surfaces of the segment, as shown in Fig. 4.2.

Base metal ('base'), as-welded and samples after heat treatment were

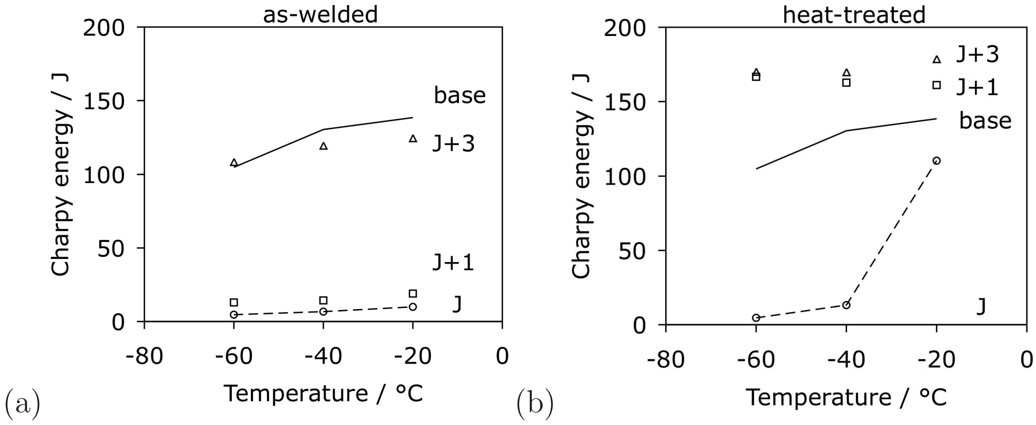

(a) (b)

Figure 4.3: Charpy impact test energy of the X65HIC pipe as a function of temperature. 'J' designates the weld junction, and when used on its own, the Charpy notch is located at the fusion surface. 'J+1' represents the case where the notch is 1 mm away from the junction. (a) As-welded condition. (b) Welded and heat-treated.

machined for Charpy testing with the V-notches located on the weld junction, 1 mm and 3 mm away from the weld junction. Each point in Fig. 4.3 is an average value of three test results. The Charpy energy of the heat-treated sample is significantly higher than that of the as-welded specimen, when the V-notches were located 1 or 3 mm away from the joint. However, when the V-notch was located on the joint, the improvement in toughness due to heat treatment was not so obvious, with no enhancement for the test temperature of −40 °C, as shown in Fig. 4.3b. Although the toughness after heat treatment exceeds the required absorbed energy at 0 °C according to the ISO standard (section 2.2.2), the increase in the ductile brittle transition temperature, particularly at the weld junction is still considered as the weak point of the structure; since these pipelines should be reliable and durable in service under extreme weather or environmental conditions. This chapter describes the investigation of the weakness of the weld junction in spite of heat treatment following welding.

4.2 Morphological microstructure

4.2.1 As-welded state

Figure 4.4 is the picture of the etched surface of the sample in the as-welded state, in which the weld can be seen clearly. It is categorised into four zones in this study, which are base metal, thermomechanically-affected zone, heat-affected zone and weld junction. The microstructure of the four zones was investigated in detail.

The microstructure of the steel unaffected by the welding, consists of allotriomorphic ferrite and a small amount of pearlite, illustrated in Fig. 4.5. As discussed in section 2.2.1, the first phase to form during cooling of the thermomechanically controlled processing of the pipeline steel is allotriomophic ferrite which enriches the remaining austenite with carbon. The latter eventually transforms into fine pearlite, visible at high resolution, as shown in the circled region in Figs. 4.5b and c. The small fraction of pearlite is due to the low average carbon concentration (0.041 wt%) of the steel. This kind of microstructure is referred to as 'base metal'.

During the welding process, the abutting edges of the pipe are pushed together whilst they are hot and plastic, thus giving rise to flow which serves two purposes: first, to expel undesirable oxides or molten matters if there is any from the weld junction, and secondly to form a metallurgical bond by breaking up the interface between the edges. There is therefore a thermomechanically-affected zone where remnants of the deformation asso-

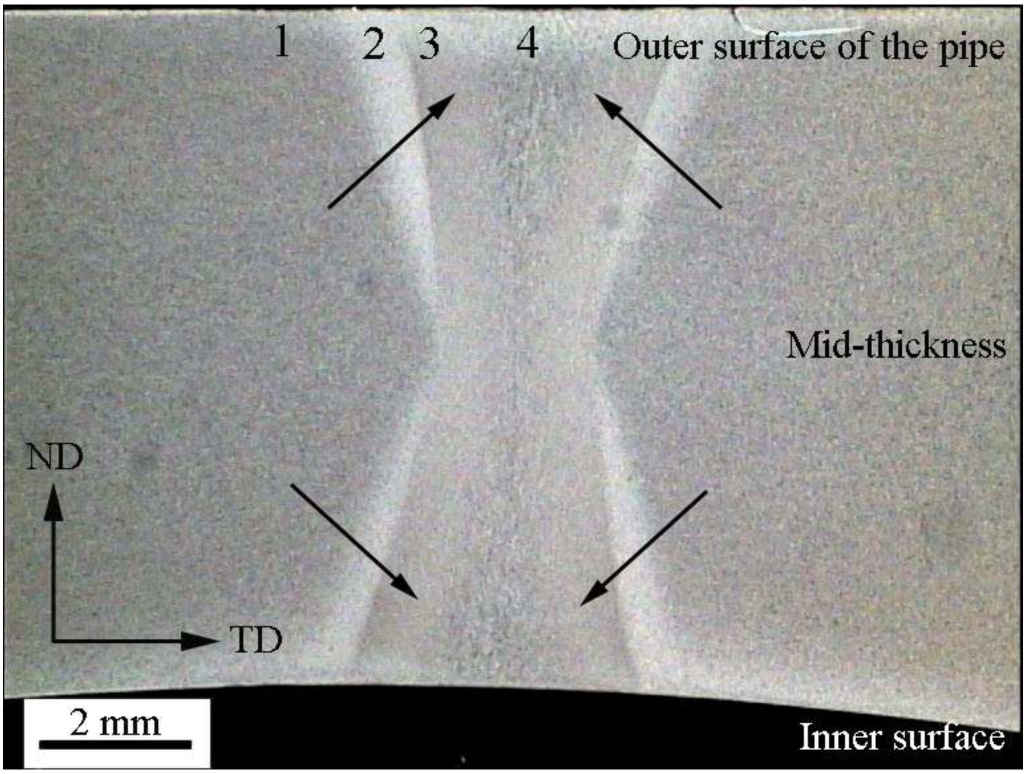

Figure 4.4: The four zones which define the X65HIC welded region: 1–base metal, 2–thermomechanically-affected zone, 3–heat-affected zone, and 4–weld junction. The arrows illustrate the directions of metal flow.

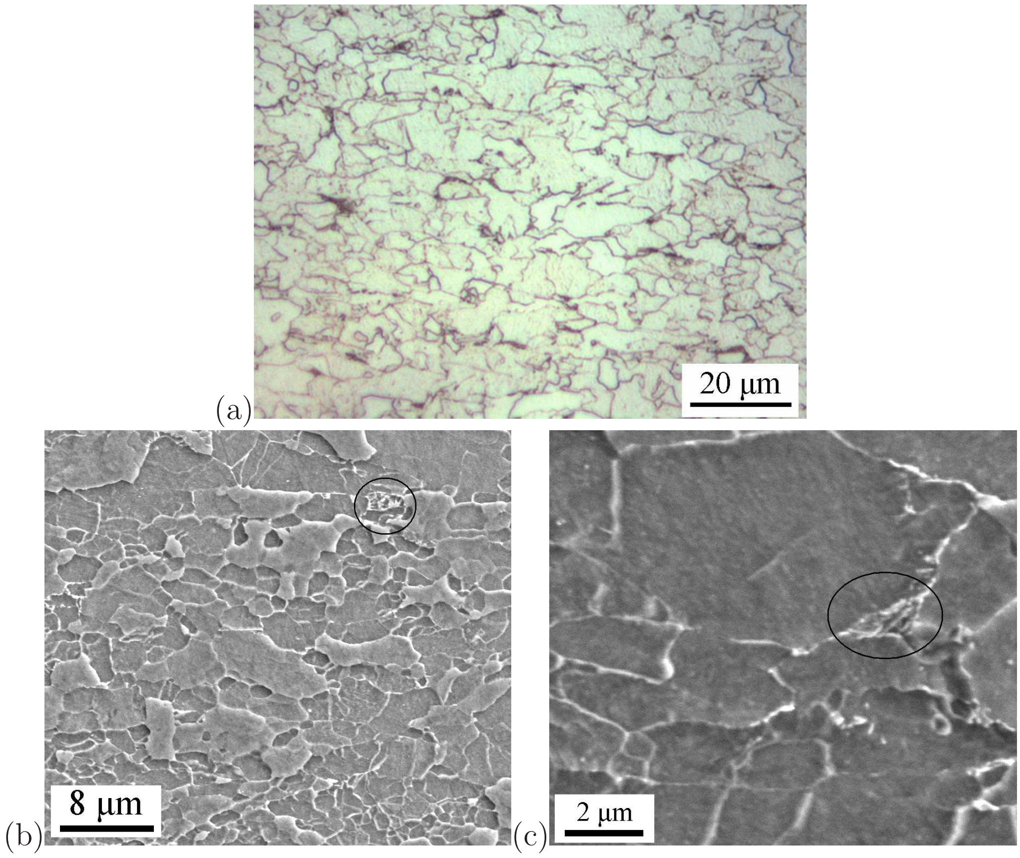

Figure 4.5: Microstructure of the unwelded X65HIC steel in pipe form: (a) optical micrograph, (b) and (c) scanning electron micrograghs.

ciated with the welding process are retained. This has a structure similar to that of the base metal, except that the shapes of the ferrite grains are anisotropic, aligned along the direction of metal flow, Fig. 4.6a. Four parts of the thermomechanically-affected zones located on both sides of the weld junction are pointed out in Fig. 4.4. There is no obvious thermomechanically-affected zone at the mid-thickness of the pipe. It is possible that the alignment observed is purely due to the deformation of ferrite, but it could also be true that the morphology is a consequence of the severe pancaking of the austenite [38, 116] before it transforms into ferrite.

The heat-affected zone on the as-welded sample consists mainly of equiaxed allotriomorphic ferrite which has reformed from the grains which become austenitic and then dynamically recrystallise, Fig. 4.6b. The gradients of microstructure expected in the wide heat-affected zone of conventional fusion welds, *i.e.*, tempered plate, intercritically heated plate and fully austenitised regions, are not obvious, partly because of the narrow dimen-

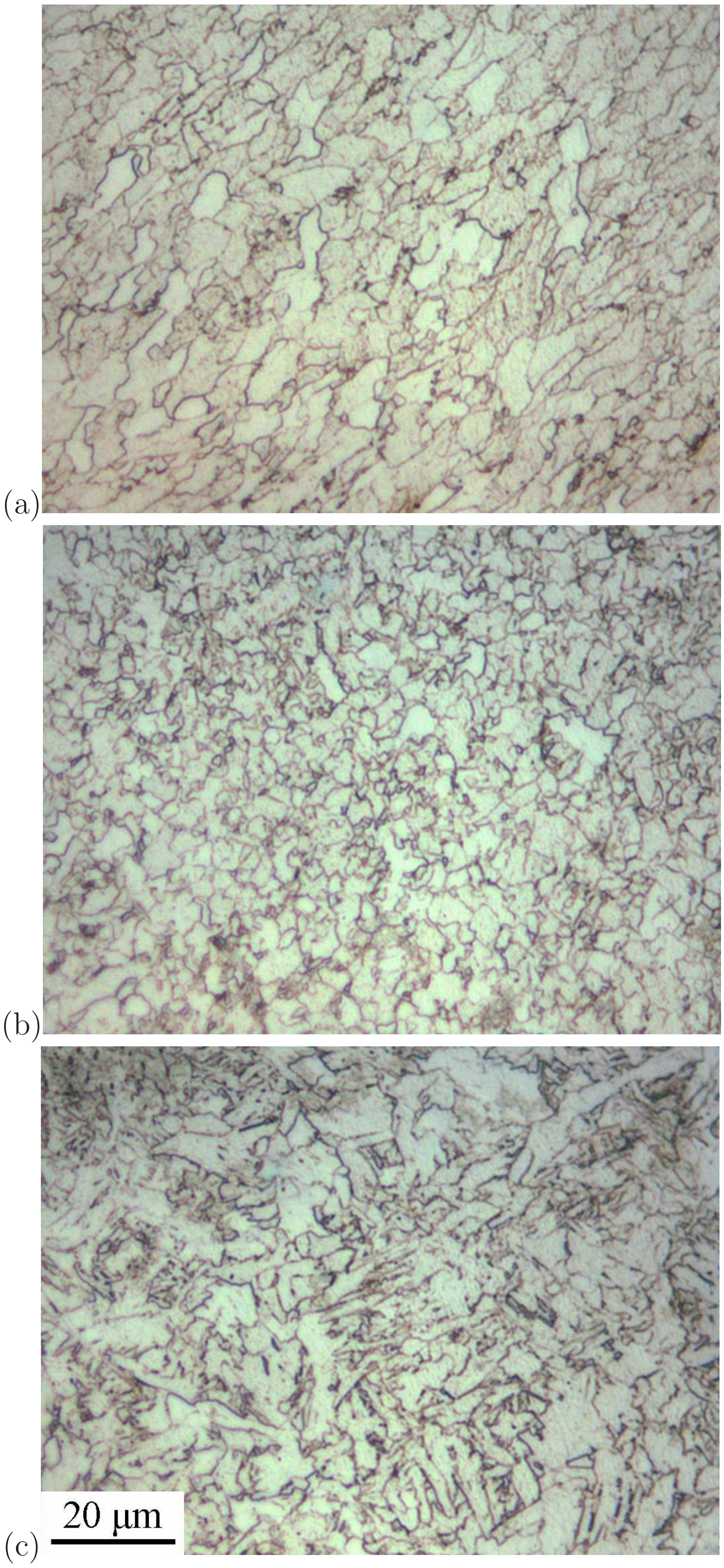

Figure 4.6: Microstructure of (a) thermomechanically-affected zone, (b) heat-affected zone and (c) weld junction on as-welded sample near the outer surface of the X65HIC pipe.

sions of the zone but also because the steel has such a low solute-content and hence, hardenability. Grain size measurements on the heat-affected zone gave an average value of 5 ± 0.5 μm, while the measurements on base metal gave 7 ± 0.6 μm.

The microstructure at the weld junction of the as-welded sample is interesting, consisting of a mixture of grain boundary allotriomorphs of ferrite, Widmanstätten ferrite and an intervening residual phase which is likely to be M–A islands, Fig. 4.6c. This is a direct consequence of the fact that the austenite grains here are expected to be coarser, since this region was heated up most effectively during the welding process. It is well-known that coarse austenite grains favour the formation of Widmanstätten ferrite [117–119]. The M–A islands etched dark as shown in the optical micrograph, Fig. 4.6c. They can be seen more clearly in the scanning electron micrograph, Fig. 4.7a. The X–ray diffraction pattern of the X65HIC as-welded sample shows the existence of small amount of austenite, as only two tiny austenite peaks can be identified in Fig. 4.8, which should be contributed by these M–A islands in the weld junction. After tempering the as-welded sample at 400 °C for 2 h, the M–A islands turned into tempered martensite, as shown in Fig. 4.7b.

At the mid-thickness of the pipe, several elongated M–A islands could be observed in the weld junction, as shown in Fig. 4.9a, but the strings were not present in other parts of the weld. Electron probe microanalysis demonstrated that they are manganese-rich phases, Fig. 4.10. After tempering they revealed the classical morphology of tempered marteniste, Fig. 4.9b. The phenomenon of strings will be further discussed in the next chapter, since it is more prevalent in the welds from X65 steels.

There are no sharp boundaries between the four different zones across the weld. The microstructure changes gradually. The micro-hardness profile across the weld on the as-welded sample is shown in Fig. 4.11a. The origin of the x-axis corresponds to the centre of the weld junction. Consistent with the tensile data (Fig. 4.1), the weld is harder than the base metal, especially near the outer surface of the pipe. The higher hardness near the outer surface of the pipe, compared to the other half, may be caused by the surface hardening effect of the induction heating. Although the microstructure of the outer layer of the pipe is not distinguishable from that of the rest, the induction heating should leave a compressive residual stress on the outer layer of the work piece [120, 121], because the surface is cooled down more quickly than the inner part.

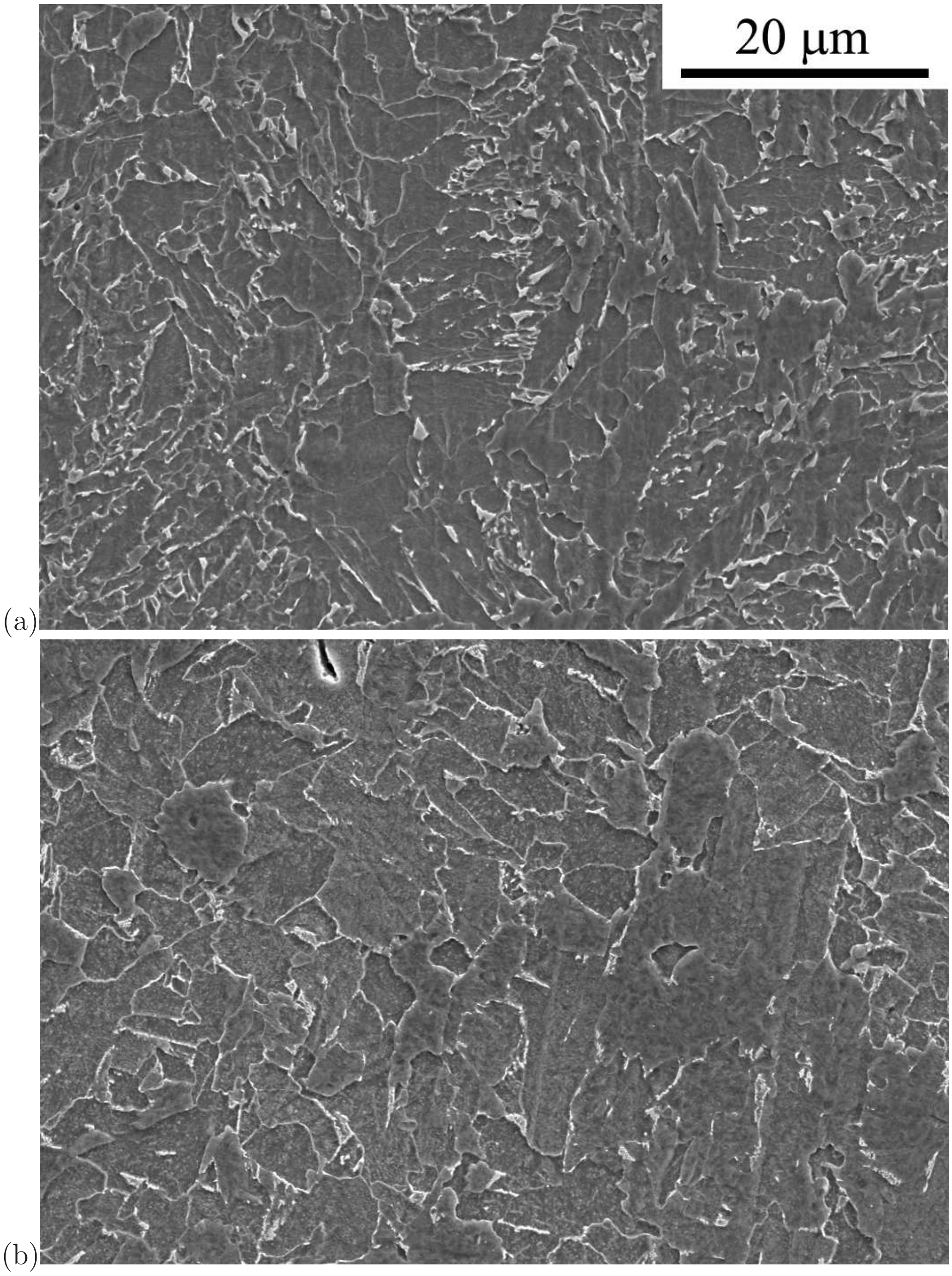

Figure 4.7: Scanning electron micrograghs of weld junction near the outer surface of the X65HIC pipe. (a) As-welded state. (b) After tempering at 400 °C for 2 h.

The hardness across the weld is scattered in the mid-thickness and near the inner surface of the pipe. The peak hardness value falls into the heat-affected zone on both sides of the weld junction near the inner surface of the pipe, since this zone is featured with the finer grain structure as mentioned

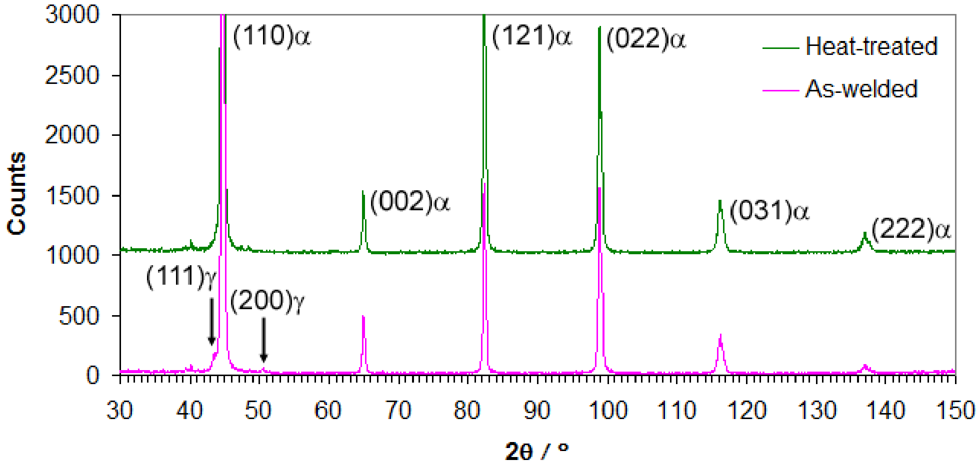

Figure 4.8: X-ray diffraction pattern for the X65HIC weld.

above. Such an increase of hardness at the mid-thickness should also be expected. However the weld is much narrower at the mid-thickness of the pipe, approximately 2 mm in width (Fig. 4.4); so the step size, 150 μm, in establishing the micro-hardness trace may not be fine enough to reveal the true distribution of hardness among different zones.

After tempering, the hardness of the weld dropped by 10 to 20 HV, compared with the as–welded state (*cf.* Fig. 4.11a and b), which also supports the existence of martensite in the as-welded sample.

4.2.2 After post-welding heat treatment

The induction post-welding heat treatment broadens the affected area from the welding process itself, as shown in Fig. 4.12. However, the microstructure across the heat-treated weld is much more uniform compared to the as-welded sample. Three microstructural domains could be recognized under extensive etching with 2 % nital, Fig. 4.12. The affected area has a microstructure similar to that of the unaffected base metal, consisting of allotriomorphic ferrite and pearlite (*cf.* Fig. 4.13a and Fig. 4.5a). The only difference is that the ferrite grains are more equiaxed in the affected area. The alignment of the grains due to rolling of the steel sheet in the base metal and forging in the former thermomechanically-affected zone has been annealed out.

Vestiges of the weld junction remained after heat treatment, since plate-like ferrite exists in the microstructure, Fig. 4.13b. Scanning electron microscopy shows evidence of decarburisation; since there is some divorced

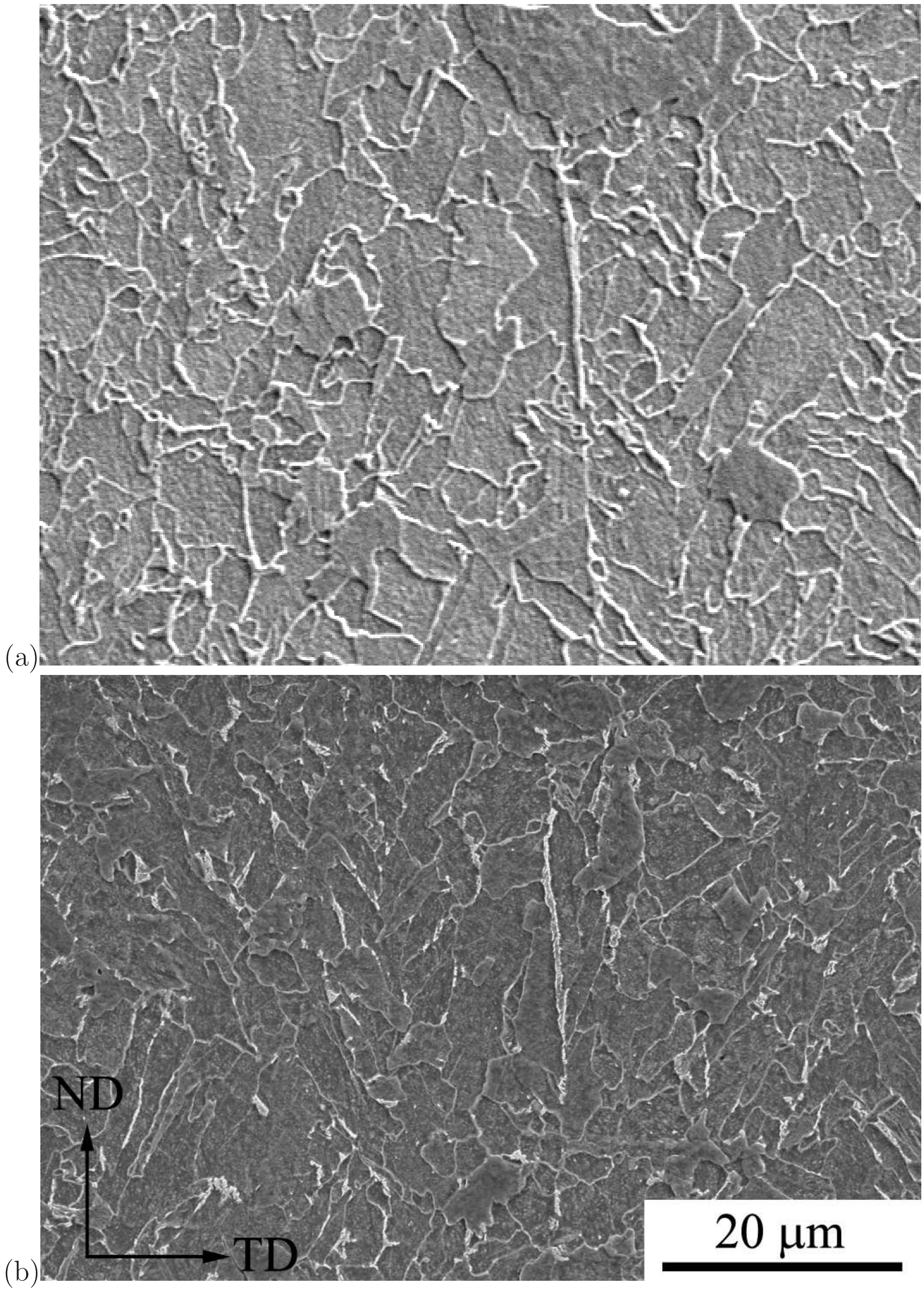

Figure 4.9: Scanning electron micrograghs of the weld junction at the mid-thickness of the X65HIC pipe. (a) As-welded state. (b) After tempering at 400 °C for 2 hours.

pearlite in the position of the original weld junction, Fig. 4.13d. The affected area away from the weld junction in comparison has more pearlite, Fig. 4.13c. This amount of decarburisation does not have significant effect

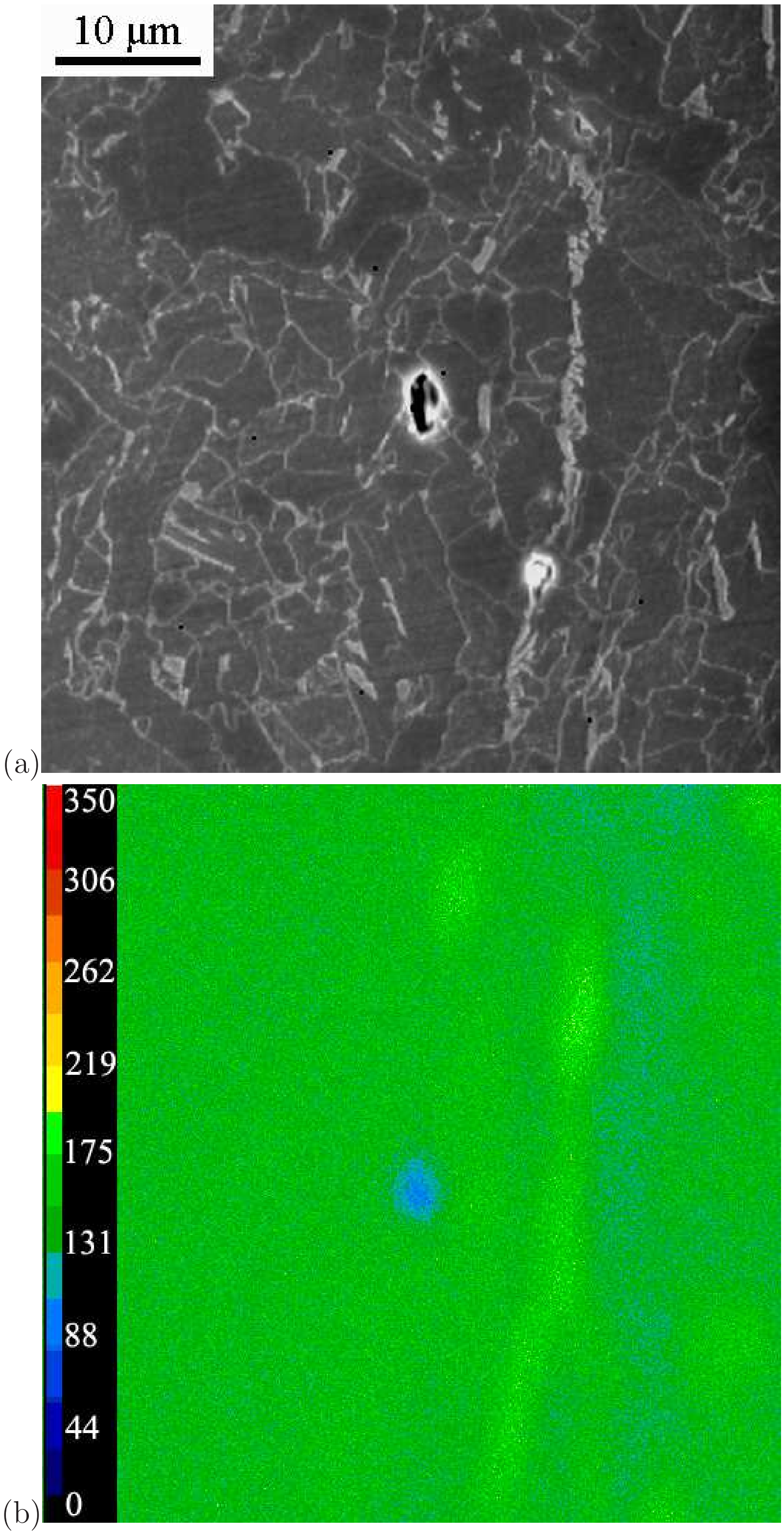

Figure 4.10: The weld junction on the as-welded X65HIC sample at the mid-thickness of the pipe. (a) Scanning electron micrograph. (b) Mn mapping of (a) using electron probe microanlaysis. This analysis can not be fully quantified due to experimental limitation. Bigger number and warmer colour means higher concentration of the elements and vice versa.

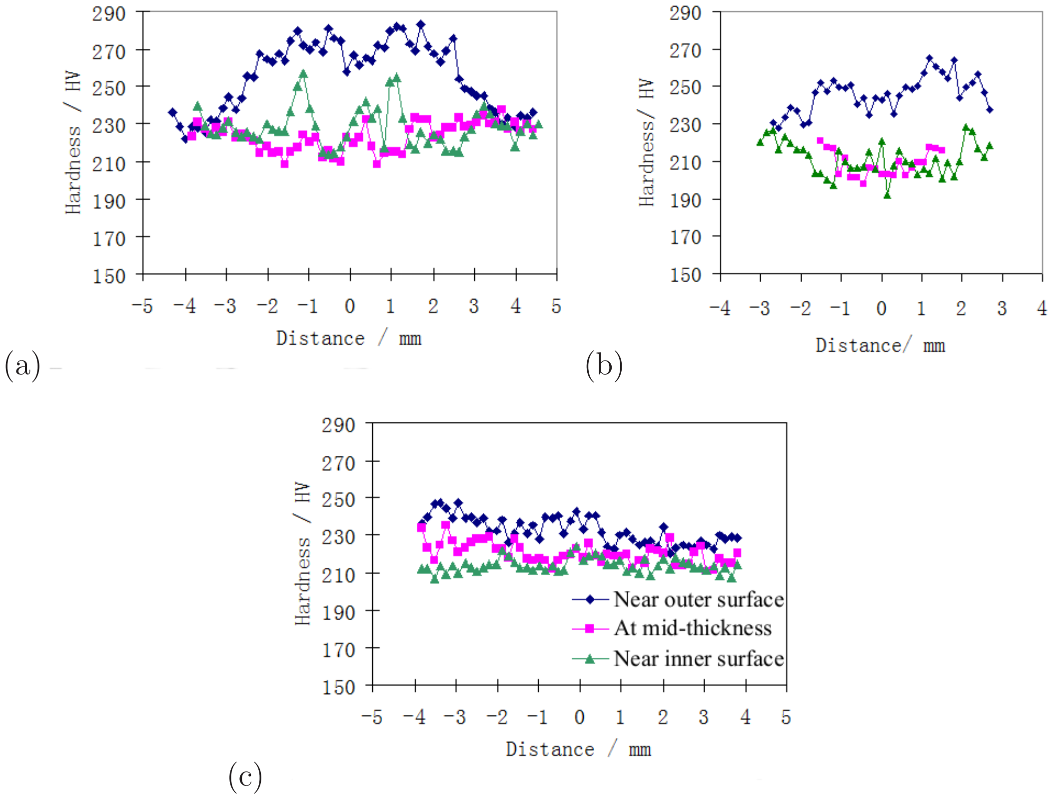

Figure 4.11: Micro-hardness distribution across the weld of the X65HIC pipe. (a) As-welded state. (b) After tempering at 400 °C for 2 hours. (c) Welded and heat-treated.

on the mechanical properties of the weld, since the hardness across the weld after post-welding heat treatment is uniform as shown in Fig. 4.11c, which is consistent with the unification of the microstructure.

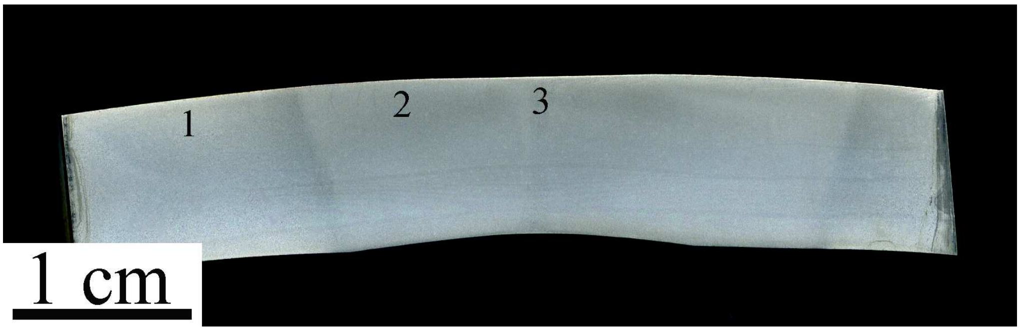

Figure 4.12: Weld segment from the X65HIC pipe after post-welding heat treatment. 1–base metal, 2–the affected area, and 3–the original location of the weld junction.

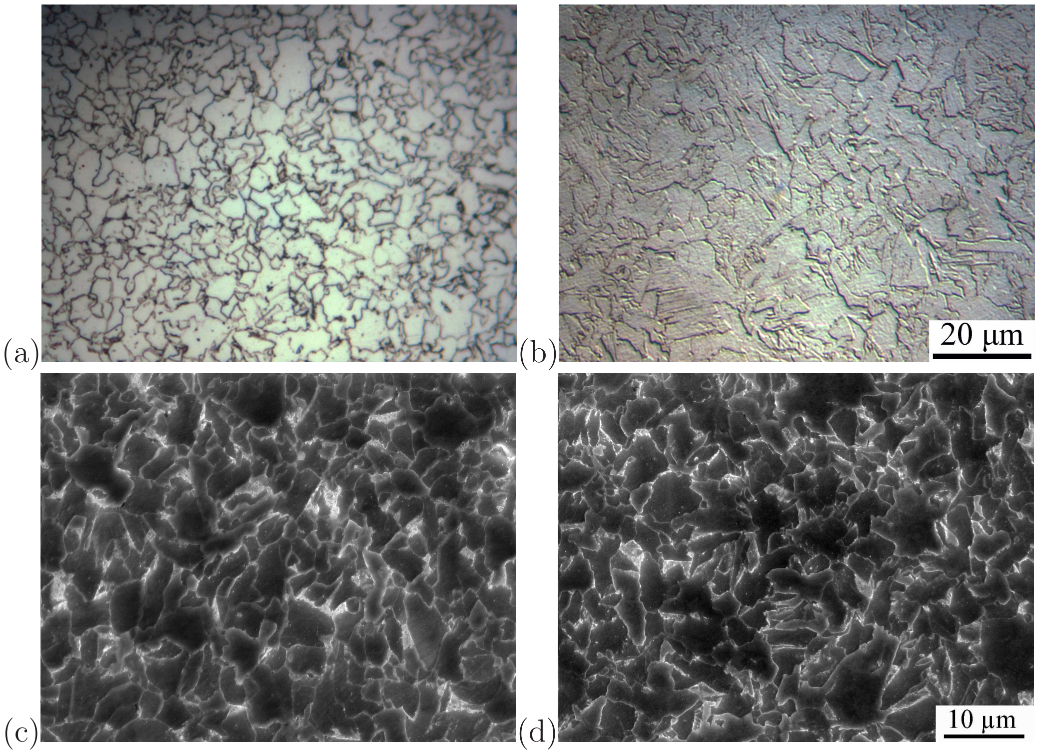

Figure 4.13: Microstructure of the sample after post-welding heat treatment near the outer surface of the X65HIC pipe. (a) Affected area. (b) The original location of the weld junction. (c) and (d) Corresponding scanning electron micrographs taken at the region of (a) and (b).

The microstructural observation did not reveal any remaining austenite in the sample after post-welding heat treatment and the X–ray diffraction pattern in Fig. 4.8 confirms its absence.

The possibility of oxides at the weld junction being the cause of poor toughness was investigated using extensive optical and scanning electron microscopy. These experiments did not reveal any role of inclusions in determining the impact properties at the junction. Broken Charpy samples from the weld junction were also examined because there is a better chance of detecting significant initiating features, but this led to the same conclusion. A typical fracture surface of the sample after post-welding heat treatment, tested at the weld junction at −40°C, is shown in Fig. 4.14.

By this point of the investigation, it was concluded that the post-welding heat treatment is effective in removal of any microstructure detrimental to the mechanical properties of the regions influenced by the welding. All the conventional causes of the low toughness seemed to be excluded from consideration: there was neither extraordinarily coarse microstructure

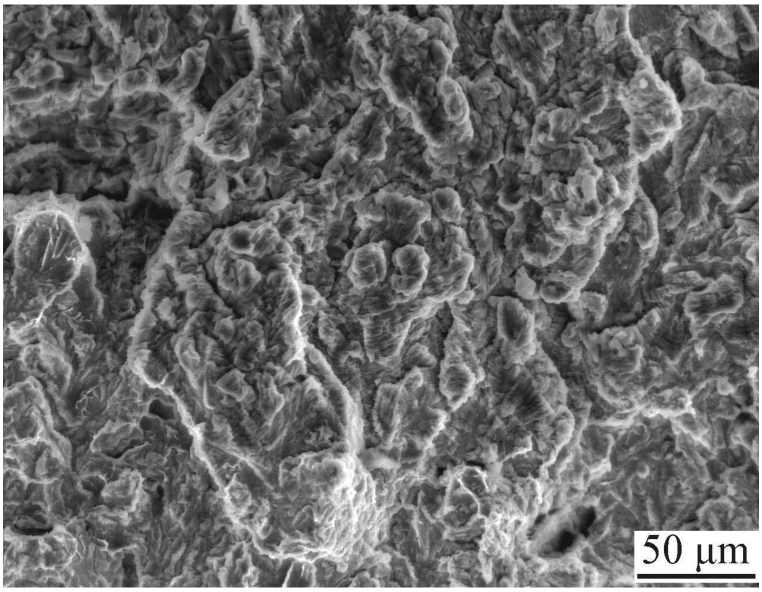

Figure 4.14: Fracture surface at weld junction of the X65HIC pipe after post–weld heat treatment, tested at −40°C.

nor substantial decarburisation in the weld junction, no retained austenite was detected, and fractographic analysis did not reveal evidence of inclusion-induced fracture. However, there was a breakthrough, as revealed in the next section, where the reason for low toughness at the weld junction is shown to be crystallographic in origin.

4.3 Crystallographic texture

A large quantity of crystallographic data were collected using EBSD in order to give a complete overview of the texture of the weld. Ferrite orientation images were constructed from 2 mm away towards the weld junction near the outer (Fig. 4.16) and inner (Fig. 4.18) surfaces of the pipe, and from 1 mm away at the mid-thickness as shown in Fig. 4.17 again because of the narrower width of the weld at the mid-thickness of the pipe. Figure 4.15 shows the colour coding of the orientation images in this study unless otherwise stated.

It is noted here that austenite was not confidently detected by EBSD scanning even in the as-welded sample, because the austenite exists in minute quantities associated with the M–A islands, the hybrid microstructure of which makes it difficult for recognition of the EBSP. In all three images, the scan starts 2 mm away from the weld junction at the top left and contin-

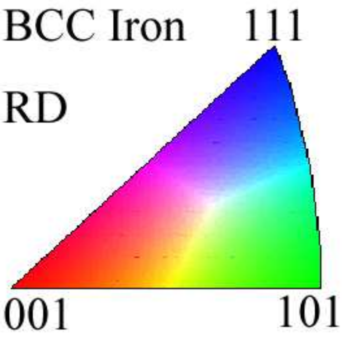

Figure 4.15: Colour codes in the orientation images, representing the inverse pole figure information projecting on the plane normal to rolling direction.

ues towards the middle of the weld junction at the bottom right. On the scanned sample, 2 mm away from the weld junction is the base metal near the outer surface of the pipe, so the microstructure variance across the weld at the as-welded state is shown clearly, Fig. 4.16. Grain boundaries in the orientation images are designated mainly by the solid black lines to be $\geq 10°$ misorientation between the neighbouring grains. A small number of thinner lines, particularly in the weld junction, represent misorientations $\geq 2°$. The coarse crystallographic grain size in the weld junction is apparent from the large clusters of grains which have a similar colour–coding. As expected and reported elsewhere [122, 123], it is different from the morphological grain size observed using optical microscopy and ordinary scanning electron microscopy.

From the crystallographic data obtained, texture analysis was conducted on different regions across the weld. Only results analysed near the inner surface of the pipe are presented here for brevity. The numbers on all the pole figures in this work indicate the pole density in "times random" unit. Figure 4.19 shows a ferrite orientation image from a region 3 mm away from the weld junction, *i.e.*, with crystal orientations unaffected by the welding process. Texture of the base metal is illustrated by the {100} pole figure. However, when the pole figure is constructed for a region approximately 20 μm^2, it is clear that there the ferrite grains within this region have a large range of orientations. Since one of the important factors influencing the absorption of energy during cleavage fracture is the deflection of propagating cracks across grain boundaries, such a texture bodes well for toughness, consistent with the base–plate data illustrated in Fig. 4.3.

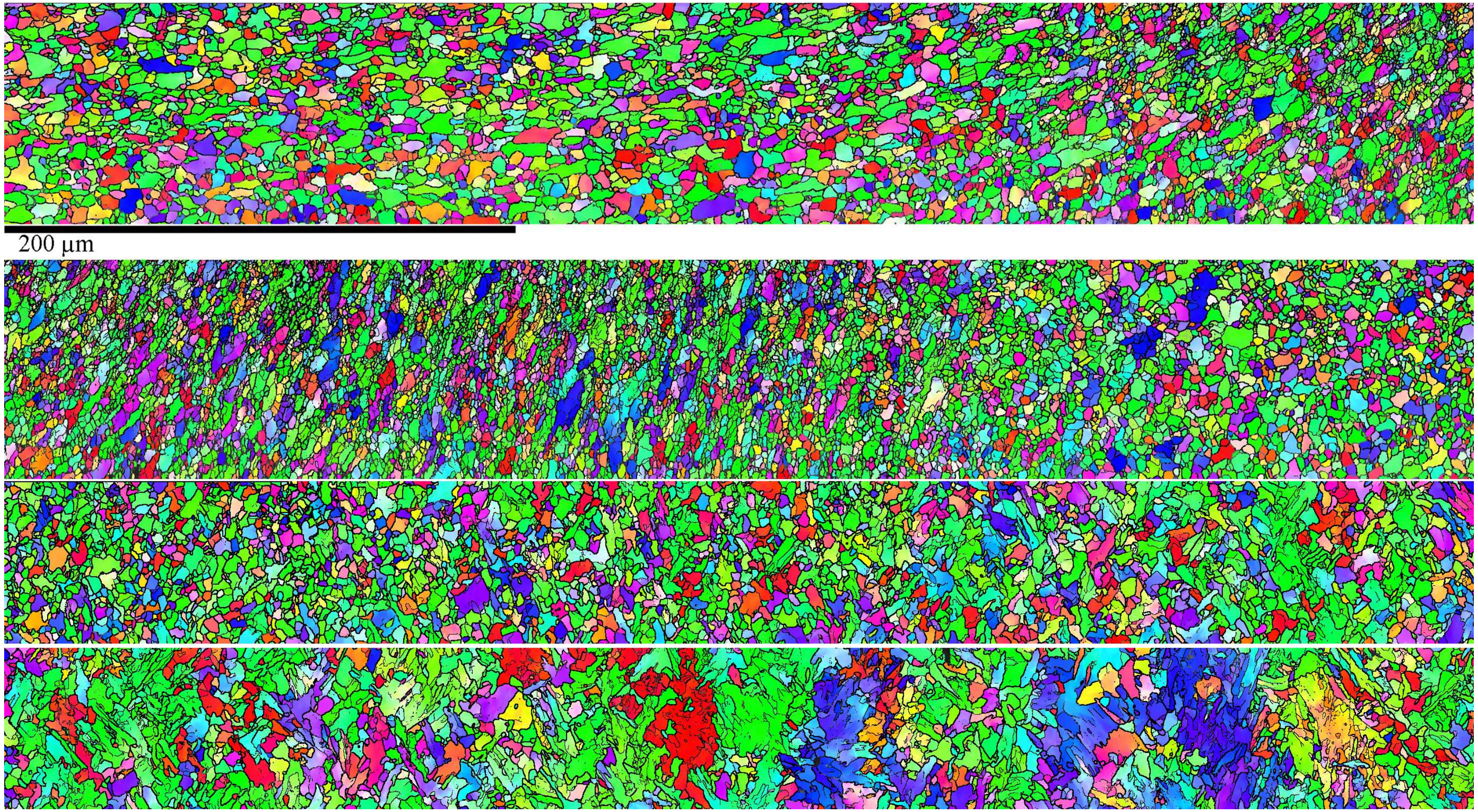

Figure 4.16: Continuous ferrite orientation image of the as-welded sample, starting from 2 mm left (top left) to the middle of weld junction (bottom right) near the outer surface of the X65HIC pipe.

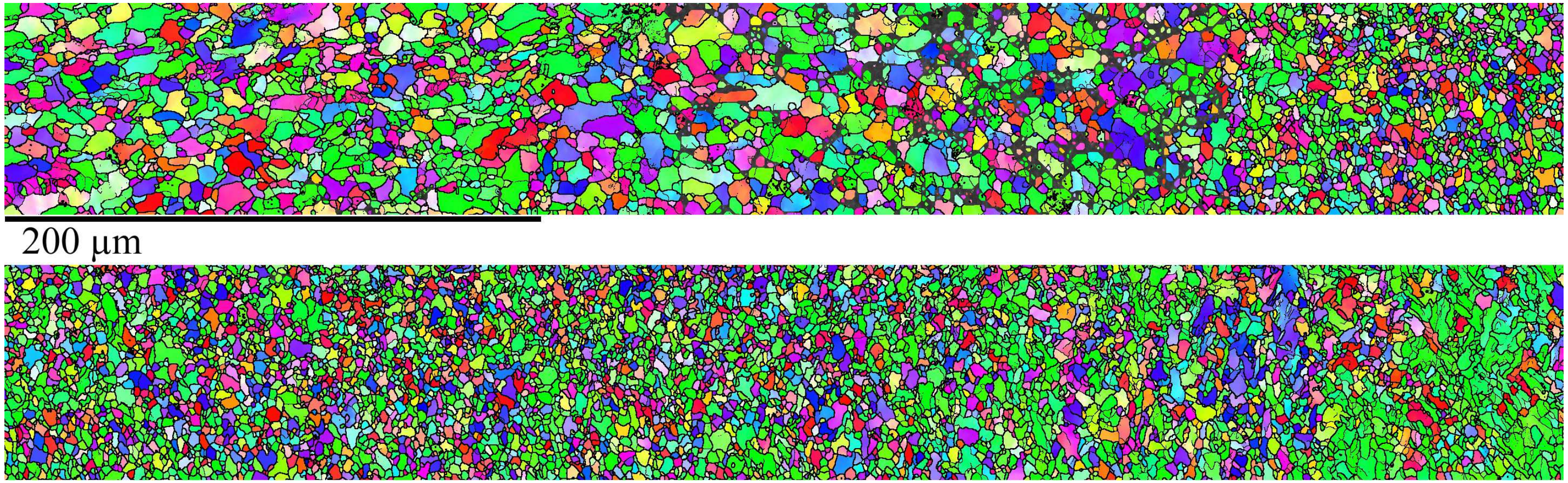

Figure 4.17: Continuous ferrite orientation image of the as-welded sample, starting from 1 mm left (top left) to the middle of weld junction (bottom right) at the mid-thickness of the X65HIC pipe.

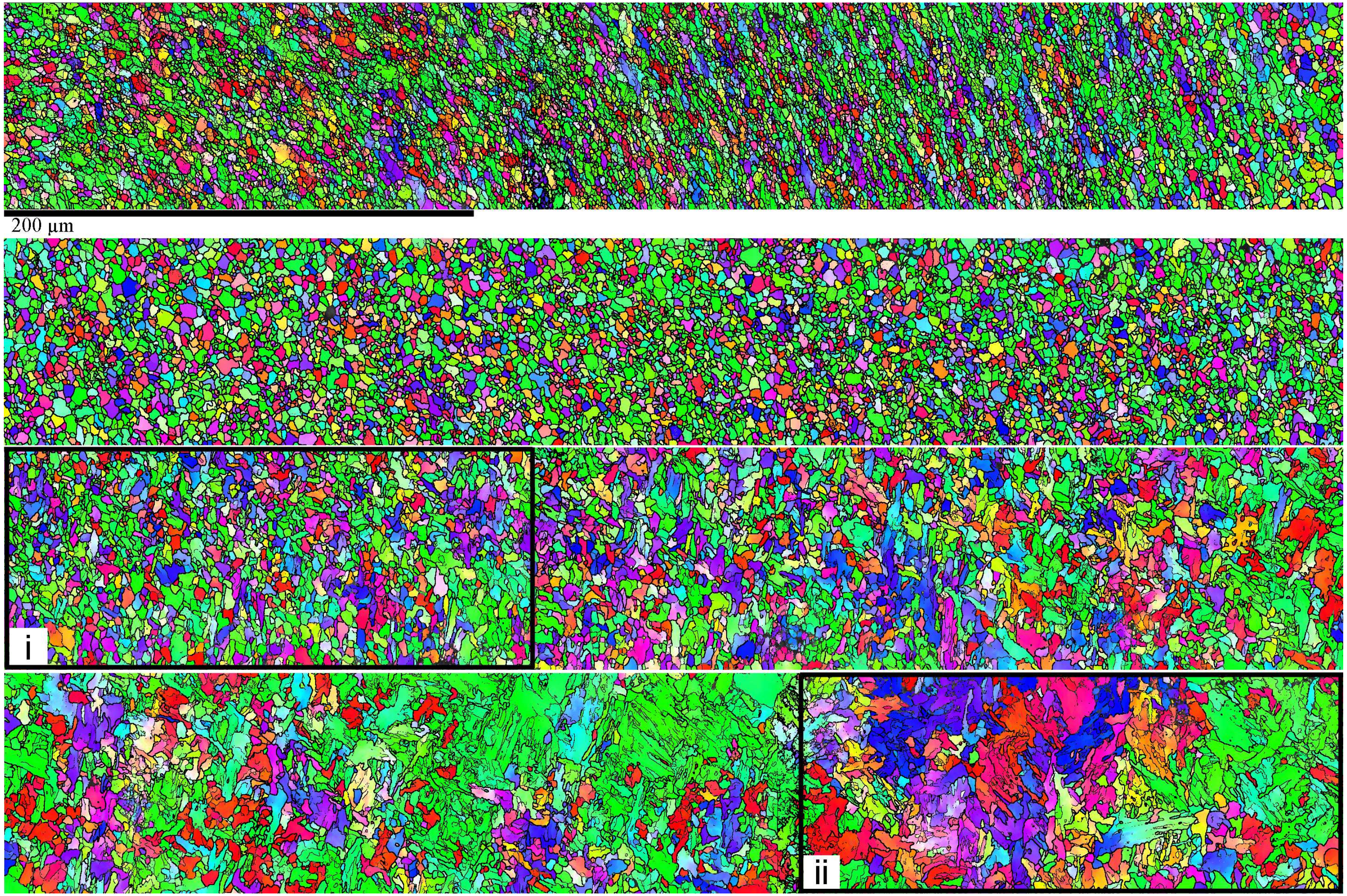

Figure 4.18: Continuous ferrite orientation image of the as-welded sample, starting from 2 mm left (top left) to the middle of weld junction (bottom right) near the inner surface of the X65HIC pipe.

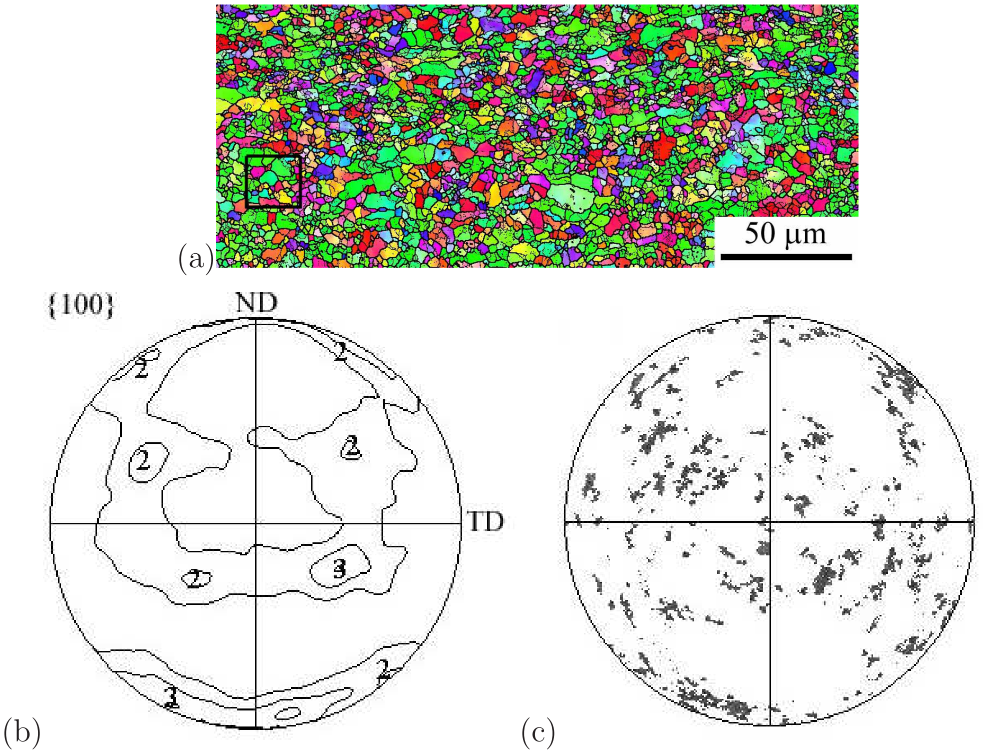

Figure 4.19: (a) Orientation image of the base metal, 3 mm away from the weld junction. (b) and (c) The {100} pole figures for the full area illustrated, and for the boxed region in (a).

The situation changes dramatically in the affected regions of the weld. The overall texture both in the region 1 mm away from the weld junction and in the weld junction itself was obtained from the boxed regions in Fig. 4.18. The size of the box is the same as the area in which the overall texture of the base metal was gained, shown in Fig. 4.19a. The texture in these regions is much sharper compared to that in base metal (*cf.* Fig. 4.19b and 4.20). The coarse crystallographic grain size coincides vividly the poor toughness recorded from Charpy tests [66] of the as–welded samples conducted on these regions, Fig. 4.3a.

The orientation images from the post–weld heat-treated sample are shown in Fig. 4.21, 4.22 and 4.23a. These images obtained from three different thicknesses of the pipe all start 1 mm away from the weld junction at the top left and continues towards the middle of the weld junction at the bottom right. They confirmed the previous observation that the post-welding heat treatment unify the microstructure across the weld. The grain size analysis based on the orientation images can also be done easily by the HKL software. The grain is recognised by critical misorientation angle between neighbouring grains, which is set at 10° and by allowing to take the

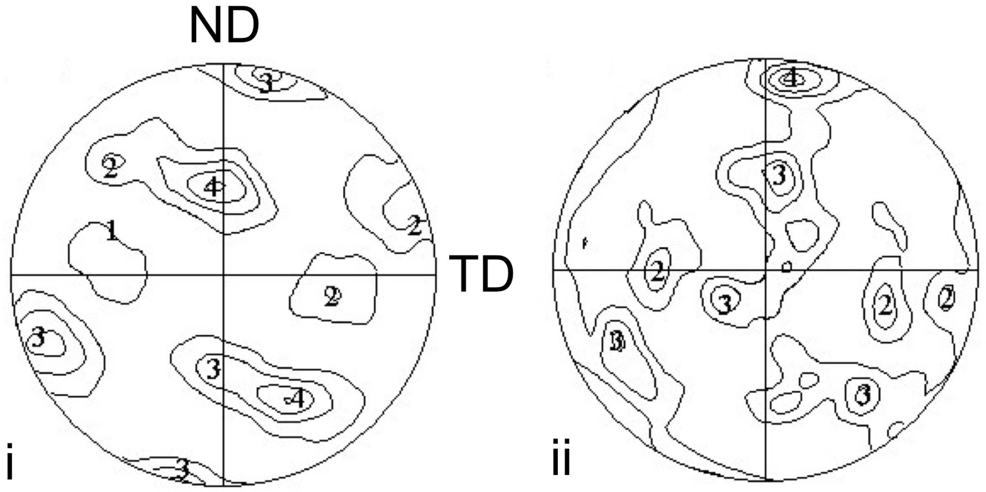

Figure 4.20: {100} pole figures from the regions marked 'i' and 'ii' in Fig. 4.18, showing the texture in a region 1 mm from the weld junction and in itself near the inner surface of the X65HIC pipe.

closest route to complete the grain boundary. The aim of this analysis is to measure the morphological grain size. The orientation images have the closest similarity to the optical micrographs when the critical misorientation angle is set at 10°. The amount of etching is critical for the metallographic experiment, since the appearance of grain boundaries is very sensitive to the etching by 2% nital. However the grain size obtained from the orientation images is insensitive to the chosen misorientation angle, which will be discussed in the end of this section. Figure 4.24 shows results, in which each line is constructed from an area with the same size of 'i' and 'ii' of Fig. 4.23. It is clear that there is no significant difference of morphological grain size in the region 1 mm away from the weld junction and in the weld junction itself.

The overall texture in the corresponding regions 1 mm away from the weld junction and in the weld junction itself was weakened relative to the as-welded state (*cf.* Fig. 4.20 and Fig. 4.23b). Although at first glance the refinement may appear to have happened, the texture analysis indicated that the extent of the crystallographic refinement was limited. In the weld junction, strong texture persists, as the typical result illustrated for region (iii) in Fig. 4.23 indicates that the orientation differences between the grains within the 20 μm interval regions are very small. Examination of the fracture surface of a broken Charpy specimen revealed facets crossing many grains, and of the same order of magnitude in scale to the clusters of similarly oriented grains, Fig. 4.25. Hence, the post–weld heat treatment does not result in an improvement of the low–temperature Charpy energy, Fig. 4.3b.

The {100} plane is the cleavage plane of the BCC iron crystal [86, 87]; so a high density of {100} planes parallel to rolling direction should lead to a low fracture energy, referring to the specification of Charpy sample in this study, Fig. 3.2b. It is useful therefore to examine the distribution of {100} planes relative to the geometry of the Charpy test.

Fig. 4.26 shows the distribution of {100} poles relative to the transverse direction, which is normal to the mean fracture plane of the Charpy specimen. A high density of poles parallel to the transverse direction implies a polycrystallography which is conducive to cleavage crack propagation. The weld junction, both before and after the heat–treatment, retains the highest density of cleavage planes in an unfavorable orientation, which is consistent with the failure to improve toughness following reaustenitisation of the welded region. The observed densities are much higher than for the region 3 mm away from the junction, *i.e.*, the plate which is unaffected by the welding process. The region 1 mm from the junction has a generally low density of {100} poles parallel to transverse direction, so the plot in Fig. 4.26 does not explain why its toughness is poor in the as–welded condition, other than due to the fact that its crystallographic grain size is large in the as–welded condition, as is clear from region (i) in Figs. 4.18 and 4.20, where strong texture exists.

Further analysis has been conducted in order to confirm the role of crystallography in the cleavage fracture process. Strings of grains (defined as those with misorientations across grain boundaries which are greater than 2°) in the close proximity of the −40°C fracture at the weld junction were analysed to examine approximately the continuity of {100} planes across grains. For comparison purposes, a similar string from a region 3 mm from the junction was also studied; the sample in this case was unbroken to avoid the plastic deformation due to the high toughness of this area, Fig. 4.27. The analysis is approximate because the edge–to–edge matching of cleavage planes between adjacent grains is not considered, but rather is based on the overall angle between planes from neighbouring crystals. The cleavage crack propagates linearly along effective grains, and is deviated at boundaries between effective grains, which was also pointed out in [124]. Fig. 4.28 shows that the weld junction compares unfavourably relative to the unaffected base plate since large cleavage facets are expected.

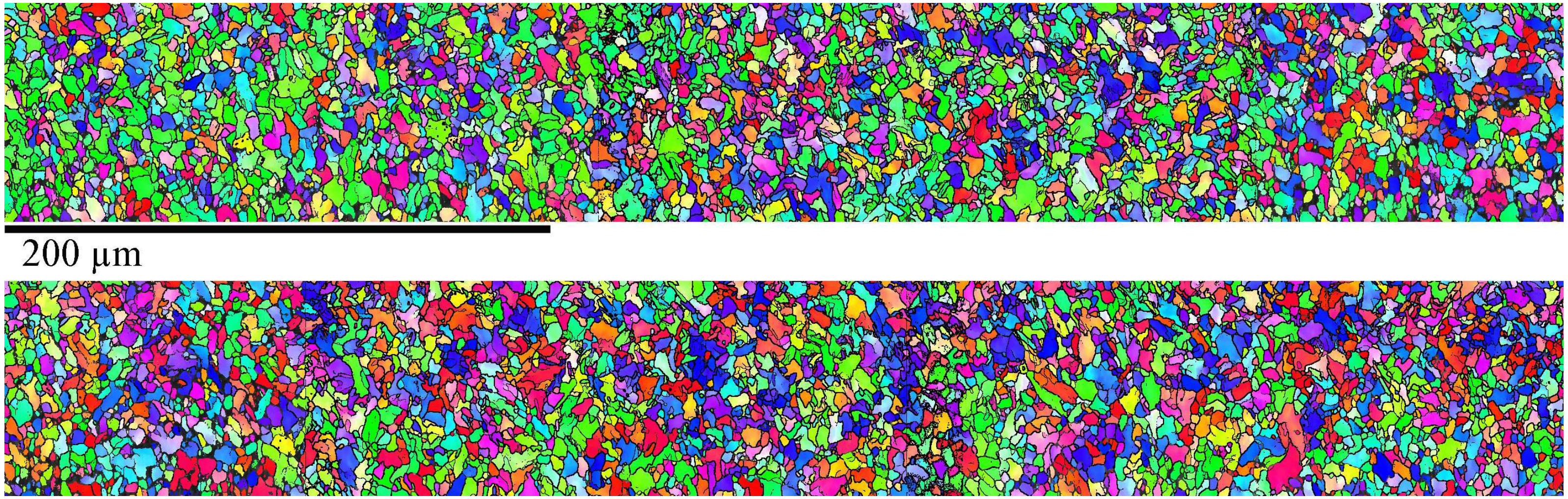

Figure 4.21: Continuous ferrite orientation image on the weld after post-welding heat treatment, starting from 1 mm left (top left) to the middle of original weld junction (bottom right) near the outer surface of the X65HIC pipe.

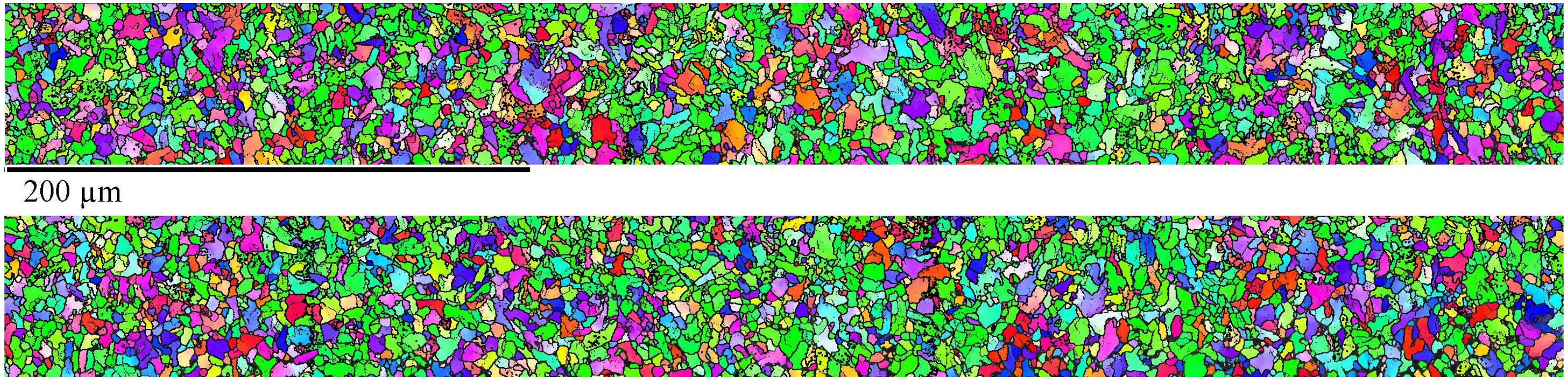

Figure 4.22: Continuous ferrite orientation image on the weld after post-welding heat treatment, starting from 1 mm left (top left) to the middle of original weld junction (bottom right) at the mid-thickness of the X65HIC pipe.

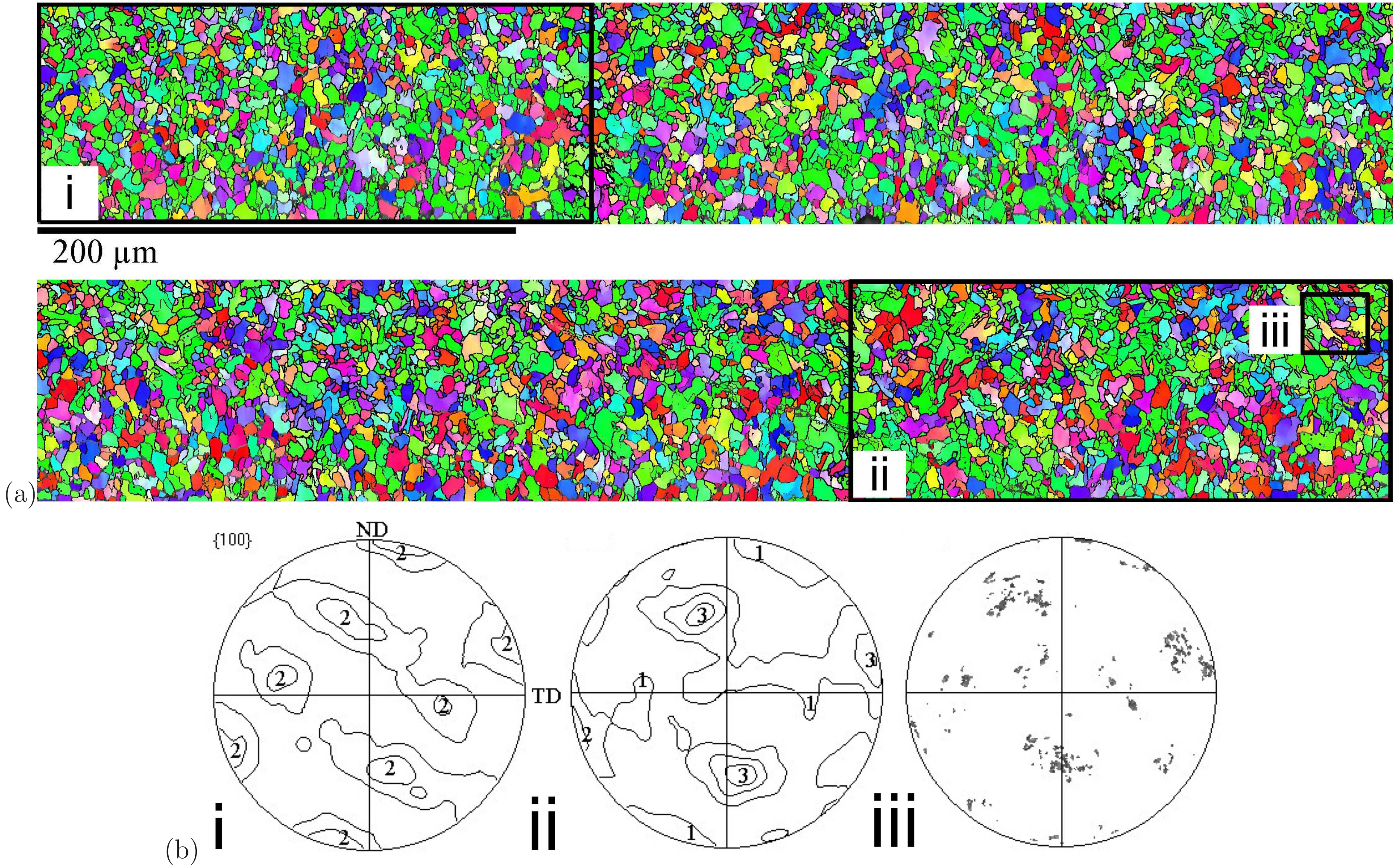

Figure 4.23: (a)Continuous ferrite orientation image on the weld after post–weld heat treatment, starting from 1 mm left (top left) to the middle of original weld junction (bottom right) near the inner surface of the X65HIC pipe. The region marked ‘iii’ is enclosed in the small box. (b) {100} Pole figures of three corresponding regions in (a).

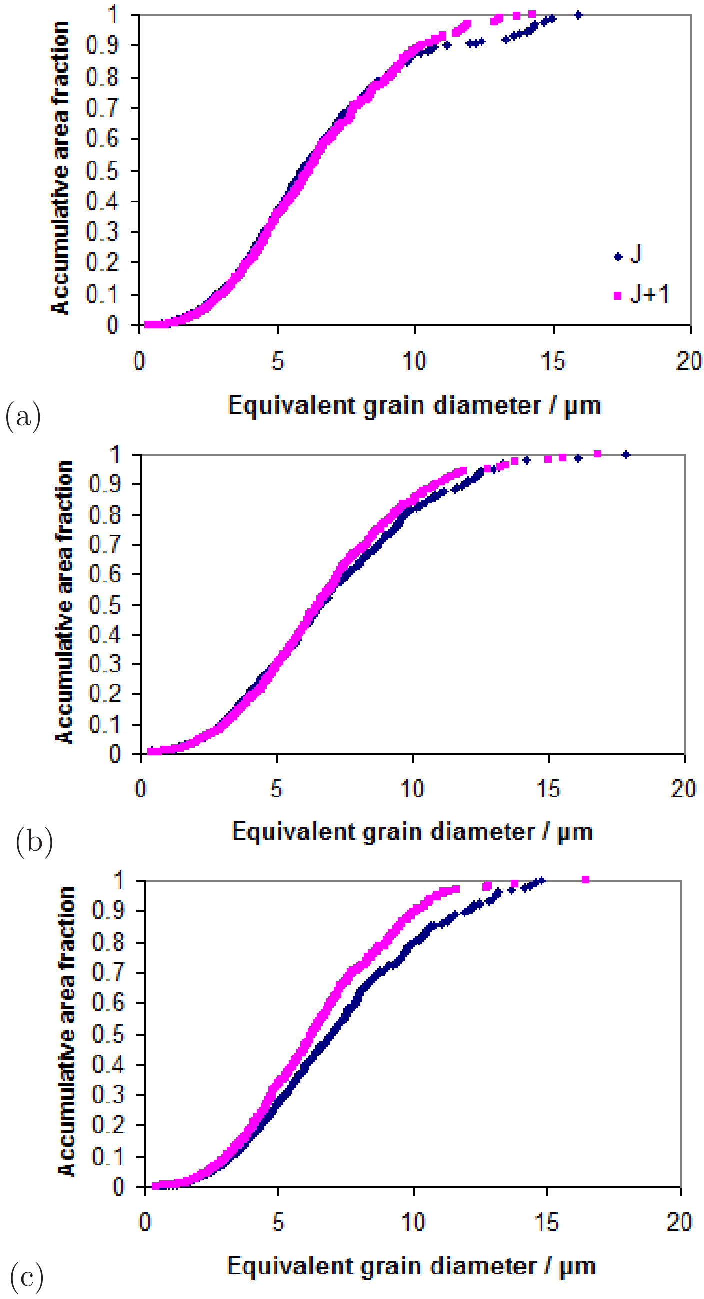

Figure 4.24: (a) Grain size analysis of the post-welding heat-treated weld from the X65HIC pipe. (a) Near the outer surface of the pipe. (b) At the mid-thickness. (c) Near the inner surface.

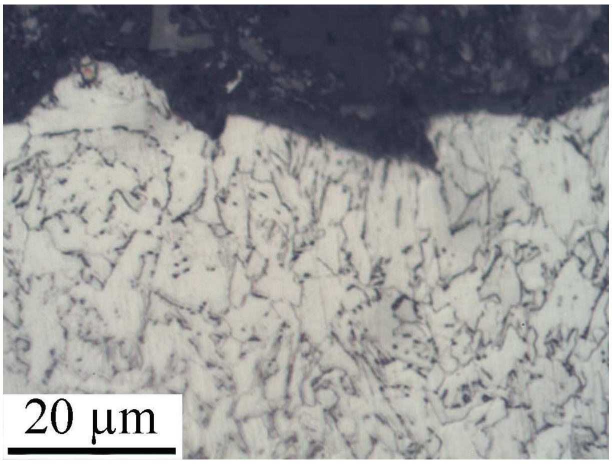

Figure 4.25: Cross-sectional fracture surface near the V-notch of the Charpy sample tested at −40°C with the V-notch located on the weld junction.

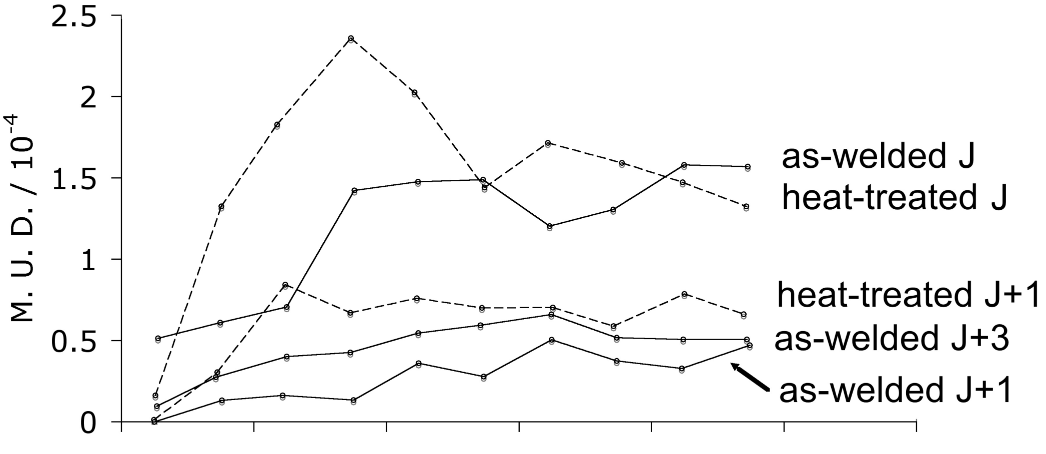

Figure 4.26: Plot of multiple of uniform density (M. U. D.) for the angle in degrees, made by {100} poles to transverse direction. Data from Fig. 4.19b, Fig. 4.20 and Fig. 4.23b (i and ii).

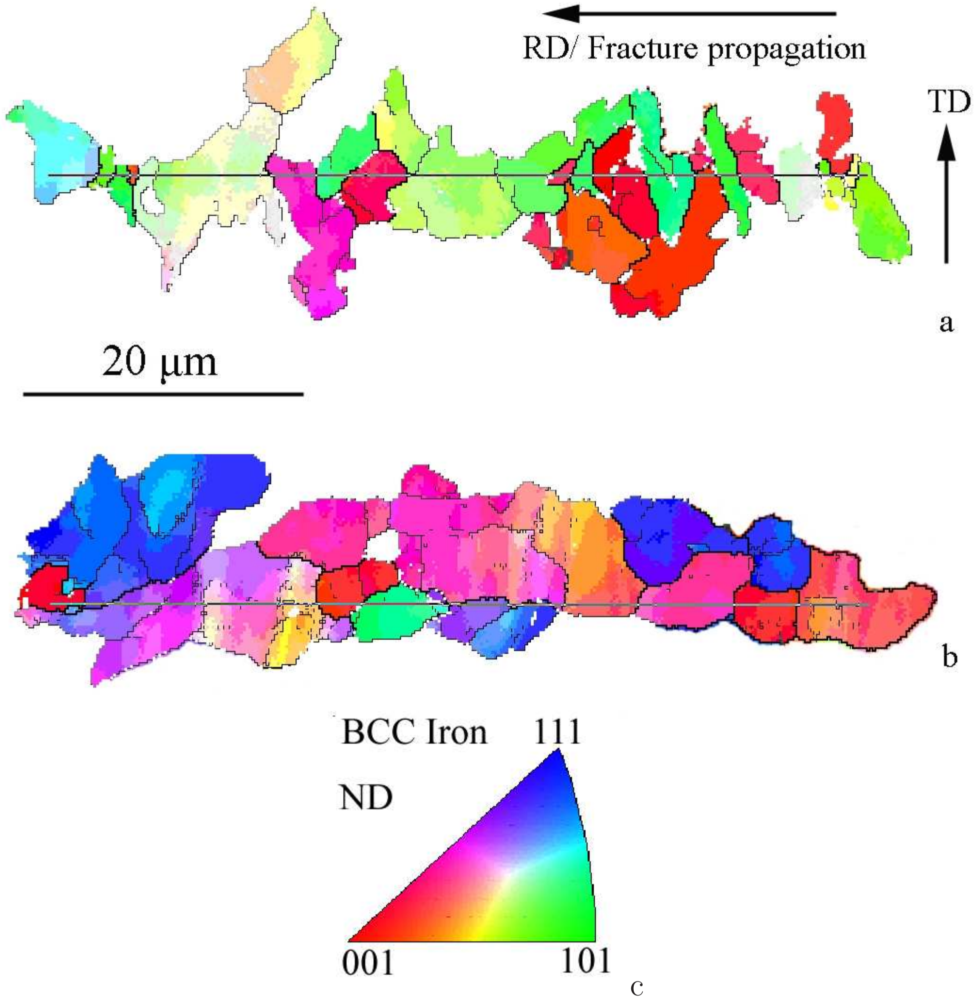

Figure 4.27: Orientation image of grains for calculation of cleavage plane propagation on (a) fractured sample after post-welding heat treatment, and (b) base metal of as-welded sample. (c) Colour coding.

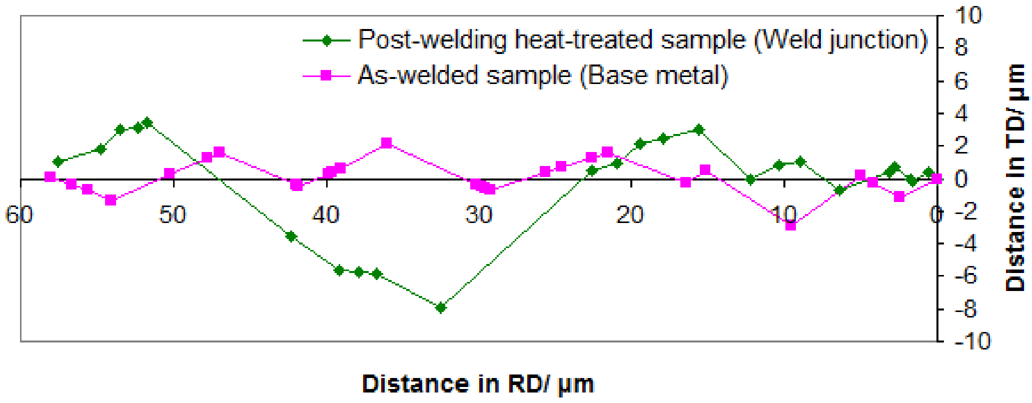

Figure 4.28: Calculated cleavage plane propagation curves.

There is published work [65, 66] suggesting the effective grain size equal to the average equivalent grain size obtained from the orientation image with a specific misorientation angle. 12° was selected in [66] based on the observation that single facets contain grains with up to 12° misorientation; while 20° was chosen in [65], when the average equivalent grain size was approaching the facet size. Similar analysis was carried out here on the heat-treated weld junction near the inner surface of the pipe (region 'ii' of Fig. 4.23). It is found that the equivalent grain diameter varies with the misorientation angle as shown in Fig. 4.29. The average equivalent grain size can not represent the facet size, which is up to ∼23 μm as shown in Fig. 4.25. There is a large amount of small grains in the heat-treated weld junction detected by the EBSD scan at a step size of 0.2 μm, but the total area fraction of the grains no larger than the average grain size in the analysed region is only around 0.1 as indicated by Fig. 4.24c. Therefore it is not appropriate to use the average or any single equivalent grain size value to represent the effective grain size of the microstructure without a normal distribution of the grain size, like in the heat-treated weld. It is supported by the fact that the facet size varies in the range approximately from 3 to 23 μm as shown in Fig. 4.25.

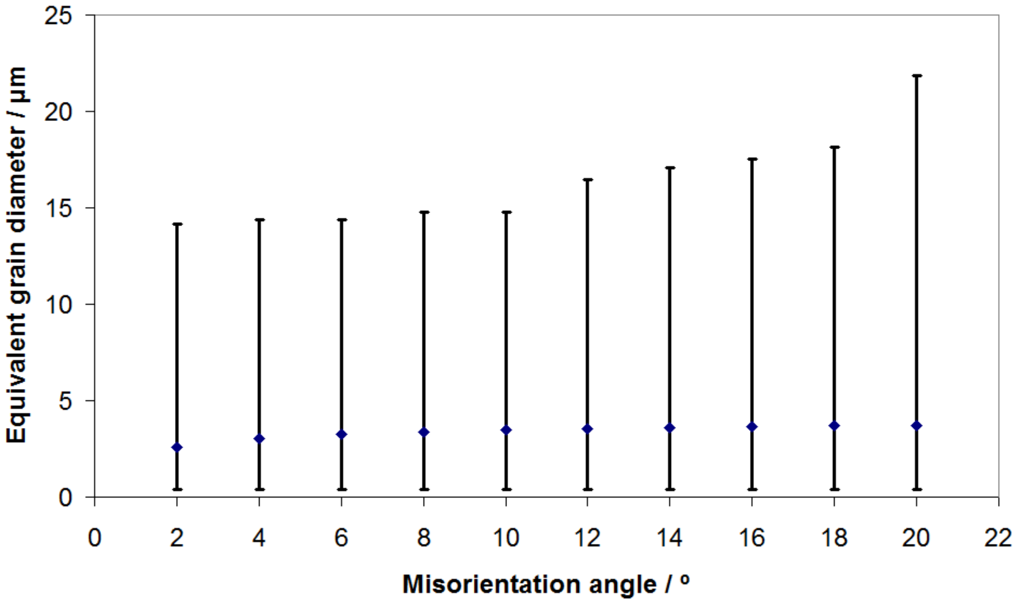

Figure 4.29: The variance of equivalent grain size obtained from region 'ii' of Fig. 4.23 with the misorientation angle. Each line shows the maximum, minimum and average values.

4.4 Conclusions

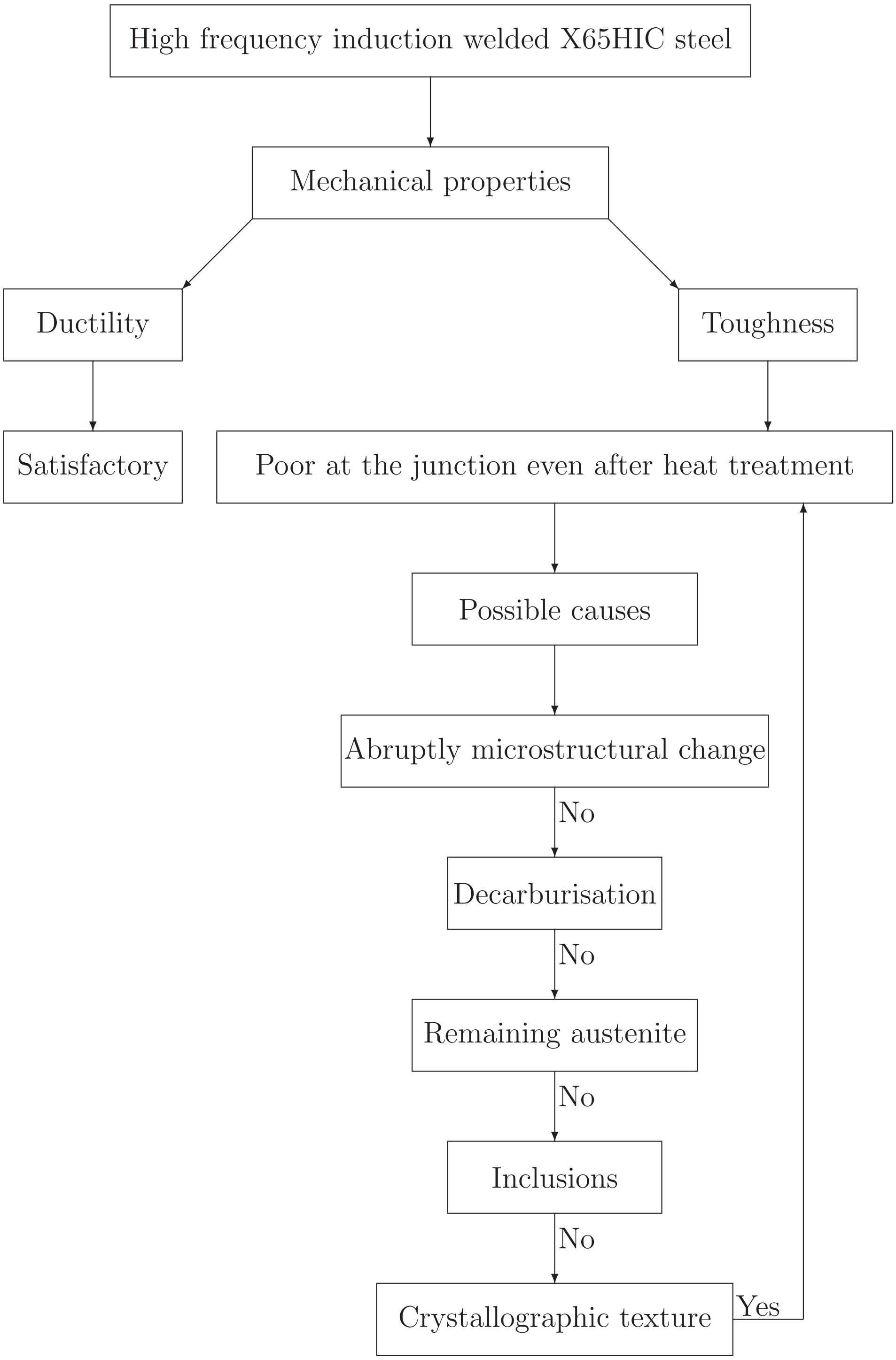

Figure 4.30: The route of investigation on X65HIC weld

The investigation on the weld of X65HIC pipe has gone through a journey as shown in Fig. 4.30. It appears that the poor toughness of the weld junction of the induction weld is substantially related to firstly the crystallographically coarse grains present there after welding. Reaustenitisation that occurs in the induction post-welding heat treatment does not improve the situation at the weld junction, because the detrimental crystallographic characteristics are reproduced on cooling. There is published work [97] indicating the existence of an austenite memory effect during rapid reaustenisation experiments. Based on this, studies on modified post-welding heat treatments to improve the toughness in the weld–affected regions will be discussed in Chapter 6.

Secondly the detrimental texture, *i.e.*, orientation of the cleavage plane prone to fracture is also found to be the cause of the low toughness of the weld junction. Systematic analysis from this point of view is reported for the welds from X65 grade of steels in Chapter 5.

Chapter 5

Welds from X65 Grade of Steels

5.1 Mechanical properties

The mechanical properties of two kinds of pipes with different wall-thicknesses at both as-welded and heat-treated states have been investigated in terms of ductility and toughness.

5.1.1 Ductility

The results of cross-weld tensile tests are shown in Table 5.1. The as-welded sample has the greatest ultimate strength but smallest elongation, and fracture occurs in the base metal. Post-welding heat treatment decreases the ultimate strength but increases the elongation of the as-welded sample. Fracture happens in the weld junction. The final tensile strength is above the minimum required by the international standard, as discussed in section 2.2.2.

The post-welding heat treatment restored the ductility of the welds, which is further proven by the bend tests carried out on weld segments of the thick-walled X65 pipe. All of the 40 mm-wide sample, both as-welded and heat-treated, fractured at the weld junction after face bends, but the heat-treated sample demonstrated a higher degree of curvature prior to fracture (*cf.* Fig. 5.1a and Fig. 5.1b). Three repeat tests were carried out in each state.

During the side bend tests of the welds from the thick-walled pipe, the as-welded sample fractured at the weld junction, as shown in Fig. 5.1c. The heat-treated sample in comparison did not fracture after forming the U shape as shown in Fig. 5.1d; however it reveals openings on the fusion

Table 5.1: Average and standard deviation of three tensile tests in each status on high frequency induction welded X65 grade pipes.

(a) With 8.6 mm wall-thickness.

	Ultimate tensile strength / MPa	Fracture elongation / %
Base metal	596±1	34.0±0
As-welded	621±1	9.2±5.3
Heat-treated	539±7	18.7±1.2

(b) With 14.8 mm wall-thickness.

	Ultimate tensile strength / MPa	Fracture elongation / %
Base metal	626±1	33.9±1.3
As-welded	637±2	6.4±1.9
Heat-treated	573±8	24.9±5.2

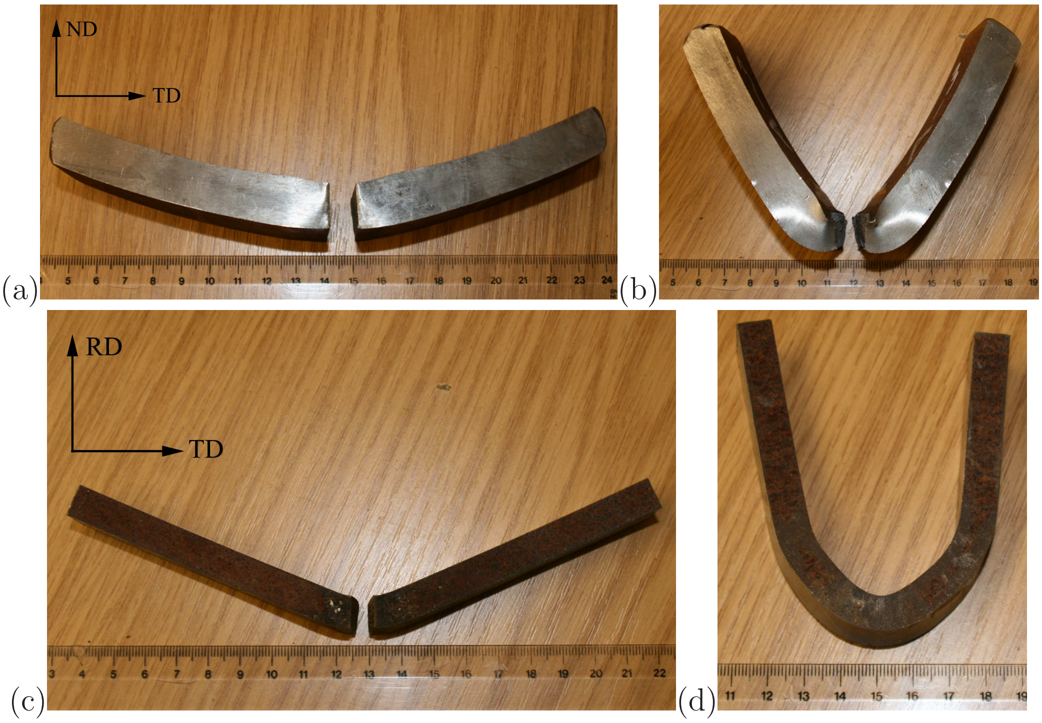

Figure 5.1: Weld segments from the pipe with 14.8 mm wall-thickness after bend testing. Scale indicated is in cm. (a) As-welded sample with 40 mm width after face bend. (b) Heat-treated sample with 40 mm width after face bend. (c) As-welded sample after side bend. (d) Heat-treated sample after side bend.

surface, Fig. 5.2a. The heat-treated sample from the thin-walled pipe were also tested and found to have developed openings on the fusion surface. The

RD–TD surface was observed by sectioning precisely on the location of one opening. Several inclusions were discovered along the fusion surface below the opening, as shown in Fig. 5.2b and c. EDX analysis showed that these inclusions possess compositions consistent with manganese and silicon oxides, Table 5.2.

Figure 5.2: Weld segments from the pipe with 14.8 mm wall-thickness after side bend. (a) Openings on the fusion surface. (b) Microstructure of the weld junction below the opening. (c) Inclusions and pull-outs.

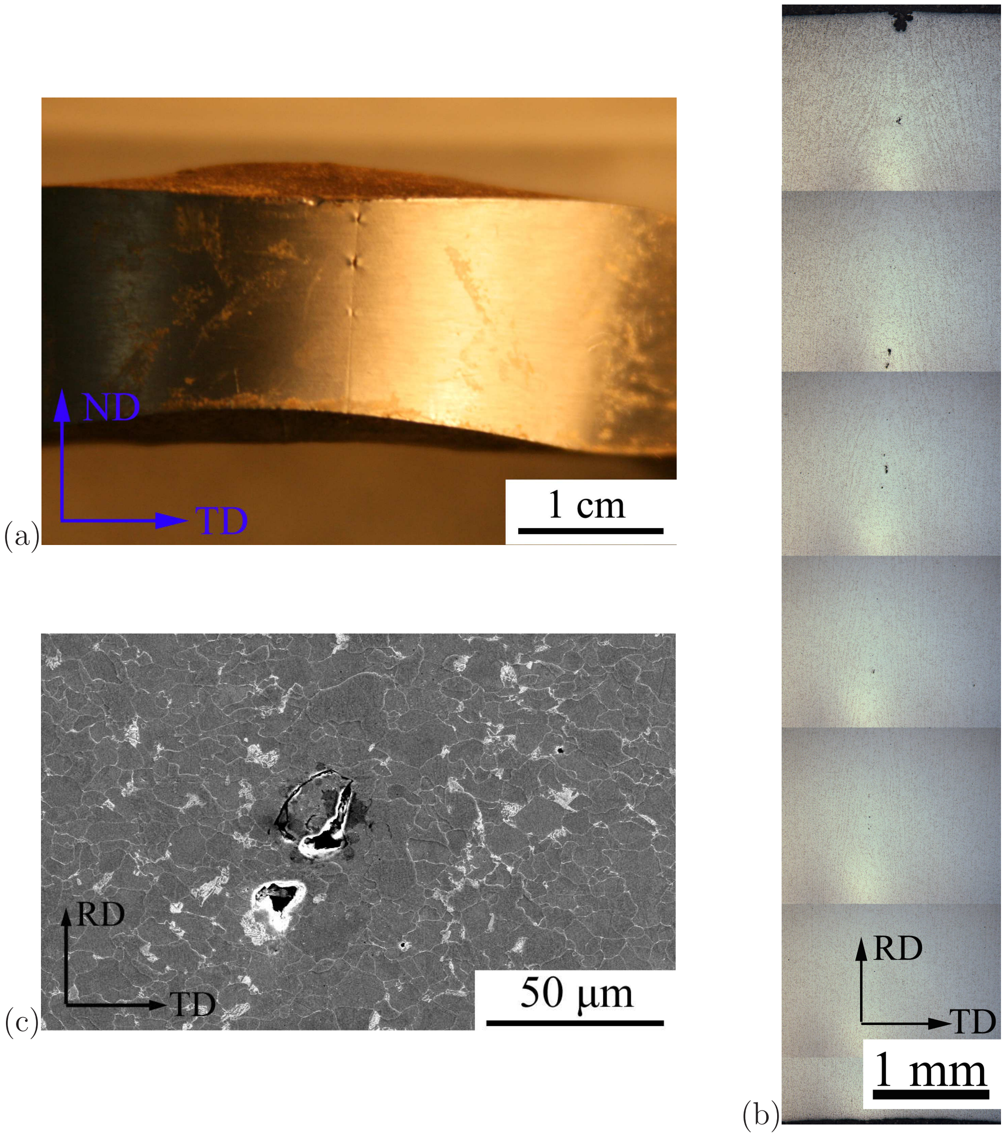

Three 20 mm-wide heat-treated samples from both thick and thin-walled pipes all passed the face bend test and they did not develop any openings or cracks on the surface after deforming into a U shape, which is

Table 5.2: Compositions of the inclusions in Fig. 5.2c using EDX analysis.

Element	Weight %
O	29.84±0.40
Al	1.19±0.10
Si	12.17±0.19
Ti	0.69±0.09
Mn	47.24±0.47
Fe	6.94±0.24
Nb	1.93±0.26

the best result obtained. In summary, due to the persistence of inclusions, post-welding heat treatment did not restore the ductility of the welds to the full extent, so some of the tested samples fractured and some others had openings or cracks on the weld junction.

5.1.2 Toughness

Fig. 5.3 shows the results of cross-weld Charpy tests on both kinds of pipes. As discussed in section 3.2.2, the experiments for the thin-walled pipe were carried out on the samples with $\frac{2}{3}$ of the size according to standard ISO 148-1, while full size samples were used for the thick-walled pipe; so the absorbed energies recorded from two kinds of pipes are not comparable. Each value on the curves is an average of three measurements. The toughness of the welded region improves as a consequence of the heat treatment when the V-notch is located away from the weld junction, but at the location of the weld junction the increase is not sufficient. Compared to the results from X65HIC pipe, the thin-walled X65 pipe is in a similar situation. Again it is important to target the cause for the increase of ductile brittle transition temperature at the weld junction. The thick-walled X65 pipe demonstrated lower toughness at the weld junction with no significant improvement at temperatures higher than $-40°$C. Identifying and assessing the factors responsible for the low toughness at the weld junctions of these two kinds of pipes needs sophisticated analysis, which will be described in the next section.

5.2 Microstructural variance across the weld

Welds from two kinds of X65 pipes showed similar microstructure, so the micrographs of the weld from only one kind of pipe are included in most of

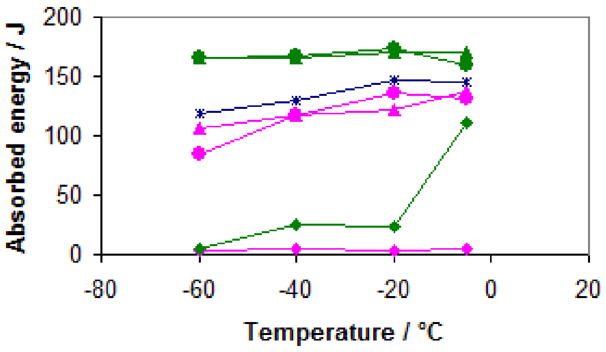

(a) X65 pipe with 8.6 mm wall-thickness.

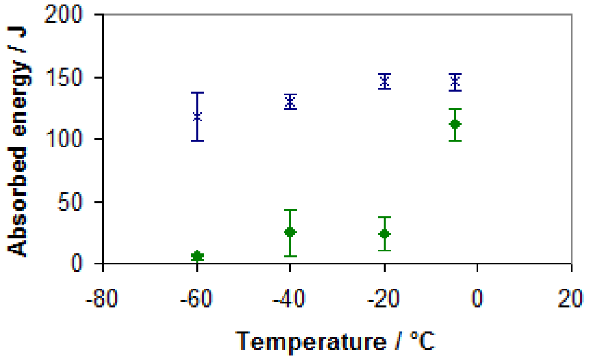

(b) Scatter of the values at the weld junction and the base metal from thin-walled X65 pipe.

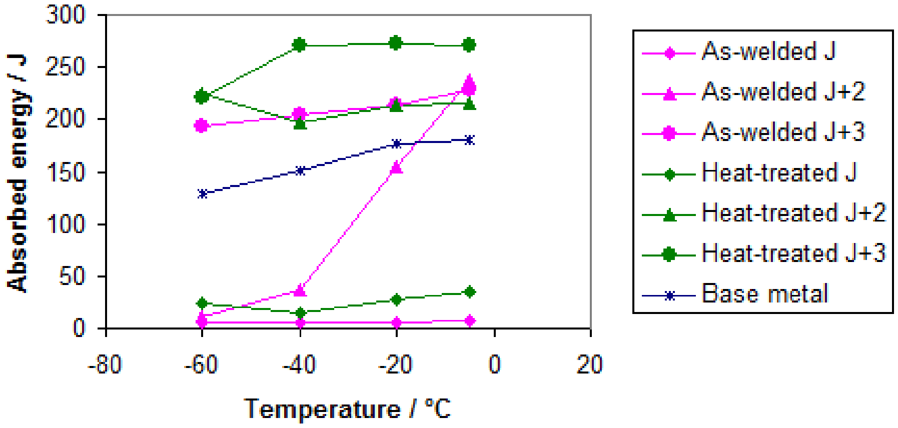

(c) X65 pipe with 14.8 mm wall-thickness.

Figure 5.3: Charpy impact energy as a function of temperature.

the cases for brevity. More pictures are shown in Appendix A.

5.2.1 As-welded state

Referring to the observation on the welds from X65HIC pipe, the as-welded sample can also be categorised into four zones: base metal, thermomechanically-affected zone, heat-affected zone and weld junction. The microstructure of the four zones was investigated. The base metal on the as-welded samples has a microstructure of allotriomorphic ferrite plus pearlite, as shown in Fig. 5.4. The larger fraction of pearlite compared to the X65HIC pipe is due to the higher carbon concentration in the X65 grade of steels, Table 3.2.

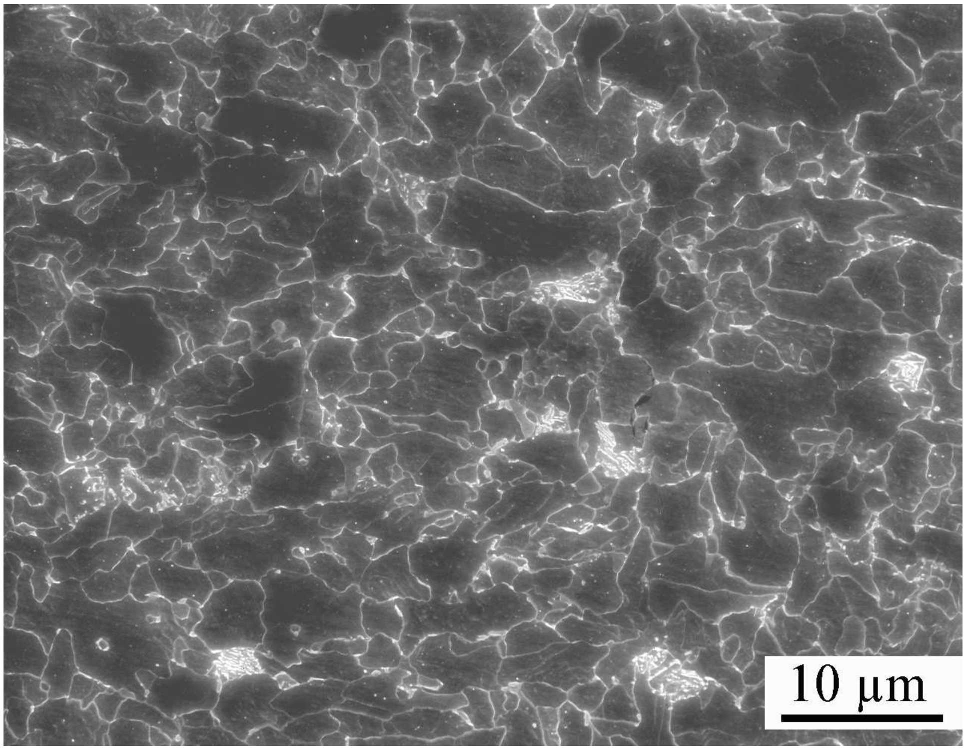

Figure 5.4: Microstructure of base metal in the as-welded X65 pipe with 8.6 mm wall-thickness.

Different from the welds of X65HIC pipe, the grains from both the thermomechanically-affected and heat-affected zones are aligned along the directions of metal flow, which are different near the outer surface, at mid-thickness and near the inner surface of the X65 pipe, as shown in Fig. 5.5. The darker part of the images is within the heat-affected zone, and the rest is in the thermomechanically affected zone. The weld junction is on the left hand side of the region where the photos were taken and the base metal is on the right hand side. The broader affected zone and greater influence from the metal flow is due to the reduction in the welding speed from $\mathrm{m\,min^{-1}}$ for the X65HIC pipe to and $\mathrm{m\,min^{-1}}$ for the X65 pipes. This suggests that there is a larger amount of heat input and deformation involved during the forging of the two abutting edges when forming the X65 pipe compared to the

speeds removed for copyright reasons

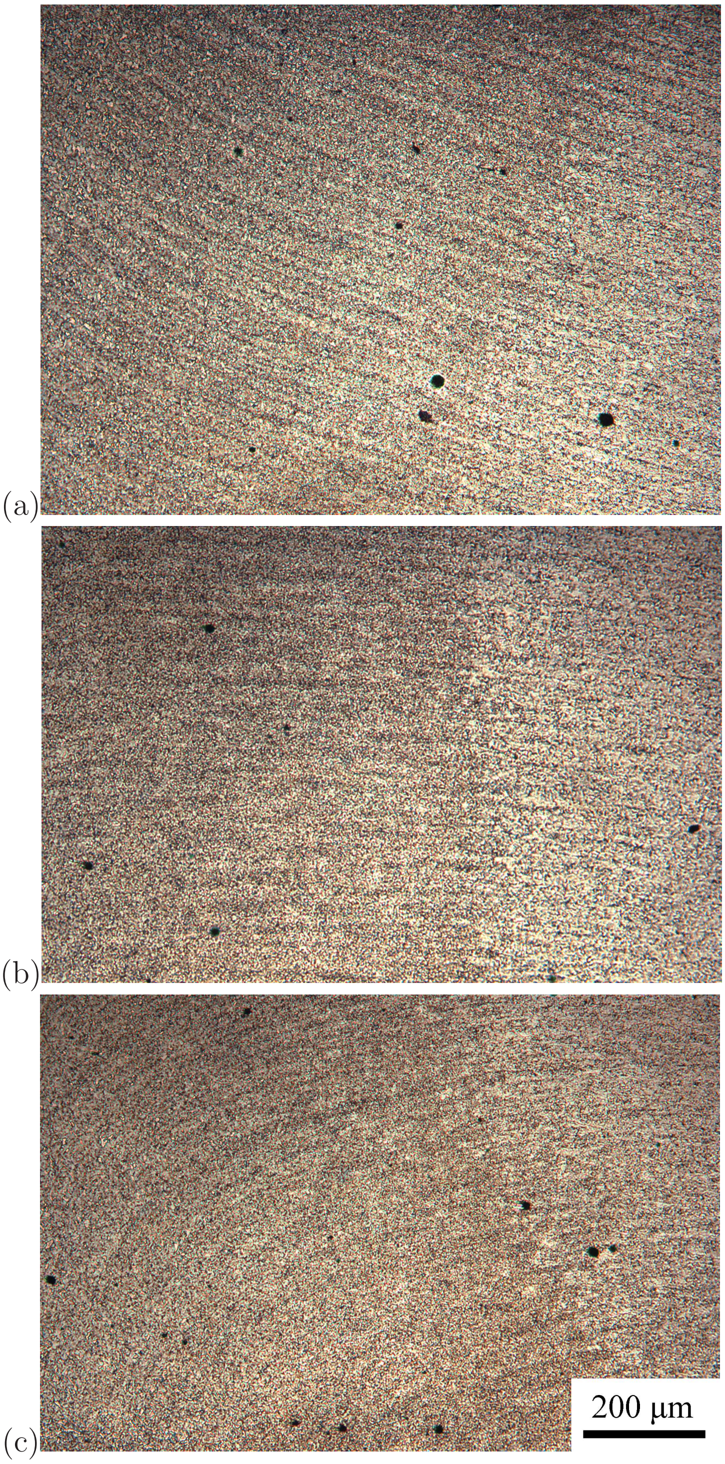

Figure 5.5: Optical micrographs of the thermomechanically-affected and heat-affected zones on one side of the weld junction. (a) Near the outer surface of the thin-walled X65 pipe. (b) At mid-thickness. (c) Near the inner surface.

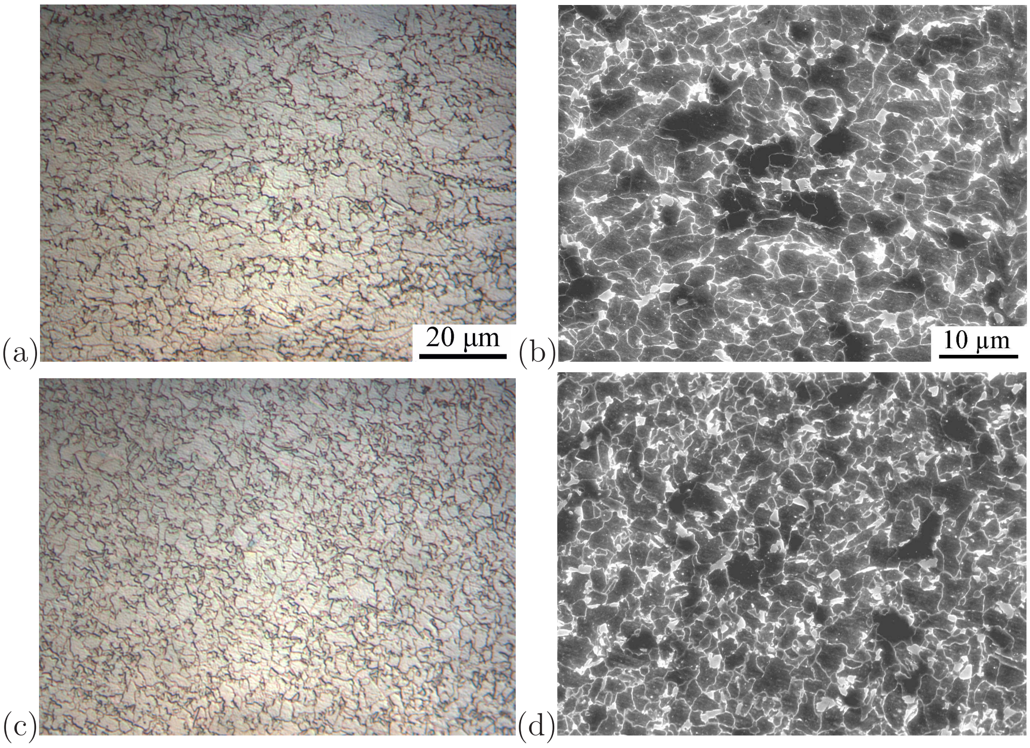

Figure 5.6: Microstructure of the thermomechanically-affected zone in the as-welded sample from X65 pipe with 8.6 mm wall-thickness. (a) Optical micrograph. (b) Scanning electron micrograph. Microstructure of the heat–affected zone. (c) Optical micrograph. (d) Scanning electron micrograph.

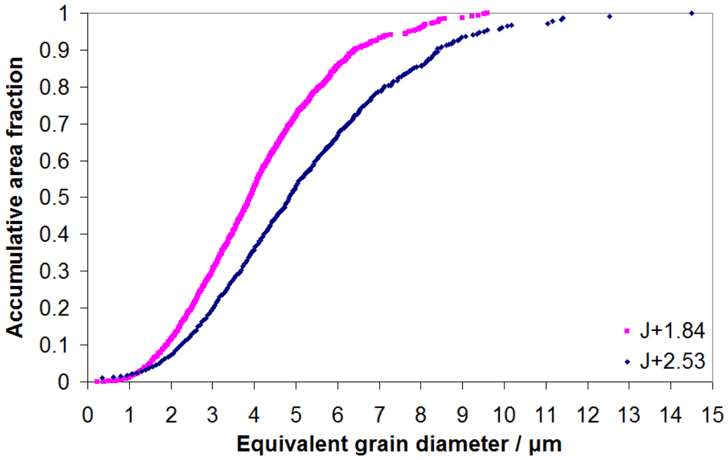

Figure 5.7: Grain size analysis of the as-welded sample near the outer surface of the X65 pipe with 8.6 mm wall-thickness. Each series represents the result from an area with the size of 242.8×100 μm^2. The regions 1.84 and 2.53 mm away from the middle of the weld junction belong to the heat-affected and the thermomechanically-affected zones respectively.

situation with X65HIC pipe. This is expected from the greater concentration of solutes in X65, and hence necessary to expel bad metal oxides or inclusions which form during the heating and produce a sound weld. Both the thermomechanically-affected and the heat-affected zones consist of allotriomorphic ferrite reformed from the grains which become austenite during the welding process, and a second phase which appears dark in optical micrographs and bright in scanning electron micrographs (*cf.* Fig. 5.6a and b, c and d). This latter phase is most likely to be the so-called M–A constituent and will be discussed later. The shape and size of the ferrite grains makes the difference in microstructure between these two domains. It is anisotropic in the thermomechanically-affected zone due to the severe pancaking of the austenite before it transforms to ferrite [38, 116]. The heat-affected zone in comparison has equiaxed and finer ferrite grains as a result of dynamic recrystallisation due to more severe deformation, as it has closer proximity to the weld junction. The grain size analysis (Fig. 5.7) was carried out on orientation images using the critical misorientation angle of 10° as discussed on page 62.

The microstructure at, and adjacent to the weld junction consists of a mixture of allotriomorphic ferrite, Widmanstätten ferrite due to the coarser austenite grains in this region, and M–A islands, Fig. 5.8. In the middle of the weld junction, the islands are aligned along the normal direction (Fig. 5.8b) throughout the wall-thickness except within 1 mm to both the inner and outer surfaces. These strings of M–A islands are normally found along the prior austenite grain boundaries [76, 125, 126] which on the fusion surface do not have much mobility under impact from two abutting edges on both sides. Results of nanoindentation, Fig. 5.9, showed that the strings are harder than the surrounding phases in the matrix. The existence of the martensite constituent was further confirmed by TEM. The TEM specimen was prepared using focused ion beam milling, by which a slice thinner that 100 nm can be cut just from a string, as shown in Fig. 5.10a and b. Figure 5.10c shows the twinned martensite within the string, which is the characteristic morphology of M–A islands in the high-strength low-alloy pipeline steels [127, 128].

Similar to the string of M–A islands found in the weld junction at the mid-thickness of the X65HIC pipe, those in the X65 pipe are also manganese-rich phases, as revealed by the elemental mapping using electron probe microanalysis in Fig. 5.11. There is possibly Mn segregation at the weld junction, because Mn is fairly active in reaction with oxygen under high temperature

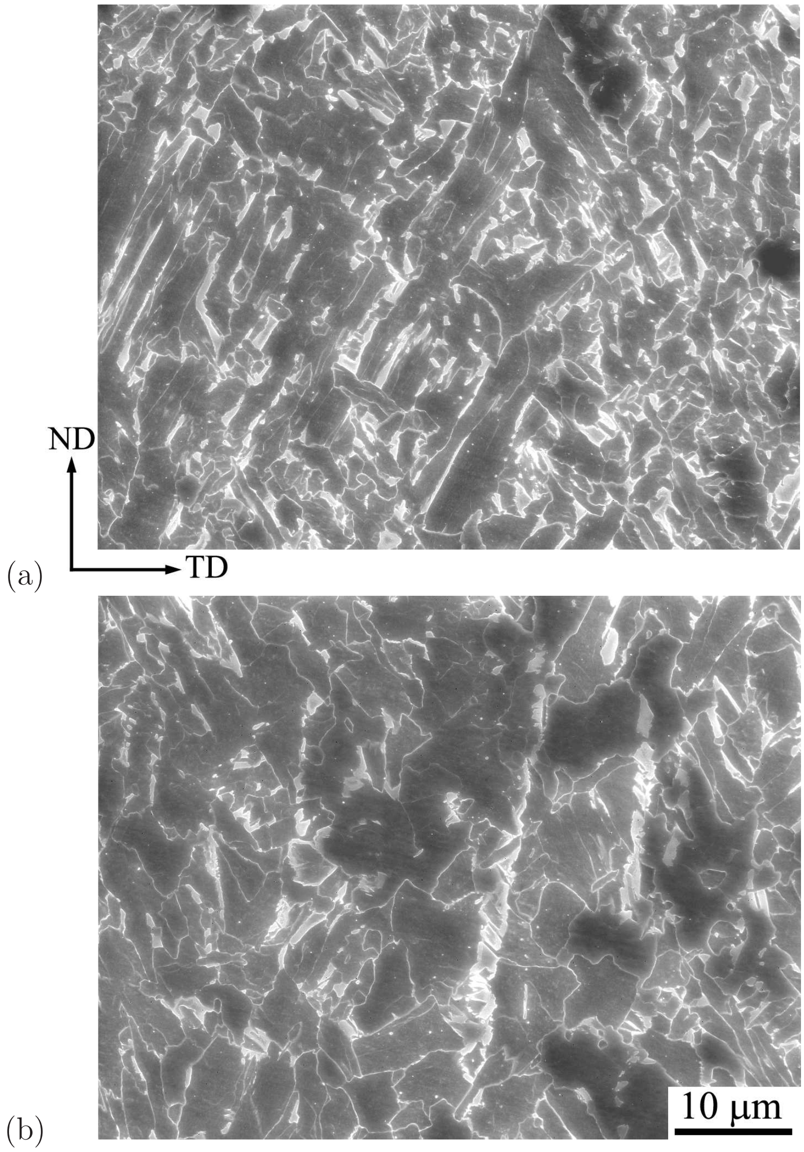

Figure 5.8: Microstructure (a) adjacent to and (b) at the weld junction in the as-welded pipe with 8.6 mm wall-thickness.

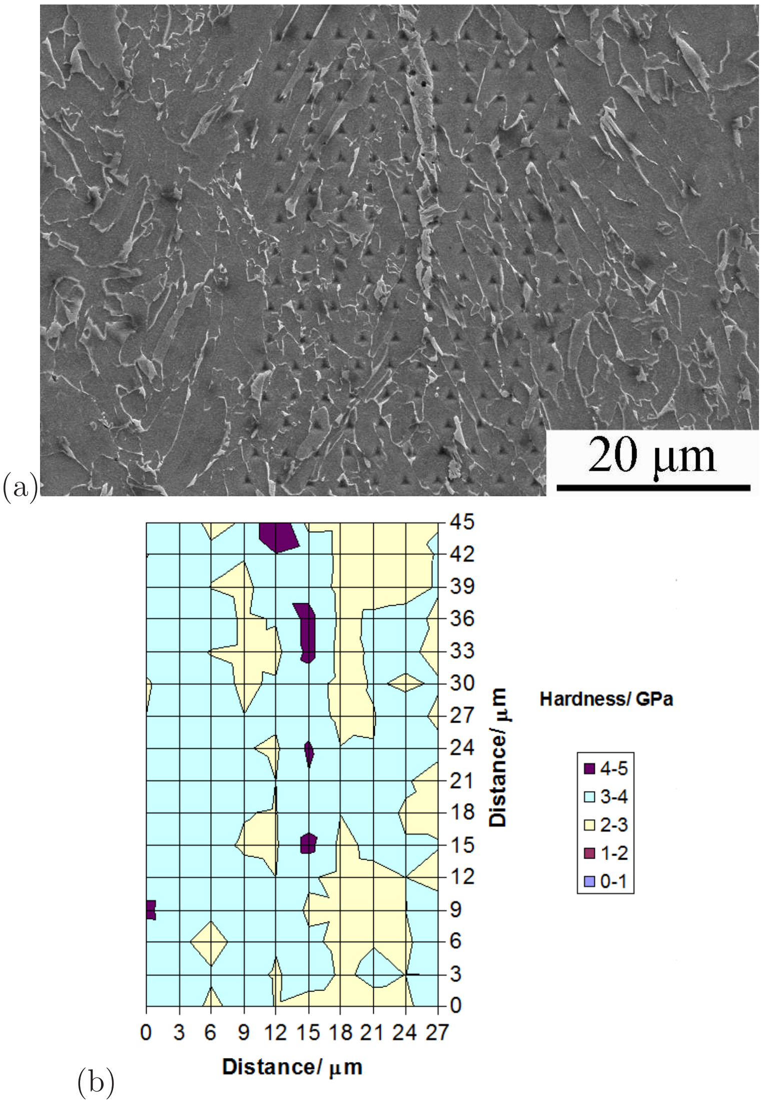

Figure 5.9: (a) Nanoindentations on a string of M–A islands in the thin-walled X65 as-welded sample. (b) Results of nanoindentation measurements.

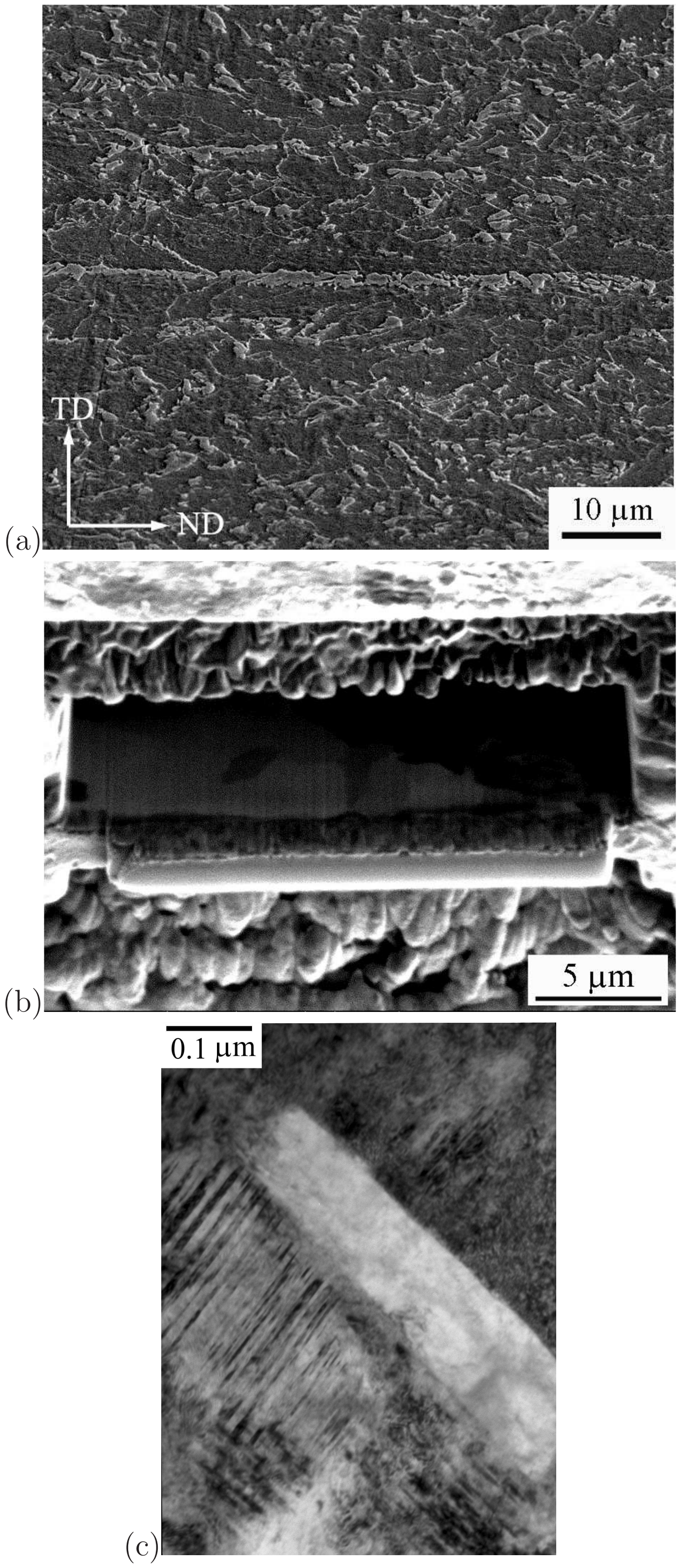

Figure 5.10: (a)Scanning electron micrograph of a string on the weld junction of the as-welded sample from thin-walled X65 pipe. (b) A slice cut using focused ion beam from the string. Micrograph is taken under the channel contrast of focused ion beam. (c) Transmission electron micrograph of this specimen.

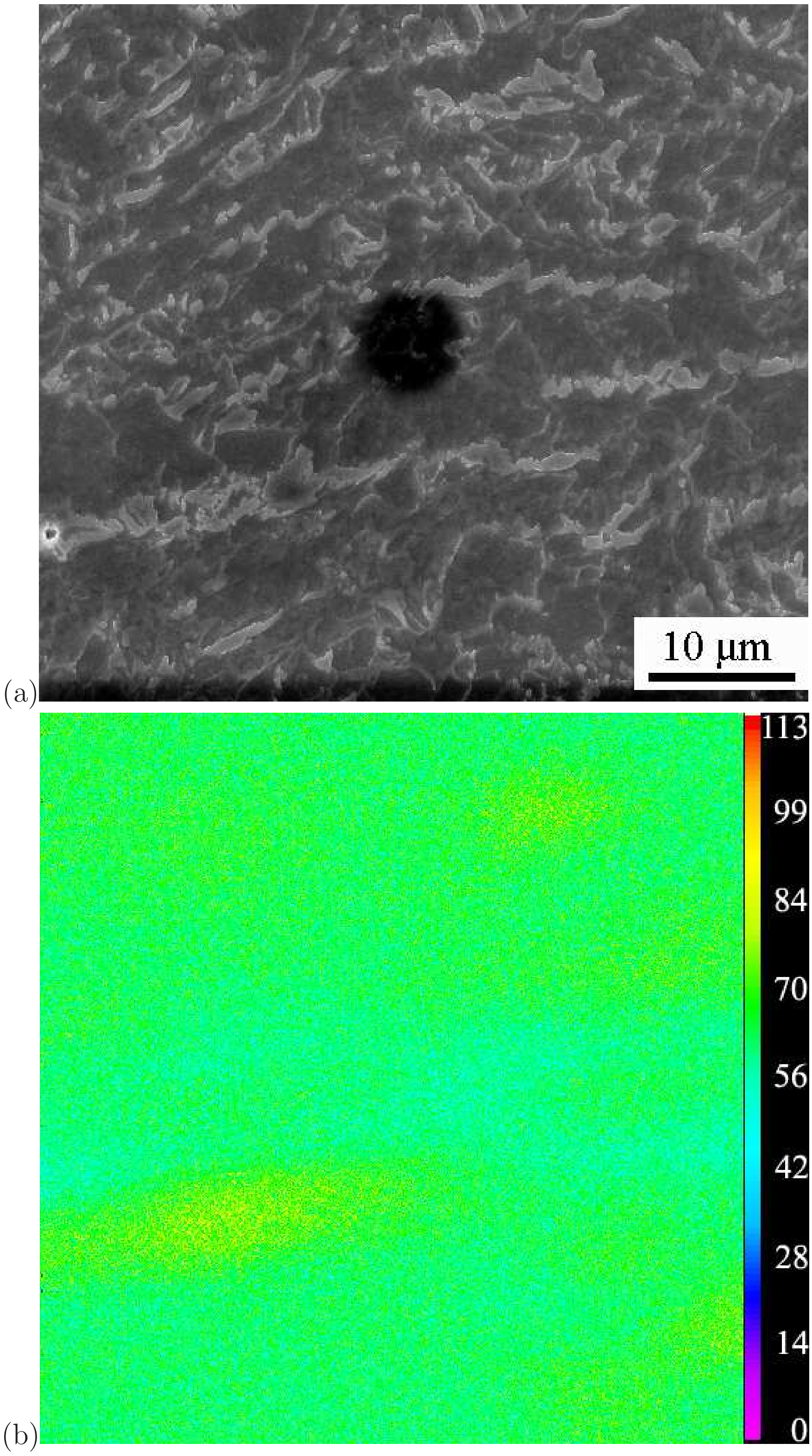

Figure 5.11: (a) Scanning electron micrograph of the weld junction of the as-welded sample from thin-walled X65 pipe. (b) Mn mapping of (a) using electron probe microanlaysis. This analysis can not be fully quantified due to experimental limitation. Bigger number and warmer colour means higher concentration of the element and vice versa.

at the joining surfaces during the welding process. The segregated Mn stabilised the remaining austenite at the weld junction and formed the strings of M–A islands. The Mn content in different phases during the equilibrium transformation of thin X65 base material calculated by MTDATA [129] is shown in Fig. 5.12. Manganese can remain in the austenite when cementite does not form in the as-welded microstructure. The existence of remaining austenite in the as-welded sample is further confirmed by X-ray diffraction, Fig. 5.13. The quantity of austenite is small and is a part of the M–A constituent so only a few of the austenite peaks could be identified in the X-ray diffraction patterns. After tempering at 400 °C for 2 h, the M–A islands in the three zones of the as-welded sample all transformed into tempered martensite, Fig. 5.14.

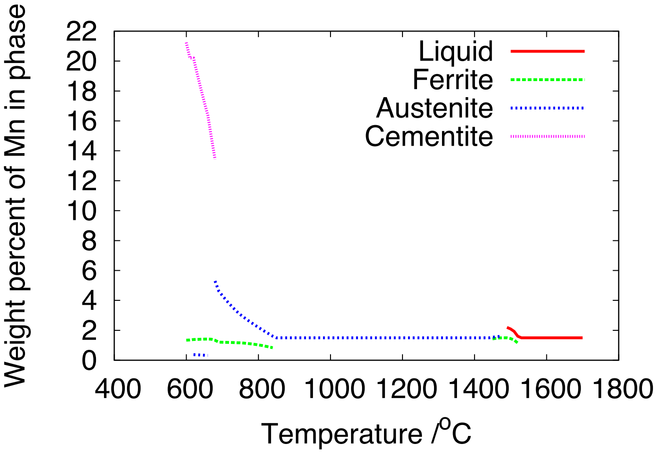

(a)

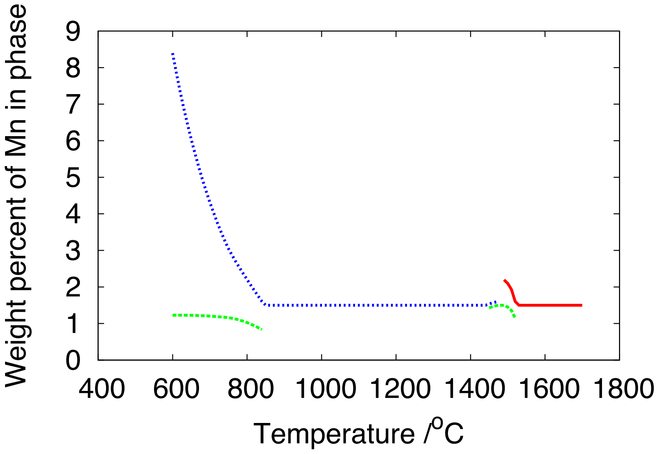

(b)

Figure 5.12: Calculated equilibrium Mn content in different phases, as a function of temperature for the thin X65 base material. (a) Allowing all the possible phases to form. (b) With no cementite formed as in the as-welded state.

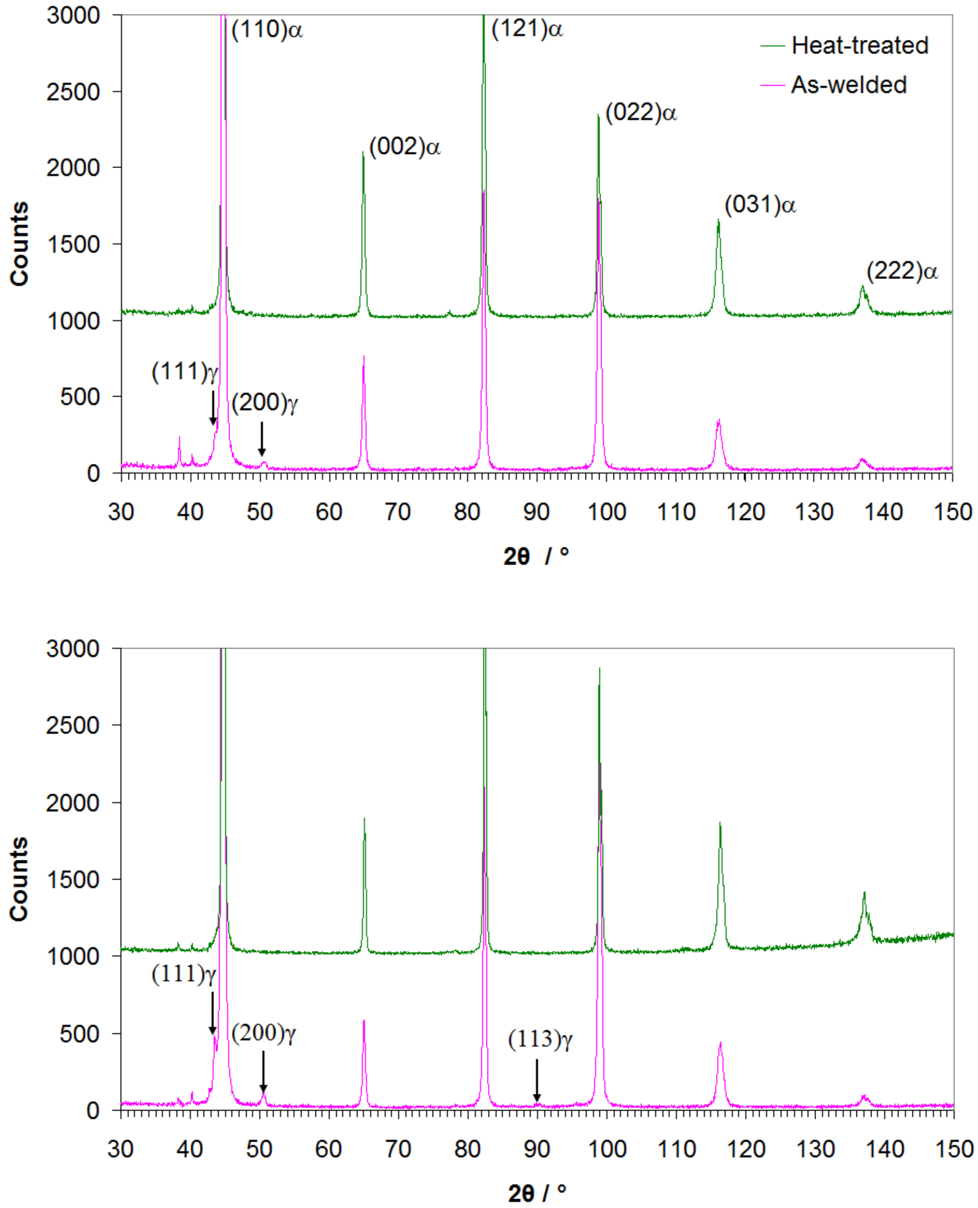

(a)

(b)

Figure 5.13: X–ray diffraction patterns from weld segments of pipes with (a) 8.6 mm wall-thickness and (b) 14.8 mm wall-thickness.

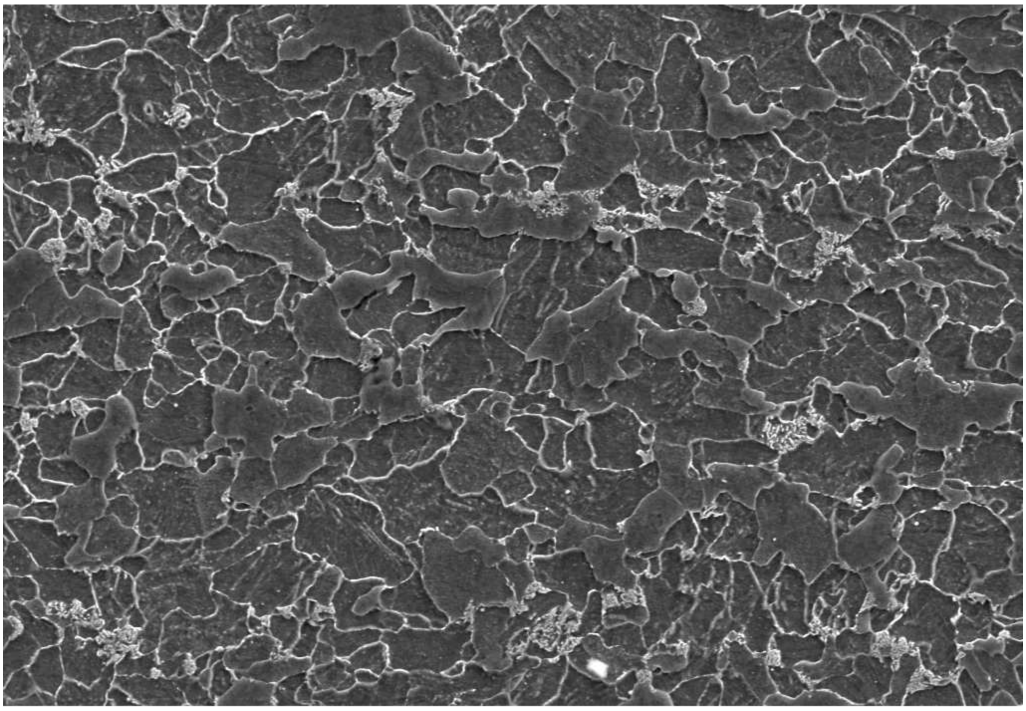

(a) Thermomechanically-affected zone.

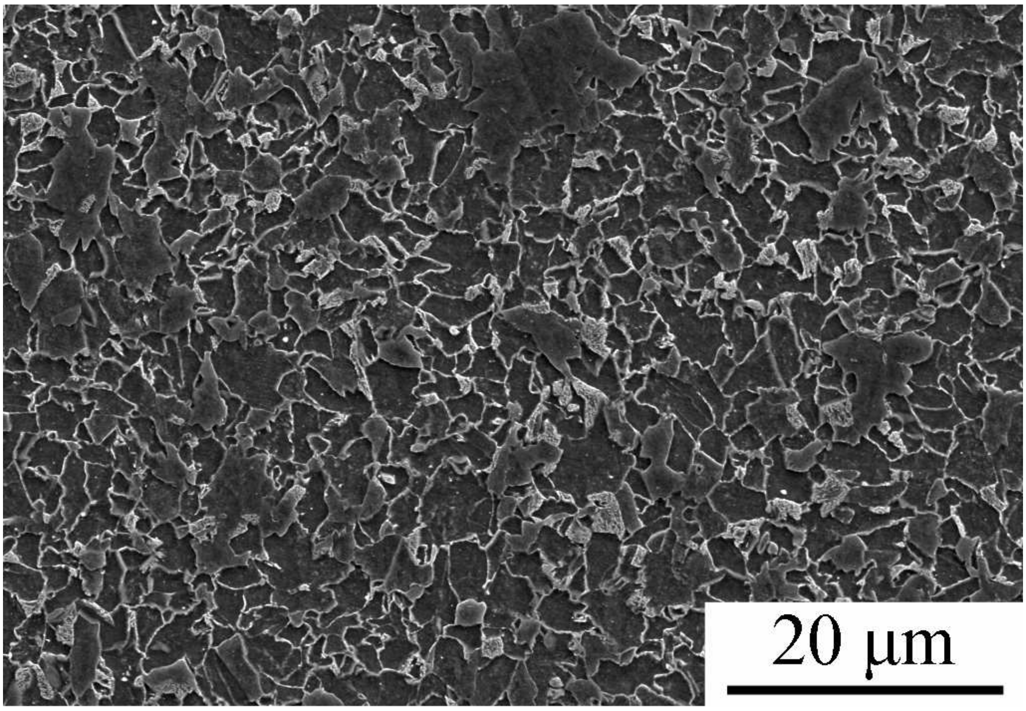

(b) Heat–affected zone.

Figure 5.14: Microstructure of the thin-walled X65 as–welded sample after tempering at 400 °C for 2 h (*continued on next page*).

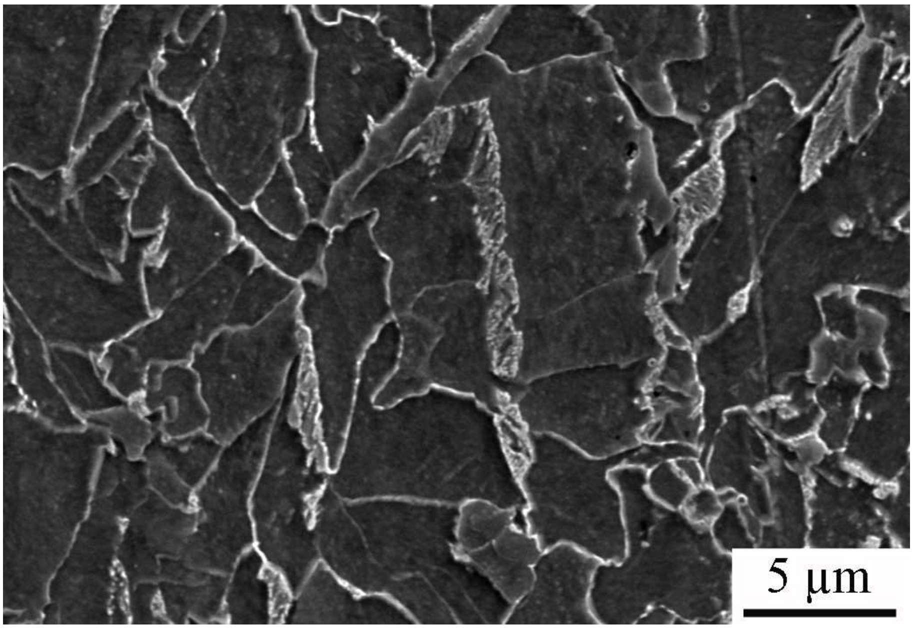

(c) Weld junction.

Figure 5.14: Microstructure of the thin-walled X65 as–welded sample after tempering at 400 °C for 2 h.

5.2.2 After post-welding heat treatment

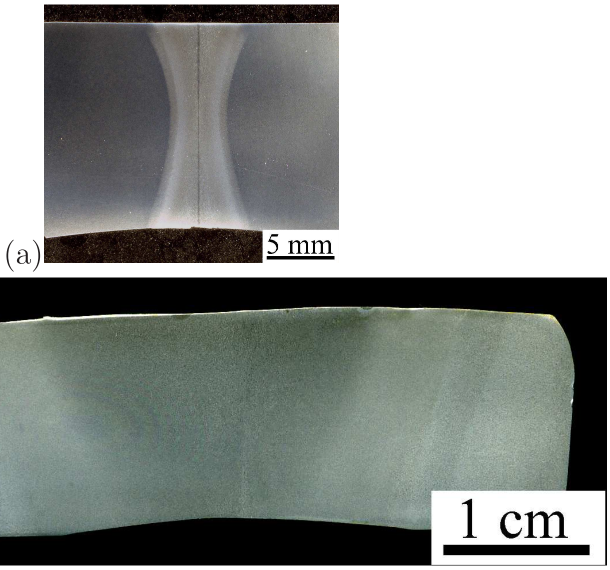

Figure 5.15: As-etched ND-TD surface of the weld from the pipe with 14.8 mm wall-thickness. (a) As-welded. (b) Heat-treated.

Similar to the X65HIC weld, post-welding heat treatment broadened the affected zone on the welds from X65 pipes as shown in Fig. 5.15. The microstructure across the weld also becomes uniform, and consists only of allotriomorphic ferrite and pearlite, Fig. 5.16a and b. The fraction of the pearlite decreases towards the unaffected steel, which makes the affected area appear darker compared to the base metal on the as-etched surface, Fig. 5.15b. X-ray diffraction patterns confirmed the absence of austenite after post-welding heat treatment, as shown in Fig. 5.13a and b. Figure 5.16b revealed clearly that the strings of M–A islands on the weld junction turned into pearlite. The difference to the X65HIC heat-treated sample is that the metal flow trace remained adjacent to the weld junction of the X65 heat-treated samples (Fig. 5.17).

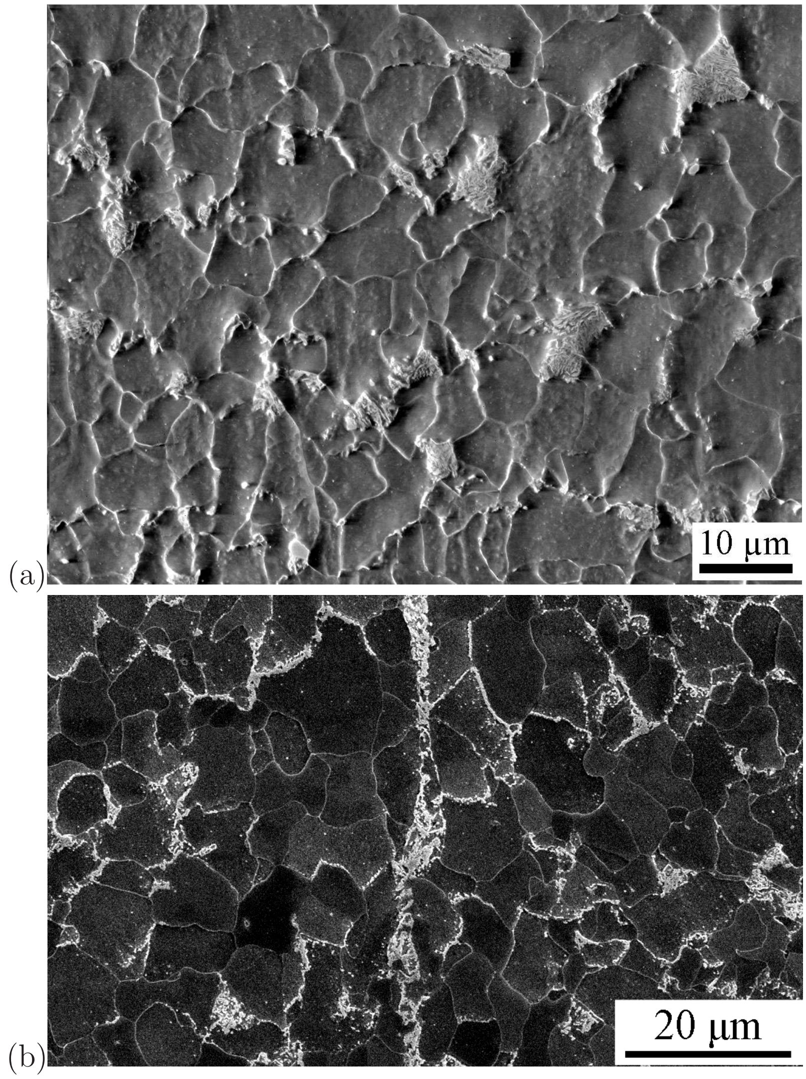

Figure 5.16: Scanning electron micrographs of the heat-treated X65 pipe with 8.6 mm wall-thickness. (a) At the vicinity of the weld junction. (b) On the weld junction.

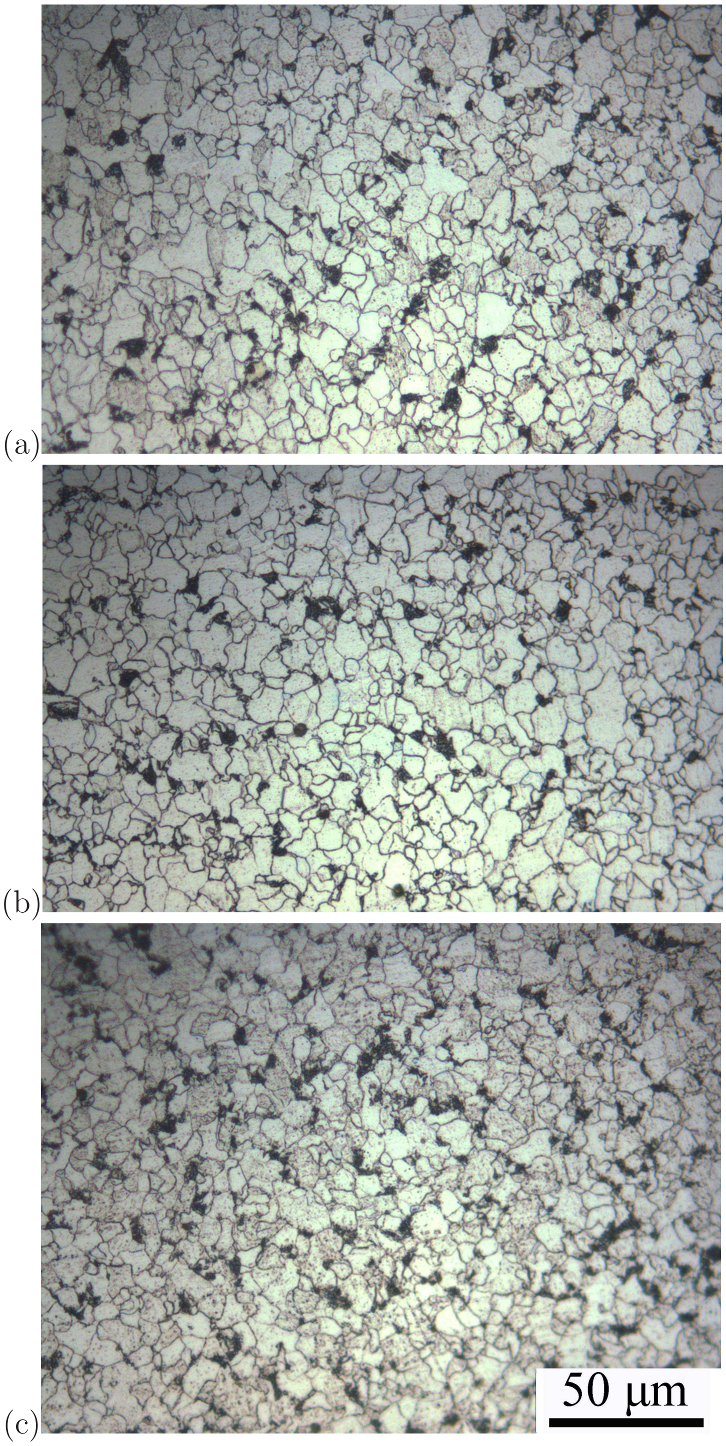

Figure 5.17: Optical micrographs showing the trace of the metal flow on one side of the weld junction: (a) near the outer surface, (b) at mid-thickness and (c) near the inner surface of the pipe.

5.3 Microhardness profile

The distributions of microhardness of the as–welded samples and heat–treated samples are shown in Fig. 5.18a and c. The origin of the x-axis still corresponds to the centre of the weld junction. On the as-welded samples, the hardness showed higher values near the outer surface of the pipe due to the surface hardening effect as discussed in section 4.2.1. There is an abrupt drop of hardness on the weld junction of both pipes, which is the evidence of decarburisation on the very location of the as-welded samples. The decarburised layer was observed in the normalised microstructure of the weld junction using optical microscopy (Fig. 5.19).

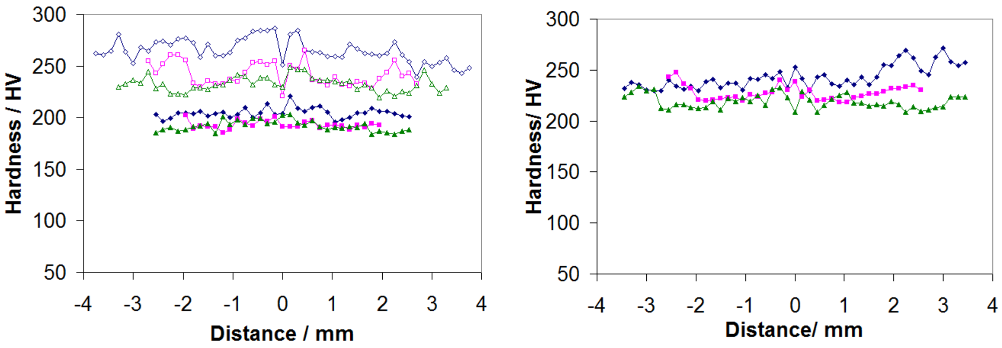

(a) As-welded and heat-treated (solid points) samples from X65 pipe with 8.6 mm wall-thickness.

(b) As-welded sample from X65 pipe with 8.6 mm wall-thickness after tempering.

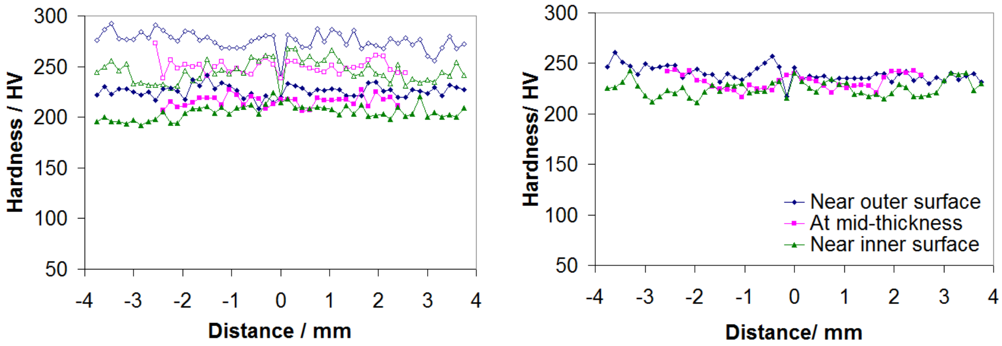

(c) As-welded and heat-treated (solid points) samples from X65 pipe with 14.8 mm wall-thickness.

(d) As-welded sample from X65 pipe with 14.8 mm wall-thickness after tempering.

Figure 5.18: Microhardness profile across the welds from X65 pipes.

Tempering the as-welded samples at 400 °C for 2 h slightly reduces the hardness value across the weld (*cf.* Fig. 5.18a and b, c and d), which is consistent with the existence of M–A islands in the as-welded microstructure.

Heat-treated samples showed a uniform distribution of hardness across the weld (solid points in Fig. 5.18a and c), which corresponds well to the unified microstructure. There is no decrease of hardness on the weld junction,

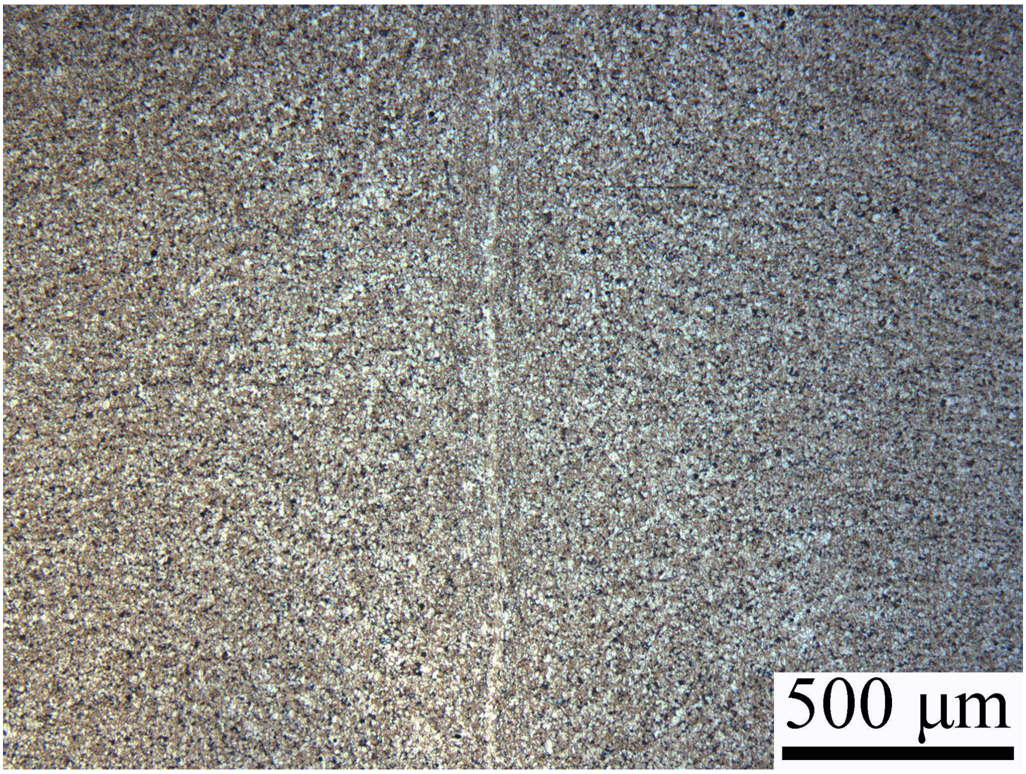

(a) ×50 magnification.

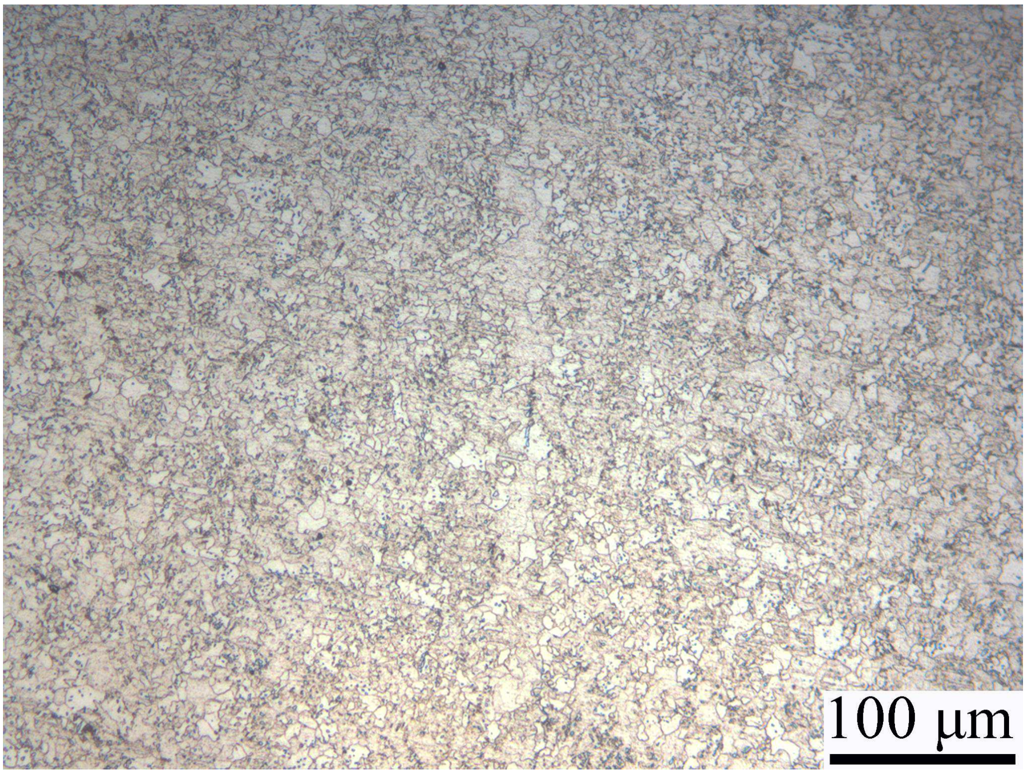

(b) ×200 magnification.

Figure 5.19: Optical micrograph of the welds from X65 pipe with 14.8 mm wall-thickness after normalisation at 900 °C for 30 min.

suggesting that post-welding heat treatment reduces the extent of decarburisation.

5.4 Inclusions

The possibility of inclusions at the weld junction was investigated using extensive scanning electron microscopy together with EDX. Bearing in mind that manganese and silicon oxides were found in the bent sample as discussed in section 5.1.1, RD–TD surfaces with the weld junction in the middle were cut and polished for investigation. In the heat-treated segment with the size of 10 mm along the rolling direction from the pipe with 8.6 mm wall-thickness, inclusions were revealed on the RD–TD surfaces near the outer and inner surfaces and at the mid-thickness of the pipe as shown in Fig. 5.20. Most of these inclusions aligned along the weld junction possess compositions consistent with manganese and silicon oxides, as shown in Table 5.3. During the welding process, these oxides formed by heating the edges of the steel plate and did not get expelled by the forging. Post-welding heat treatment was not able to attack the inclusions. At mid-thickness of the thin-walled X65 pipe, several aluminium and calcium rich oxides were also found (Fig. 5.20b and Table 5.3). Fractography carried out on the tested Charpy sample from the weld junction also revealed inclusions with similar compositions of manganese and silicon oxides as shown in Fig. 5.21 and Table 5.3, which suggests that the inclusions are detrimental to the toughness of the weld.

Table 5.3: Compositions for the inclusions (wt% with σ) by EDX.

	O	Al	Si	Ca	Ti	Mn	Fe
Fig. 5.20a	31.43	2.04	16.46	0.59	1.48	45.07	2.92
	±0.31	±0.1	±0.19	±0.09	±0.12	±0.36	±0.27
Fig. 5.20b	31.50	2.79	14.98	0.62	1.40	40.50	8.22
	±0.33	±0.1	±0.19	±0.09	±0.13	±0.39	±0.31
Fig. 5.20b	34.77	27.71	1.29	11.69	–	–	24.55
(circles)	±0.33	±0.24	±0.08	±0.17			±0.34
Fig. 5.20c	36.42	2.43	19.40	0.51	1.91	37.36	1.98
	±0.35	±0.11	±0.22	±0.08	±0.13	±0.38	±0.25
Fig. 5.21	31.38	1.42	16.48	0.41	0.96	46.06	3.28
	±0.26	±0.08	±0.13	±0.05	±0.07	±0.24	±0.15

Surprisingly when the same investigation on the RD–TD surfaces was carried out on the heat-treated weld from the pipe with 14.8 mm wall-thickness, no inclusions were found. Three pairs of Charpy fracture surfaces

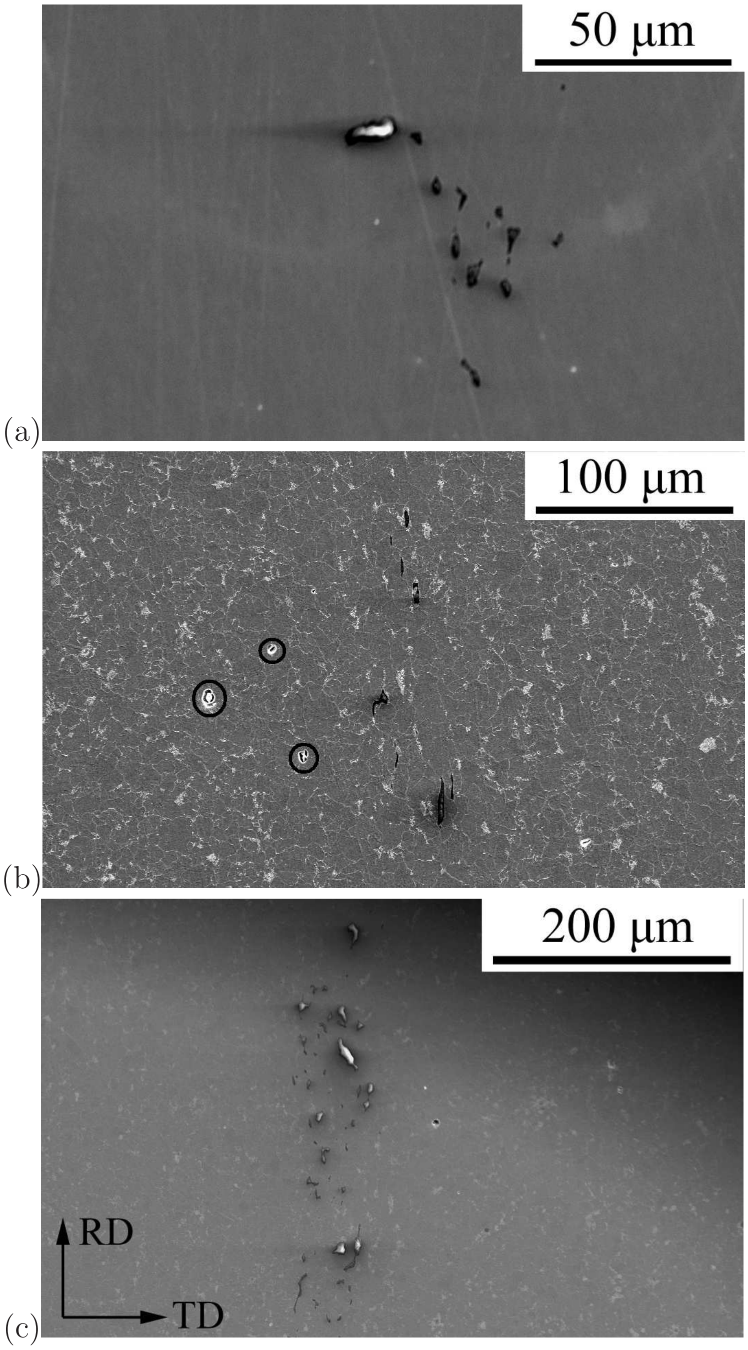

Figure 5.20: Scanning electron micrographs of the inclusions on the weld junction of the heat-treated sample of X65 pipe with 8.6 mm wall-thickness (a) Near the outer surface. (b) At mid-thickness. (c) Near the inner surface.

from the weld junction tested at −40°C were also examined. No clue of inclusion initiated fracture was discovered. These three Charpy samples all showed an absorbed energy value comparable to what the sample illustrated in Fig. 4.14 gave. It might be the fact that the manganese and silicon oxides

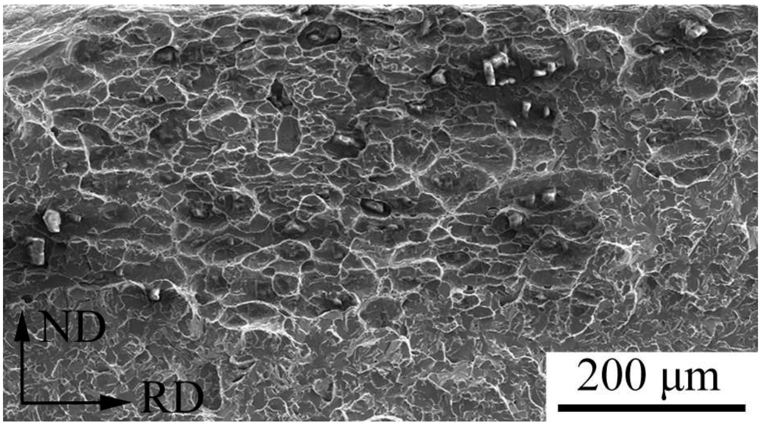

Figure 5.21: Fracture surface at weld junction after post-weld heat treatment from the pipe with 8.6 mm wall-thickness, tested at −40°C.

were not present continuously along the rolling direction, which is also the welding direction, but it is more likely that there is another factor playing an important role in causing the low toughness at the weld junction. In the case of the pipe with 8.6 mm wall-thickness, the inclusions in Fig. 5.21 were found on the tested sample giving the absorbed energy of 6 J, which is lower than the mean value as shown in Fig. 5.3b. The highest value of absorbed energy from the tests with the same condition is 44 J. This scatter is consistent with the haphazard distribution of the inclusions along the weld. However, it is not explained that even the highest value of absorbed energy at the weld junction is still much lower than the result from the base metal at the same testing temperature, which is above 120 J. The next section describes the importance of crystallographic texture in affecting the toughness of the weld.

5.5 Crystallographic analysis

Continuous scans on the ND–TD surface along the transverse direction near the outer and inner surfaces, and at the mid-thickness of both pipes have been carried out using the EBSD technique. Only the ferrite orientation images from the pipe with 14.8 mm wall thickness (Fig. 5.22–5.27) are displayed here for brevity. More images are included in Appendix A. Austenite could not be detected with confidence as discussed in section 4.3. Grain boundaries in the orientation images are designated mainly by the solid black lines describing misorientation, $\phi \geq 10°$ between the neighbouring grains and a minority of thinner lines for $\phi \geq 2°$. The orientation images of the as-welded sample showed clearly a gradual change of the microstructure from base metal to thermomechanically-affected zone, heat-affected zone and to the weld junction, Fig. 5.22–5.24. The post-welding heat treatment significantly unified the microstructure as shown in Fig. 5.25–5.27. What it did not change completely is the texture originating from the welding.

Figure 5.28a shows a ferrite orientation image from the base metal, which is an area 4 mm away from the weld junction on the as-welded sample. The crystal orientations within this region are not uniformly distributed, as illustrated by the {100} pole figure (Fig. 5.28c), but the ferrite grains have a large range of orientations. More importantly, there is no accumulation of {100} poles around the transverse direction. This means there are few {100} planes parallel or nearly parallel to the ND–RD surface, which is the fracture surface of the Charpy samples in this study, as shown in Fig. 3.2. The {100} plane is the cleavage plane of BCC iron crystal [86, 87], so a low density of {100} planes parallel to ND–RD surface should lead to a higher fracture energy. Figure 5.28b shows the scattered grains having their {100} planes oriented within 10° to the fracture surface, which represents only 3% of the area in Fig. 5.28a. The results are consistent with the base-metal toughness data illustrated in Fig. 5.3c. Conversely, a high density of {100} planes parallel to the fracture surface leads to a lower toughness. The as-welded junction is strongly textured with only one main orientation, and there is high concentration of {100} poles around the transverse direction (Fig. 5.28f). Some 19% of the area in Fig. 5.28d is occupied by clusters of grains oriented for easy fracture, Fig. 5.28e, which accounts for the poor toughness of this region, Fig. 5.3c. The intensity of the weld-junction texture decreased following post-welding heat treatment, as illustrated in Fig. 5.28i, but the accumulation of {100} planes around transverse direction was not diminished. Bear in mind that the as-welded junction consists of both shear products (Widmanstätten ferrite and M–A islands) and diffusional products (allotriomorphic ferrite) from the transformation, so part of the prior austenite grain structure formed during the welding process was reproduced by the rapid heating of the induction heat treatment due to the austenite memory effect [97]. Fig. 5.28h shows that grains possessing cleavage planes within 10° to the fracture surface still take up 10% of the area in Fig. 5.28g. This explains why the improvement of toughness on the weld-junction by post-welding heat treatment is not as much as being comparable to the base metal, Fig. 5.3c.

Table 5.4 gives a general view of the area percentage of {100} planes similarly oriented with the fracture surface for both kinds of pipes. Each value in the table is obtained from an EBSD scan of an area with the same size of Fig. 5.28a, d or g, *i.e.*, $242.8\times100\ \mu\mathrm{m}^2$. For both kinds of pipes, the base metal has the lowest density of cleavage planes oriented for easy fracture, while the as-welded junction has the highest. After post-welding heat treatment, the density did not go down to the base metal level.

Similar to the calculation carried out to construct Fig. 4.27, three angles between three {100} planes and the ND–RD surface of all the grains from the scanned areas of base metal and heat-treated weld junction respectively were calculated using the Euler angles obtained by EBSD technique. The minimum of the three angles for each grain is selected to plot the distributions shown in Fig. 5.29, with each line representing the same size of the areas either in base metal or in weld junction. For both pipes, firstly there is higher fraction of grains with unfavourably oriented cleavage planes in the heat-treated weld junction compared to the base metal (Fig. 5.29a and c), which makes the former more prone to cleavage. Secondly, base metal has higher fraction of grains with their cleavage planes oriented in the angles between 40 and 50° to the fracture surface, which is the favourable orientation against fracture. Besides, substantially larger number of grains contribute to this range in the base metal than in the heat-treated weld junction (Fig. 5.29b and d); since the former has finer grains, which is also noticeable in the orientation images (*cf.* Fig. 5.28a and g). Larger number of grains oriented against the fracture produce more deviation for the crack propagation across more grain boundaries, which leads to higher absorbed energy and toughness.

5.6 Conclusions

It is found that the high frequency induction welded junctions from two X65 grade steel pipes with different wall-thickness possess unsatisfactory ductility and toughness after post-welding heat treatment, even though the microstructure across the weld was uniform and there is no decarburisation and remaining austenite after post-welding heat treatment. Meticulous investigation has then identified three causes of the weakness: the existence of non-metallic inclusions, crystallographic texture, and larger grain size. Persistence of manganese and silicon rich oxides have a negative effect on these properties, especially the ductility, but these inclusions only exist occasionally along the welding direction. Low toughness in the weld-junction is substantially related to the grain orientation favouring fracture. This 'bad' texture is produced during the welding process. Reaustenitisation during the post-welding heat treatment reduces the intensity of the texture but dose not alter it. The heat-treated weld-junction was also found to have coarser grains than the base metal does, which helps to enlarge the difference in toughness between the two samples.

The ΔITT from base metal to the heat-treated weld junction of the thick-walled X65 pipe is more than 80°C estimated from Fig. 5.3c. The results of grain size analysis are shown in Fig. 5.30. They were carried out on orientation images using the critical misorientation angle of 10° as discussed on page 62. Taking the equivalent grain diameter value at 0.5 accumulative area fraction from Fig. 5.30b, the contribution of the grain size difference to ΔITT from base metal to the heat-treated weld junction of the thick-walled X65 pipe is estimated at 35°C according to equation 2.14 by Pickering [69]. The contribution of crystallographic texture is assessed by correlating the thick-walled X65 pipe to the X65HIC pipe. ΔITT for the X65HIC pipe is more than 40°C as estimated from Fig. 4.3, which is fully explained by the crystallographic texture. The area percentage of grains containing {100} planes within 10° to the ND–RD surface increased 7.6% from base metal to the heat-treated weld junction of the X65HIC pipe. This increase is 5.7% in the thick-walled X65 pipe as listed in Table 5.4b. Supposing the intensity of the {100} texture has a linear relation with the transition temperature, the change of crystallographic texture results in at least 30°C to ΔITT from base metal to the heat-treated weld junction of the thick-walled X65 pipe. The rest of ΔITT may be caused by the content of the non-metallic inclusions. This assessment gives an attempt to predict ΔITT after high frequency induction welding by quantification of the potential contributors.

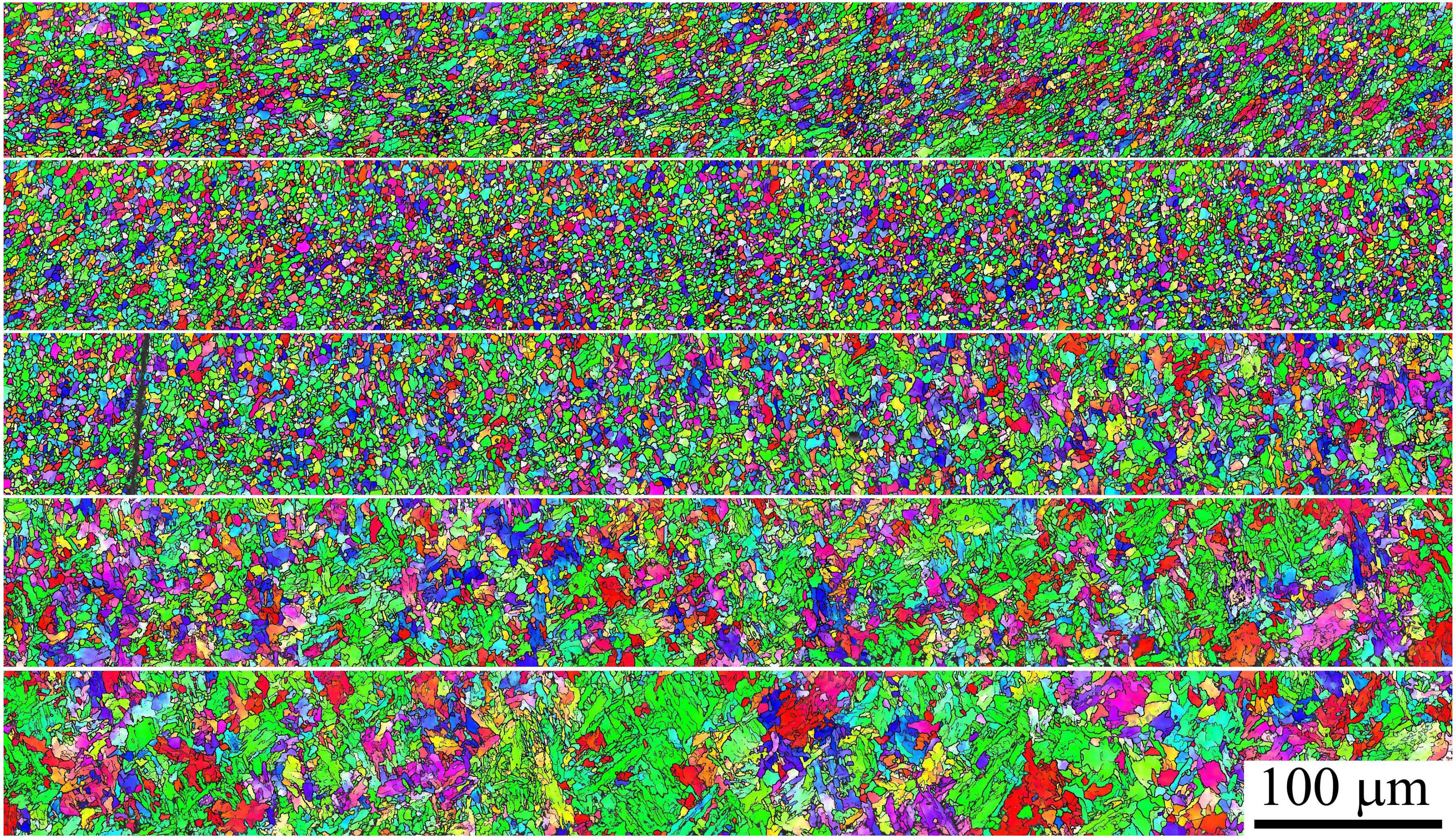

Figure 5.22: Ferrite orientation image of the as-welded sample near the outer surface of the thick-walled X65 pipe. The image is continuous from the base metal at the top left to the middle of the weld junction at the bottom right.

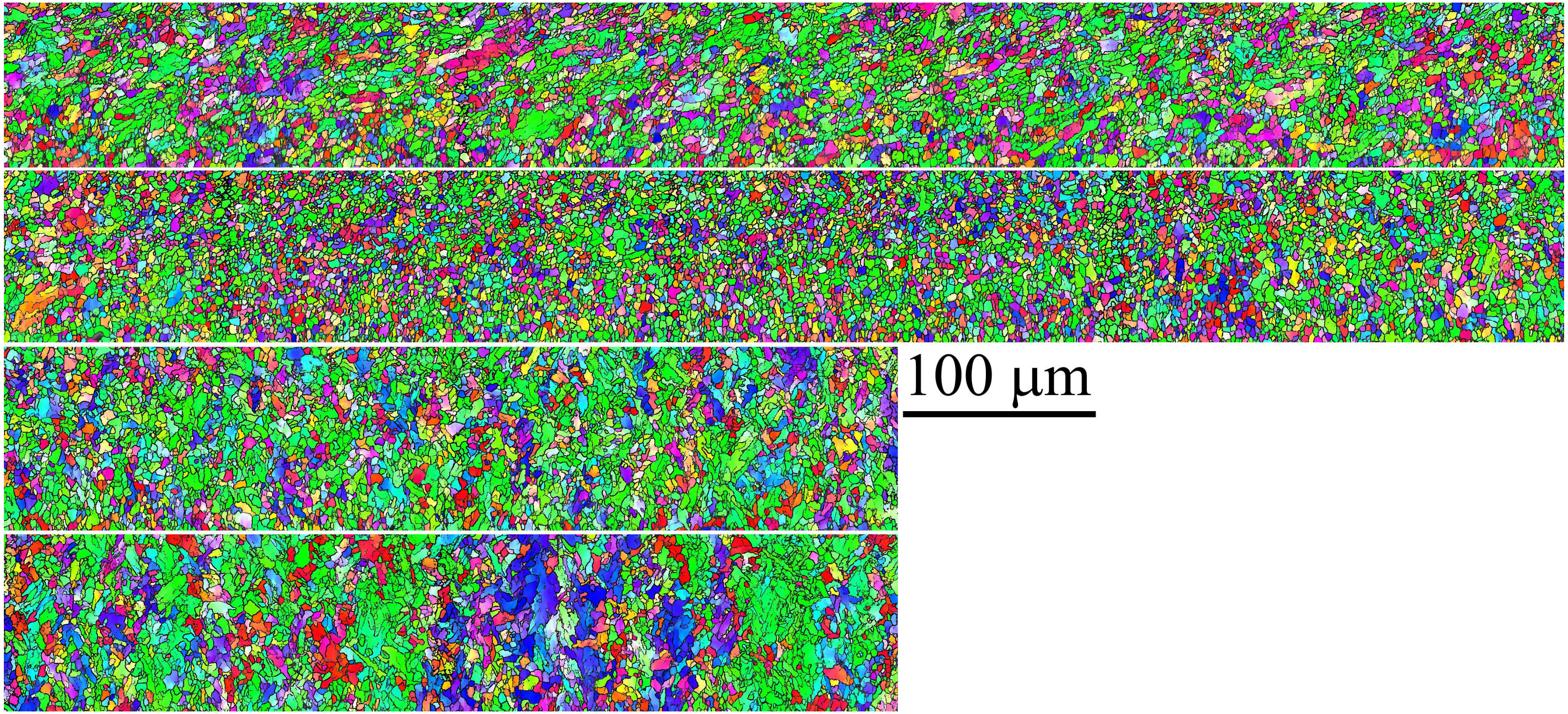

Figure 5.23: Ferrite orientation image of the as-welded sample at mid-thickness of the thick-walled X65 pipe. The image is continuous from the base metal at the top left to the middle of the weld junction at the bottom right.

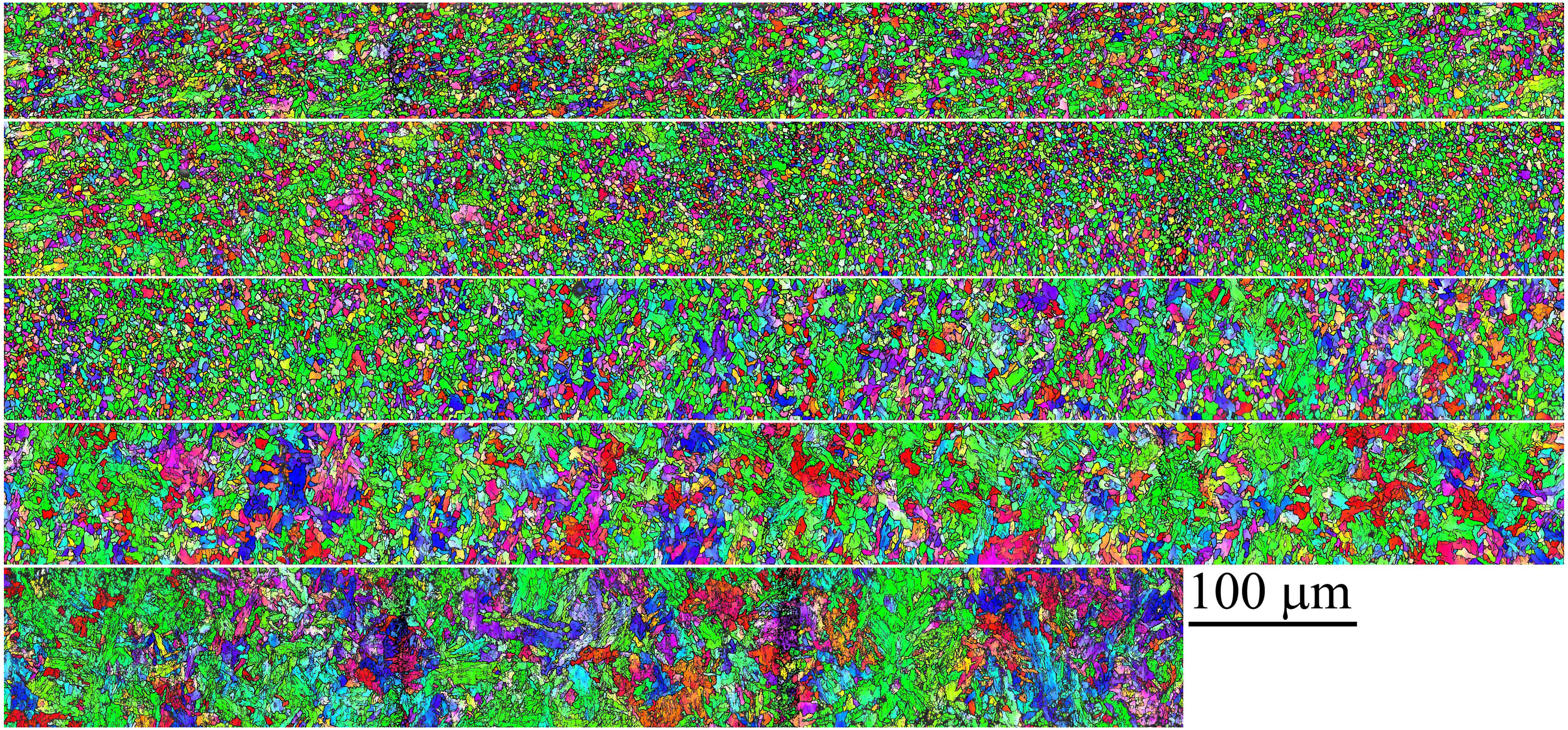

Figure 5.24: Ferrite orientation image of the as-welded sample near the inner surface of the thick-walled X65 pipe. The image is continuous from the base metal at the top left to the middle of the weld junction at the bottom right.

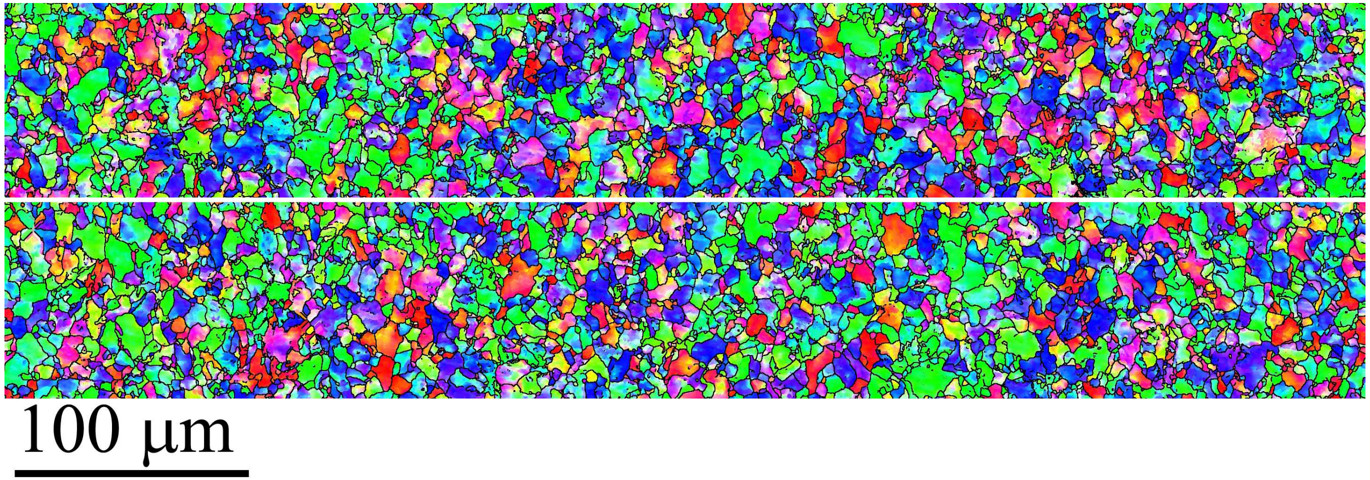

Figure 5.25: Continuous ferrite orientation image from 1 mm left towards the middle of the weld junction on the sample after post-welding heat treatment near the outer surface of the thick-walled X65 pipe.

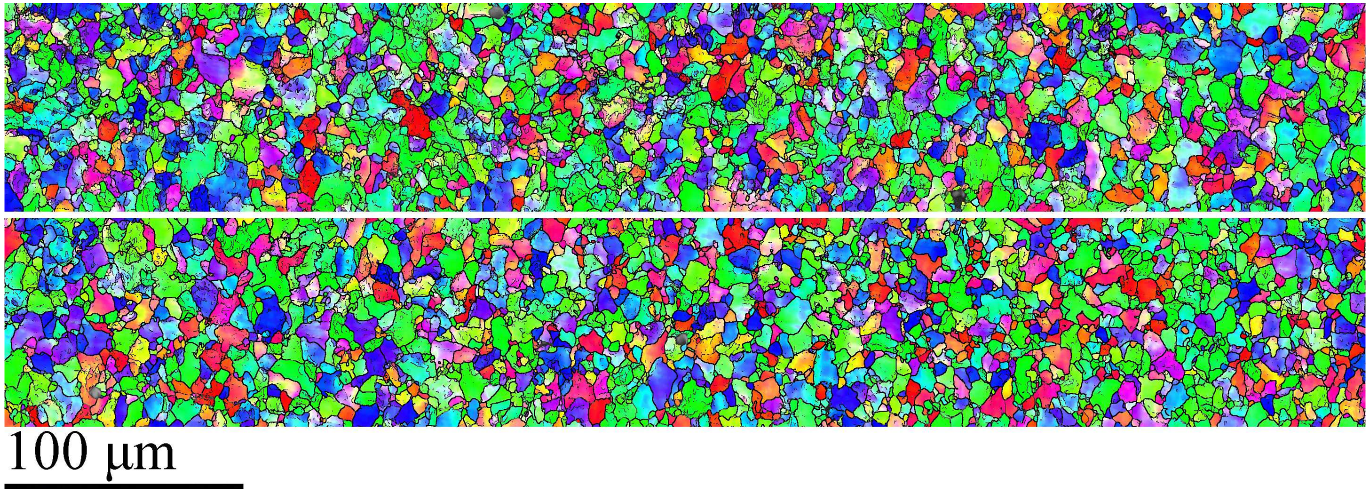

Figure 5.26: Continuous ferrite orientation image from 1 mm left towards the middle of the weld junction on the sample after post-welding heat treatment at mid-thickness of the thick-walled X65 pipe.

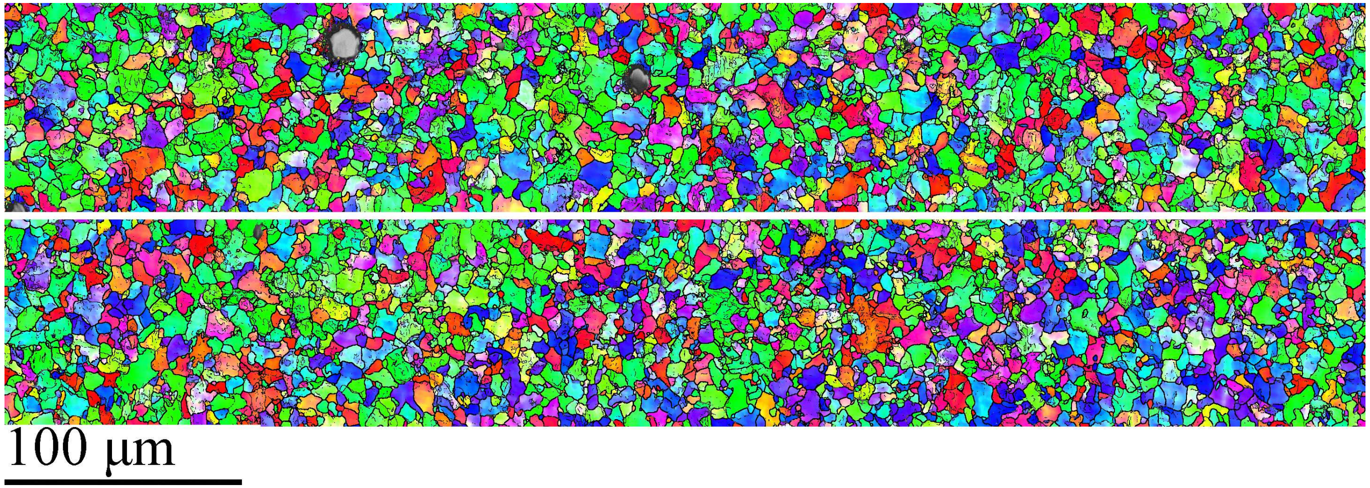

Figure 5.27: Continuous ferrite orientation image from 1 mm left towards the middle of the weld junction on the sample after post-welding heat treatment near the inner surface of the thick-walled X65 pipe.

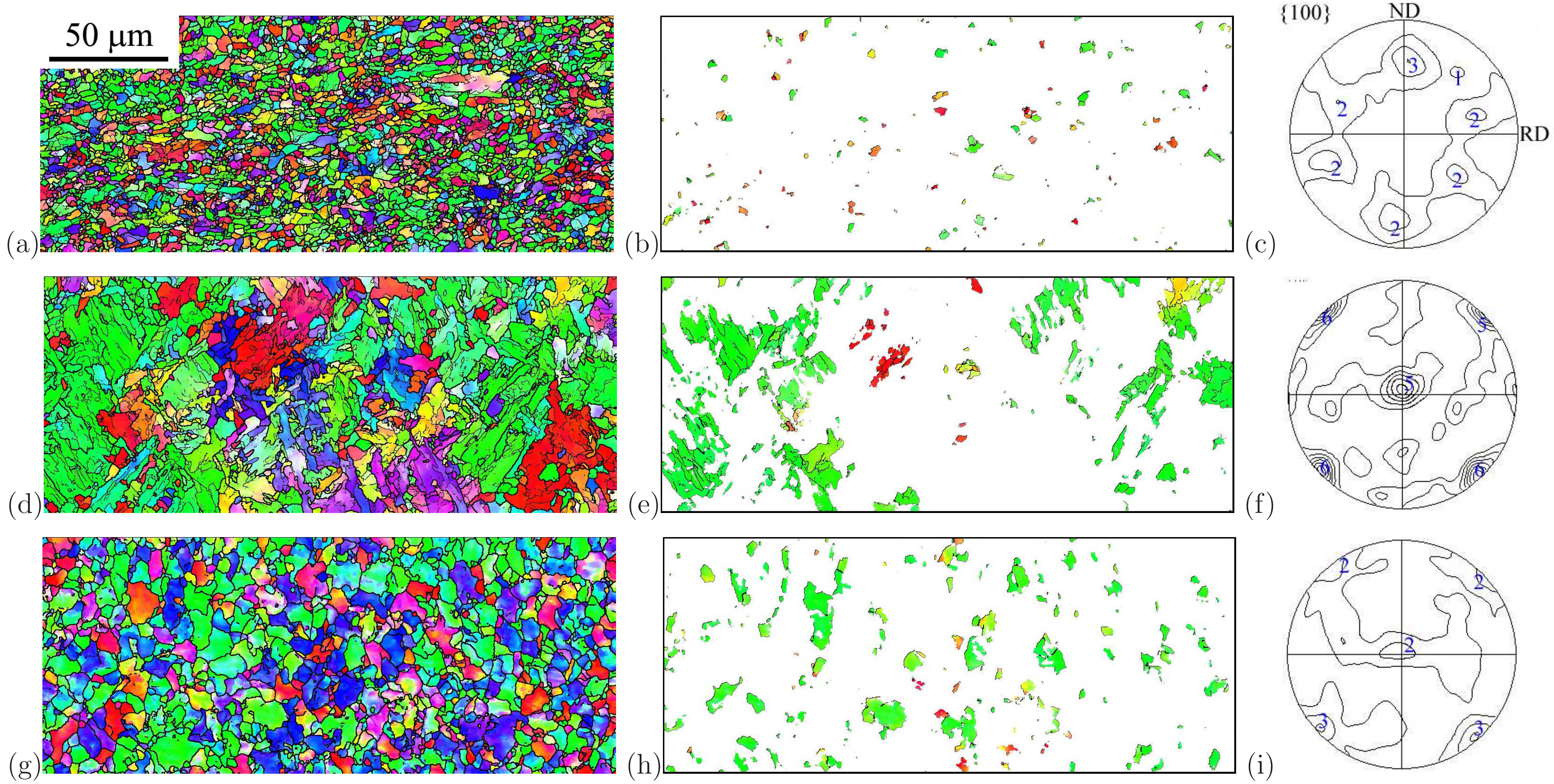

Figure 5.28: (a) Orientation image of base metal near the outer surface of the pipe with 14.8 mm wall-thickness. (b) Orientation image of grains in the same area of (a), oriented in the way that their {100} planes are within 10° to ND–RD surface. (c) Pole figure from the area of (a). (d)(e)(f) and (g)(h)(i) Equivalent images for the as-welded and the heat-treated weld junctions respectively.

Table 5.4: Area percentage of grains containing {100} planes within 10° to the ND–RD surface.

(a) Pipe with 8.6 mm wall-thickness.

	Base metal	Weld junction	
		As-welded	Heat-treated
Near outer surface	2	12	9
At mid-thickness	2	24	10
Near inner surface	2	12	7
Average	2	16	8.7

(b) Pipe with 14.8 mm wall-thickness.

	Base metal	Weld junction	
		As-welded	Heat-treated
Near outer surface	3	19	10
At mid-thickness	3	12	10
Near inner surface	4	14	7
Average	3.3	15	9

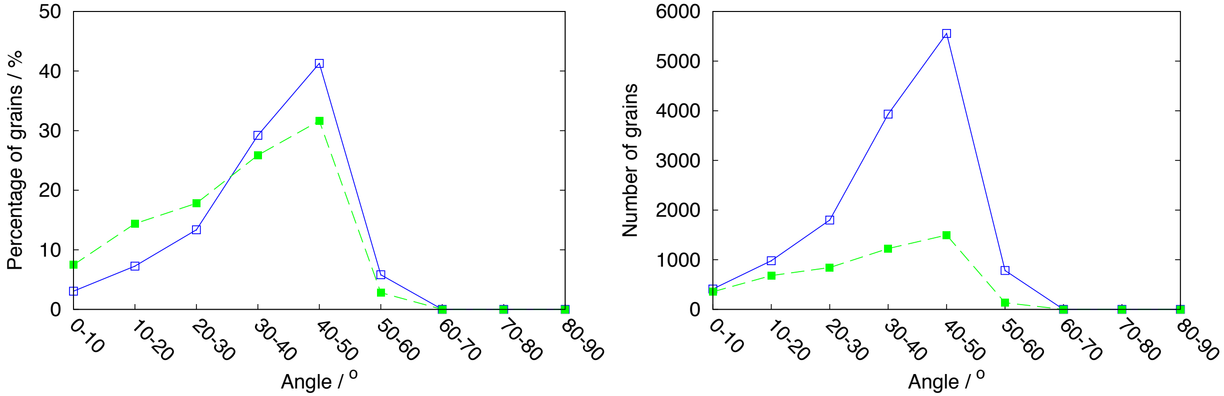

(a) Pipe with 8.6 mm wall-thickness.

(b) Pipe with 8.6 mm wall-thickness.

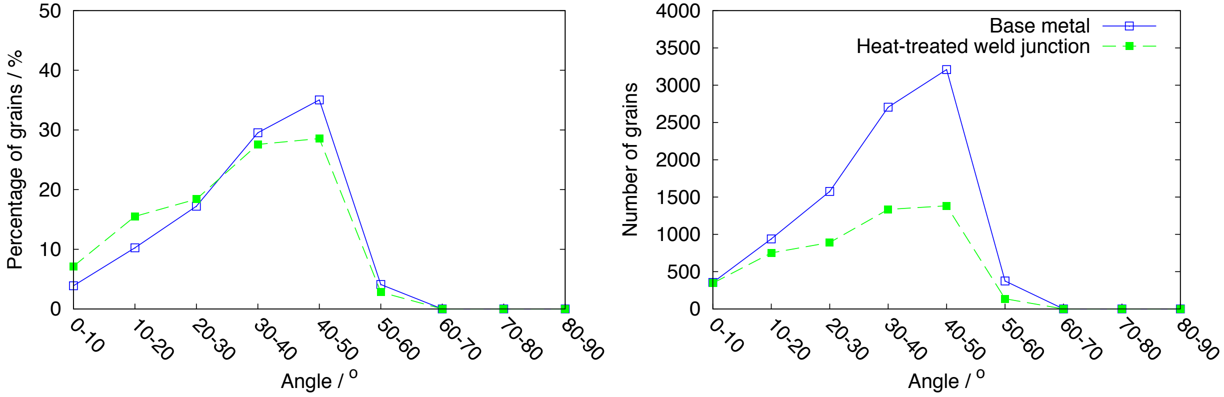

(c) Pipe with 14.8 mm wall-thickness.

(d) Pipe with 14.8 mm wall-thickness.

Figure 5.29: Distribution of the minimum angle between {100} plane and the ND–RD surface for all the grains scanned by EBSD technique.

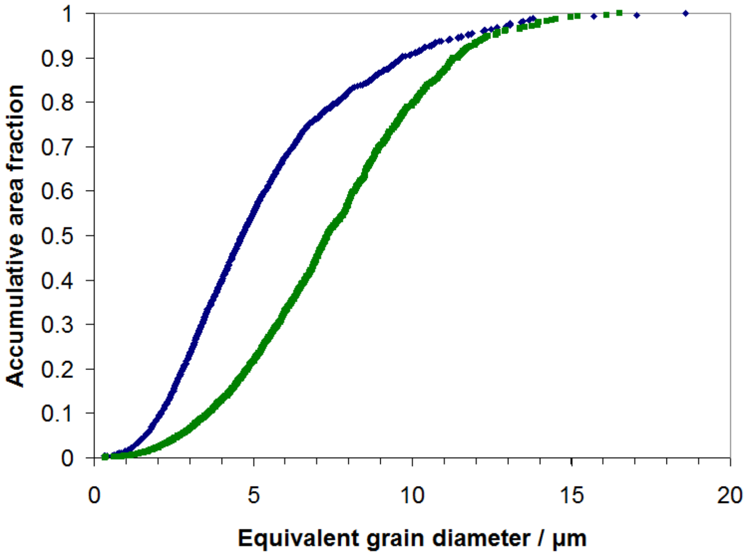

(a) Pipe with 8.6 mm wall-thickness.

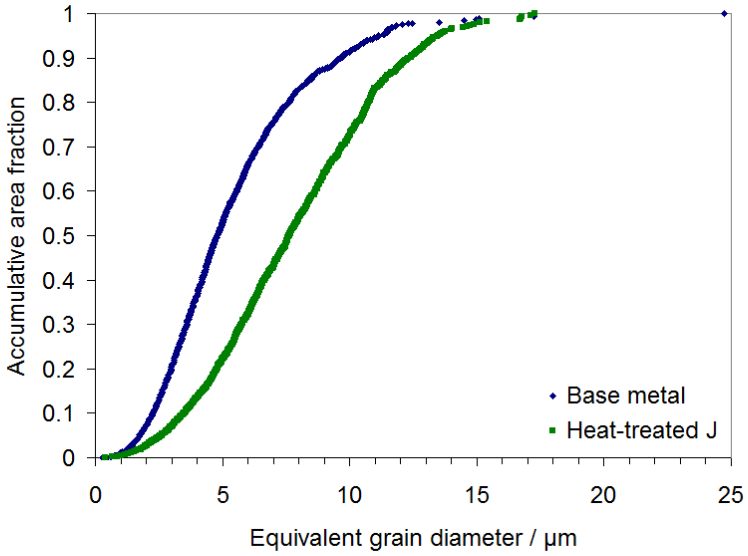

(b) Pipe with 14.8 mm wall-thickness.

Figure 5.30: Grain size analysis carried out on the areas with the same size on the base metal and heat-treated weld junction.

Chapter 6

Simulations of the High Frequency Induction Welding and Post-Welding Heat Treatment

6.1 Welds from X65HIC pipe

6.1.1 Welding process

Experiments were carried out to simulate the induction welding process on X65HIC base metal, the thermal history of which is shown in Fig. 6.1. The sample was heated up at 20 °C s^{-1} to 1450 °C and then cooled down at the same rate to room temperature. The peak temperature is chosen because the pyrometer reading for the temperature of the pipe just after passing through the induction coil is in a range of 1400–1500 °C and the sample should not be melted due to an experimental limitation of the equipment used. Calculations using MTDATA [129] showed that the X65HIC steel should not melt until 1500 °C under equilibrium conditions, Fig. 6.2. This calculation takes into account 11 elements and 4 phases, which are Fe, C, Mn, P, Si, Al, Cu, Ni, Cr, Nb, V, ferrite, austenite, cementite and liquid. The peak temperature of 1450 °C should match that of the actual temperature experienced by the material in close vicinity of a weld junction, since any molten material is expelled due to the forging pressure.

The microstructure obtained by the simulation is shown in Fig. 6.3. It consists of platelets of ferrite, which has a great similarity to the microstructure of granular bainitic ferrite and acicular ferrite which have been referred in a large amount of literature as typical microstructure in continuously-cooled low-carbon steels [130–133]. The former is also known as granular

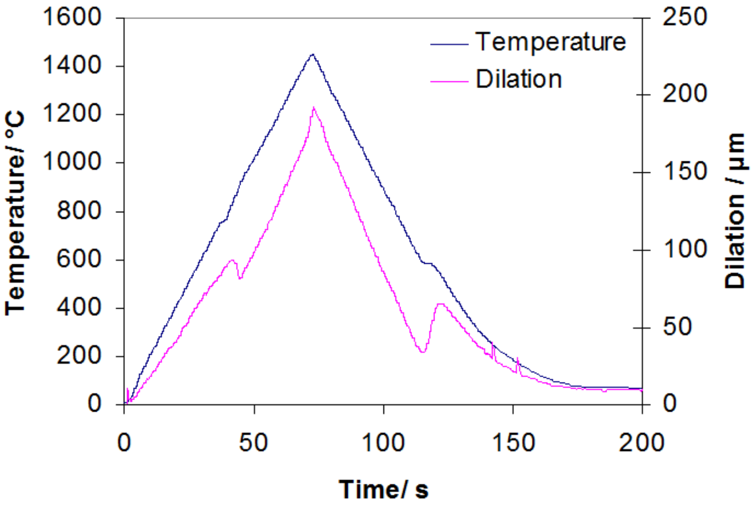

Figure 6.1: Simulation of induction welding on X65HIC base metal.

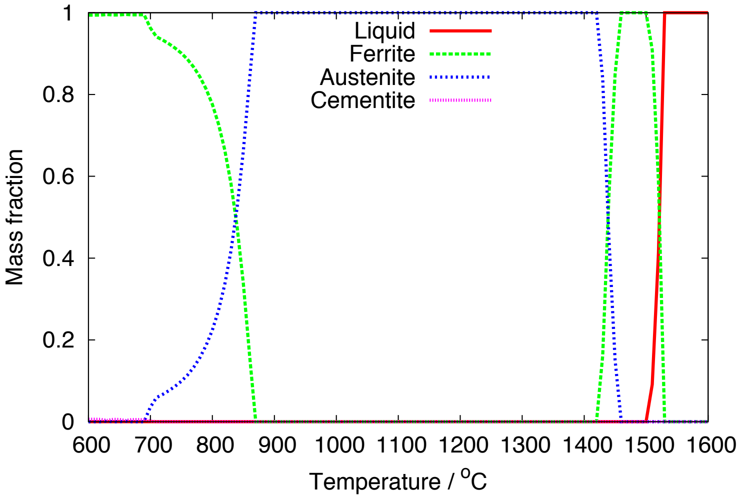

Figure 6.2: Calculated equilibrium transformation of X65HIC base metal.

bainite [134]. The black regions in the optical micrograph, Fig. 6.3, are most likely to be dispersed retained austenite or M–A islands in an either equiaxed or elongated morphology. Confirmation of these phases needs further characterisation, which was not pursued in this study because this microstructure is not similar to that of any zone observed in the as–welded sample (section 4.2.1). This suggests that the cooling rate after the welding process may not be as high as the one used in the simulation. The induction heating however should be much faster, but there are no data available for the heating rate associated with induction in the production line. Additionally, the welding process in practice involves force to press the two abutting edges of the steel plate together, which is not applied in this simulation.

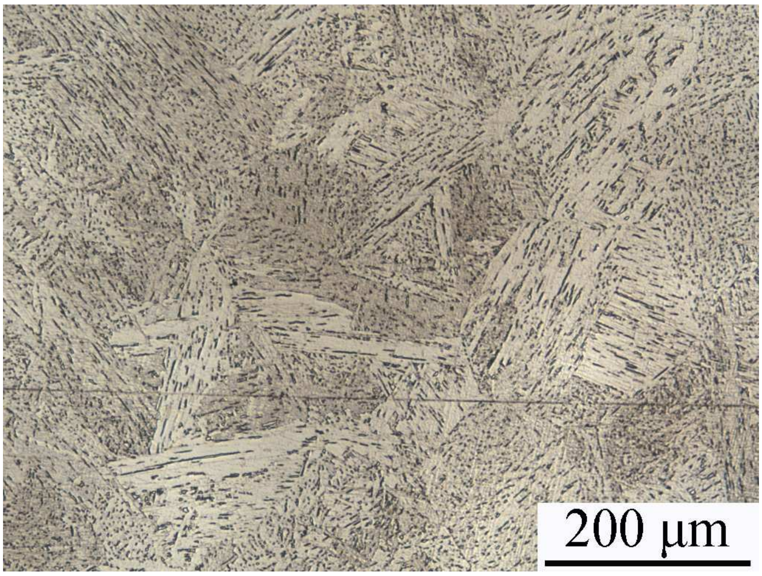

Figure 6.3: Microstructure of X65HIC base metal after simulated welding process.

6.1.2 First cycle of post-welding heat treatment

Since production samples extracted after the first cycle of the post-welding heat treatment were not available, simulation of the heat treatment (austenisation followed by cooling) was carried out on the as-welded sample in order to understand every step of the whole process. After the austenisation, air cooling gave the microstructure at the weld junction as shown in Fig. 6.4, consisting of ferrite and pearlite. At the mid-thickness of the pipe, there is pearlite aligned in a line (Fig. 6.4b), which is supposed to transform from the string in the as-welded sample (page 49). This demonstrates that accelerated cooling is necessary after austenistation to produce a finer final grain structure content with optimum mechanical properties.

Austenisation followed by quenching in iced brine gives the microstructure shown in Fig. 6.5. It should be similar to that from the industrial process, although the heating rate by induction (estimated $\sim 50\,^{\circ}\mathrm{C\,s^{-1}}$) should be more rapid than by placing the sample into a furnace at 960 °C ($\sim 10\,^{\circ}\mathrm{C\,s^{-1}}$). The microstructure at the weld junction, especially near the outer (Fig. 6.5a) and inner (Fig. 6.5e) surface of the pipe, consists of grain boundary allotriomorphs of ferrite and packets of plate-like grains which are likely to be low-carbon martensite or bainite. The microstructure at the mid-thickness of the pipe (Fig. 6.5c) mainly consists of fine-grained allotriomorphic ferrite. This difference is probably due to the faster cooling rate near the edge of the sample during quenching. The microstructure at the domain of original base metal (Fig. 6.5b, d and f) is similar to the one at the weld junction except for a finer grain size, which is most likely caused by the smaller austenite grains formed in the base metal. Since coarse austenite grains form at the weld junction (page 49), the austenisation during post-welding heat treatment does not reduce the autenite grain size in the weld junction to that in the base metal due to the austenite memory effect [97].

6.1.3 Modified post-welding heat treatments

In the industrial process, the peak temperature for the first cycle post-welding heat treatment is °C, substantially above the calculated A_{e3} temperature of the steel, 870 °C as shown in Fig. 6.2. The material is supposed to be fully austenised during the heat treatment. As discussed on page 30, the prior austenite grain is reconstructed above A_{c3} due to the austenite memory effect, so an intercritical annealing followed by quenching and then tempering is proposed for the post-welding heat treatment in order to prevent the acicular austenite formed above A_{c1} coalescing, which may lead to the grain refinement as evidenced in [98].

Temperature removed for copyright reasons

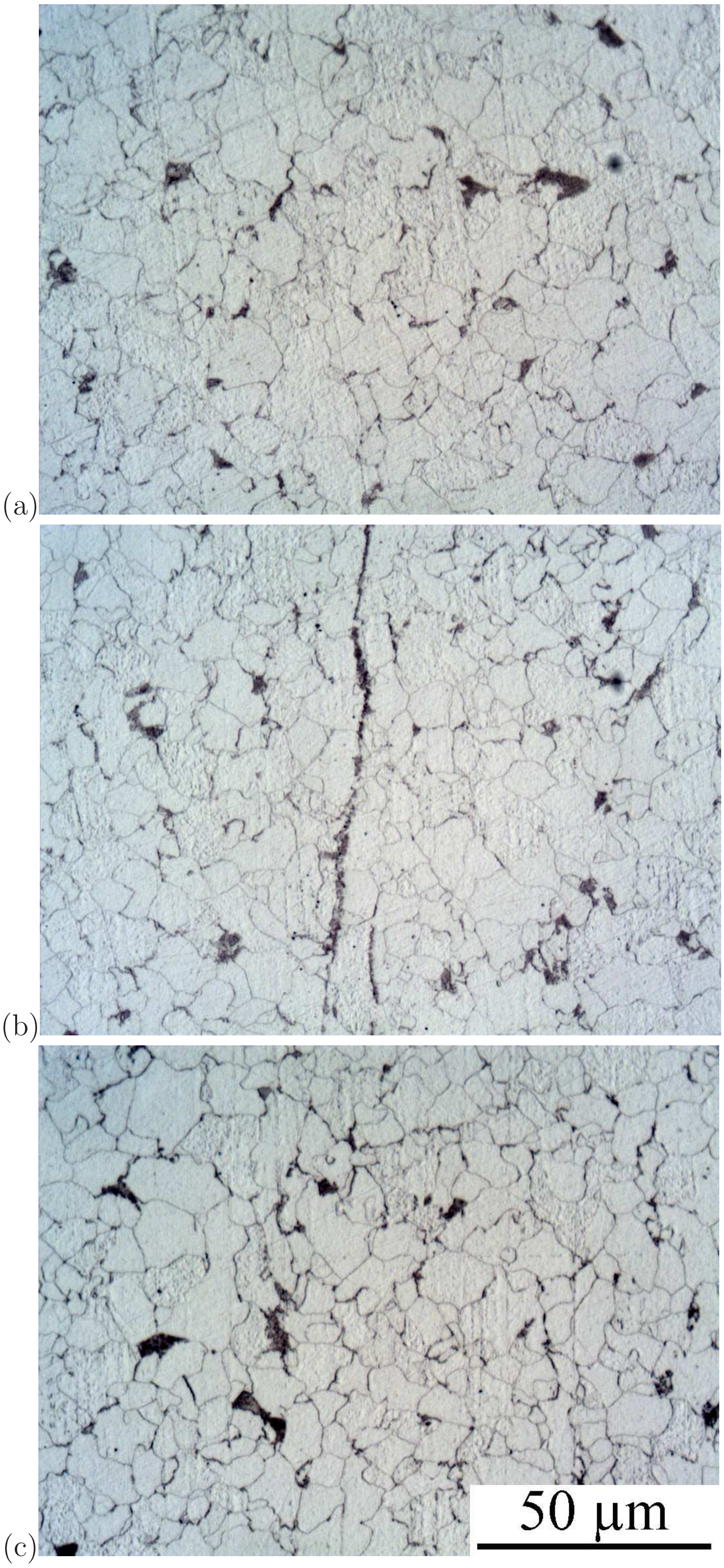

Figure 6.4: Microstructure at the weld junction after heating the X65HIC as-welded sample to 960 °C followed by an air cool. (a) Near the outer surface of the pipe. (b) At the mid-thickness (c) Near the inner surface.

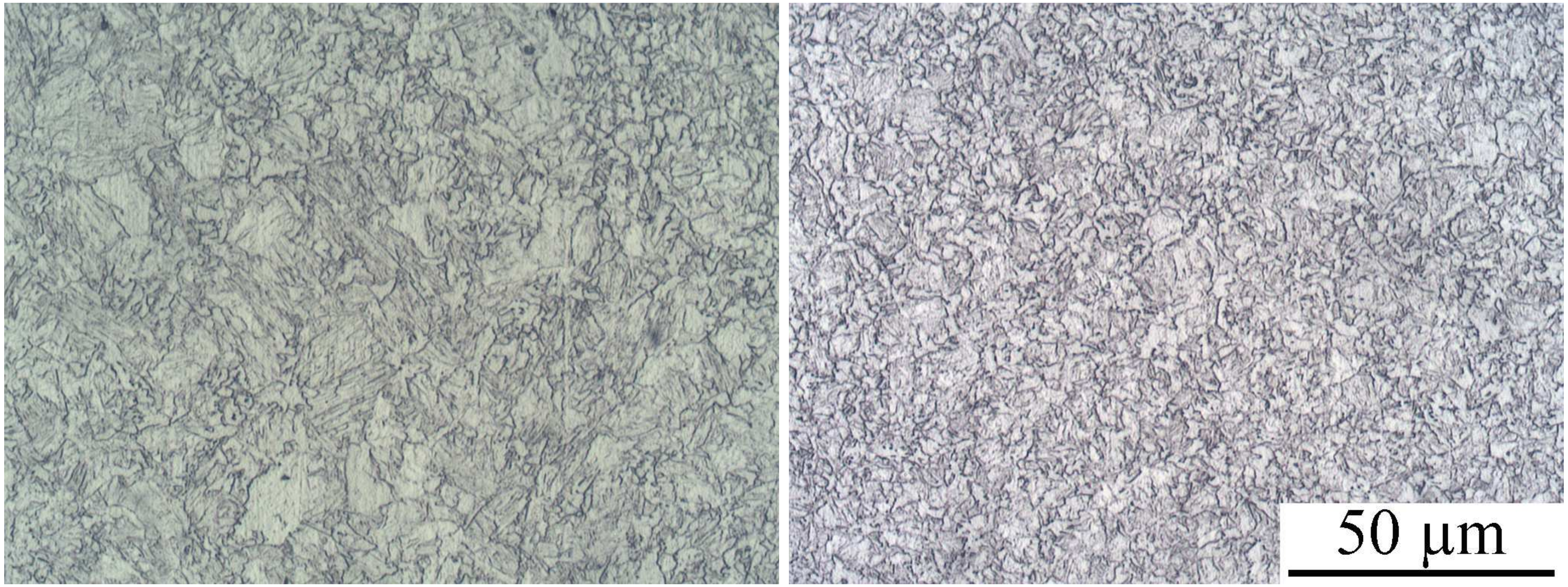

(a) Optical micrograph taken at the location of original weld junction.

(b) Optical micrograph taken at the location of original base metal.

Figure 6.5: Microstructure of as–welded sample after heating to 960 °C followed by quenching in iced brine near the outer surface of the X65HIC pipe (*continued on next page*).

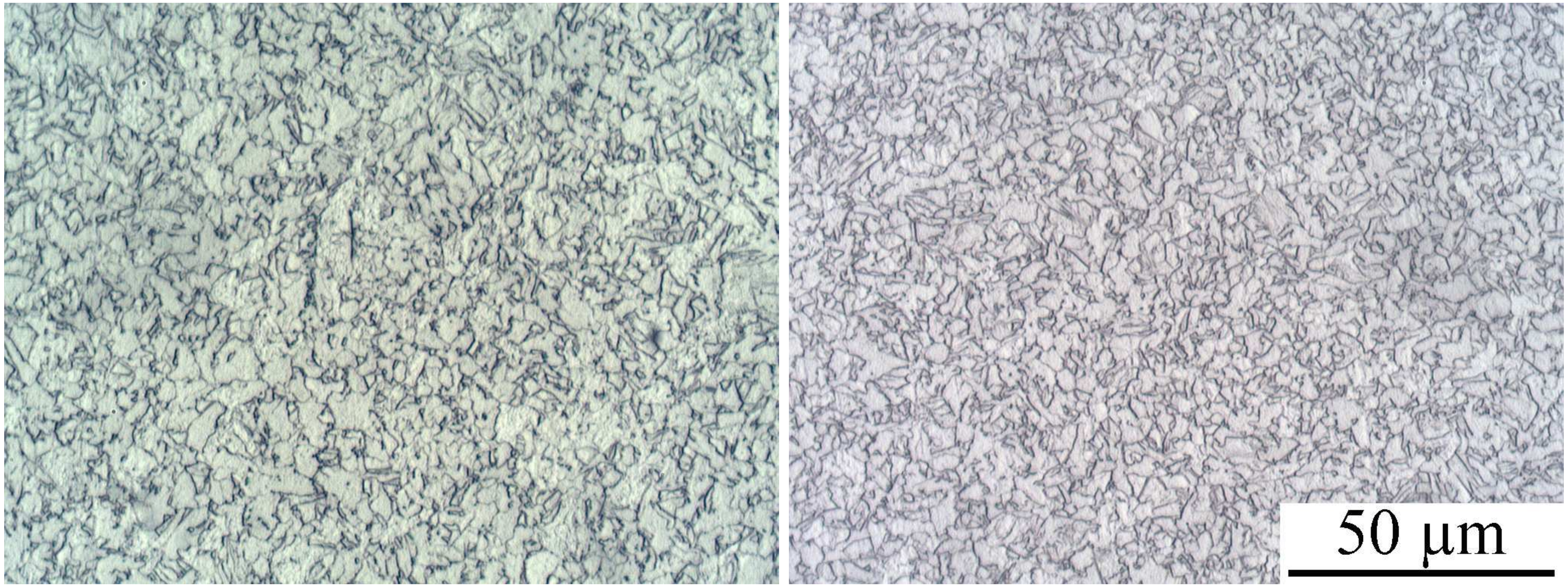

(c) Optical micrograph taken at the location of original weld junction.

(d) Optical micrograph taken at the location of original base metal.

Figure 6.5: Microstructure of as–welded sample after heating to 960 °C followed by quenching in iced brine at the mid-thickness of the X65HIC pipe (*continued on next page*).

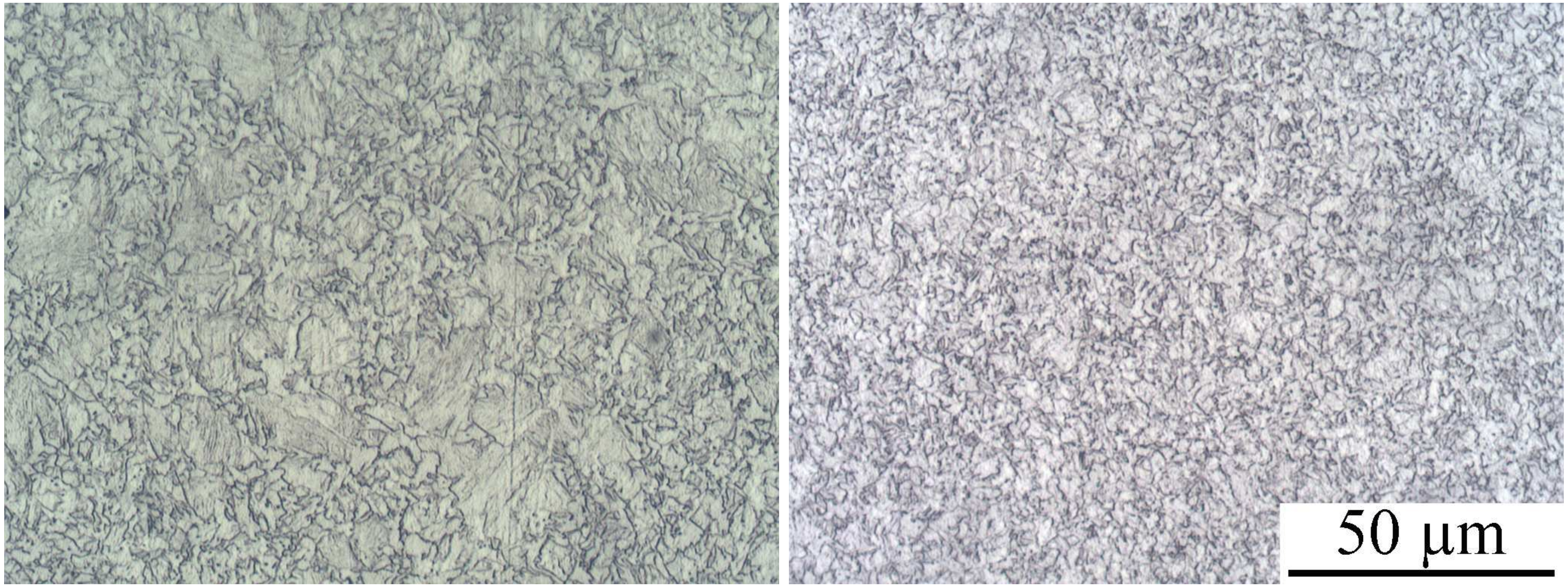

(e) Optical micrograph taken at the location of original weld junction.

(f) Optical micrograph taken at the location of original base metal.

Figure 6.5: Microstructure of as–welded sample after heating to 960 °C followed by quenching in iced brine near the inner surface of the X65HIC pipe.

The calculated A_{e1} and A_{e3} of X65HIC are 700 and 870 °C respectively (Fig. 6.2). The A_{c1} is 838±13 °C and the A_{c3} is 911±2 °C when the sample is heated at 20 °C s^{-1} using the thermomechanical simulator, as shown in Fig. 6.1. The heating rate applied in the experiments by placing sample into the furnace with preset temperatures was around 10 °C s^{-1}, which suggests the A_{c1} to A_{c3} should be between 700–870 °C and 838–911 °C; since the austenisation temperature increases with the heating rate. Therefore the peak temperature for the first intercritical annealing heat treatment (Treatment 1) was chosen to be 830 °C. The temperature profile of this experiment is shown in Fig. 6.6.

The microstructure of the weld (Fig. 6.7) did not change much following heat treatment. It can still be categorised into four domains similar to the as-welded sample (Fig. 4.5a and 4.6). This indicates that the intercritical annealing treatment at 830 °C was not effective. The A_{c1} to A_{c3} range of this material at the heating rate used is approaching 838–911 °C obtained at the heating rate of 20 °C s^{-1}, so 830 °C is probably too low.

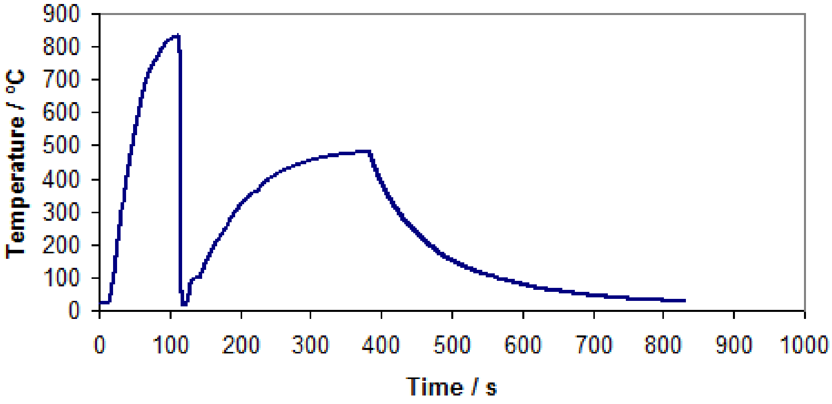

Figure 6.6: Thermal history of modified post-welding heat treatment 'Treatment 1' on X65HIC as–welded sample.

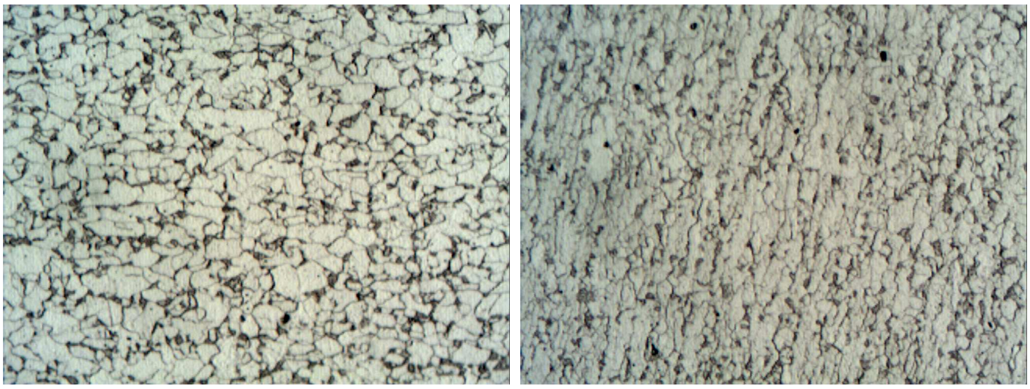

(a) Base metal. (b) Thermomechanically affected zone.

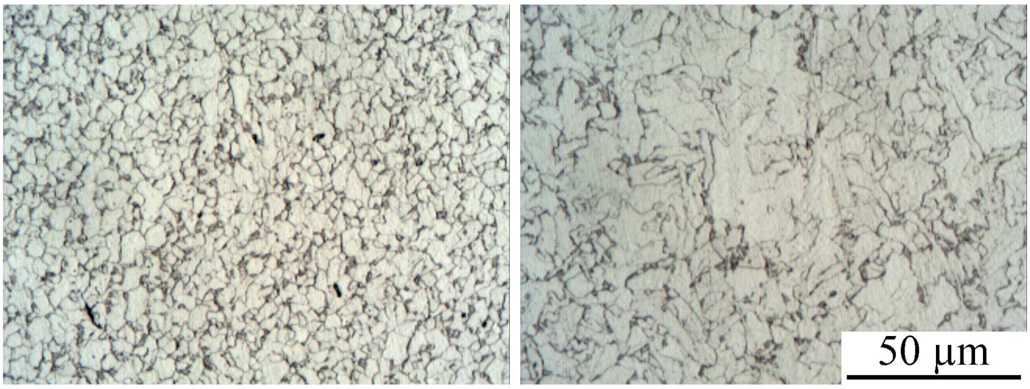

(c) Heat-affected zone. (d) Weld junction.

Figure 6.7: Microstructure of the X65HIC as–welded sample after 'Treatment 1'.

A second intercritical annealing heat treatment (Treatment 2) was conducted as shown in Fig. 6.8, with the peak temperature of the first cycle raised to 890 °C and the second cycle is still a simulation of the industrial process. The resulted microstructure becomes more uniform with no noticeable difference as a function of distance from the weld junction as shown in Fig. 6.9a–c, although a relatively coarse microstructure still persists in the weld junction.

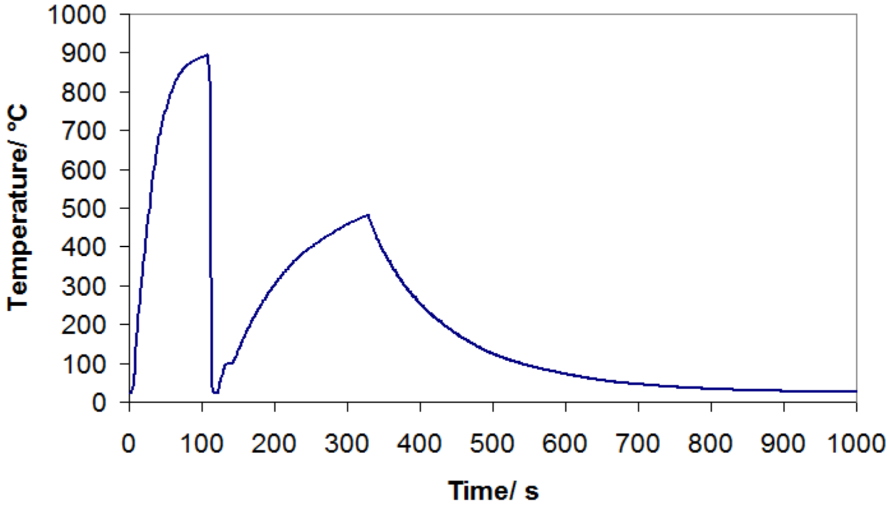

Figure 6.8: Thermal history of 'Treatment 2' on X65HIC as–welded sample.

Orientation images revealed a large crystallographic grain size at the weld junction, inherited from the as-welded sample. According to Fig. 6.10, the industrially produced sample still has a relatively more uniform distribution of crystal orientations. It is possibly caused by high intercritical annealing temperature, at which the acicular austenite has already started to coalesce into coarse austenite grains. The industrial process on the other hand, by austenising above A_{c3}, possibly induced an extent of recrystallisation, which led to grain refinement. Supposing the newly formed acicular austenite did not coalesce at 890 °C, as parts of the prior austenite grain they may transform upon cooling into the martensite or bainite with similar orientations to the ones after welding. Thus the heat-treated weld maintained the coarse crystallographic grains although the morphological grain size was reduced.

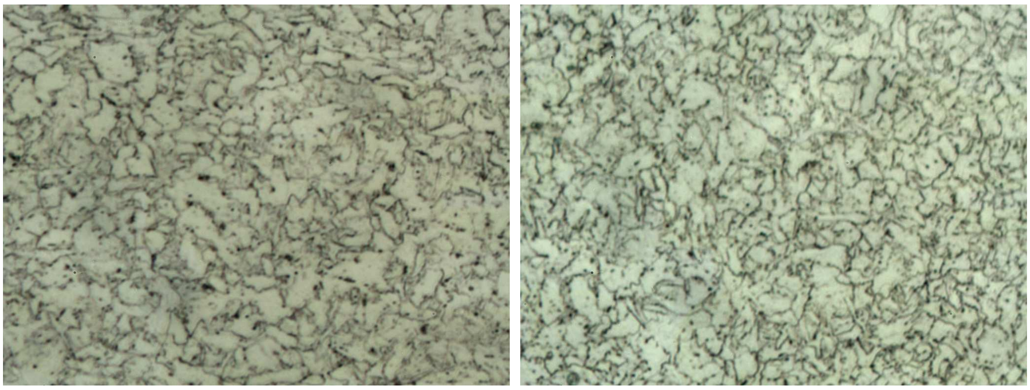

(a) At the location originally belonging to the base metal.

(b) Thermomechanically affected zone.

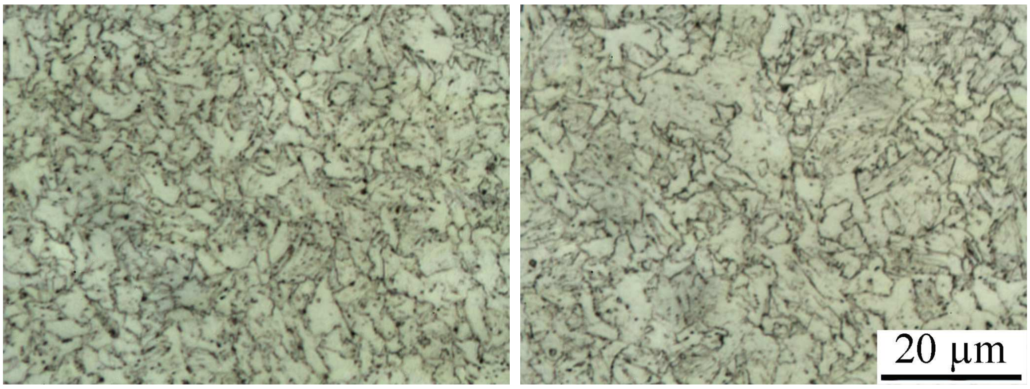

(c) Heat-affected zone.

(d) Weld junction.

Figure 6.9: Microstructure of the X65HIC as–welded sample after 'Treatment 2'.

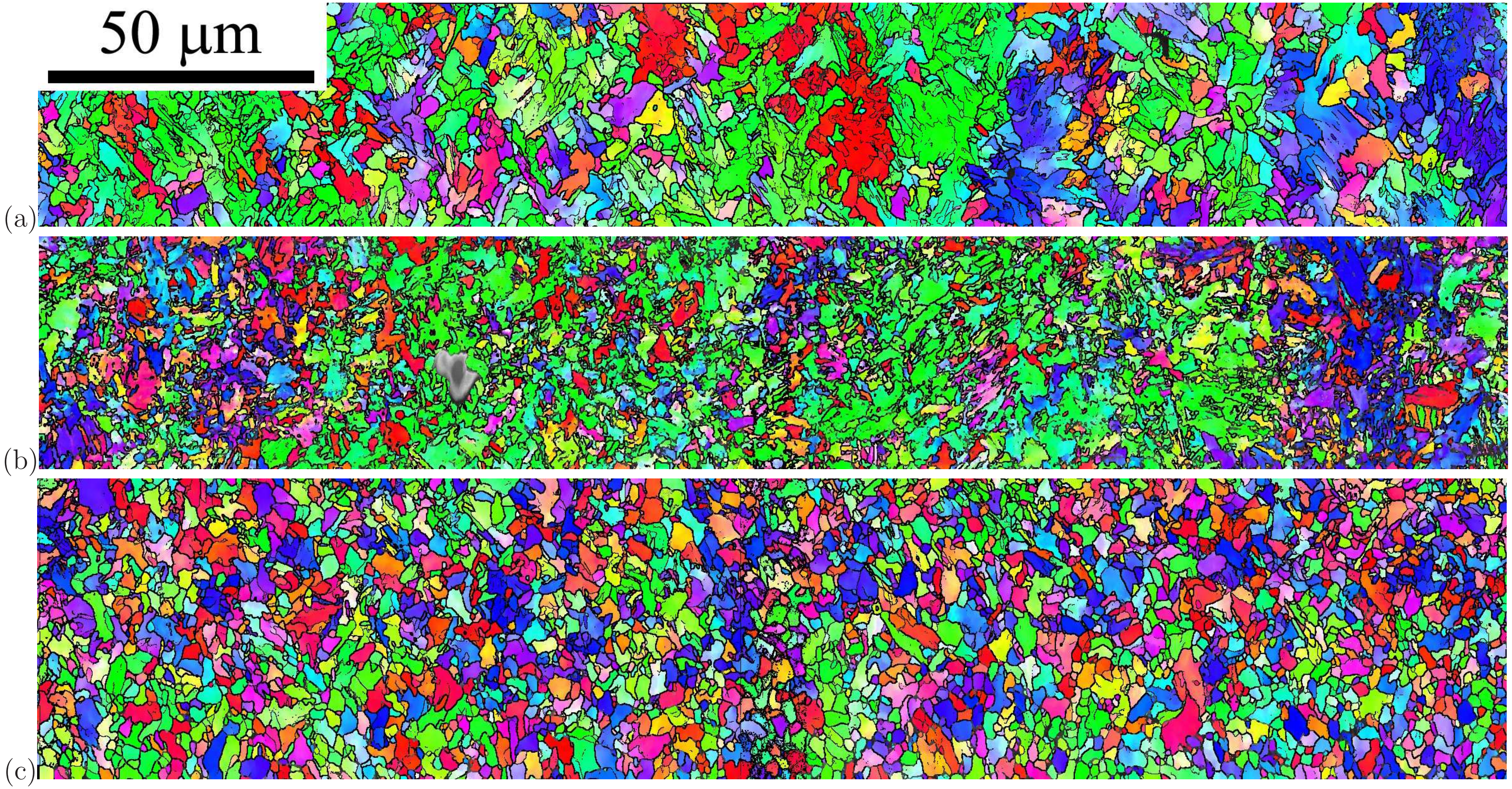

Figure 6.10: Ferrite orientation images in the vicinity of weld junction near the outer surface of the X65HIC pipe. (a) As-welded sample. (b) After 'Treatment 2' (c) After post-welding heat treatment.

The modified post-welding heat treatment was then aimed at austenisation at higher temperature than 960 °C which is employed during the industrial process, in order to promote the austenite recrystallisation and grain refinement. The new process, 'Treatment 3', involves heating the as-welded sample up to 1000 °C followed by quenching in water and then tempering up to 480 °C finished by air cooling to ambient temperature, Fig. 6.11.

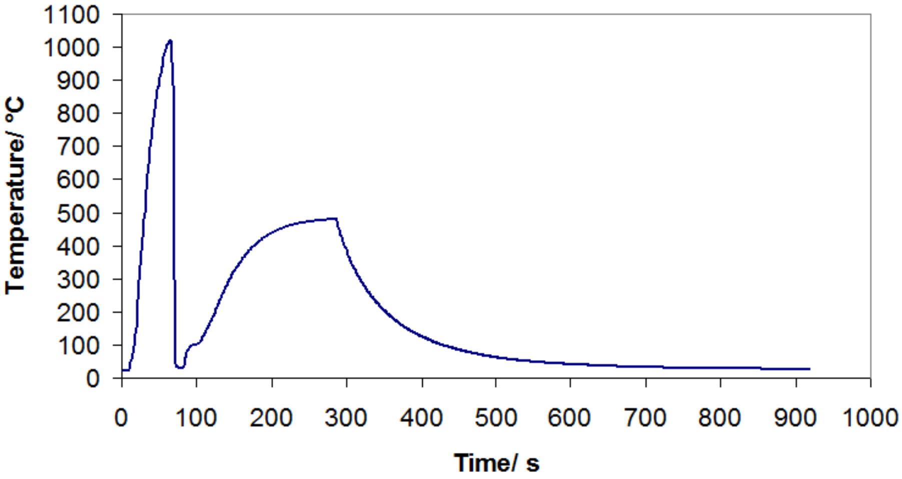

Figure 6.11: Thermal history of 'Treatment 3' on X65HIC as–welded sample.

After 'Treatment 3', the microstructure is clearly uniform across the weld. Fig. 6.12 shows the scanning electron micrographs obtained at the locations of the original weld junction and base metal. The microstructure contains fine plates of ferrite. The bright regions in the scanning electron micrographs are most likely to be fine carbides formed during the tempering.

Compared to the industrially heat-treated weld junction, the sample after 'Treatment 3' demonstrates a more uniform distribution of the crystal orientations as shown in Fig. 6.13. Pole figures generated from these data further prove this point, since the texture in the 'Treatment 3' sample is weaker than in the industrial sample (*cf.* Fig. 6.14abc and def). Indeed there is relatively little accumulation of cleavage planes ($\{100\}$) parallel to the fracture surface (normal to TD) in the sample after 'Treatment 3'. Grains possesing $\{100\}$ planes oriented within 10° to the fracture plane occupy only 6% of the scanned area compared to 10.3% in the industrial sample, Fig. 6.15.

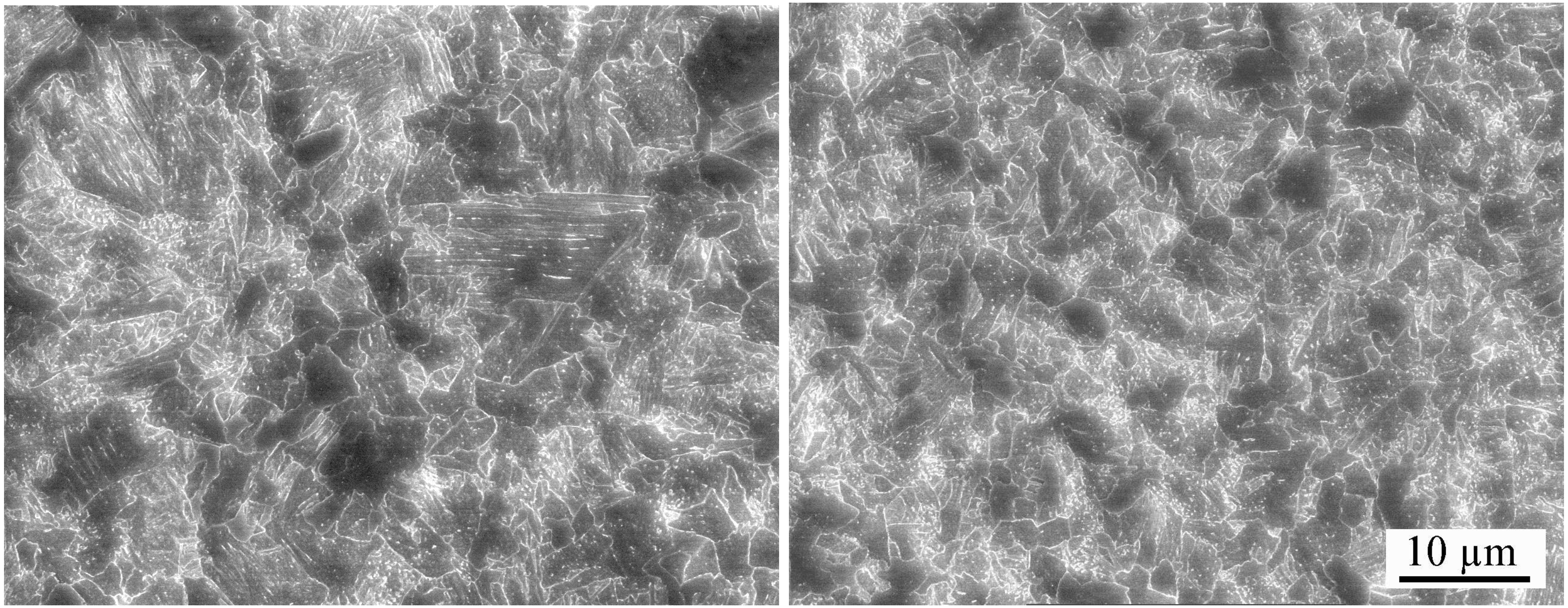

(a) Scanning electron microgragh taken at the location of original weld junction.

(b) Scanning electron microgragh taken at the location of original base metal.

Figure 6.12: Microstructure of the as–welded sample after 'Treatment 3' near the outer surface of the X65HIC pipe (*continued on next page*).

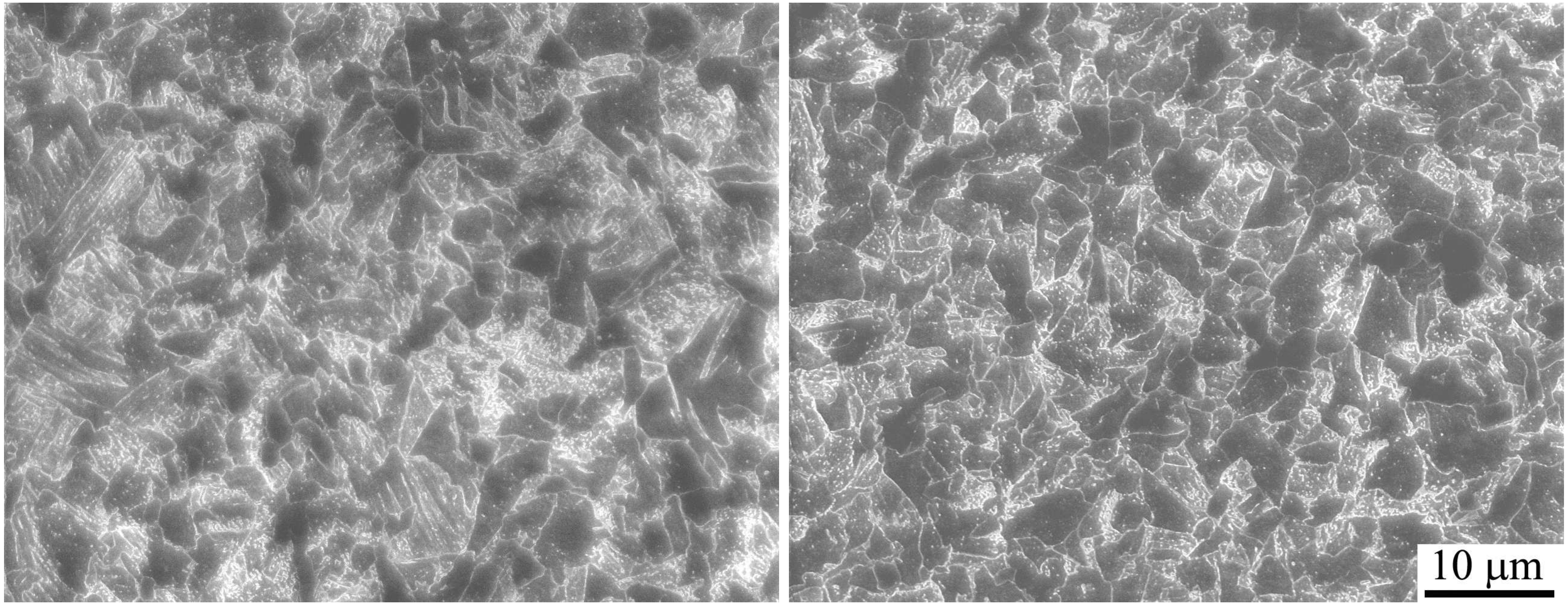

(c) Scanning electron micrograph taken at the location of original weld junction.

(d) Scanning electron micrograph taken at the location of original base metal.

Figure 6.12: Microstructure of the as–welded sample after ‘Treatment 3’ at mid-thickness of the X65HIC pipe (*continued on next page*).

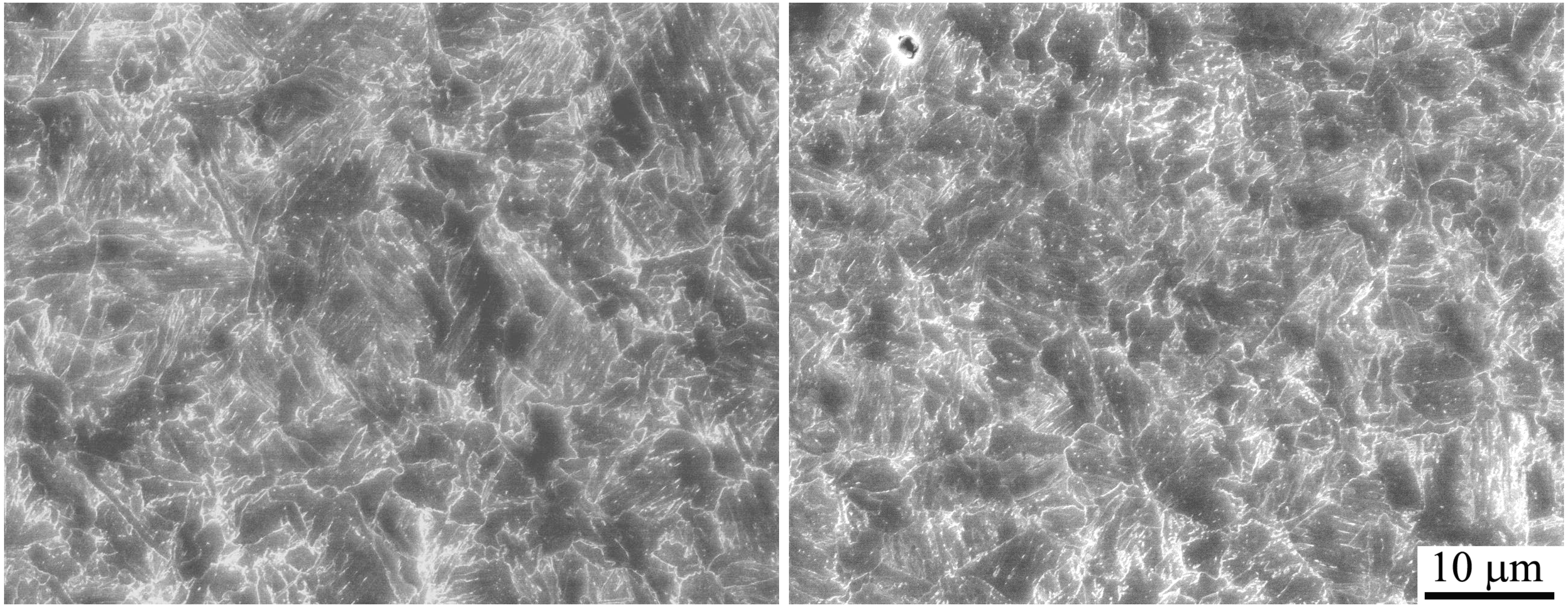

(e) Scanning electron micrograph taken at the location of original weld junction.

(f) Scanning electron micrograph taken at the location of original base metal.

Figure 6.12: Microstructure of the as–welded sample after ‘Treatment 3’ near the inner surface of the X65HIC pipe.

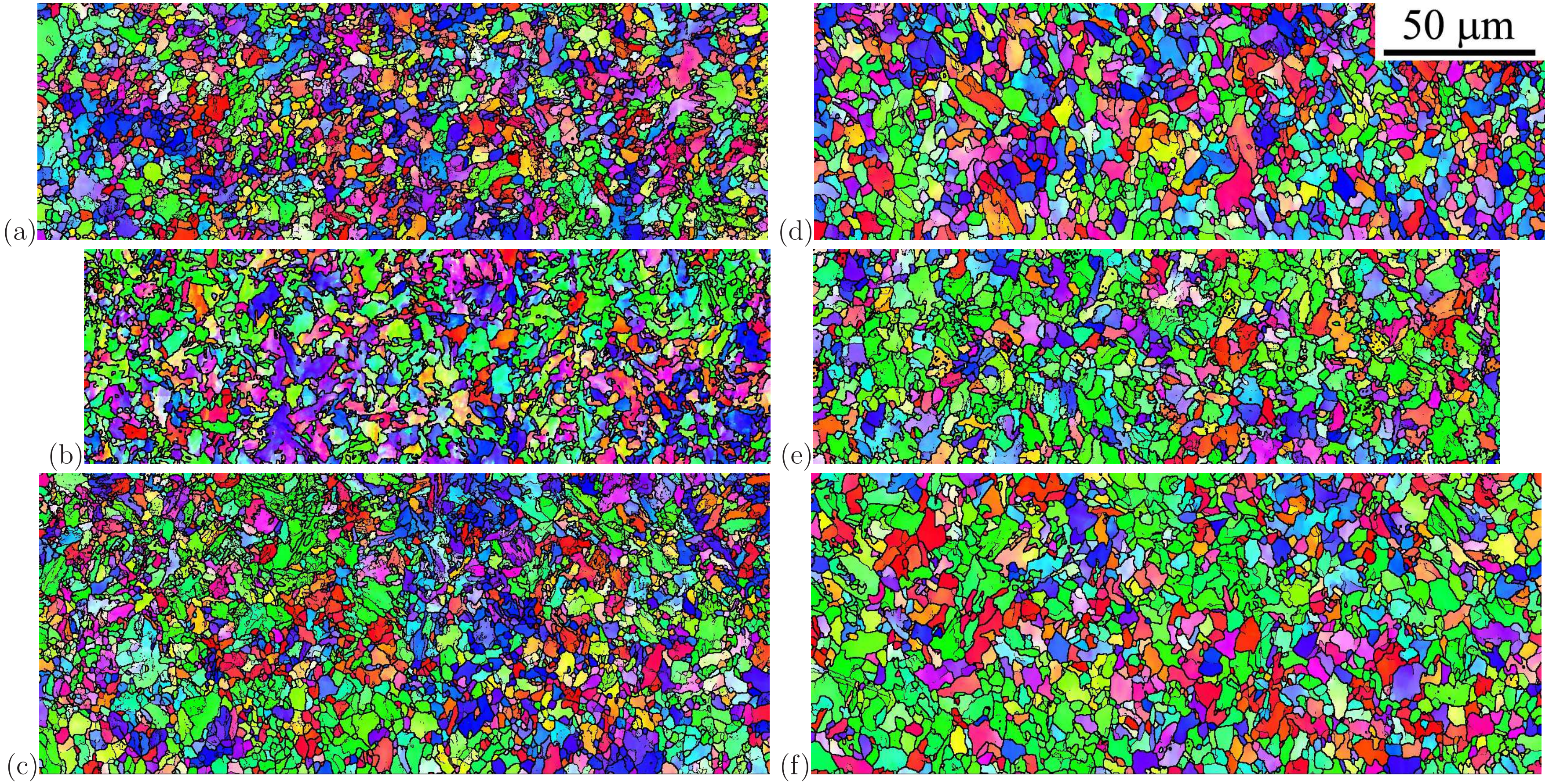

Figure 6.13: Ferrite orientation images of the weld junctions on the sample after 'Treatment 3' (a) near the outer surface, (b) at the mid-thickness and (c) near the inner surface of the X65HIC pipe; and on the sample after industrial post-welding heat treatment (d) near outer surface, (e) at mid-thickness and (f) near inner surface.

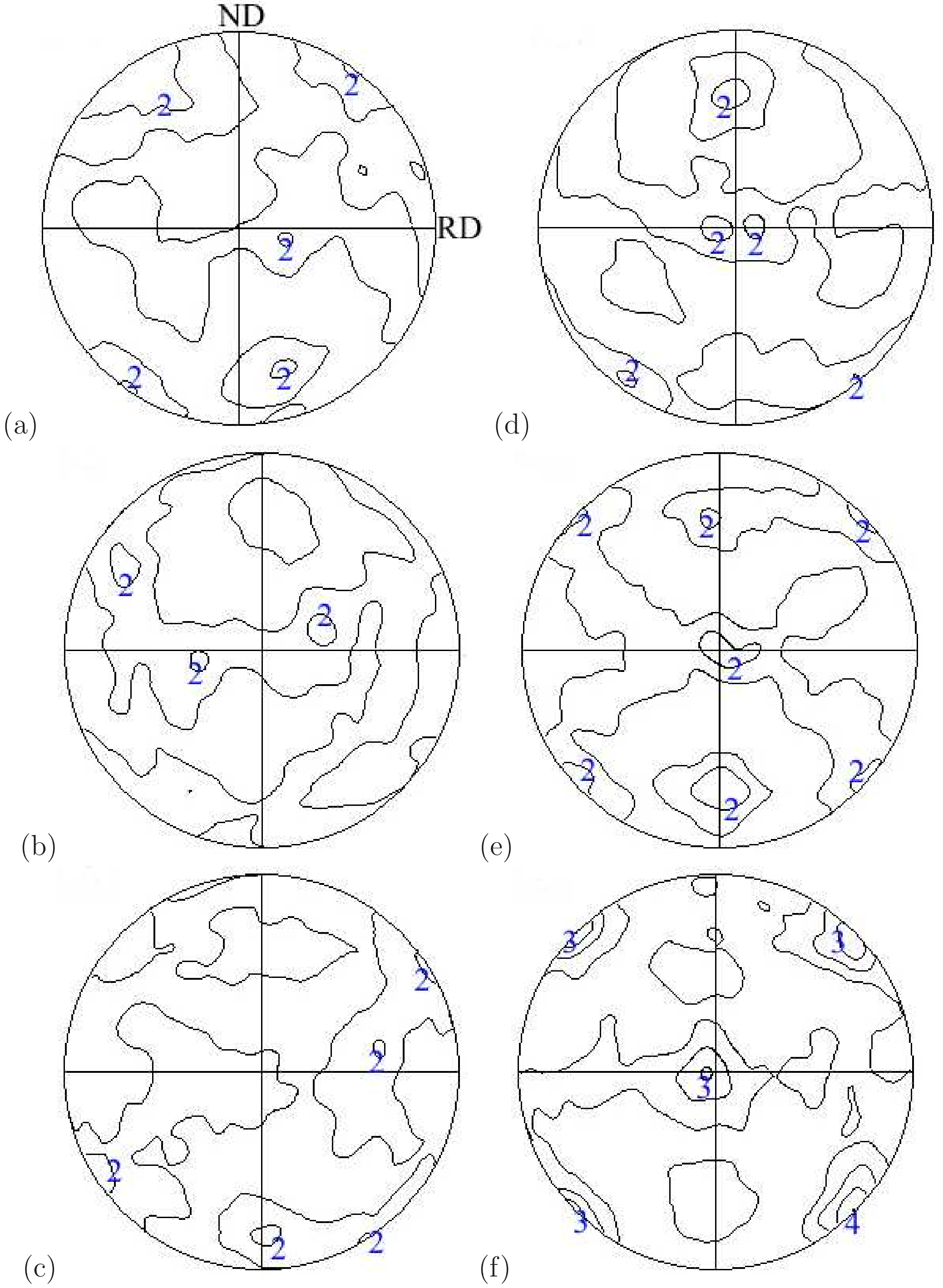

(a) (d) (b) (e) (c) (f)

Figure 6.14: {100} pole figures obtained from corresponding orientation images in Fig. 6.13.

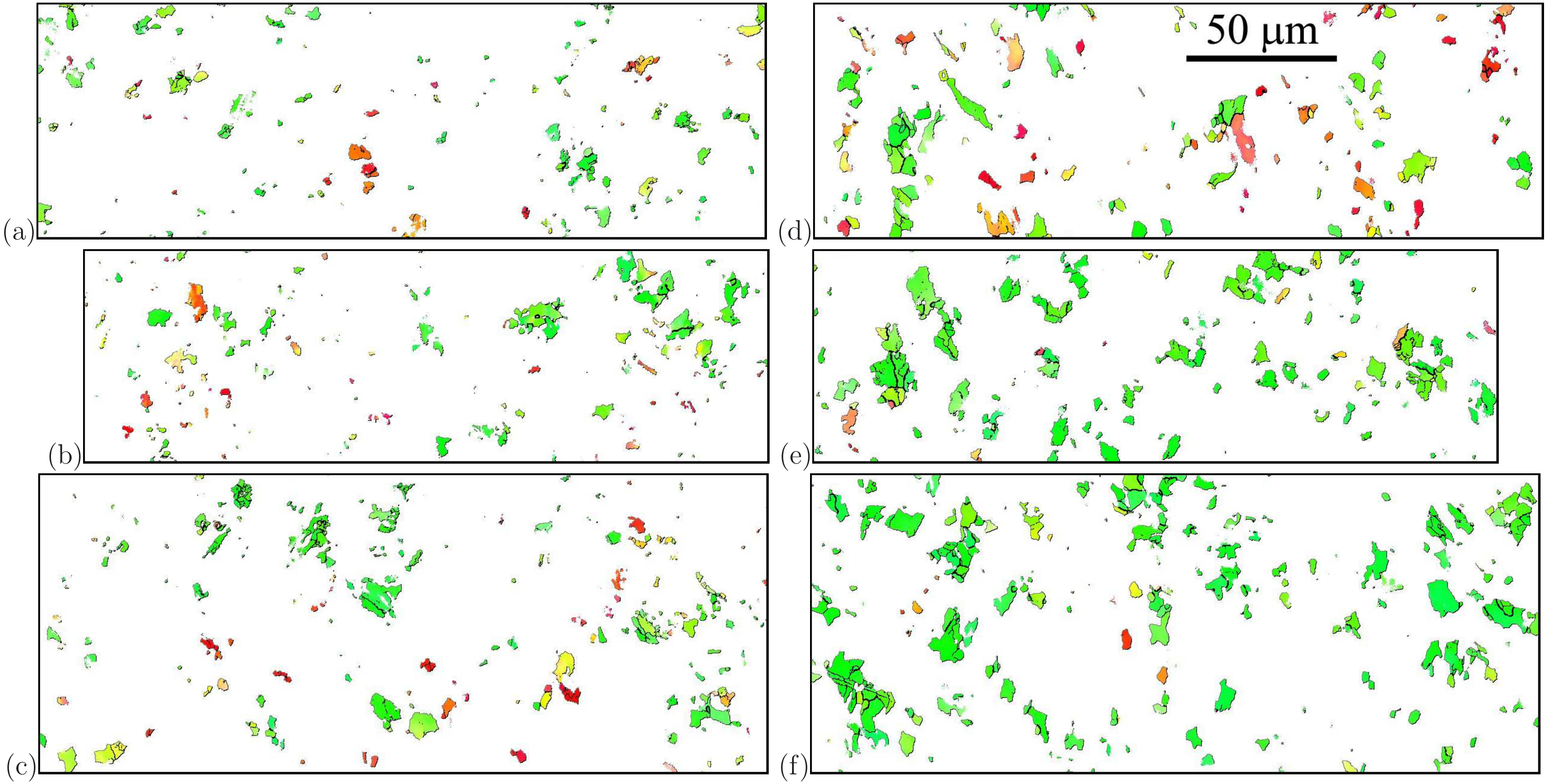

Figure 6.15: Grains owning {100} planes oriented within 10° to the ND–RD surface in the corresponding orientation images of Fig. 6.13.

All of this evidence supports the notion that 'Treatment 3' reduces the fracture-prone crystallographic texture on the weld junction which forms during welding process, and persists after the industrial post-welding heat treatment. Figures 6.13 and 6.15 also show that the morphological grain size of 'Treatment 3' sample is refined compared to the industrial sample as confirmed by the grain size analysis shown in Fig. 6.16. Finer grains are essential to improved toughness.

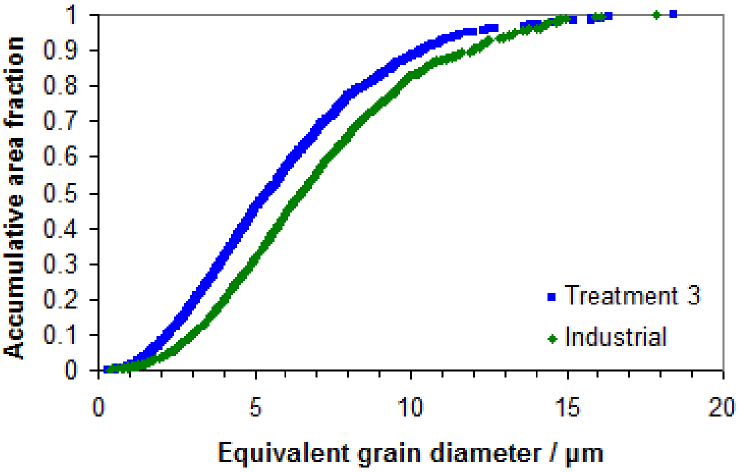

Figure 6.16: Grain size analysis based on the orientation images in Fig. 6.13 from Modified3 sample and industrially heat-treated sample respectively.

6.2 Welds from thin-walled X65 pipe

Heat treatments were carried out on as-welded samples from thin-walled X65 pipe in order to assess the relationship with toughness of the weld. The first comparison was made between single- and double-cycle post-welding heat treatments. Three pairs of simulations with and without the second cycle were carried out under the conditions shown in Table 6.1. All the samples were quenched at the end of the first cycle of the heat treatment but air cooled at the end of the second. The toughness of the simulated samples was measured with the Charpy V-notch located on the weld junction. Figure 6.17 shows that the second cycle of the post-welding heat treatment is absolutely essential to improve the toughness of the weld. After the first cycle of the heat treatment, the sample shows a microstructure (Fig. 6.18) similar to the X65HIC as-welded sample after its first cycle heat treatment (Fig. 6.5a and e), containing allotriomorphic ferrite and low-carbon martensite which may not be a desirable phase for satisfactory toughness. The hardness of the sample remains at the level of as-welded sample (∼260 HV), much higher than the industrially heat-treated sample (∼200 HV) as shown in Fig. 5.18a.

Table 6.1: Simulated post-welding heat treatments on as-welded samples from X65 pipe with 8.6 mm wall thickness. '-C' represents complete post-welding heat treatments and '-Q' represents heat treatments stopped after the first cycle.

Sample	1st cycle		2nd cycle	
	Peak temperature / °C	Holding time / s	Peak temperature / °C	Holding time / s
A-C	1054	12	922	12
A-Q	1054	12	–	–
B-C	1054	12	890	23
C-C	1054	12	922	23
D-C	1054	12	950	23
E-C	1150	12	922	23
E-Q	1150	12	–	–
F-C	1054	23	922	23
G-C	1054	27	922	38.4
G-Q	1054	27	–	–

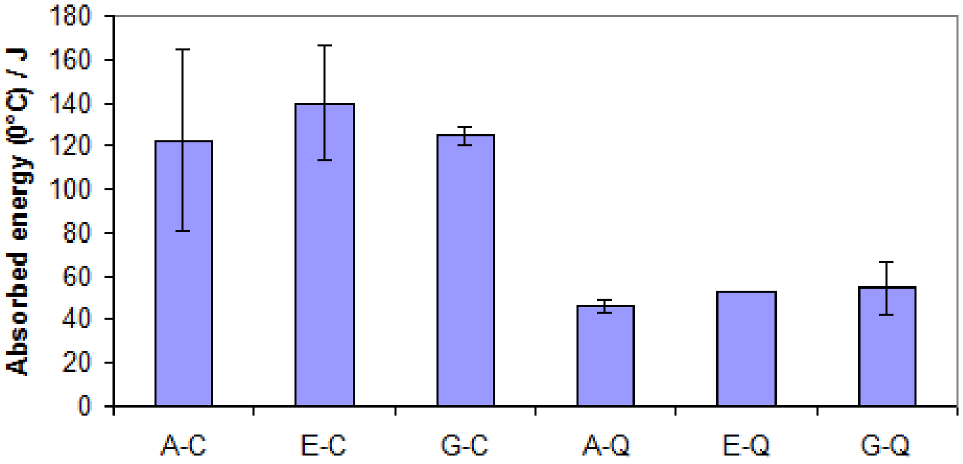

Figure 6.17: Difference in toughness of the simulated samples with double- or single-cycle heat treatments. The error bar represents two standard deviations of the Charpy impact tests results.

The next stage was to investigate a set of simulations with variation in the parameters of the first cycle of the post-welding heat treatment and

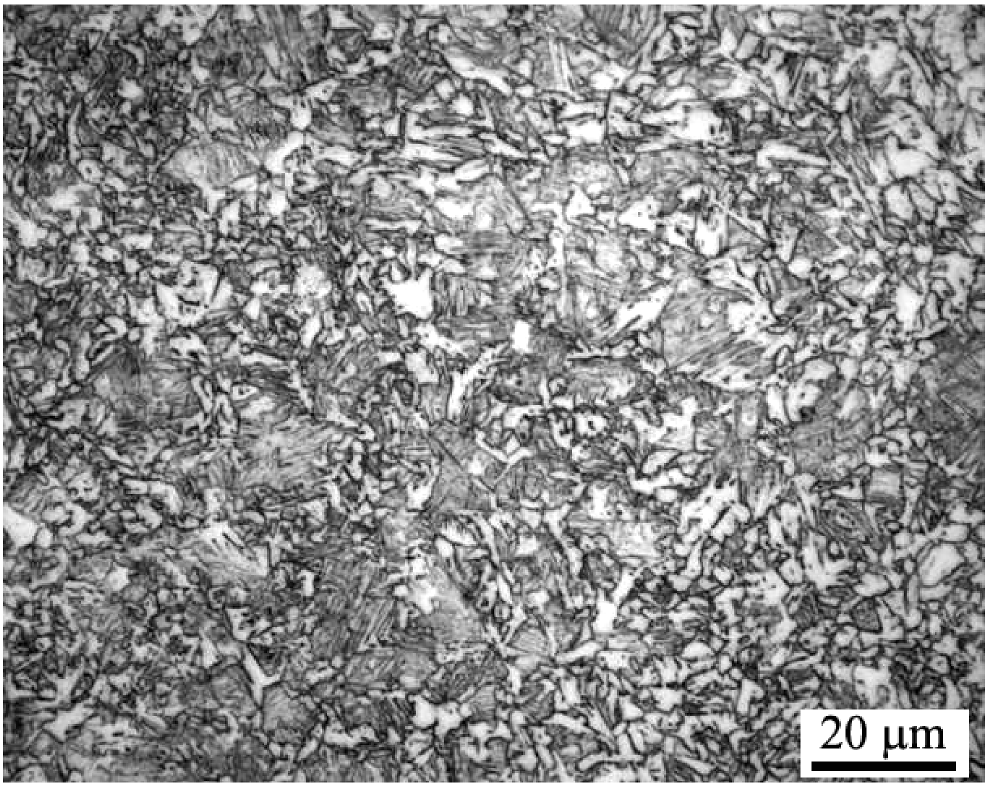

Figure 6.18: Optical micrograph of the weld junction on the simulated sample 'A-Q'. (This figure is taken at the ArcelorMittal Research and Development laboratory in Ghent.)

the same conditions for the second cycle (holding at the peak temperature of 922 °C for 23 s) as shown in Table 6.1. Figure 6.19 shows that the toughness of three samples does not vary significantly. Similarly, the samples after the same first cycle heat treatment, holding at the peak temperature of 1054 °C for 12 s as shown in Table 6.1, the toughness did not vary significantly with the different parameters of the second cycle, Fig. 6.20.

Charpy impact tests over a range of temperatures were carried out on sample 'C-C', whose thermal history is shown in Fig. 6.21, with impact toughness data compared with the industrially heat-treated sample in Fig. 6.22. The weld junction of sample 'C-C' demonstrated significantly higher absorbed energy in the low temperature range than the industrially heat-treated junction. The ultimate tensile strength is comparable for the two samples, although the hardness of the 'C-C' sample is slightly lower (Fig. 6.23).

Microstructure of the sample 'C-C' contains ferrite as the matrix and minor quantities of pearlite and austenite, which are shown in white, black and grey in the optical micrograph, Fig. 6.24a. The scanning electron micro-

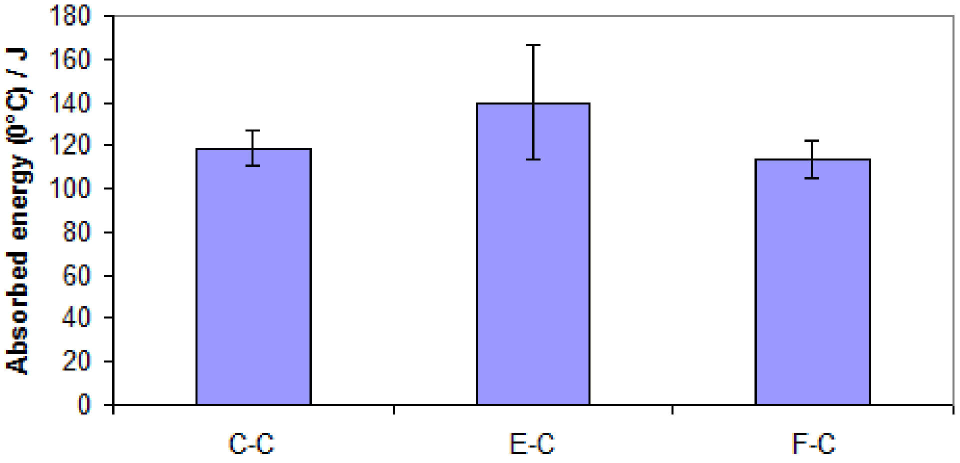

Figure 6.19: Variation in toughness of the simulated samples with different parameters of the first cycle of the heat treatment. The error bar represents two standard deviations of the Charpy impact tests results.

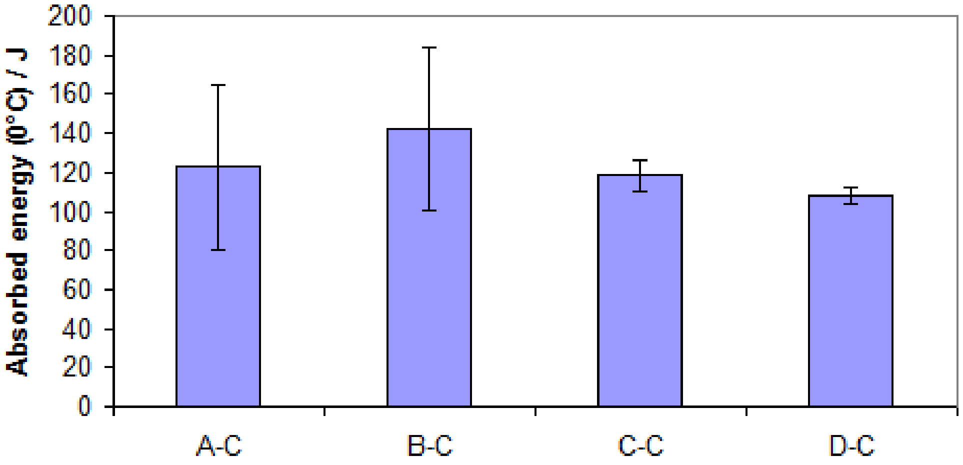

Figure 6.20: Variation in toughness of the simulated samples with different parameters of the second cycle of the heat treatment. The error bar represents two standard deviations of the Charpy impact tests results.

graph, Fig. 6.24b, clearly revealed that the pearlite started to form from some remaining austenite grains (white featureless). The existence of austenite is further confirmed by the X-ray diffraction pattern as shown in Fig. 6.25. It suggests that the cooling rate at the end of industrial post-welding heat treatment is slower than the one applied on sample ‘C-C’, because the industrially heat-treated sample does not contain any retain austenite, as confirmed in Fig. 5.13a. The austenite had enough time to transform into pearlite. This

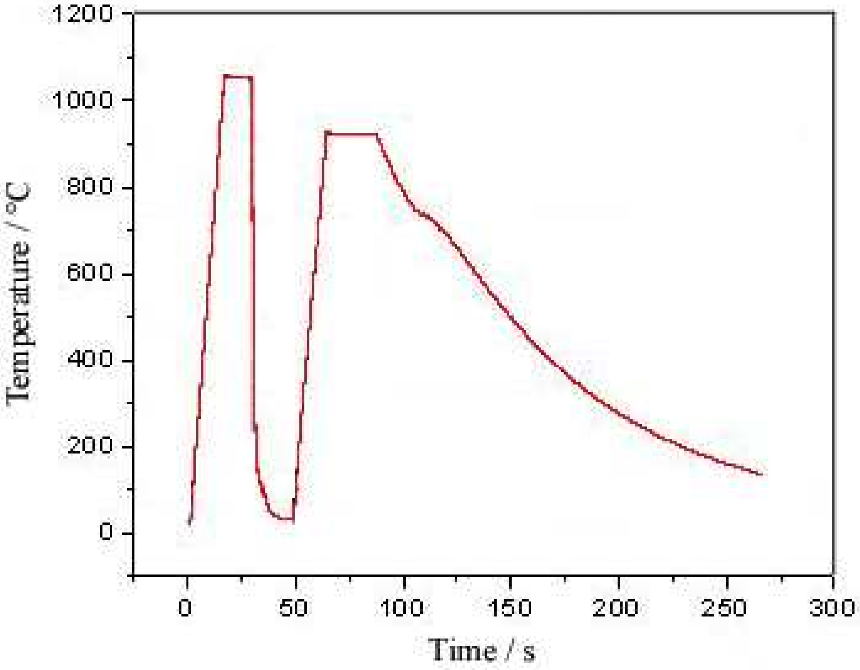

Figure 6.21: Thermal history of the simulated post-welding heat treatment on sample 'C-C'.

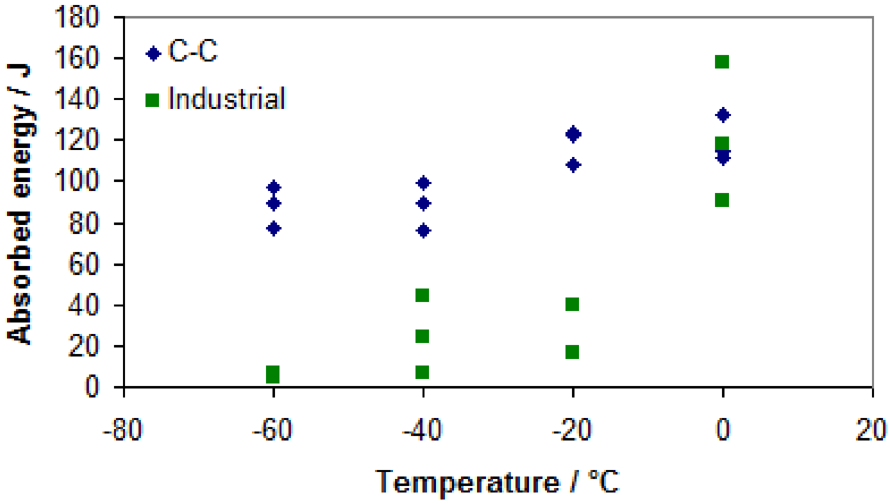

Figure 6.22: Results of Charpy impact tests on simulated sample 'C-C' and the industrially heat-treated sample from the X65 pipe with 8.6 mm wall-thickness.

trace amount of austenite in sample 'C-C' seems not to be detrimental to the toughness of the weld junction.

Crystallographic analysis using the EBSD technique was also carried

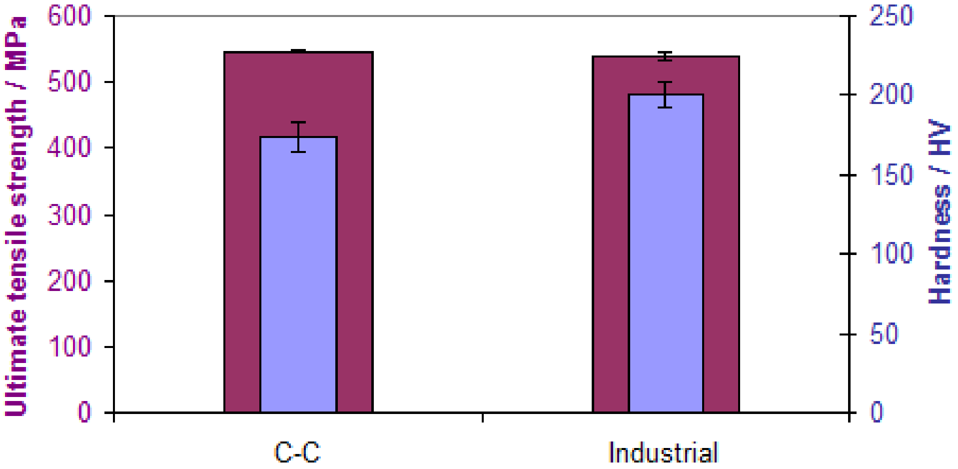

Figure 6.23: Results of cross-weld tensile and microhardness tests on the simulated sample 'C-C' and the industrially heat-treated sample from the X65 pipe with 8.6 mm wall-thickness. Three tensile tests were carried out and the value of hardness was obtained from 10 indents on each sample.

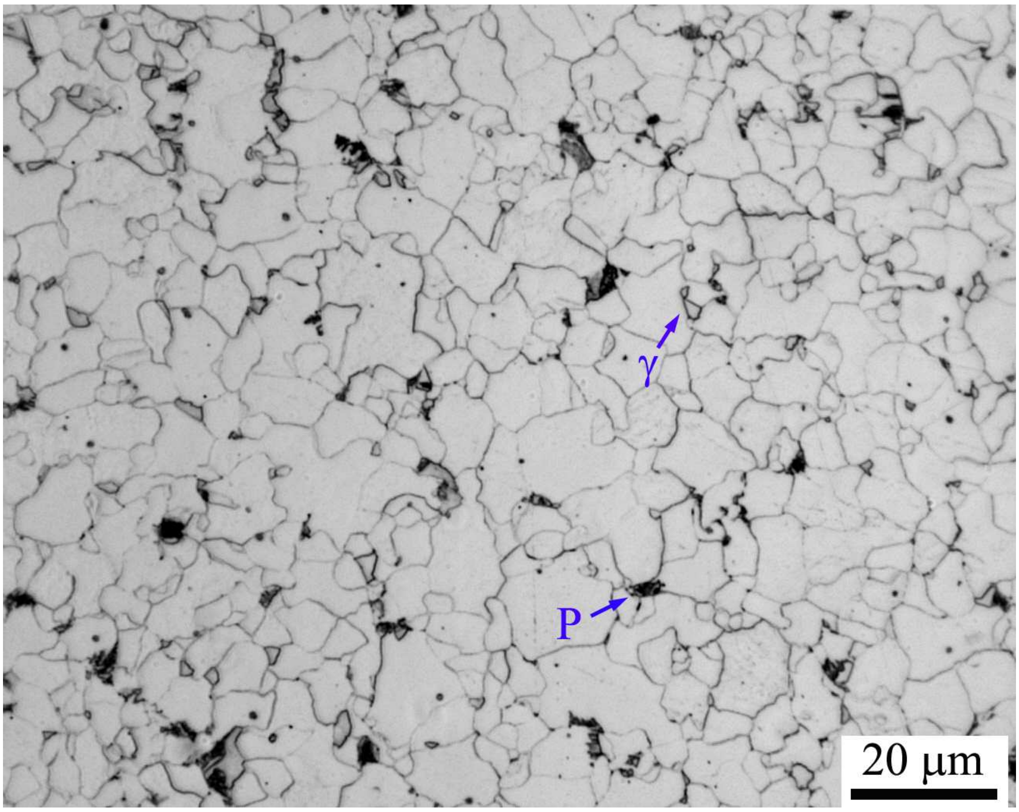

(a) Optical micrograph.

Figure 6.24: Microstructure of the weld junction on sample 'C-C'. 'P' and 'γ' represent the examples of pearlite and austenite (*continued on next page*).

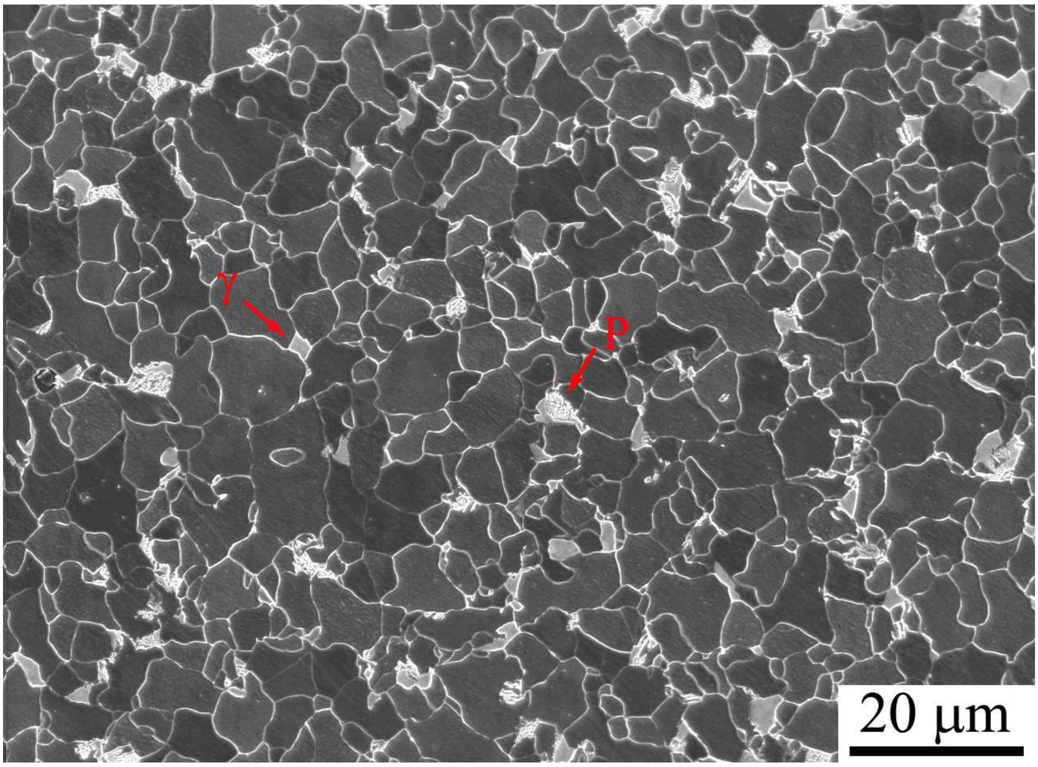

(b) Scanning electron micrograph.

Figure 6.24: Microstructure of the weld junction on sample ‘C-C’. ‘P’ and ‘γ’ represent the examples of pearlite and austenite.

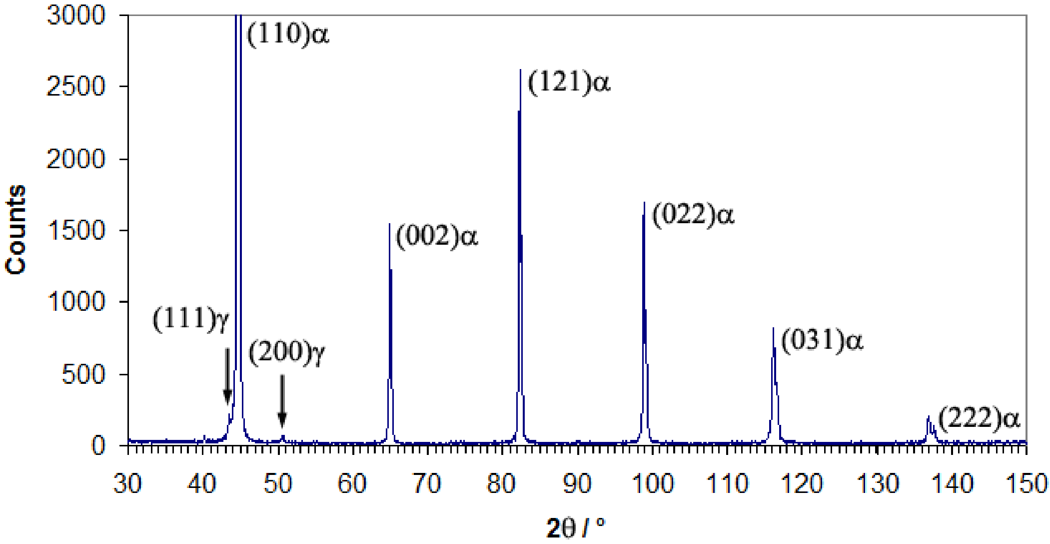

Figure 6.25: X-ray diffraction pattern obtained on the simulated sample ‘C-C’.

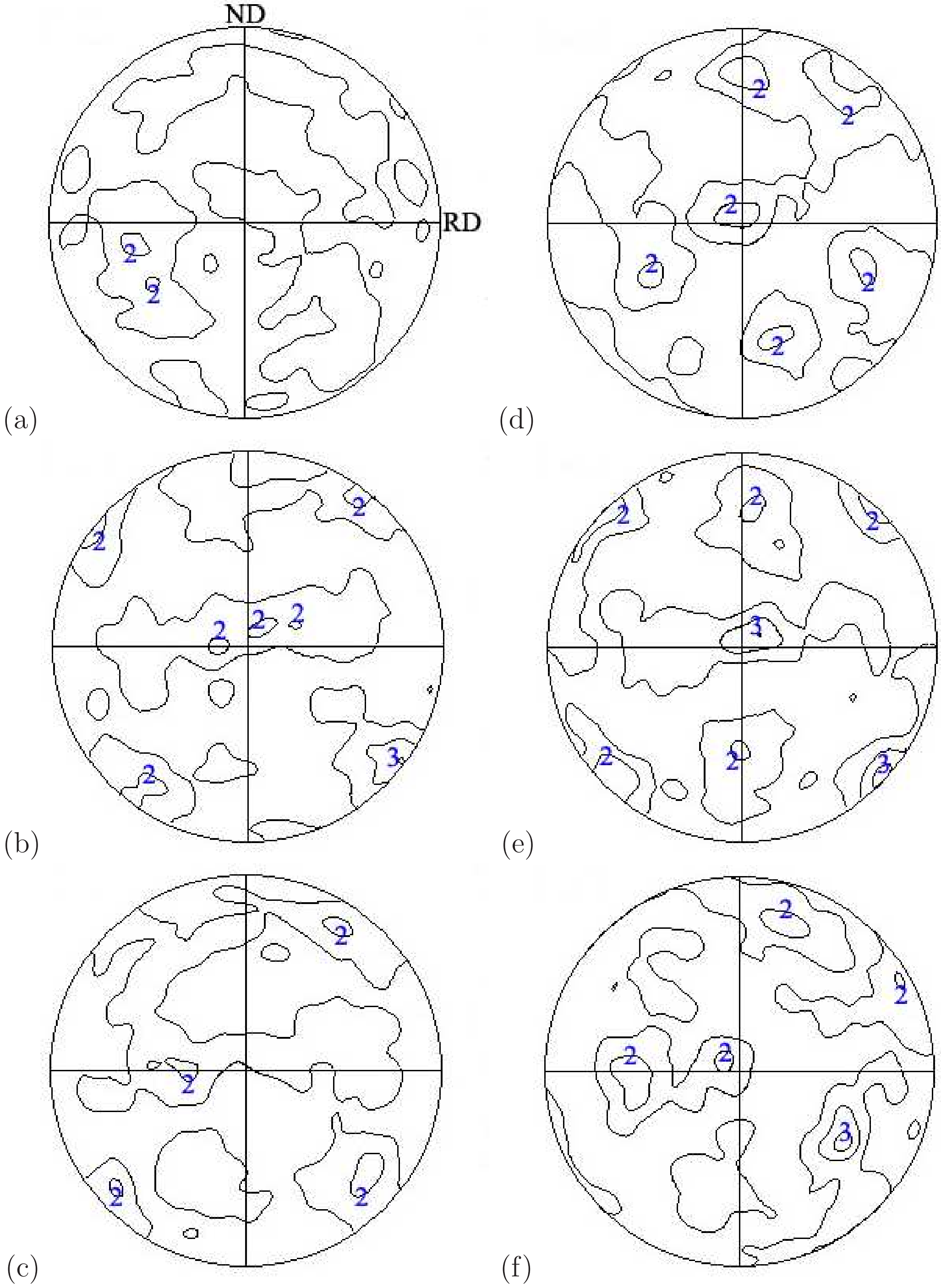

(a) (b) (c) (d) (e) (f)

Figure 6.26: Ferrite {100} pole figures generated from scanned areas by EBSD technique with the same size on the weld junctions of sample 'C-C' (a) near the outer surface, (b) at the mid-thickness and (c) near the inner surface of the X65 pipe with 8.6 mm wall thickness; and on the sample after industrial post-welding heat treatment (d) near outer surface, (e) at mid-thickness and (f) near inner surface.

out on the sample ‘C-C’. Comparison of the ferrite {100} pole figures obtained from the areas with same size on the weld junctions of both sample ‘C-C’ and the industrially heat-treated sample at three pipe thicknesses is shown in Fig. 6.26. The crystal orientations are more uniformly distributed on the weld junction of ‘C-C’ sample and there is obviously a lower density of {100} poles normal to the ND–RD fracture surface compared to the industrially heat-treated sample. Grains possessing {100} planes oriented within 10° to the ND–RD surface occupy 5% of the scanned area on the weld junction of the ‘C-C’ sample; in comparison this number rises to 8.7% of the scanned area with same size on the weld junction of the sample after industrial heat treatment. These results are consistent with the higher toughness of the ‘C-C’ weld junction than the industrially heat-treated one. Furthermore, the weld junction of the former sample has finer grains as shown in Fig. 6.27, which leads to better toughness.

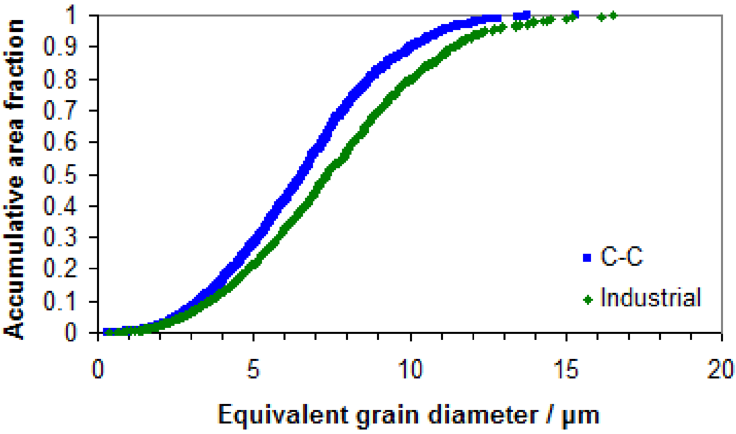

Figure 6.27: Grain size analysis carried out on the areas with the same size on the weld junctions of the simulated sample ‘C-C’ and industrially heat-treated sample from the thin-walled X65 pipe.

6.3 Conclusions

For the welds from X65HIC grade of steel, an approximate simulation of the high frequency induction welding has been carried out using a thermomechanical simulator. Although a microstructure identical to the commercial weld was not obtained, the experiment suggests that the cooling rate after welding in the production line might be lower than the one used in the simulation, which is $20\,^{\circ}\mathrm{C\ s^{-1}}$; because bainitic ferrite, if it is confirmed in the simulated microstructure, results from faster cooling than that which gives Widmanstätten ferrite in the as-welded sample.

Simulations of the first cycle of the post-welding heat treatment were carried out on both X65HIC and thin-walled X65 welds in a chamber furnace and a Gleeble simulator respectively. Both simulated samples showed a microstructure consisting of allotriomorphic ferrite and a plate-like structure which is most likely to be low-carbon martensite or bainite, and is not a desirable microstructure for satisfactory toughness property of the weld; so the second cycle of the heat treatment was proven to be useful in improving toughness.

Modified post-welding heat treatment could not give a sufficient intercritical annealing by setting the peak temperature of first cycle at 830 °C, since the A_{c1} was raised well above A_{e1} by placing the as-welded sample into the furnace with the preset temperature. Intercritical annealing at 890 °C and tempering on the weld from X65HIC pipe did not remove crystallographically coarse grains. The lack of method to predict the temperature at which the acicular austenite starts to coalesce and the shortage of as-welded sample laid big obstacles to pursue more intercritical annealing experiments. Austenisation at a higher temperature than in the industrial process, followed by similar quenching and tempering, resulted in a much better structure and crystallography. This may be because the austenite memory effect was removed. The resulting crystallographic orientations are more uniformly distributed and should make fracture more difficult.

Variation in the parameters (peak temperature and holding time for both cycles) of the post-welding heat treatment in a range, did not significantly affect the upper shelf energy of the weld junction from the thin-walled X65 pipe. However one selected sample that was cooled possibly faster at the end of the simulation than the industrially heat-treated sample, achieved higher lower shelf energy at the weld junction. It is evident that uniformly distributed crystal orientations and smaller grain sizes lead to improved toughness.

Chapter 7

General Conclusions and Proposed Future Research

The work presented in this thesis had the primary goal of resolving an observation that the toughness at the induction welded junction is poor in spite of sophisticated heat treatments. Two varieties of X65 pipeline steel have been studied, one designed to resist hydrogen induced cracking. After much investigation of factors associated with inclusions or decarburisation, it was discovered that the problem is associated with the formation of pernicious coarse "crystallographic grains" which do not adequately resist fracture. It is believed that this texture, which manifests itself as the clustering of similarly oriented grains, is produced during the welding process and is regenerated upon subsequent heat treatment involving rapid heating and cooling due to an austenite memory effect which has previously been reported in the published literature.

Attempts were made therefore to modify the post-welding heat treatment aimed at the removal of this 'memory'. Simulation using austenisation at higher temperature than the industrial process succeeded in producing a weld junction containing a more uniformly distributed set of crystallographic orientations and at the same time, finer crystallographic and morphological grain sizes. This new treatment can in principle be adopted in production, but steel availability restricted validation in the full scale production facility. This constitutes future work in the event that X65HIC pipe is ordered by customers. However such a trial should be preceded by detailed mechanical characterisation on a laboratory scale. The improvement of toughness on the weld junction through a simple change of the processing parameter has the potential to enormously affect the pipeline-making industry.

When it comes to the normal X65 pipes which are less pure, manufactured by the same technique, inclusions become an issue. The weld junctions of two pipes with different wall-thicknesses were found to develop openings at the locations of embedded inclusions during bend tests. Nevertheless, the inclusions are infrequently located at the positions of poorest toughness and hence are deemed to be of secondary consequence. Similar to the welds from X65HIC pipe, the toughness of the weld junction after post-welding heat treatment is significantly lower than that of the base metal. Crystallographic analysis showed cleavage-prone texture persistent throughout the process, which adversely affects toughness, more so than the inclusions which are occasionally present along the rolling direction of the pipe.

The frequency of inclusions can be reduced by expelling more material from the weld junction during the induction welding process. Most of the inclusions are manganese and silicon oxides which form due to oxidation on the surfaces of the abutting edges of the steel plate during the welding process. Employing more force onto the pressure rolls or a redesign of the layout in the welding mill is recommended to eject the material uniformly along the rolling/welding direction. Both methods need systematic calculations using actual data obtained on the production line.

More carefully designed post-welding heat treatment should be able to modify the crystallographic texture in the weld junction. The present work has shed light on how to achieve this. More studies are proposed to identify any difference between the industrial process and the laboratory simulations, e.g., the effect of cooling rate at the end of heat treatment on the toughness of the weld junction.

In practice, the X65HIC pipe is heat-treated using an austenisation and then a tempering cycle. The X65 pipes on the other hand are given double austenisation cycles. The initial trial of austenisation followed by tempering at °C on the thin-walled X65 pipe showed a decrease in toughness compared to the one that had been austenised twice, but the reason is not understood. Further research should be carried out on the post-welding heat treatment involving austenisation plus tempering by either experimental or computational simulations, because the X65HIC pipe following this route gave satisfactory mechanical properties and it will build up on the understanding of the "heat treatment—microstucture—mechanical properties" relation. Assuming that double austenisation does give better ughness, the weld from X65HIC pipe should be tested using this approach in the hope of enhancing toughness.

Post-welding heat treatment using high frequency induction is a complex process involving numerous variables, e.g., the chemical compositions of the material, detailed thermal treatment and parameters associated with the induction process. It is feasible that appropriate industrial data can be accumulated in the long term to enable them to be subjected to a Bayesian neural network analysis [135, 136] in order to recognise patterns within these complex phenomenon. If such data are not likely to become available, they should be collected through simulations such as those described in this thesis. The current work seems to have made a good start in this respect.

Appendix A

Additional supporting evidence for Welds from X65 Pipes

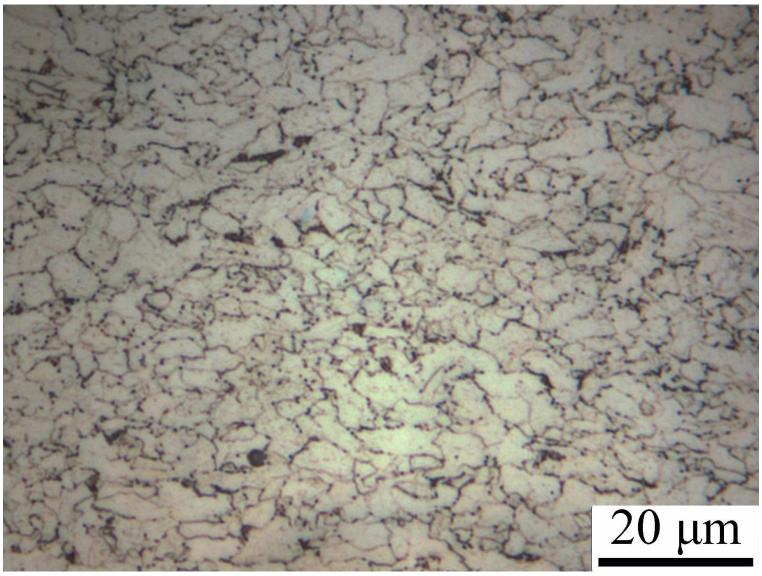

(a) Base metal.

Figure A.1: Microstructure of the weld from the as-welded X65 pipe with 14.8 mm wall-thickness (*continued on next page*).

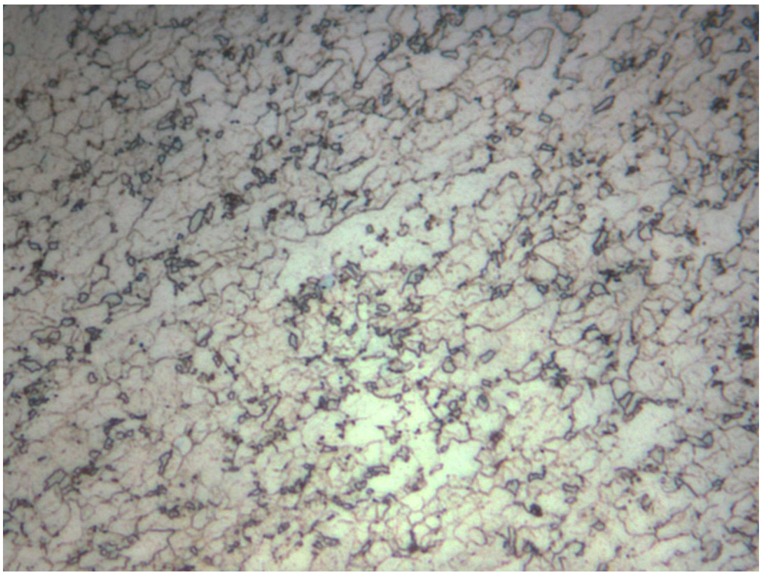

(b) Thermomechanically-affected zone.

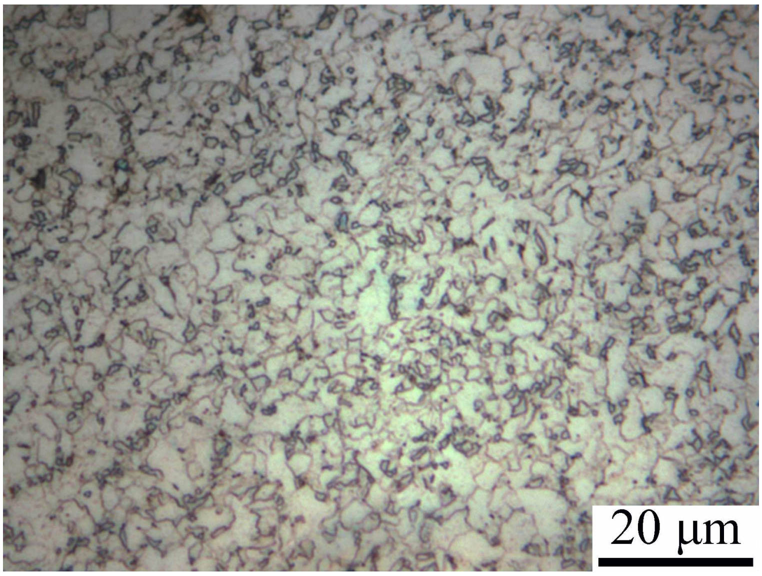

(c) Heat-affected zone.

Figure A.1: Microstructure of the weld from the as-welded X65 pipe with 14.8 mm wall-thickness (*continued on next page*).

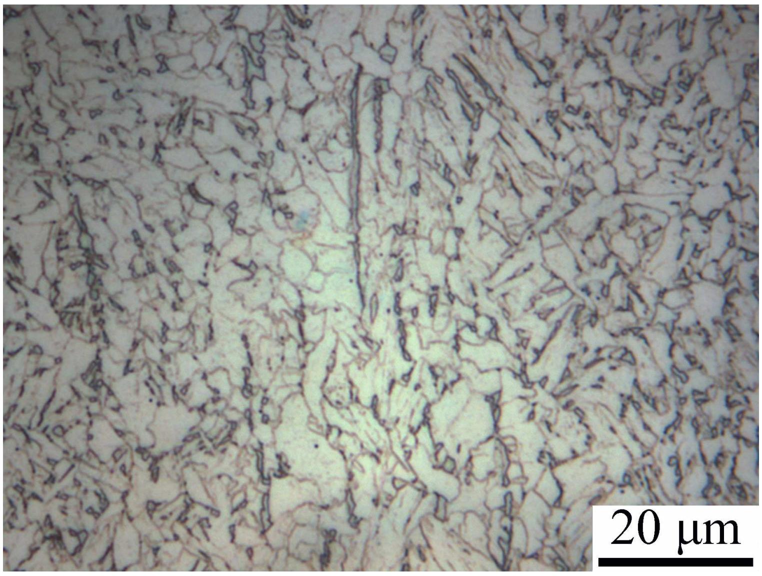

(d) Weld junction.

Figure A.1: Microstructure of the weld from the as-welded X65 pipe with 14.8 mm wall-thickness.

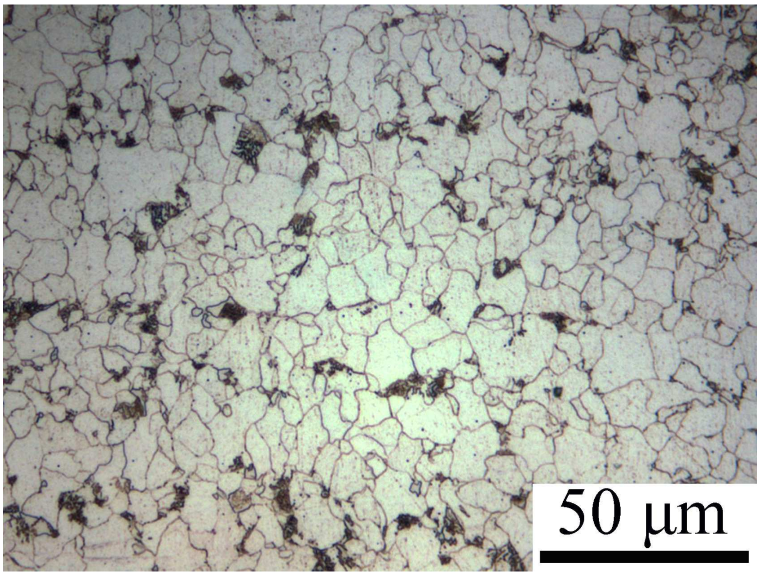

(a) Adjacent to the weld junction.

Figure A.2: Microstructure of the heat-treated weld from X65 pipe with 14.8 mm wall-thickness (*continued on next page*).

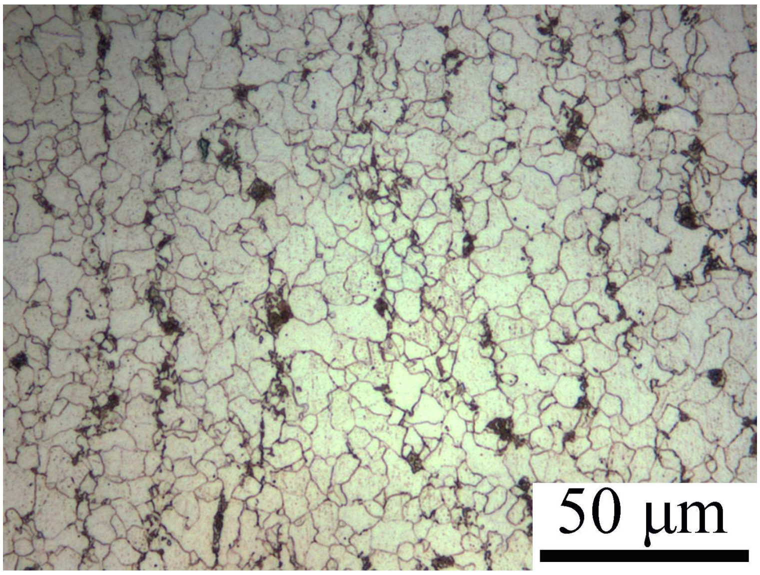

(b) On the weld junction.

Figure A.2: Microstructure of the heat-treated weld from X65 pipe with 14.8 mm wall-thickness.

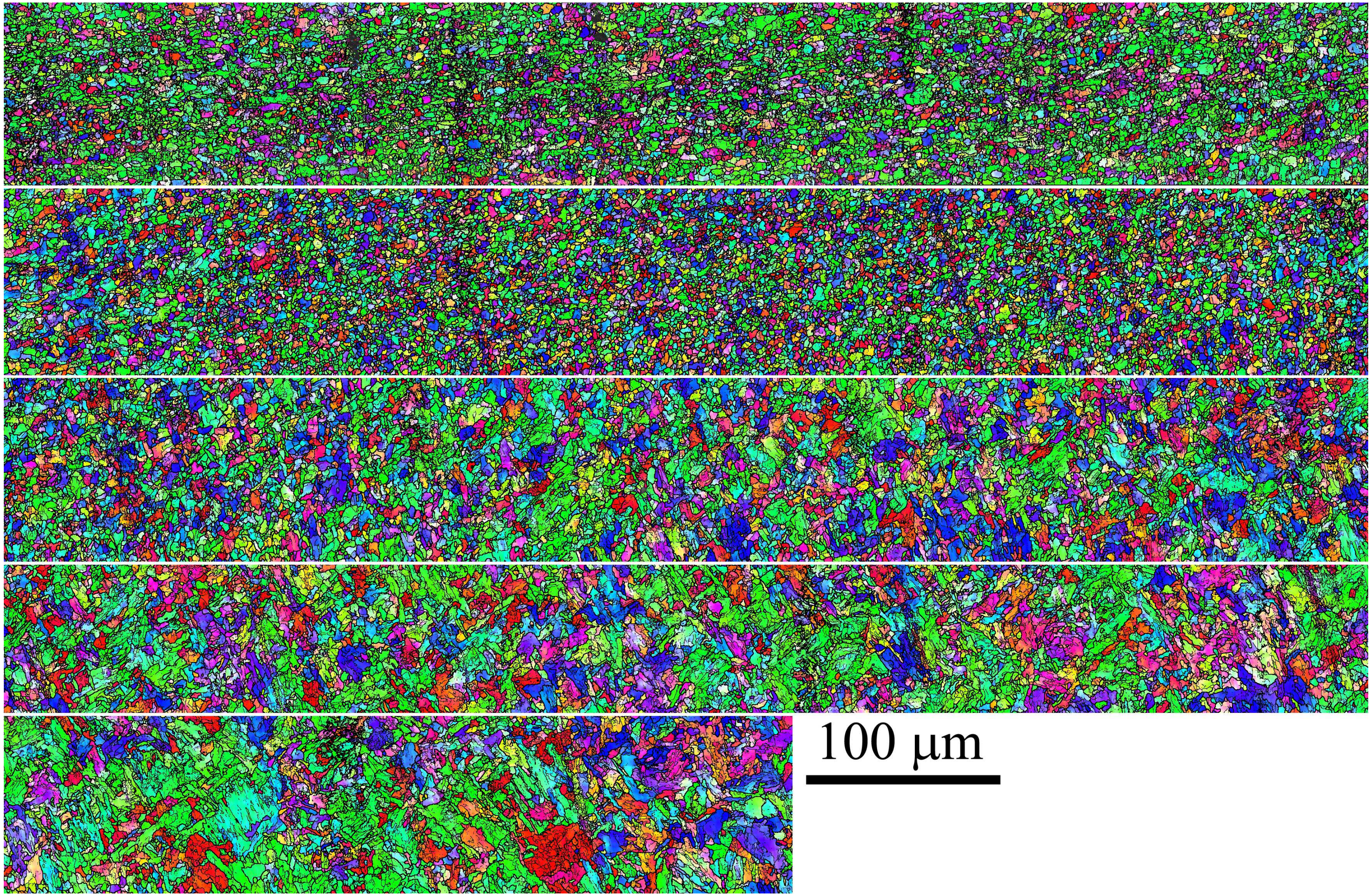

(a) Near the outer surface.

Figure A.3: Ferrite orientation image of the as-welded sample from X65 pipe with 8.6 mm wall-thickness. The image is continuous from the base metal at the top left to the middle of the weld junction at the bottom right (*continued on next page*).

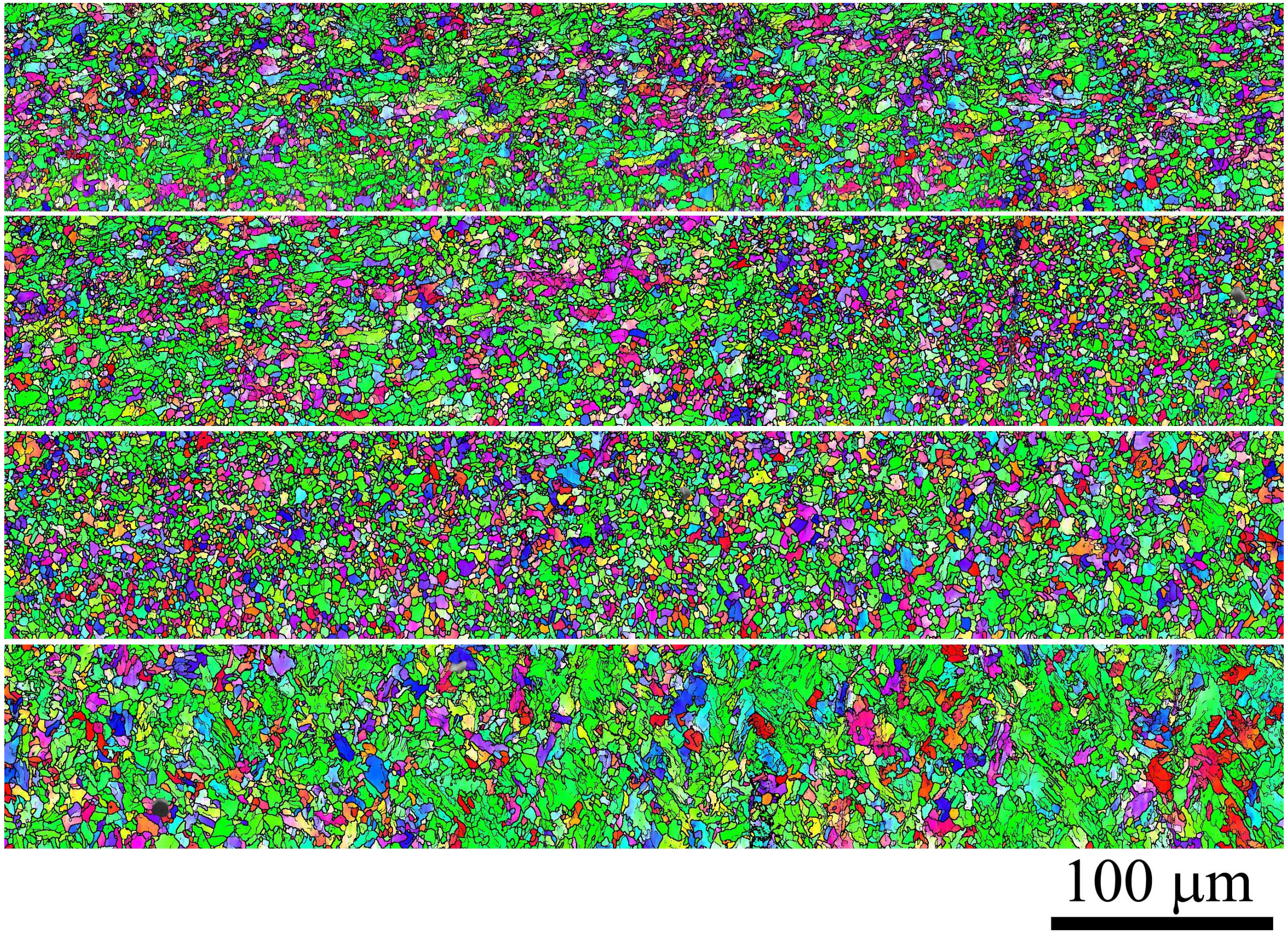

(b) At mid-thickness.

Figure A.3: Ferrite orientation image of the as-welded sample from X65 pipe with 8.6 mm wall-thickness. The image is continuous from the base metal at the top left to the middle of the weld junction at the bottom right (*continued on next page*).

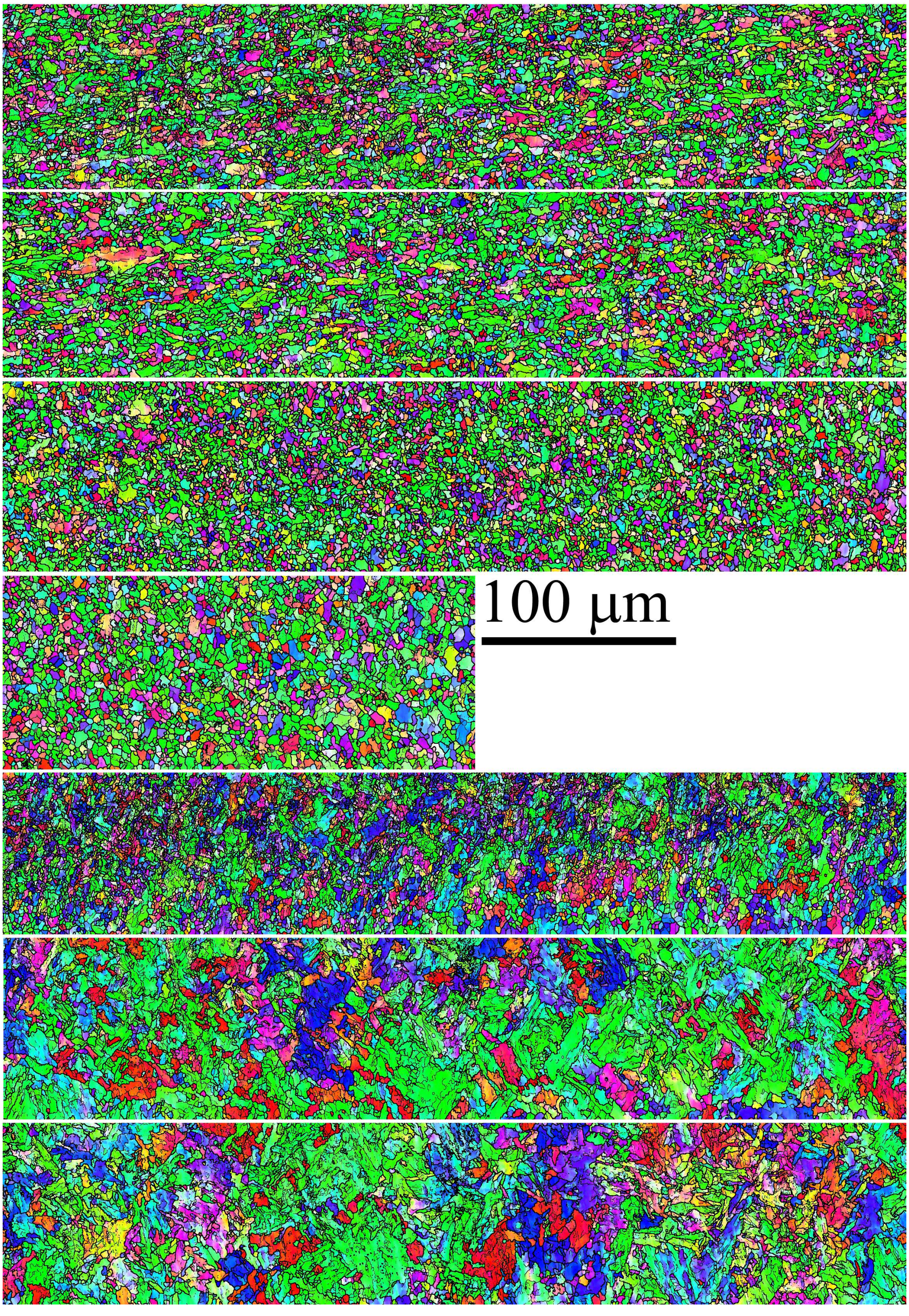

(c) Near inner surface.

Figure A.3: Ferrite orientation image of the as-welded sample from X65 pipe with 8.6 mm wall-thickness. The image is continuous from the base metal at the top left to the middle of the weld junction at the bottom right.

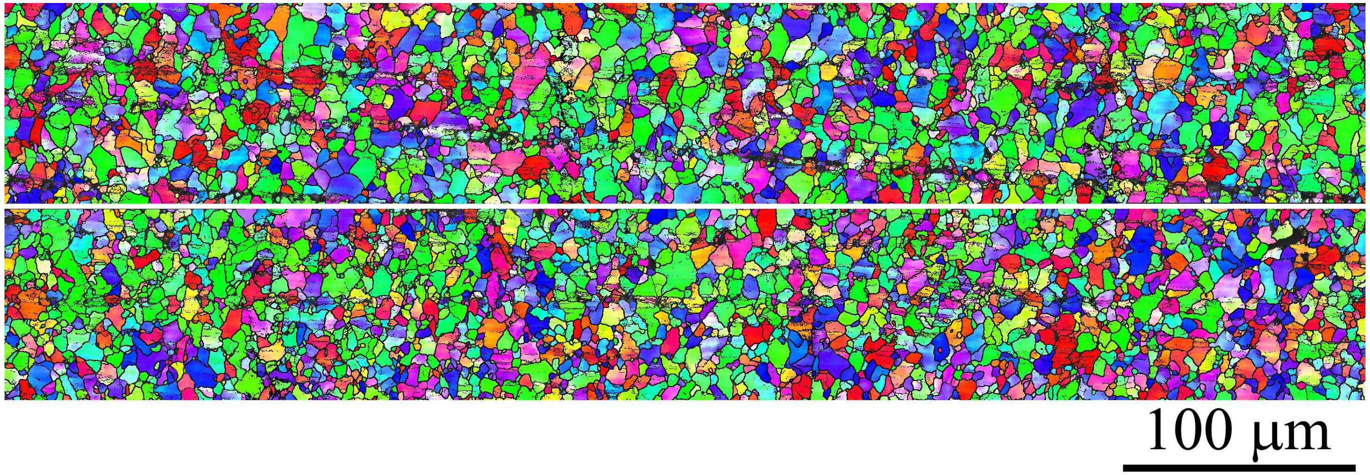

(a) Near the outer surface.

Figure A.4: Continuous ferrite orientation image from the 1 mm left towards the middle of the weld junction on the sample after post-welding heat treatment from X65 pipe with 8.6 mm wall-thickness (*continued on next page*).

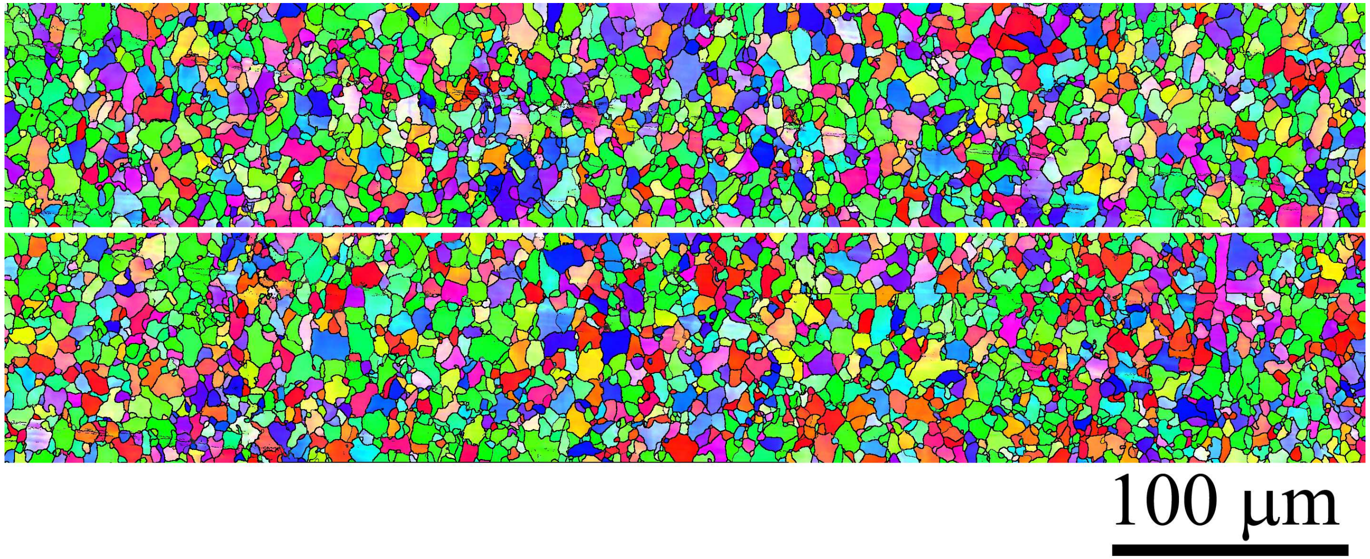

(b) At mid-thickness.

Figure A.4: Continuous ferrite orientation image from the 1 mm left towards the middle of the weld junction on the sample after post-welding heat treatment from X65 pipe with 8.6 mm wall-thickness (*continued on next page*).

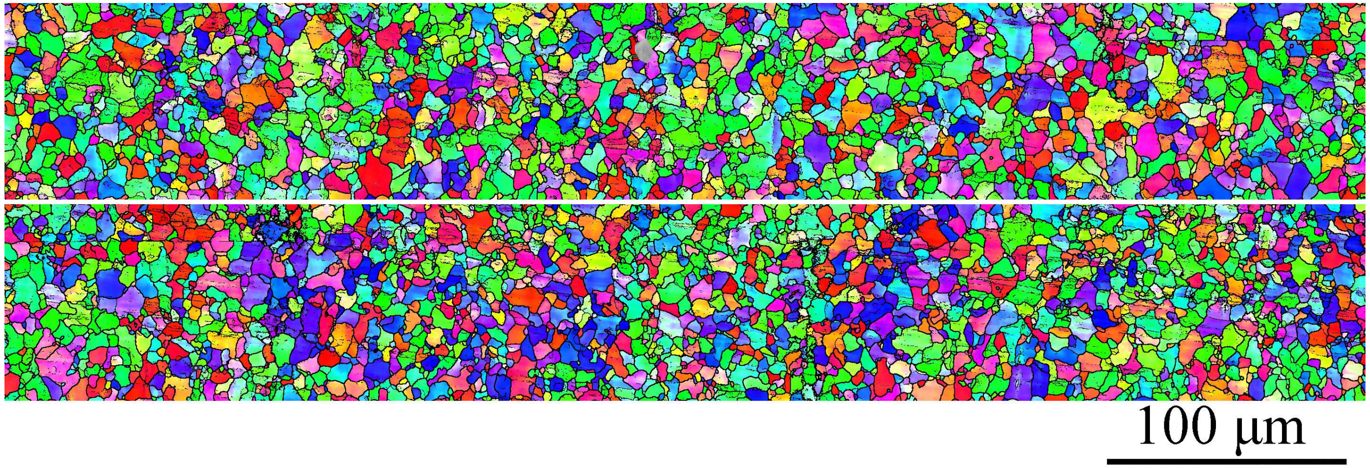

(c) Near inner surface.

Figure A.4: Continuous ferrite orientation image from the 1 mm left towards the middle of the weld junction on the sample after post-welding heat treatment from X65 pipe with 8.6 mm wall-thickness.

Bibliography

[1] K. D. Houghton. *Journal of Offshore Technology*, 3(2):46–48, 1995.

[2] J. Grosse-Wördemann and S. Dittrich. Circumferential welding of high–tensile line pipe steels under severe weather conditions (trans-Alaska pipeline and north sea projects). In A. B. Rothwell and J. M. Gray, editors, *Welding of HSLA (microalloyed) structural steels*, Materials/Metalworking Technology, pages 750–771. American Society for Metals, Ohio, 1978.

[3] J. G. Williams, C. R. Killmore, F. J. Barbaro, A. Meta, and L. Fletcher. In *Microalloying '95 Conference Proceedings*, pages 117–138. Iron and Steel Society, 1995.

[4] C. Yu. *Tube International*, pages 153–155, March 1996.

[5] E. Treiss. *3R International*, 20(11):627–630, 1981.

[6] R. R. Preston. A review of high strength, low alloy steel metallurgy in Europe. In A. B. Rothwell and J. M. Gray, editors, *Welding of HSLA(microalloyed) structural steels*, Materials/Metalworking Technology, pages 24–25. American Society for Metals, Ohio, 1978.

[7] E. Runte. *The Brown Boveri Review*, 55(3):113–118, 1968.

[8] W. H. Kearns, editor. *High Frequency Welding*, volume 3. American Welding Society, Florida, USA, 7th. edition, 1980.

[9] S. Ramo, J. R. Whinnery, and V. Duzer. *Fields and Waves in Communication Electronics.* John Wiley & Sons, 1984.

[10] L. F. Warren. *Tube International*, pages 184–186, May/June 2001.

[11] P. F. Scott and W. Smith. *Tube International*, pages 147–152, March 1996.

[12] Ö. E. Güngör, P. Yan, P. Thibaux, M. Liebeherr, H. K. D. H. Bhadeshia, and D. Quidort. In *Proceedings of the 8th international pipeline conference*, number IPC2010-31372, Calgary, Alberta, Canada, 27th Sep.–1st Oct. 2010.

[13] E. Yokoyama, A. Ejima, S. Watanabe, Y. Yoshimoto, and Y. Hirano. Effects of welding conditions and Mn/Si ratio on the penetrator defect occurrence in ERW high manganese line pipe. Technical report, Kawasaki Steel Corporation, September 1979.

[14] J. H. Choi, Y. S. Chang, C. M. Kim, J. S. Oh, and Y. S. Kim. *Welding Journal*, 83(1):27s–31s, 2004.

[15] M. D. Chapetti, J. L. Otegui, and J. Motylickl. *Int. Journal of Fatigue*, 24(1):21–28, 2002.

[16] J. F. Kiefner. In *API's 51st Annual Pipeline Conference & Cybernetics Symp.*, pages 1–13, New Orleans, LA, 2000. American Petroleum Institute.

[17] G. R. Yoder, T. W. Crooker, and L. A. Cooly. *Journal of Eng. Mat. and Tech.*, 101(1):86–90, 1979.

[18] H. Suzuki and A. J. McEvily. *Metall. Trans. A*, 10A(4):475–481, 1979.

[19] C. M. Kim, J. K. Kim, and C. S. Kim. *Key Engineering Materials*, 297–300:3–9, 2005.

[20] M. Beller and E. Holden. *Pipes & Pipeline International*, 46(6):26–34, 2001.

[21] N. Pradhan, N. Banerjee, B. B. Reddy, S. K. Sahay, D. S. Basu, P. K. Bhor, S. Das, and S. Bhattyacharya. *Scandinavian J. of Metall.*, 34(4):232–240, 2005.

[22] I. V. Zakharova, E. A. Chichkarev, V. G. Vasiliev, A. I. Trotsan, A. Ya. Dejneka, and O. S. Kiryukhin. *The Paton Welding Journal*, pages 14–17, August 2001.

[23] R. W. K. Honeycombe and H. K. D. H. Bhadeshia. *Steel.* Edward Arnold, London, 2nd edition, 1995.

[24] K. Easterling. *Introduction to the Physical Metallurgy of Welding*. Butterworth-Heinemann, 2nd edition, 1992.

[25] *Guide to the Welding and Weldability of C-Mn Steels and C-Mn Microalloyed Steels*. Publication Document IIS/IIW-382-71. International Institute of Welding, 1971.

[26] J. G. Williams, C. R. Killmore, F. J. Barbaro, J. Piper, and Fletcher. *Mater. Forum*, 20:13–28, 1996.

[27] M. C. Zhao, K. Yang, and Y. Shan. *Materials Science and Engineering A*, 335(1–2):14–20, 2002.

[28] A. Bakkaloğlu. *Materials Letters*, 56(3):263–272, 2002.

[29] J. Q. Wang, A. Atrens, D. R. Cousens, and N. Kinaev. *J. Mater. Sci.*, 34(8):1721–1728, 1999.

[30] M. Militzer, R. Pandi, and E.B. Hawbolt. *Metall. Trans. A*, 27A(6):1547–1556, 1996.

[31] R. G. Kamat, E. B. Hawbolt, L. C. Brown, and J. K. Brimacombe. *Metall. Trans. A*, 23A(9):2469–2480, 1992.

[32] R. A. Vandermeer. *Acta Metall. Mater.*, 38(12):2461–2470, 1990.

[33] J. R. Bradley and H. I. Aaronson. *Metall. Trans. A*, 12A(10):1729–1741, 1981.

[34] S. P. Gupta. *Steel Res.*, 64(12):623–629, 1993.

[35] M. Avrami. *J. Chem. Phys.*, 7(12):1103–1112, 1939.

[36] E. B. Hawbolt, B. Chau, and J. K. Brimacombe. *Metall. Trans. A*, 14A(9):1803–1815, 1983.

[37] P. C. Campbell, E. B. Hawbolt, and J. K. Brimacombe. *Metall. Trans. A*, 22A(11):2779–2790, 1991.

[38] I. Tamura. *Trans. ISIJ*, 27(10):763–779, 1987.

[39] M. Enomoto and H. I. Aaronson. *Metall. Trans. A*, 17A(8):1381–1384, 1986.

[40] M. Enomoto and H. I. Aaronson. *Metall. Trans. A*, 17A(8):1385–1397, 1986.

[41] M. Enomoto, W. F. Lange III, and H. I. Aaronson. *Metall. Trans. A*, 17A(8):1399–1407, 1986.

[42] W. F. Lange III, M. Enomoto, and H. I. Aaronson. *Metall. Trans. A*, 19A(3):427–440, 1988.

[43] T. Gladman. *The physical metallurgy of micralloyed steels*. Maney, London, 2002.

[44] J. Bauer, P. Flüss, E. Amoris, and V. Schwinn. *Ironmaking and Steelmaking*, 32(4):325–330, 2005.

[45] J. D. Verhoeven. *J. Mater. Eng. Performance*, 9(3):286–296, 2000.

[46] R. Grossterlinden, R. Kawalla, U. Lotter, and H. Pircher. *Steel Res.*, 63(8):331–336, 1992.

[47] E. R. Johnson and W. J. Buechling. *Trans. ASM*, pages 249–256, March 1934.

[48] A. S. Bor. *ISIJ Int.*, 31(12):1445–1446, 1991.

[49] W. C. Lyons and G. J. Plisga. *Standard handbook of petroleum and natural gas engineering*. Gulf Professional Publishing, 2nd edition, 2005.

[50] Carbon and low-alloy steels. In *ASM Handbook*, volume 1, Properties and Selection: Irons, Steels and High Performance Alloys. ASM International, 2002.

[51] G. Domizzi, G. Anteri, and J. Ovejero-García. *Corrosion Sci.*, 43(2):325–339, 2001.

[52] Y. Nakaj, H. Kurahashi, T. Emi, and O. Haida. Development of steels resistant to hydrogen induced cracking in wet hydrogen sulfide environment. Technical report, Kawasaki Steel Corporation, September 1980.

[53] S. Kyriakides and E. Corona. *Mechanics of offshore pipelines*, volume 1. Buckling and collapse. Elsevier, Oxford, UK, 1st edition, 2007.

[54] SAE J310: high strength low alloy steel. In *SAE Handbook*, volume 1, Materials. Society of Automotive Engineers, 1989.

[55] Fracture toughness and fracture mechanics. In *ASM Handbook*, volume 8: mechanical testing and evaluation. ASM International, 2002.

[56] A. H. Cottrell. *Trans. TMS-AIME*, pages 192–203, April 1958.

[57] N. J. Petch. *Fracture.* Wiley, New York, 1959.

[58] N. S. Stoloff. *Fracture*, volume VI: fracture of metals, chapter 1: effects of alloying on fracture Characteristics. Academic Press, New York, 1969.

[59] D. Lonsdale and P. E. J. Flewitt. *Metall. Trans. A*, 9A(11):1619–1623, 1978.

[60] P. Brozzo, G. Buzzichelli, A. Mascanzoni, and M. Mirabile. *Metal Science*, pages 123–129, April 1977.

[61] A. F. Gourgues, H. M. Flower, and T. C. Lindley. *Mater. Sci. Technol.*, 16(1):26–40, 2000.

[62] J. R. Yang, C. Y. Huang, C. F. Huang, and J. H. Aoh. *J. Mater. Sci. Lett.*, 12(16):1290–1293, 1993.

[63] E. Bouyne, H. M. Flower, T. C. Lindley, and A. Pineau. *Scripta Mater.*, 39(3):295–300, 1998.

[64] F. B. Pickering. In *Proc. Symp. Transformation and hardenability in steels*, pages 109–129, Ann Harnor, MI, 1967. Climax Molybdenum Co. and the University of Michigan.

[65] M. C. Kim, Y. J. Oh, and J. H. Young. *Scripta Mater.*, 43(3):205–211, 2000.

[66] D. Bhattacharjee, J. F. Knott, and C .L. Davis. *Metall. Mater. Trans. A*, 35A(1):121–130, 2004.

[67] D. E. McRobie and J. F. Knott. *Mater. Sci. Technol.*, 1(5):357–365, 1985.

[68] D. Franҫois and A. Pineau. *From Charpy to present impact testing.* Elsevier, 2002.

[69] F. B. Pickering. In R. W. Cahn, P. Haasen, and E. J. Kramer, editors, *Materials Science and Technology*, volume 7: constitution and properties of steels. VCH, 1992.

[70] A. A. Griffith. *Philos. Trans. R. Soc. A*, pages 163–198, 1921.

[71] J. H. Tweed and J. F. Knott. *Metal Science*, 17(2):45–54, 1983.

[72] Ø. Grong, A. O. Kluken, and B. Bjørnbakk. *Joining and Materials*, 1:164–169, 1988.

[73] R. Kiessling. *Non-metallic inclusions in steel, Part V.* The Institute of Metals, London, 1989.

[74] V. M. Radhakrishnan. *Welding technology and design.* New Age International, 2007.

[75] Ø. Grong and A. O. Kluken. *Key Engineering Materials*, 69–70:21–46, 1992.

[76] C. L. Davis and J. E. King. *Mater. Sci. Technol.*, 9(1):8–15, 1993.

[77] F. Matsuda, Y. Fukada, H. Okada, C. Shiga, K. Ikeuchi, Y. Horii, T. Shiwaku, and S. Suzuki. *Welding in the World*, 37(3):134–154, 1996.

[78] K. J. Irvine and F. B. Pickering. *J. Iron Steel Inst.*, pages 518–531, June 1963.

[79] T. Gladman, B. Holmes, and I. D. McIvor. In *Effect of Second-Phase Particles on the Mechanical Properties of Steel*, pages 68–78. The Iron and Steel Institute, 1971.

[80] B. Mintz, W. B. Morrison, and A. Jones. *Metals Technology*, pages 252–260, July 1979.

[81] G. E. Dieter. *Mechanical Metallurgy.* McGraw–Hill, UK, 1988.

[82] B. L. Bramfitt and A. R. Marder. *Processing and Properties of Low Carbon Steel.* AIME, New York, 1973.

[83] G. F. Melloy and J. D. Dennison. In *The Microstructure and Design of Alloys*, pages 60–64, Cambridge, England, 1973. The Institute of Metals and The Iron and Steel Institute.

[84] R. L. Plaut. PhD thesis, Sheffield University, UK, 1974.

[85] W. B. Morrison. In *Controlled Processing of HSLA Steels*. Sheffiled: British Steel Corperation, 1976.

[86] W. R. Tyson, R. A. Ayres, and D. F. Stein. *Acta Metallurgica*, 21(5):621–627, 1973.

[87] V. M. Goritskii and D. P. Khromov. *Problemy Prochnosti*, pages 81–82, June 1984.

[88] G. J. Baczynski, J. J. Jonas, and L. E. Collins. *Metall. Mater. Trans. A*, 30A(12):3045–3054, 1999.

[89] J. W. Christian. *Metall. Trans. A*, 14A(7):1237–1256, 1983.

[90] J. Ju, J. Lee, and J. Jang. *Materials Letters*, 61(29):5178–5180, 2007.

[91] H. Yu. *Journal of University of Science and Technology Beijing, Mineral, Metallurgy, Material*, 15(6):683–687, 2008.

[92] R. Rittmann and K. Freier. In *Niobium Science and Technology: Proc. International Symp. Niobium 2001*, Orlando, Florida, USA.

[93] D. A. Hughes and N. Hansen. *Acta Metallurgica*, 45(9):3871–3886, 1997.

[94] S. Mironov, Y. S. Sato, and H. Kokawa. *Acta Materialia*, 56(11):2602–2614, 2008.

[95] S. Li, I. J. Beyerlein, and M. A. M. Bourke. *Materials Science and Engineering A*, 394(1–2):66–77, 2005.

[96] S. Kundu. PhD thesis, University of Cambridge, 2007.

[97] S. T. Kimmins and D. J. Gooch. *Metal Science*, 17(11):519–532, 1983.

[98] S. Matsuda and Y. Okamura. *Trans. Iron Steel Inst. Jpn.*, 14(1):444–449, 1974.

[99] S. Matsuda and Y. Okamura. *Trans. Iron Steel Inst. Jpn.*, 14(1):363–368, 1974.

[100] R. Homma. *Trans. Iron Steel Inst. Jpn.*, 14(1):434–443, 1974.

[101] J. Hilliard. *Metal Progress*, pages 99–100, May 1964.

[102] P. J. Goodhew, J. Humphreys, and R. Beanland. *Electron microscopy and analysis*. Taylor & Francis, 3rd. edition, 2001.

[103] Oxford Instruments. *Manual of HKL Technology Channel 5*, 2007.

[104] J. R. Michael. In N. Yao and Z. L. Wang, editors, *Handbook of microscopy for nanotechnology*, chapter 13: characterization of nanocrystalline materials using electron backscatter diffraction in the scanning electron microscope. Kluwer Academic Publishers, New York, 2005.

[105] S. X. Ren, E. A. Kenik, K. B. Alexander, and A. Goyal. *Microsc. Microanal.*, 4(1):15–22, 1998.

[106] S. Kikuchi. *Proc. Imp. Acad.*, 4(6):271–278, June 1928.

[107] P. V. C. Hough. Method and means for recognizing complex patterns. US patent 3,069,654, 1962.

[108] D. J. Dingley. In *Electron backscatter diffraction in materials science*, chapter 1: the development of automated diffraction in scanning and transmission electron microscopy. Kluwer Academic Publishers, New York, 2000.

[109] G. S. Rohrer. *Structure and bonding in crystalline materials*. Cambridge University Press, 2001.

[110] B. L. Adams, S. I. Wright, and K. Kunze. *Metall. Trans. A*, 24A(4):819–831, 1993.

[111] J. R. Michael. In *Electron backscatter diffraction in materials science*, chapter 7: phase identification using electron backscatter diffraction in the scanning electron microscope. Kluwer Academic Publishers, New York, 2000.

[112] Y. Li, X. Han, L. Ji, Y. Feng, and C. Huo. In *Proceedings of 7th international pipeline conference*, Calgary, Alberta, Canada, 2008.

[113] V. Venegas, F. Caleyo, J. L. González, T. Baudin, J. M. Hallen, and R. Penelle. *Scripta Mater.*, 52(2):147–152, 2005.

[114] V. Venegas, F. Caleyo, J. M. Hallen, T. Baudin, and R. Penelle. *Metall. Mater. Trans. A*, 38A(5):1022–1031, 2007.

[115] L. S. Birks. In P. J. Elving and I. M. Kolthoff, editors, *Electron probe microanalysis*, volume 17 of *Chemical analysis*. Wiley-Interscience, 1963.

[116] G. R. Speich, L. J. Cuddy, C. R. Gordon, and A. J. DeArdo. In A. R. Marder and J. I. Goldstein, editors, *Phase Transformations in Ferrous Alloys*, pages 341–389, Warrendale, Pennsylvania, USA, 1984. TMS–AIME.

[117] R. L. Bodnar and S. S. Hansen. *Metall. Mater. Trans. A*, 25A(4):665–675, 1994.

[118] S. Jones and H. K. D. H. Bhadeshia. *Metall. Mater. Trans. A*, 28A(10):2005–2103, 1997.

[119] S. Jones and H. K. D. H. Bhadeshia. *Acta Materialia*, 45(7):2911–2920, 1997.

[120] H. Kristoffersen and P. Vomacka. *Materials and Design*, 22(8):637–644, 2001.

[121] K. Fujita, A. Yoshida, and K. Nakase. *Bull. JSME*, 22(169):994–1000, 1979.

[122] A. Lambert-Perlade, A. F. Gourgues, and A. Pineau. *Acta Materialia*, 52(8):2337–2348, 2004.

[123] Y. M. Kim, S. Y. Shu, H. Lee, B. Hwang, S. Lee, and N. J. Kim. *Metall. Mater. Trans. A*, 38A(8):1731–1742, 2007.

[124] S. Y. Shin, S. Y. Han, B. Hwang, C. G. Lee, and S. Lee. *Materials Science and Engineering A*, 517(1–2):212–218, 2009.

[125] Y. Li and T. N. Baker. *Mater. Sci. Technol.*, 26(9):1029–1040, 2010.

[126] J. H. Chen, Y. Kituta, T. Araki, M. Yoneda, and Y. Matsuda. *Acta Metallurgica*, 32(10):1779–1788, 1984.

[127] C. Wang, X. Wu, J. Liu, and N. Xu. *Materials Science and Engineering A*, 438–440:267–271, 2006.

[128] S. Lee, B. C. Kim, and D. Kwon. *Metall. Trans. A*, 23A(10):2803–2816, 1992.

[129] National Physical Laboratory. NPL MTDATA software, 2006. Teddington, UK.

[130] G. Krauss and S. W. Thompson. *ISIJ Int.*, 35(8):937–945, 1995.

[131] Y. E. Smith, A. P. Coldren, and R. L. Cryderman. In *Proc. Symp. Toward improved ductility and toughness*, pages 119–142, Ann Harnor, MI, 1971. Climax Molybdenum Co.

[132] S. W. Thompson, D. J. Colvin, and G. Krauss. *Metall. Trans. A*, 21A(6):1493–1507, 1990.

[133] *Atlas for bainitic microstructures*, volume 1. ISIJ, Tokyo, 1992.

[134] L. J. Habraken and M. Economopoulos. In *Proc. Symp. Transformation and hardenability in steels*, pages 69–107, Ann Harnor, MI, 1967. Climax Molybdenum Co. and the University of Michigan.

[135] D. J. C. MacKay. In H. Cerjak, editor, *Mathematical Modelling of Weld Phenomena*, volume 3, pages 359–389. Institute of Materials, Minerals and Mining, 1997.

[136] R. C. Eberhart and R. W. Dobbins. *Neural Network PC Tools A practical guide.* Academic Press, California, 1990.